



Performance Evaluation of Lattice-Based Wicking Structures and Surface Roughness Reduction in Additively Manufactured Heat Pipes

Llywelyn Rhys Hughes

Thesis submitted to Cardiff University for the degree of Engineering Doctorate

Resilient Decarbonised Fuel Energy Systems
Centre of Doctoral Training

Supervisors: Dr. Daniel Pugh, Prof. Philip Bowen & Prof. Richard Marsh

Industrial Partner: HiETA Technologies Ltd. / Parker Aerospace

September 2024



*Camau bach
i gopa'r mynydd*



Summary

This thesis investigates the integration of Additive Manufacturing (AM) and heat pipe technologies. Reducing energy demand throughout the entire economy is key to cutting our dependency on fossil fuels and combating the effects of climate change. As passive thermal transfer devices, heat pipes present an opportunity to reduce system complexity and parasitic losses as well as overall system volume and mass. With the development and identified applications of AM increasing globally, an opportunity arises to integrate AM into heat pipe technologies, contributing to the benefits of Industry 4.0. This integration has several advantages including improved system integration, reduced heat transfer interface resistances and enhanced manufacturability of novel and innovative wicking structures which may otherwise be impossible to create. However, whilst AM's potential is undeniable, challenges such as the inherently high surface roughness, dimensional accuracy at micro-scale level and achievable pore dimensions may influence overall performance as characterised throughout this thesis.

A range of Body-Centred Cubic AlSi₁₀Mg lattice structures ranging in cell sizes and strut thicknesses down to 0.70mm and 0.15mm, respectively, were manufactured in both horizontal and vertical orientations to push the boundaries of Laser Powder Bed Fusion with commercially available feedstock. The samples underwent rigorous testing to characterise their geometric accuracy with the use of 3D profilometry, standard microscopy, SEM, μ XCT and a newly developed Lattice Analysis Tool (LAT). Further experiments were conducted and benchmarked against other literature-based AM and conventional wicking structures to determine their capillary performance and permeability; two key heat pipe performance indicators. The vertical samples were overall found to be superior to the horizontally printed equivalents with sample V12 showing most promising results indicating an optimal capillary performance of 0.782 μ m and a Darcyan permeability of 2.16x10⁻⁹ m².

Chemical polishing of the AlSi₁₀Mg lattice samples was undertaken for the first time to investigate the effects of reducing surface roughness on the fluidic performance of the wicking structures. Results found the complete removal of agglomerated particles and a 60% reduction in surface roughness, 36.8% increase in capillary performance and a 130% increase in permeability. The identified delay in the onset of the Forchheimer regime, together with



the improvements in capillary performance, shows the potential of chemical polishing in allowing for extended operating flows, thermal loads and heat pipe lengths increasing their scope of applications.

The advantages and limitations of the AM wicking structures identified in this research make them particularly suited for applications working with gravity (as opposed to against gravity with condenser below evaporator) or in zero gravity environments such as spacecraft technology in addition to other high value sectors. This study highlights the potential of AM wicking structures for heat pipe applications and their performance enhancement through post-processing offering significant prospects for future developments.

Acknowledgments

I would like to take this opportunity to show my deepest appreciation to my supervisory team: Daniel Pugh, Phil Bowen and Richard Marsh for the unwavering support, guidance and encouragement they have provided over the past few years.

I am extremely grateful for the support of Steve Morris, Jack Thomas and Tony Giles at the Gas Turbine Research Centre with conducting the permeability experiment, Angela Sobrienski and Tyrone Jones at the Technology Research Hub for facilitating the chemical polishing study and to Elizabeth Evans at the Henry Royce Institute for the acquisition of the XCT data. I would like to extend my gratitude to the wider CDT team, in particular Robin Irons and Claudia Matz for leading the programme and to Gina Goddard-Bell for her continuous assistance and annual supply of tomato plants!

I am thankful for the financial support of HiETA Technologies Ltd./ Parker Aerospace in addition to their experience and knowledge in getting the samples manufactured.

This would not have been possible without the support, laughter and positivity of both old and new friends.

Hoffwn ddiolch o waelod fy nghalon i fy nheulu am ei charedigrwydd a chefnogaeth dros y blynyddoedd. Ac i fy ngwraig, Sarah. Mae dy gariad, dy amynedd a dy gred ynof fi wedi fy nghefnogi ac ysbrydoli drwy cyfnodau anoddaf y daith. Hedbba chdi ni allaf wedi medru ei gwblhau. Nid allaf fynegi pa mor ffodus ydw i i gael teulu mor garedig yn rhan o fy mywyd.



Nomenclature

Parameters

A	Area
D_{eq}	Equivalent Diameter
g	Gravitational Acceleration
h	Rise Height
K	Permeability
L	Length
M	Merit Number
mLEP	Minimum Liquid Entry Pressure
P_c	Capillary Pressure
P_h	Hydrostatic Pressure
P_f	Frictional Pressure Loss
r	Pore Radius
S_a	Arithmetic Mean Height
S_q	Root Mean Square Height
S_p	Maximum Peak Height
S_v	Maximum Valley Height
S_z	Maximum Height
v	Fluid Velocity
ε	Porosity
σ	Surface Tension
μ	Viscosity
ρ	Density
θ	Contact Angle

Abbreviations

AM	Additive Manufacturing
BCC	Body-Centred Cubic
CP	Chemical Polishing
CHP	Conventional Heat Pipe
DfAM	Design for Additive Manufacturing
EBM	Electron Beam Melting
EDX	Energy Dispersive X-Ray
EP	Electro Polishing
HP	Heat Pipe
LAT	Lattice Analysis Tool
LHP	Loop Heat Pipe
LP	Laser Polishing
NCG	Non-condensable Gas
PBF	Powder Bed Fusion
PHP	Pulsating Heat Pipe
RSD	Relative Standard Deviation
RSE	Relative Standard Error
SE	Standard Error
SEM	Scanning Electron Microscopy
SLM	Selective Laser Melting
VCHP	Variable Conductance Heat Pipe
XCT	X-ray Computed Tomography



List of Figures

Figure 1-1: Globally averaged combined land and ocean surface temperature anomaly. Figure reproduced from [2]	1
Figure 1-2: Globally averaged greenhouse gas concentration. Figure reproduced from [3]	1
Figure 1-3: Global average per-capita GHG. Figure reproduced from [4].....	2
Figure 1-4. Illustration of conventional heat pipe.	4
Figure 1-5: Idealised cycle of a heat pipe, figure apated from [16].....	5
Figure 1-6: Typical temperature - entropy diagram of a heat pipe, figure apated from [16].	6
Figure 1-7. LPBF Process flow Summary.....	7
Figure 1-8. Simplified LPBF/ EBM printer components.	8
Figure 2-1. Simplified schematic of a Loop Heat Pipe, figure reproduced from [33].....	12
Figure 2-2. Two configurations of pulsating heat pipe: (i) open loop an (ii) closed loop, figure reproduced from [30].	13
Figure 2-3. Variable Conductance Heat Pipe schematic, figure reproduced from [37].	14
Figure 2-4. Schematic of Vapour Chamber, figure reproduced from [39].	15
Figure 2-5. SEM images of composite wick with two kinds of sintered powder (a) irregular powder (Sample: CI75–110); (b) spherical powder (Sample: CS75–110), figure reproduced from [43].	19
Figure 2-6. Novel biomimetic-based heat pipe wick design, figure reproduced from [45].	20
Figure 2-7. Triple and critical temperature point and useful temperature range for various heat pipe working fluids.....	22
Figure 2-8. Merit number for a range of typical heat pipe working fluids at varying temperature with logarithmic scale.	23

Figure 2-9. Horizontal force balance of a two fluid phase system on a solid surface, where σ , σ_{ws} and σ_{nws} represent the liquid surface tension, wetting-solid interfacial tension and non-wetting-solid surface energy.	25
Figure 2-10. Schematic of Young's model (top), Wenzel's Model (bottom-left) and the Cassie-Baxter Model (bottom-right).....	26
Figure 2-11. Example of hydrophilic nature of a Hosta plant.....	28
Figure 2-12. Superhydrophobic nature of Salvinia Molesta at different magnifications, figure reproduced from [63]......	28
Figure 2-13. Typical heat pipe performance map, figure reproduced from [65].	31
Figure 2-14. Flattened and bent heat pipe for forced convection laptop thermal management (left) and CPU heat pipe cluster heat exchanger (right).	32
Figure 2-15. Scopus search analysis with keywords: ("heat pipe" OR "heat pipes") AND ("satellite" OR "satellites" OR "spacecraft"), data collected 29/08/2024.	33
Figure 2-16. Orbiting spacecraft heating simplified overview, figure reproduced from [70].	34
Figure 2-17. Kilopower system conceptual design and the thermal management system, figure reproduced from [77]......	37
Figure 2-18. Micro-heat pipe embedded in a bipolar plate, figure reproduced from [14].	38
Figure 2-19. PEMFC stack cooled by flat-plate heat pipes, figure reproduced from [80]. ...	39
Figure 2-20. Scopus results for ("Additive Manufacturing" OR "3D Printing"); ("Heat Pipe" OR "Heat Pipes"); [("Additive Manufacturing" OR "3D Printing") AND ("Heat Pipe" OR "Heat Pipes")], data collected 17/06/2024.....	41
Figure 3-1. Lattice geometry parameters (Top) and 3D trimetric view (bottom)	51
Figure 3-2. Proposed Build plate layout (Left) and printed components with traveller samples (Right).....	52
Figure 3-3. Sensofar S Mart 3D optical sensor. Figure reproduced from [126].	55

Figure 3-4. Example 3D Optical scan of unit cell lattice structure: Stacked image (top left), Topography (top right) and extracted profile of a single strut (bottom).	56
Figure 3-5. Comparison of large (left) and small (right) layer height on the overall intended design.....	57
Figure 3-6. Example image of areal Primary Surface (top), Roughness Surface (middle) and Waviness Surface (bottom).....	58
Figure 3-7. Example image of profile Primary Surface (top), Roughness Surface (middle) and Waviness Surface (bottom) along approximately one-and-a-half-unit cell.	59
Figure 3-8. Main components of SEM process, figure adapted from [132].	61
Figure 3-9. Nikon Metrology “High Flux” Bay.....	62
Figure 3-10. Example of ring artifact seen within the reconstructed slices	64
Figure 3-11. Workflow of porosity determination via XCT analysis.	64
Figure 3-12. Example of histogram identifying the voids and solid classes of sample V1 ..	65
Figure 3-13. Example of fully segmented sample, identifying the Solid (orange), main pores (purple) and defective pores (multicoloured) for sample V1.....	65
Figure 3-14. Formed meniscus surrounding sample during capillary rise experiment.	68
Figure 3-15. Capillary Rate-of-Rise experimental setup	72
Figure 3-16. Initial trial showing the high contact angle and hydrophobicity of water on the manufactured porous surface.	73
Figure 3-17. Effects over overcoming the LEP with DI water. (a) drop with no forced pressure, (b) applying forced pressure with syringe, (c) t: 0s, (d) t: 0.45s, (e) t:1.50s and (f) t: 1.80s.....	75
Figure 3-18. Example of code segmentation with raw IR image (Right), greyscale image (centre) and binarised image (Left)	76
Figure 3-19. Comparison between rise height of developed automatic Matlab code and manual ImageJ measurements.....	77

Figure 3-20. Comparison between manual and automatic rise heights of several samples with line of best fit.....	78
Figure 3-21. Designed setup for permeability test.....	81
Figure 3-22. Impact of back pressure on measured differential pressure across a range of flow rates.....	82
Figure 3-23. The effects of both temperature and pressure on the resultant dynamic viscosity with an enlarged view, data collected with CoolProp [51].....	83
Figure 3-24. Image of designed casting mould assembly (Left) and manufactured seal with sample (Right).....	84
Figure 3-25. Developed FlexLogger graphical user interface.....	85
Figure 3-26. Sample holder for chemical polishing.....	87
Figure 4-1. LAT User Interface.....	89
Figure 4-2. LAT Workflow.....	90
Figure 4-3. Scaling user interface example. Initial instruction window (Top), user input (Bottom-Left) and scaled results (Bottom-Right).....	90
Figure 4-4. 2D scanned images of lattice coupons identifying masking options. From left to right: Circle, rectangle, polygon and freehand.....	91
Figure 4-5. Binarised image with a Gaussian filter standard deviation of 0.01 (Top) and 2 (Bottom).....	92
Figure 4-6. Histogram of greyscale image.....	93
Figure 4-7. Threshold level: too low (Left), acceptable (Centre), too high (Right) for lattice structure.....	94
Figure 4-8. LAT pore identification.....	94
Figure 4-9. Area histogram (Left) and diameter heatmap (Right).....	96
Figure 4-10: LAT diameter heatmap function example Matlab code.....	96
Figure 4-11 Strut analysis example of an additively manufactured lattice structure with units generalised to pixel count.....	97

Figure 4-12 Example of inverted image with struts detected (white) and pore space (black)	98
Figure 4-13. Canny Edge Detection example of analysed lattice structure with thresholding values of 0 (left) and 0.5 (right).	98
Figure 4-14. Example of edge detection and manual measurement feature.	99
Figure 4-15: Example of CAD Comparison function where the red lines represent the detected boundary of microscope image.....	100
Figure 4-16. Example of manual measurements performed via profilometry.....	101
Figure 4-17 Measurement comparison between LAT and SensoScan.	102
Figure 5-1. Samples 7 Horizontal (Bottom) and vertical (Top), identifying the severity of warpage in the horizontal sample, with magnified sections each section.....	103
Figure 5-2. Example of dislocated struts on sample H12 (bottom) compared to V12 (top), where the large dislocation (circle) is shown and the differing colours highlighted on the labels (square).	104
Figure 5-3. SEM Image of sample H12 showing dislocated struts at centre of front face.	105
Figure 5-4. Measurement locations of strut analysis	106
Figure 5-5. Comparative analysis of measured strut diameters at various positions along their lengths for both horizontal (Top) and vertical (Bottom) samples with error bars representing the standard deviation.....	107
Figure 5-6. Strut Diameter percentage deviation from mean for both horizontal (Top) and Vertical (Bottom) samples.	109
Figure 5-7. Comparison between desired and measured average strut diameter.	110
Figure 5-8. Deviation (Top) and normalised percentage deviation (Bottom) of the measured strut diameters from the designed CAD.	111
Figure 5-9. Comparative analysis of measured cell sizes for horizontal (top) and vertical (bottom) sample sets, with the standard deviations represented by the error bars.....	113



Figure 5-10. Cell Size percentage deviation from mean for both horizontal (top) and vertical (bottom) samples.....	114
Figure 5-11. Comparison between desired and measured average cell size.	115
Figure 5-12. Deviation (Top) and normalised percentage deviation (Bottom) of the measured cell sizes from the designed CAD.....	116
Figure 5-13. Investigated surfaces for pore analysis. LH (left), Front (middle) and RH surface (right).....	117
Figure 5-14. Average measured pore diameter for the front, left and right faces of both horizontal (Top) and vertical components (Bottom), with standard deviation represented by the error bars.....	118
Figure 5-15. Average sample pore diameter.	119
Figure 5-16. Pore size deviation from designed CAD.....	120
Figure 5-17. Pore size % deviation from designed CAD.....	120
Figure 5-18. Horizontal (Top) and Vertical (Bottom) heatmap pore diameter distribution of samples 1 (Left), 6 (Centre) and 11 (Right).....	122
Figure 5-19. Arithmetic mean surface roughness at the top, middle and bottom locations for both horizontal (top) and vertical (bottom) samples.	125
Figure 5-20. Averaged arithmetic mean surface roughness, S_a , for both horizontal and vertical samples.	126
Figure 5-21. SEM Image of sample H6 (Top) and V6 (bottom).....	127
Figure 5-22. Root Mean Square height at the top, middle and bottom locations for both horizontal (top) and vertical (bottom) samples.....	129
Figure 5-23. Averaged Root Mean Square height, S_q , for both horizontal and vertical samples.	130
Figure 5-24. Maximum Peak height at the top, middle and bottom locations for both horizontal (top) and vertical (bottom) samples.....	131
Figure 5-25. Maximum peak height difference.	132

Figure 5-26. Maximum Peak height, S_p , for both horizontal and vertical samples.....	133
Figure 5-27. Maximum Valley height at the top, middle and bottom locations for both horizontal (top) and vertical (bottom) samples.....	134
Figure 5-28. Maximum valley height difference between measurement locations.	135
Figure 5-29. Averaged maximum valley height, S_v , for both horizontal and vertical samples.	136
Figure 5-30. Maximum height at the top, middle and bottom locations for both horizontal (top) and vertical (bottom) samples.....	137
Figure 5-31. Maximum height difference between measurement locations.....	138
Figure 5-32. Maximum height, S_z , for both horizontal and vertical samples.....	139
Figure 5-33. Comparison between averaged arithmetic mean surface roughness of side and front faces of horizontal samples and the front face of the vertical samples.....	140
Figure 5-34. Comparison between root mean square height of side and front faces of horizontal samples and the front face of the vertical samples.	141
Figure 5-35. Apparent porosities for both horizontal and vertical sample sets.....	145
Figure 5-36. 3D plot for apparent porosities of both horizontal and vertical samples.	146
Figure 5-37. True porosities for both horizontal and vertical sample sets.....	146
Figure 5-38. 3D plot for true porosity comparison.....	147
Figure 5-39. 3D plot for porosity deviation from CAD.....	148
Figure 5-40. 3D plot for porosity percentage deviation from CAD.....	148
Figure 5-41. 3d reconstruction (top) and sliced example(bottom) of samples V1, H1 and V4 (left – right).....	150
Figure 5-42. Histogram of sample V4 (top) and H4 (bottom).....	151
Figure 5-43. Grayscale image (left) and segmented image (right) for sample V4.....	152
Figure 5-44. 10 largest pores (left) and remaining smaller non-interconnecting pores (right) for sample V4.....	152

Figure 5-45. Half-cell height evolution for sample V5 (left) and V12 (right)	153
Figure 5-46. XCT Apparent porosity results for vertical (top) and horizontal (bottom) samples.	155
Figure 5-47. XCT True porosity results for vertical (top) and horizontal (bottom) samples.	156
Figure 5-48. Example slice (left) and segmented image (right) of Sample V1.....	157
Figure 5-49. XCT Trapped porosity results for vertical (top) and horizontal (bottom) samples.	158
Figure 5-50. Identification of internal damage to sample H12.....	159
Figure 5-51. XCT image of a single layer of unit cells of samples H12 (top) and V12 (bottom.	160
Figure 6-1. Dynamic rise height of several samples	163
Figure 6-2. Averaged maximum equilibrium rate of rise height for each sample, with the error bars representing the standard deviation of repeated results.	164
Figure 6-3. Deviation between the maximum rise height of the horizontal samples from the vertical counterpart.	165
Figure 6-4. The effects of pore diameter on the maximum equilibrium height for all samples showing linear relationship.....	166
Figure 6-5. Maximum Jurin's height and % deviation of measured rise heights from theoretical values.....	167
Figure 6-6. The relationship between the measured percentage deviation of the maximum height and Jurin's height with the line of best fit for the vertical samples.	168
Figure 6-7. Example plot of $1/h$ against dh/dt for 8 different test points with several lines of best fits.	169
Figure 6-8. Averaged slope of each raw sample where $x = 1/h$ and $y = dh/dt$ with the standard deviation represented by the error bars.	170

Figure 6-9. Averaged capillary performance (K/r_{eff}) of each raw sample with the standard deviation represented by the error bars.	171
Figure 6-10. Effects of pore size (top) and porosity (bottom) on the capillary performance with histogram distribution, line of best fits for each strut thickness (T) grouping and the standard deviation represented by the error bars.	173
Figure 6-11. Inherent system noise for sample H3 at 4.00g/s and V9 at 1.00g/s with 2s moving average and enlarged section of sample V9.	176
Figure 6-12. Histogram of calculated combined SE for 300 test points.	178
Figure 6-13. Variations of combined SE with differential pressure with distribution curves.	178
Figure 6-14. Relative Standard Deviation of repeated test.	179
Figure 6-15. Differential pressure of selected samples over varying mass flow rates.	180
Figure 6-16. Calculated permeability of selected samples over varying mass flow rates.	181
Figure 6-17. Effects of velocity on calculated Re_K values.	184
Figure 6-18. Permeability-based Reynolds Number (Re_K) at transition point for each sample.	185
Figure 6-19. Influence of pore diameter (top) and porosity (bottom) and calculated permeability-based Reynolds number transition.	186
Figure 6-20. Darcy Permeability with respective uncertainty identified by the error bars.	187
Figure 6-21. Effects of change in porosity (Top) and pore diameter (Bottom) on measured Darcy permeability.	190
Figure 6-22. Example of fitted curves for a range of samples for determination of the Darcyan and non-Darcyan Forchheimer coefficients.	191
Figure 6-23. Forchheimer Permeability (K_1) for each sample along with % difference from Darcy permeability (K) values.	192
Figure 6-24. Forchheimer inertial term (K_2) for each sample.	193

Figure 7-1. SEM Image and XCT analysis of Sample V1.2.	196
Figure 7-2. Element spectrum of EDX map scan on sacrificial sample V1.2	197
Figure 7-3. Combined EDX map of sample V1.2 after hydrochloric acid etch.....	199
Figure 7-4. Chemically Polished (Left) and Raw (Right) stacked microscopy images of samples V6 (Top) and V12 (Bottom).....	201
Figure 7-5. Damaged side face of sample H12 following chemical polishing.....	202
Figure 7-6. Microscope image of Chemically polished sample H12.	202
Figure 7-7. Measured strut diameters of polished samples with reduction from raw state and deviation from original CAD design. N.B. Sample H10 shows significant damage.....	205
Figure 7-8. Microscope image of Sample V1 identifying surface keyhole pores.....	207
Figure 7-9. Sample V1 surface keyhole pores identification with LAT.	207
Figure 7-10. Pore diameter heatmap for sample H1 identifying surface keyhole pores (left) and warpage (right) with smaller keyhole pores disregarded.....	208
Figure 7-11. Measured pore diameters of polished samples with increase from raw state and deviation from original CAD design. N.B. Sample H10 shows significant damage.....	209
Figure 7-12. Arithmetic mean surface roughness of chemically polished samples with error bars representing the standard deviation of repeated measurements and percentage difference from raw state. N.B. Sample H10 shows significant damage.....	210
Figure 7-13. Root mean square height of chemically polished samples with error bars representing the standard deviation of repeated measurements and percentage change from raw state. N.B. Sample H10 shows significant damage.	212
Figure 7-14. Apparent porosity with a 8% uncertainty error and apparent porosity change of chemically polished samples. N.B. Sample H10 shows significant damage.	214
Figure 7-15. True porosity with a 8% uncertainty error and apparent porosity change of chemically polished samples. N.B. Sample H10 shows significant damage.	214
Figure 7-16. Equilibrium rise heights (Acetone) of the polished samples % reduction from their raw state and standard deviation represented by the error bars.	215

Figure 7-17. Effects of pore diameter on the equilibrium rise height with the standard deviations represented by the error bars.....217

Figure 7-18. Percentage deviation of equilibrium rise heights from Jurin's law for both raw (R) and polished (P) samples.....218

Figure 7-19. Averaged capillary performance of both raw (R) and polished (P) samples with standard deviation represented by the error bars and percentage change from their raw state.219

Figure 7-20. Effects of pore size (top) and porosity (bottom) on the capillary performance of acetone with the standard deviation represented by the error bars.221

Figure 7-21. Maximum rise heights of water for the polished samples, with percentage change from acetone and the error bars representing the standard deviations of the repeated trials.....224

Figure 7-22. Calculated Bond numbers for all polished samples for acetone and water with a characteristic length of r_p and r_{eff}225

Figure 7-23. SEM images of samples V5 (top) and H5 (bottom) with blue squares representing EDX scan area.226

Figure 7-24. Capillary performance of polished samples with water as the working fluid and percentage change from acetone and the error bars representing the standard deviations of the repeated trials.227

Figure 7-25. Effects of pore size (top) and porosity (bottom) on the capillary performance of water with the standard deviation represented by the error bars.229

Figure 7-26. Exaggerated illustration of defective channel (Red) along the side edge of samples.230

Figure 7-27. Averaged differential pressure measurements over a range of mass flow rates of the polished samples.....231

Figure 7-28. Measured permeability over a range of mass flow rates for all polished samples (P).....232

Figure 7-29. Influence of velocity on the permeability-based Reynolds number of the polished samples.....233

Figure 7-30. Transitional permeability-based Reynolds number for all polished samples with % change from raw state.233

Figure 7-31. Darcy permeability (K) and Forchheimer permeability (K_1) of all polished samples with their respective % increase from the raw state and standard deviation represented by the error bars.235

Figure 7-32. Determined Forchheimer correction (K_2) of polished samples with % increase from their raw state and standard deviation represented by the error bars.236

Figure 7-33. Comparison of the measured and predicted $\Delta P/L$ for both raw (bottom) and polished (top) samples where the error bars of the polished samples are represented by the standard deviation and that of the raw samples by the previously determined RSD (Table 6-1).237

Figure 7-34. Literature comparison of capillary performance of raw samples with acetone (R), polished samples with acetone (P) and polished samples with water (W) to other AM-based wicking structures.241

Figure 7-35. Literature comparison of permeability of raw samples (R) and polished samples to other AM-based wicking structures.243

Figure 7-36. Literature comparison of capillary performance of raw samples with acetone (R), polished samples with acetone (P) and polished samples with water (W) to other conventional wicking structures.....245

Figure 7-37. Literature comparison of permeability of raw samples (R) and polished samples to other conventional wicking structures.....247

Figure 11-1. drawing of PLA capillary test rig.272

Figure 11-2. XCT sample mounting rig.....273

Figure 11-3 Comparative analysis of both automatic and manual strut measurement features.....275

Figure 11-4. Heat exchanger channels cross-section. Original (Left), region identifier (Right).	276
Figure 11-5. Example area heatmap of heat exchanger channels.....	277
Figure 11-6. Analysed optical microscope images of mesh wick with Al ₂ O ₃ /DI nanofluids as working fluid (a) at 0 months of manufacturing, (b) after 9 months of successive heat input of 72 W, and (c [x100] ,d [x200]) after 9 months of successive heat input of 12 W. Figure adapted from [175].	278
Figure 11-7. Wire comparative analysis with LAT's automatic strut analysis and manual features.....	279
Figure 11-8. Al ₂ O ₃ nanoparticle analysis regions from TEM [175].	280
Figure 11-9: Defective AM Counterflow Burner Cooling Nozzle cross-section (Left) and Canny Edge detection (Right) with orange dashed lines representing the direction of porosity inline with the build plane	281
Figure 11-10 Visualisation of heatmap distribution of the pore diameter within the nozzle cross-section.	282
Figure 11-11. Calibration curves for PT1 and PT2.....	291

Content

1. Introduction.....	1
1.1 A Climate Change Perspective.....	1
1.2 Heat Pipe Overview.....	4
1.3 Additive Manufacturing Overview.....	7
1.4 Additively Manufactured Heat Pipes for the Passive Transfer of Heat.....	10
1.5 Research Aim:.....	10
2. Theoretical foundations and Literature Review.....	11
2.1 Types of Heat Pipes.....	11
2.1.1 Conventional Heat Pipe.....	11
2.1.2 Looped Heat Pipe.....	12
2.1.3 Pulsating Heat Pipe.....	13
2.1.4 Variable Conductance Heat pipe.....	13
2.1.5 Vapour Chamber.....	15
2.2 Wicking Structures.....	15
2.2.1 Traditional Wicking Structures.....	16
2.2.2 Biomimetic Wicking Structures.....	19
2.3 Working Fluids.....	21
2.4 Contact Angle.....	25
2.4.1 Wenzel State.....	26
2.4.2 Cassie-Baxter Regime.....	27
2.4.3 Wettability in Natural structures.....	28
2.5 Operating Limits.....	30
2.6 Applications.....	31
2.6.1 Electronic Components.....	31
2.6.2 Spacecraft Technology.....	33
2.6.3 Fuel Cells.....	37
2.6.4 Additional Applications.....	40

2.7 Heat Pipe and Additive Manufacturing Integration	41
2.8 Surface Roughness Enhancements in the Additive Manufacturing Industry	45
2.9 Review Summary & Opportunities.....	48
2.10 Objectives.....	49
3. Experimental Design and Theoretical Frameworks.....	50
3.1 CAD Preparation.....	50
3.2 Manufacturing.....	52
3.3 Porosity Measurements	53
3.4 Geometry Validation	54
3.4.1 3D Profilometry	54
3.4.2 Scanning Electron Microscope	61
3.4.3 X-ray Computed Tomography (μ -XCT)	62
3.5 Experimental Campaign	67
3.5.1 Capillary Rate-of-Rise	67
3.5.2 Permeability.....	79
3.5.3 Chemical Polishing.....	86
4. Lattice Analysis Tool (LAT).....	89
4.1 File Import & Scaling.....	90
4.2 Mask & Crop.....	91
4.3 Binarise.....	91
4.4 Pore Analysis	94
4.5 Heatmaps & Histograms.....	96
4.6 Strut Analysis.....	97
4.7 Manual Measurements	98
4.8 CAD Comparison.....	100
4.9 LAT Robustness and Accuracy	101
5. Geometric Validation.....	103
5.1 Visual Inspection.....	103
5.2 Dimensional Accuracies.....	106
5.2.1 Strut Analysis	106
5.2.2 Cell Size Analysis.....	112



5.2.3 Pore Analysis.....	117
5.2.4 Dimensional Accuracy Summary	123
5.3 Surface Roughness	124
5.3.1 Arithmetic Mean Height, Sa	124
5.3.2 Root Mean Square height, Sq.....	128
5.3.3 Maximum Peak Heights, Sp	130
5.3.4 Maximum Valley Heights, Sv	133
5.3.5 Maximum Height, Sz.....	136
5.3.6 Comparison of Horizontal Faces.....	140
5.3.7 Surface Roughness Summary	143
5.4 Porosity Analysis.....	144
5.4.1 Apparent Porosity.....	145
5.4.2 True Porosity.....	146
5.5 XCT Analysis.....	150
5.5.1 XCT Porosity Analysis.....	154
5.5.2 Internal Defect Identification	159
5.6 Chapter Summary.....	161
6. Assessment of Raw AM Components.....	163
6.1 Capillary Rate-of-Rise	163
6.1.1 Max Height.....	164
6.1.2 Capillary Performance	169
6.2 Permeability	175
6.2.1 Determination of Measurement Uncertainties.....	175
6.2.2 Differential Pressure.....	180
6.2.3 Darcy – Forchheimer Transition	184
6.2.4 Darcy’s Permeability	187
6.2.5 Forchheimer Correction	191



6.3 Chapter Summary.....	194
7. Effects of Chemical Polishing & Literature Comparison.....	196
7.1 Initial Investigation.....	196
7.2 Analysis of polished samples.....	200
7.3 Geometric Impact.....	205
7.3.1 Strut Thickness.....	205
7.3.2 Pore Characteristics.....	207
7.3.3 Surface Roughness.....	210
7.3.4 Porosity.....	213
7.4 Capillarity of Polished Samples.....	215
7.4.1 Maximum Rise Height.....	215
7.4.2 Capillary Performance.....	219
7.4.3 Water Trials.....	222
7.5 Permeability of Polished Samples.....	230
7.6 Literature-Based Performance Benchmarking.....	241
7.6.1 AM Benchmarking.....	241
7.6.2 Conventional Benchmarking.....	245
7.7 Chapter Summary.....	238
7.7.1 Geometric Summary of Chemical Polishing.....	238
7.7.2 Capillary Summary of Chemical Polishing.....	239
7.7.3 Permeability Summary of Chemical Polishing.....	240
8. Conclusions.....	241
9. Recommendations for Further Work.....	251
10. References.....	252
11. Appendix.....	264
11.1 Patent information of various heat pipe and heat exchanger designs and system integration.....	265
11.2 Merit Number Matlab Script.....	269
11.3 Fixture Drawings.....	272



11.4 LAT Practical Case Studies	274
11.4.1 Additively Manufactured Lattice Structure	274
11.4.2 AM Heat Exchanger Channel	276
11.4.3 Screen Mesh Wick Deterioration	278
11.4.4 AM Counterflow Burner Cooling Nozzle	281
11.5 Capillary Rise Matlab Script.....	283
11.6 Pressure Transducer Calibration	290

1. Introduction

1.1 A Climate Change Perspective

Existing concerns surrounding climate change call for innovative approaches when developing new and existing technologies for reducing the environmental impact of humans. Adopted by 196 parties at the 21st Conference of Parties in 2015, the Paris Agreement is a legally binding treaty that aims to limit global warming to well below 2°C, preferably 1.5°C, of pre-industrial levels [1]. Global average temperature has been steadily increasing over the years, as shown in Figure 1-1. Consequently, land, habitats and species have been lost because of the ubiquitous threat of natural disasters and extreme weather events.

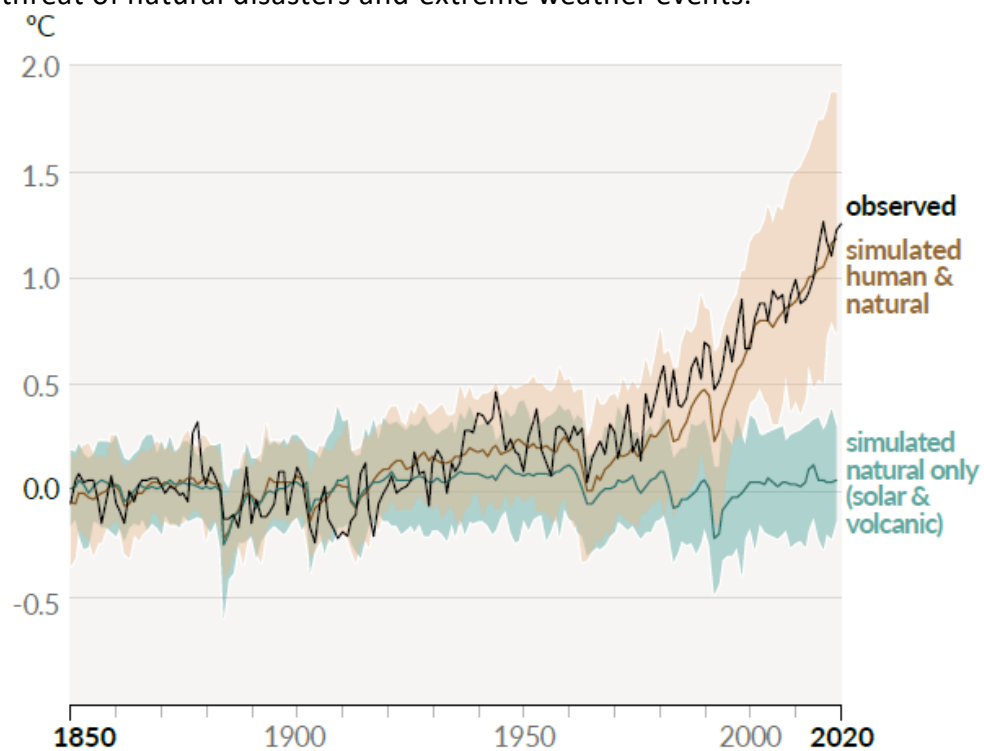


Figure 1-1: Globally averaged combined land and ocean surface temperature anomaly. Figure reproduced from [2]

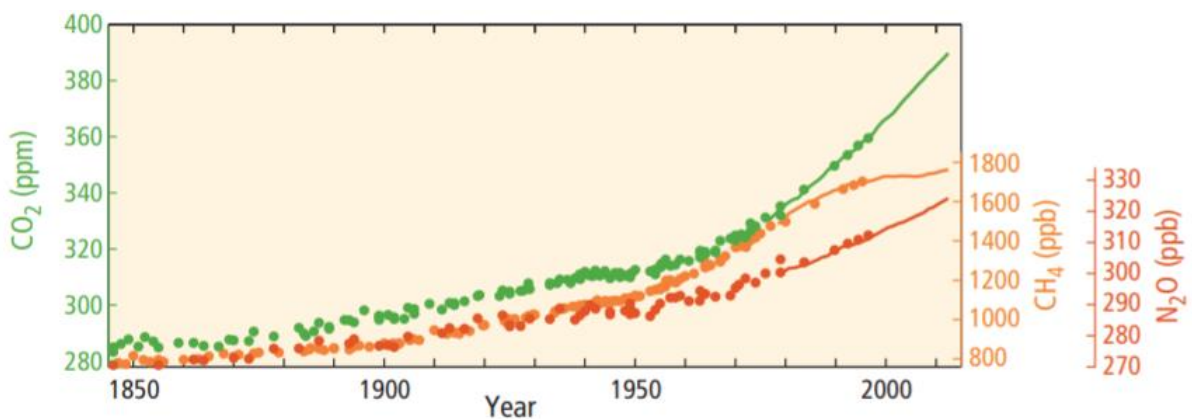


Figure 1-2: Globally averaged greenhouse gas concentration. Figure reproduced from [3]



As observed by the IPCC [2], there is a clear connection between human behaviour and the climate system, as anthropogenic emissions of greenhouse gases (GHGs) are currently the highest in recorded history, shown in Figure 1-2. Figure 1-1 and Figure 1-2 show the relationship between global average temperature and GHG emissions. Furthermore, the rate of increase of both GHG emissions and global average temperature have grown since the industrialisation of society, mainly driven by population and economic growth, as visualised in Figure 1-3.

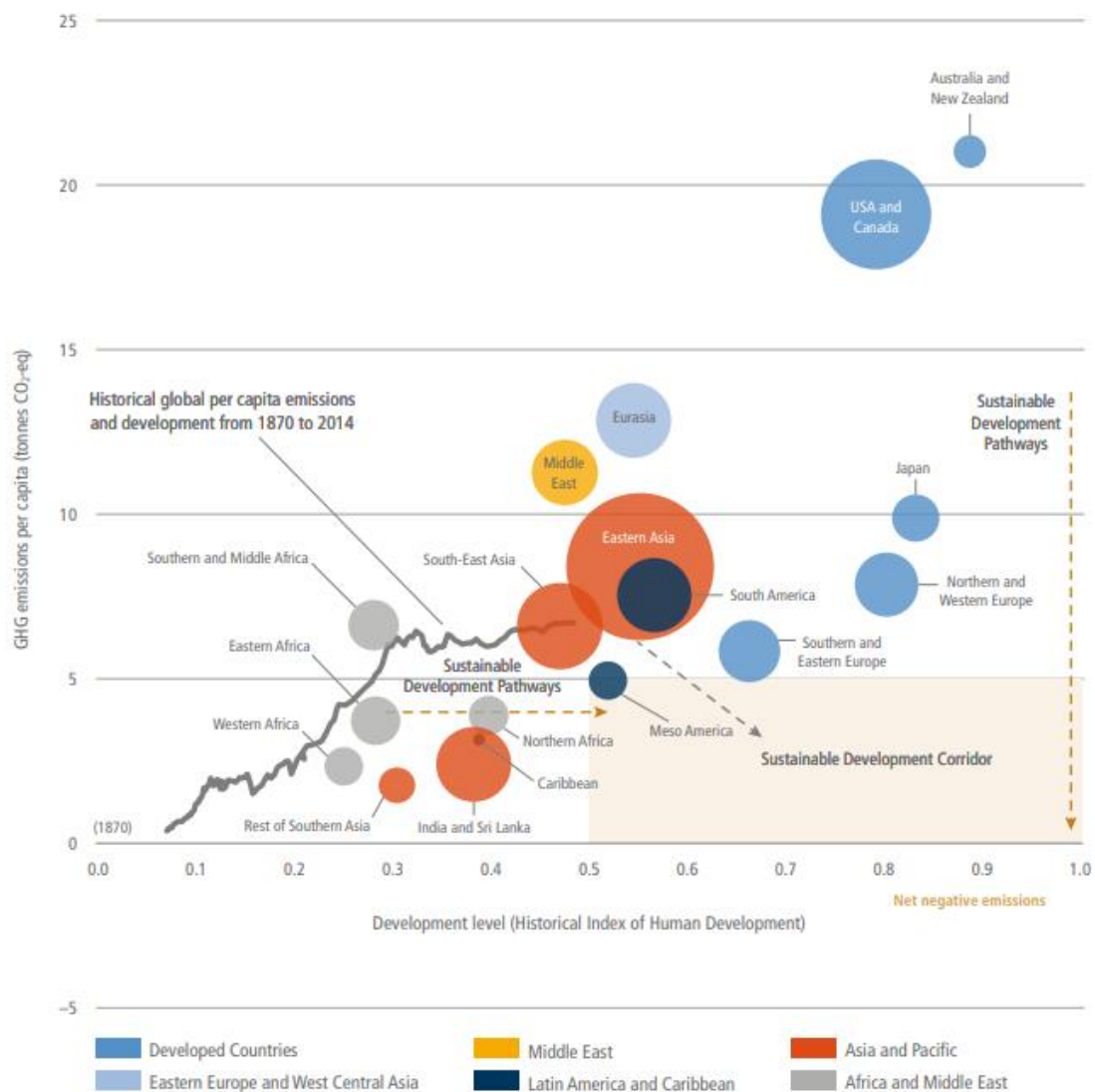


Figure 1-3: Global average per-capita GHG. Figure reproduced from [4]

The challenges surrounding climate change are recognised globally, with the UK government becoming the first major economy to pass laws to achieve net-zero emissions of all GHGs by 2050 [5] with a total of 120 other countries announcing similar targets to date [6].



Abundant studies are underway, and governments worldwide are collaborating to decarbonise energy intensive sectors, such as industry and transport, using novel technologies, electrification and alternative fuels. The UK's GHG emissions have reduced by 40% between 1990 to 2019, leading the way amongst G20 nations, which has mainly been driven by developments in the power sector [7].

If society is to achieve the required GHG emissions reduction and limit the effect of climate change, drastic shifts need to be made in the way we manage energy from generation and supply to consumption. The circular economy concept is based around improving products and services through implementing sustainable design and manufacturing practices. This includes improving the lifespan of products and reusing and recycling raw materials in addition to minimising waste. This concept and the reduction and recovery of waste can be considered for whole-system energy and heat applications. Several technologies have been implemented for heat recovery applications which often incur additional operational costs and energy for ancillary equipment which deviate from the circular economy concept [8].

As global population increases and society becomes more reliant on technology and electronic devices, behavioural change and consumer acceptability may be key barriers and delivery risks to reducing overall energy consumption [9]. However, further progress in improving system efficiency and minimising parasitic losses will play a vital role moving forward and reduce demand across the economy. Improvements such as these may offset 30% of the CO₂ increase linked to expanding demand for energy services by 2030 [10]. This may also result in reduced cost of the low-carbon power, hydrogen and CCUS-based systems [9].



1.2 Heat Pipe Overview

Methods for improving energy efficiency will differ from application to application. However, this research concentrates on advancing methods to recover and transfer waste heat within a system while reducing parasitic losses. One such way of transferring heat in a passive manner is utilising heat pipe technology. Heat pipes (HPs) have been utilised throughout industry since the development of the Perkins tube in the 1830s, and became commercially viable in 1944, initially for refrigeration system applications [8]. As is further discussed in Section 2.6, HPs have proven to be efficient devices for a wide range of applications at varying operating temperatures, including:

- computer and electronic components with typical operating temperatures of between 50 and 100°C at around 100W [11];
- space applications where no convective heat transfer to external environments will occur due to the lack of air and heat dissipation is purely reliant on conduction and radiation alone [12];
- fuel cell thermal management where typical efficiencies are between 40 and 60% of the fuel's lower heating value [13, 14].

Since their creation, the capabilities and development of heat pipes, specifically wicked heat pipes, has largely been limited by the manufacturing technology available. A wicked internal structure allows the devices to operate against gravity, which was not possible for their earlier wickless counterparts, also known as thermosyphons.

Heat pipes are widely considered as heat super conductors, which have thermal conductivity values several hundred times that of solid copper while maintaining an almost uniform temperature distribution across their length [15]. The two-phase system consists of three main sections – the evaporator, adiabatic and condenser sections – as shown in Figure 1-4.

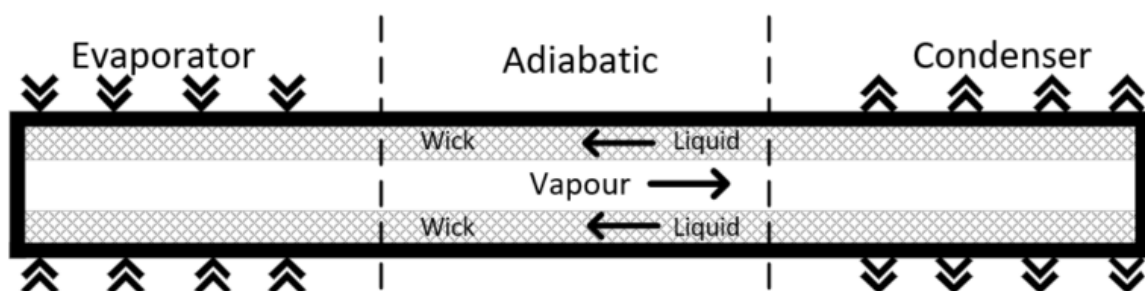


Figure 1-4. Illustration of conventional heat pipe.



The heat pipe is enclosed at both ends, with any air drawn out to sub-atmospheric pressure and a small amount of working fluid incorporated inside. Failure to sufficiently draw out air prior to fluid charging will result in the presence of non-condensable gases within the heat pipe which will limit the heat pipe's performance. The choice of working fluid is dependent on the application and the given operating temperatures and heat dissipation requirements. This is discussed further in Section 2.3. As heat is supplied to the evaporator end, it is transported through the pipe wall via conduction, where the working fluid evaporates and undergoes a phase-change. Due to the high internal vapour pressure, the vapour travels at near-sonic speed through the adiabatic section to the condenser end of the HP where the latent heat of vaporisation is released and condenses back into its liquid-phase. The idealised heat pipe cycle and T-S diagram is shown in Figure 1-5 and Figure 1-6, respectively.

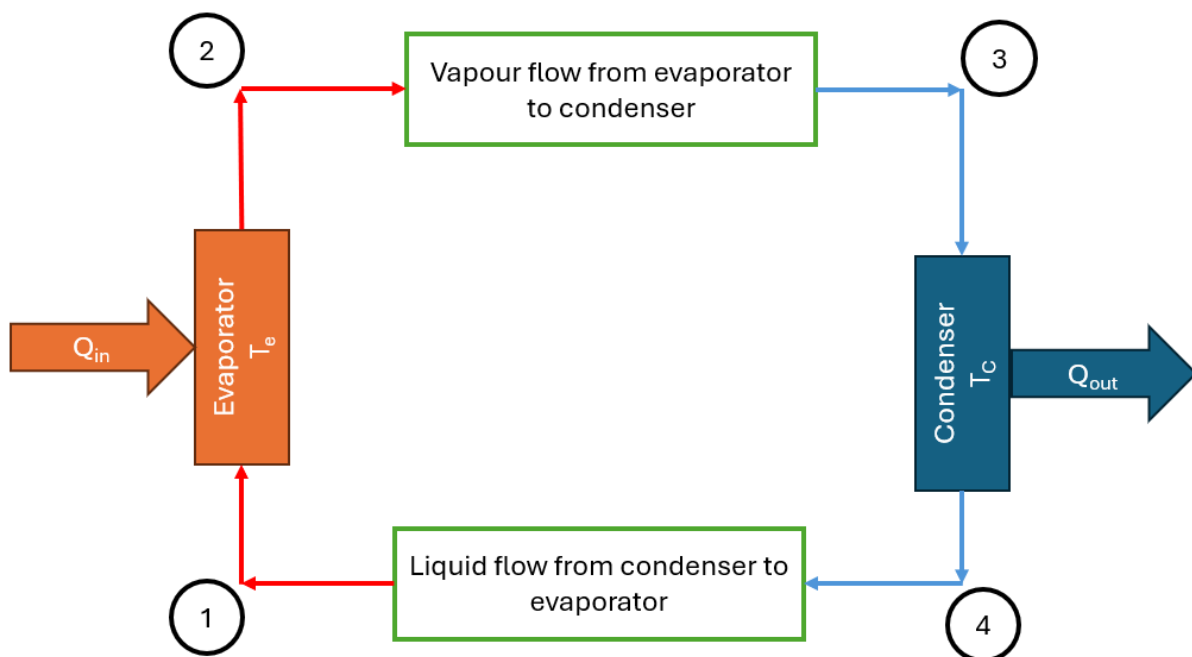


Figure 1-5: Idealised cycle of a heat pipe, figure apated from [16].



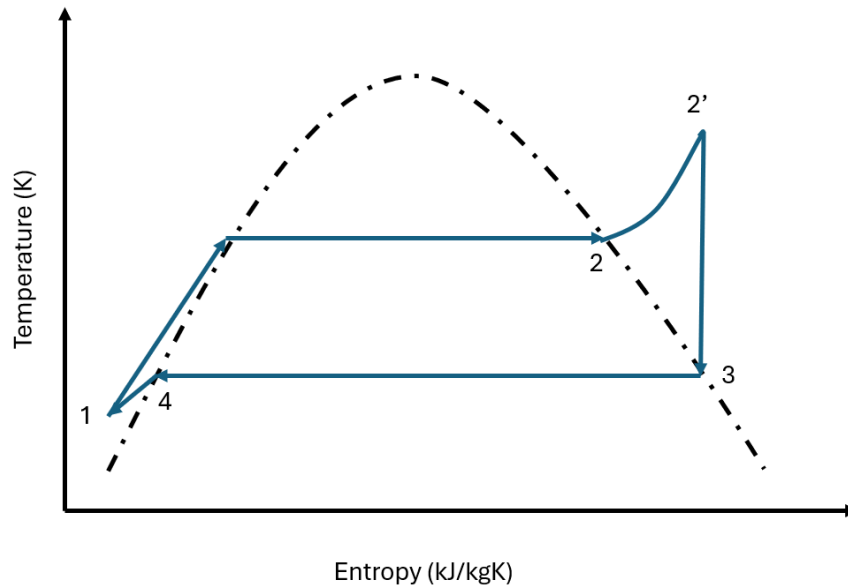


Figure 1-6: Typical temperature - entropy diagram of a heat pipe, figure adapted from [16].

Typically, the inner wall is constructed of a fine porous wicking structure to provide the required capillarity to complete the evaporation-condensation cycle. The capillarity is governed by the liquid surface tension, contact angle and pore radius of the wicking structure, as shown in Equation (1-1).

$$\Delta P_c = \frac{2\sigma \cos\theta}{r_p} \quad (1-1)$$

Evidently, a reduced pore size results in higher capillary pressure. However, a reduction in both pore size and porosity can increase the overall pressure losses along the heat pipe. The pressure loss within a heat pipe can be related to its permeability, as shown in Equation (1-2).

$$\frac{\Delta P}{L} = \frac{\mu}{K} v \quad (1-2)$$

Further analysis and review of the capillarity and permeability theory is shown in Sections 3.5.1.1 and 3.5.2.1, respectively. The trade off of capillary pressure and permeability is dependent on several factors including heat pipe length, operating orientation and heat load. Efficient wick enhancements may lead to reduced cycle recirculation time and hence improved heat transfer rates. There are a myriad of ways of manufacturing heat pipes and wick structures in particular and is reviewed further in Section 2.2. Advances in new



manufacturing techniques provide the opportunity for innovative development and optimisation.

1.3 Additive Manufacturing Overview

Integrating smart and intelligent technologies into virtual and physical environments is key for transforming traditional manufacturing and industrial practices into the fourth industrial revolution, also referred to as Industry 4.0 [17]. Additive Manufacturing (AM) has been shown to be a key enabler for the development of Industry 4.0, allowing for increased manufacturing flexibility, reduced waste, mass customisation and improved quality and productivity [18]. By allowing for the manufacturability of complex geometries that were previously impossible or very difficult to manufacture through conventional processes, AM aids in improving the thermal, fluidic and structural properties of a component while also enabling possibilities for mass reduction and parts consolidation [19]. Being an enabler of the circular economy, AM promotes opportunities for product lifespan improvement and supports multiple product life cycles [20]. AM as a whole is rapidly developing with an increased array of materials becoming printable including polymers, metallic alloys, ceramics and composites. However, all processes follow the same underlying principle of generating a 3D model layer by layer, as described in Figure 1-7. Due to the availability of equipment, material characteristics and process capabilities and limitations, only metallic based AM processes are considered for this research, specifically metal powder bed fusion (PBF).

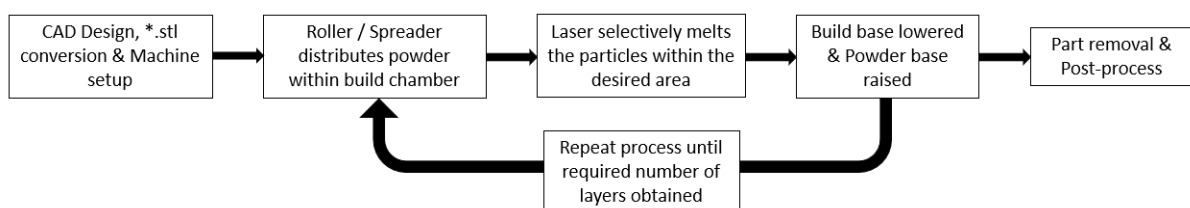


Figure 1-7. LPBF Process flow Summary.

Metallic PBF is one of the most common industrial AM techniques. It utilises a beam energy source to selectively melt together fine particles of metallic powder. Either a laser (LPBF) or electron beam (EBM) can be used as the energy source, each with specific advantages and disadvantages. LPBF was first developed in Germany in 2002 with Selective Laser Melting (SLM) technology [21], while EBM was first conceptualised and patented in 1997 by Arcam AB in Sweden [22]. Both processes are based on similar principles, however, a LPBF based system takes place within an inert environment, whereas EBM system occurs under a vacuum,



as shown in Figure 1-8. Both systems aim to reduce the oxygen within the build chamber while also reducing the risk of hydrogen embrittlement within the printed component.

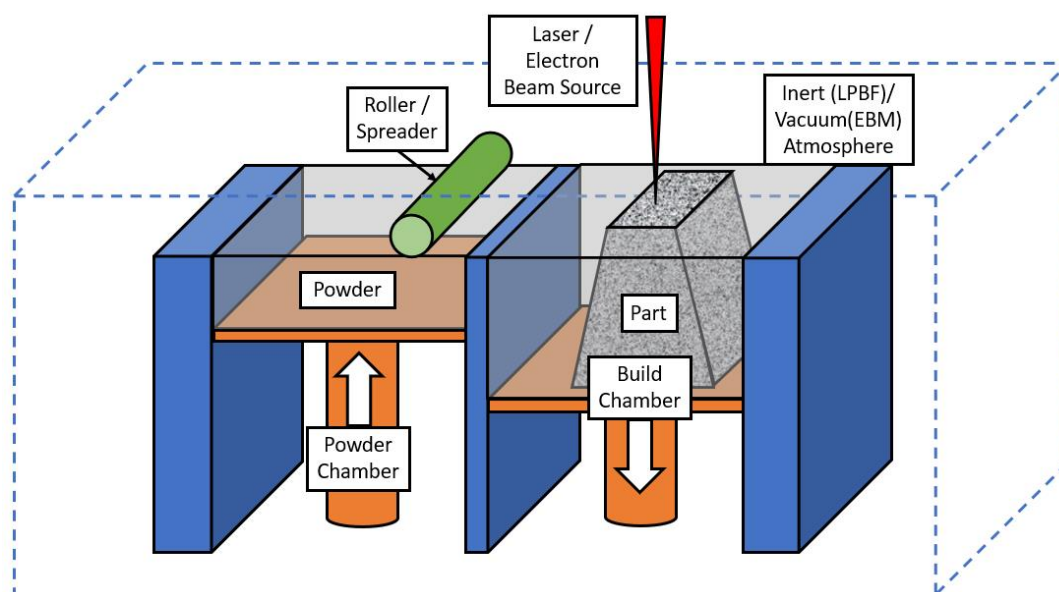


Figure 1-8. Simplified LPBF/ EBM printer components.

The vacuum chamber within the EBM system aids in minimising heat loss which reduces the thermally induced residual stresses within the component. Typically, the material within an EBM machine cools down to around 650-700°C whereas the build chamber temperature of a LPBF printer is around 30-60°C [23]. This does however vary, dependent on the material to be manufactured. The flow of cold inert gas used for the LPBF process increases heat transfer through forced convection, which increases cooling rates and the likelihood of internal thermally induced stresses. Another advantage of EBM over LPBF is the increased scanning speed due to the use of inertia free electromagnetic lenses to direct the beam. This creates opportunities for unique and innovative heating and melting strategies as the ability to maintain higher temperatures between layers with the EBM process results in less residual stresses within the components.

Both processes utilise similar methods for powder deposition with a spreader or roller based system to evenly distribute the powder in consistently fine layers, typically 20-100µm and 100µm for LPBF and EBM respectively [24]. The increased layer thickness, larger powder particles and larger beam diameter associated with EBM inherently results in an increased surface roughness of $R_a = 25-35\mu\text{m}$ compared to a value of $R_a = 11\mu\text{m}$ for LPBF[22]. Dependant on the application in hand, additional postprocessing may therefore be required.



LPBF is considered to be the most versatile AM process with a greater number of printable materials and underlying industrial research surrounding the technology due to it being one of the first commercialised AM processes [25]. Printable materials include (but are not limited to) a range of iron-based alloys, titanium alloys, aluminium alloys and nickel-based alloys. Iron-based steels may be sub-categorised as stainless steel, high strength steel, and die steel. Stringent requirements must be met for efficient printing of the metallic powder. Particle size, size distribution, sphericity, fluidity and bulk density are some of the parameters that must be strictly controlled [21].

Although PBF and other AM processes show great potential for future development and utilisation, numerous challenges still exist and need addressing. These challenges include anisotropic characteristics, speed, accuracy, process control and cost effectiveness [19]. Furthermore, consistency and repeatability may be improved through the development of in-process quality monitoring and closed loop control systems. This could aid in reducing raw material waste and manufacturing time. However, one of the key challenges currently facing the AM sector is the need to upskill of the present workforce of machinists, designers and engineers to fully adapt and utilise Design for Additive Manufacturing (DfAM) practices and implement Industry 4.0 strategies. This challenge is especially prevalent in the near-term future, as the AM sector will encounter a hybrid skills pool of a typical subtractive-based manufacturing workforce and one with emerging skills specific to AM [26]. As time goes on and understanding of AM improves, the development of the workforce will further aid in unlocking the full potential of AM.



1.4 Additively Manufactured Heat Pipes for the Passive Transfer of Heat

Technological advances are often at the forefront of innovation as seen with recent developments in the AM sector. As discussed, AM, specifically LPBF, offers greater design freedom, improving the manufacturability of innovative designs whilst also enabling possibilities to enhance the structural and thermal properties of components. This could prove to be a key driver for the advancement of heat pipes and other capillary-driven devices reliant on novel porous wick designs. AM enables the possibility for specifically designed wicking structures tailored to the thermal and fluidic requirements at each stage of the heat pipe, such as maximising heat transfer at both condenser and evaporator sections while limiting heat loss and prioritising fluid flow through the adiabatic zone. Through improving system integration, AM can enable heat pipes to be manufactured directly into larger components, such as heat exchangers and heat sinks, reducing interfacial thermal resistances for enhanced performance and simplification of the assembly process.

However, as the thermal conductivity of the powder is less than that of the solid material, effective powder removal from the manufactured structures is essential, and hence AM may be limited in achieving the desired pore size and prove impracticable in delivering the required capillary pressure of the passive device [27]. Furthermore, AM suffers from inherently large surface roughness which may increase internal pressure drop of the structures and negatively impact the contact angle between the working fluid and the wicking structure thus proving to be detrimental to the capillarity of the wicking structure [28]. This phenomenon is a result of a combination of many factors including stair-stepping of the geometry due to the layering process, agglomerated and semi-sintered particles, local melt-pool characteristics and behaviour and laser scan tracking and power [29]. This will be further explored in Section 3.5.

1.5 Research Aim:

Additive manufacturing as a sector is still relatively new and shows great potential for further improving and enhancing thermal management technologies, specifically heat pipe and other lattice-based heat transfer designs. The aim of this research is to further the development and understanding of AM lattice-based structures for heat pipe applications through the investigation of change in build and processing characteristics.

The objectives identified for this research are set out in Section 2.10.



2. Theoretical foundations and Literature Review

The advancement of AM heat pipes, and specifically AM lattice-based wicking structures, represents a significant innovation in thermal management systems, offering unique opportunities for customised design and enhanced performance. To effectively position this research within the existing body of knowledge, it is essential to conduct a comprehensive literature review. This review will explore current studies on material selection, fabrication techniques, and performance characteristics of 3D-printed lattice-based wicking structures. Ultimately, this literature review aims to ensure that the proposed study not only builds upon but also advances the understanding and application of additively manufactured heat pipes across various industries, while setting out the underpinning theoretical foundations.

2.1 Types of Heat Pipes

Heat pipes can be categorised as either wicked or wickless (thermosyphon). There are numerous variations of wicked heat pipe designs, each at various stages of commercialisation and deployment, as summarised by Vasiliev [30] and Faghri [31].

2.1.1 Conventional Heat Pipe

The conventional heat pipe (CHP) or constant conductance heat pipe (CCHP) is described in Section 1.2 and shown in Figure 1-4. However, there are also derivatives of the conventional heat pipe designed for specific applications. Such derivatives include the flat-pipe heat pipe, miniature / micro heat pipes (MHP) as well as the annular heat pipe. These types of heat pipes are commonly employed for electronic and refrigeration applications. However, with the smaller channels, achieving extremely high heat fluxes near 1000 W/cm^2 is possible, but are mostly only suitable for applications below 10W [32]. The flat-pipe heat pipe is used for applications where conductive heat transfer is prioritised but are particularly prone to suffer restrictions in terms of sonic and entrainment limits and therefore reduce the amount of heat that can be transported.

Annular heat pipes are another derivative of the CHP with the main difference being that the vapour space is annular instead of circular, allowing for additional wicking material to be placed on the inside of the outer pipe as well as the outside of the inner pipe. The surface area and thus heat transfer is increased without significantly increasing the HP outer diameter. The additional wick incorporated into the design enhances both liquid return and



capillary limit of the HP. Such design has been used for isothermal furnace applications, where a flattening of the temperature gradient was achieved as well as enabling a fast response to any variation in conditions [31].

2.1.2 Looped Heat Pipe

Looped heat pipes (LHP) are a more complex form of a HP with the addition of a compensation chamber attached to the body of the evaporator, as shown in Figure 2-1. Unlike the CHP, a LHP's condenser does not have a wick structure. A primary wick is located within the evaporator section and a secondary wick within the compensation chamber, supplying additional liquid to the evaporator if required.

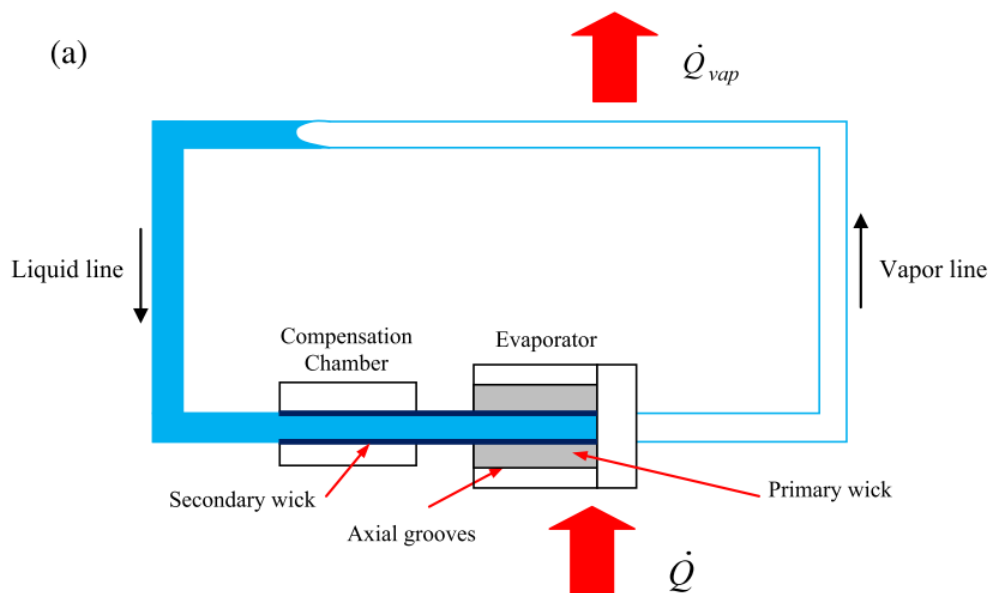


Figure 2-1. Simplified schematic of a Loop Heat Pipe, figure reproduced from [33].

The key features of this design improve its resistance to the effects of gravitational forces as well as improving its system integrability since smooth pipes may be used for the condenser section. This, in addition to the vapour and liquid flowing in co-current, aids in reducing the pressure drop across the system thus increases the maximum separation distance of the evaporator and condenser. Traditionally, the evaporator is of annular geometry, but recent advancements in flat evaporators support the improvements in system integration, performance and mass reduction through eliminating the need for additional heat transfer surfaces, such as a saddle, between the evaporator and heat source [34].



2.1.3 Pulsating Heat Pipe

Pulsating heat pipes (PHP), often referred to as Oscillating heat pipes, are manufactured from a long capillary tube bent into a number of turns. Their designs may be in an open or closed-loop fashion with the condenser and evaporator located at each end, as shown in Figure 2-2.

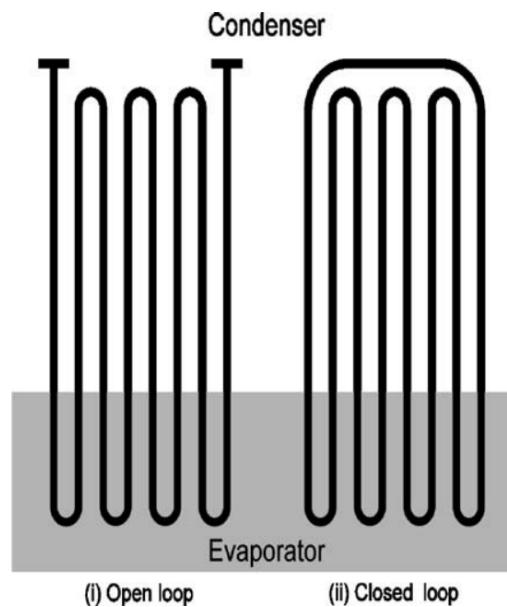


Figure 2-2. Two configurations of pulsating heat pipe: (i) open loop and (ii) closed loop, figure reproduced from [30].

As heat is supplied to the evaporator end, the working fluid evaporates where bubbles form and grow. This forces the movement of liquid towards the condenser end resulting in vapour condensation. The oscillating motion is caused by the growth and collapse of the bubbles [35]. One of the main advantages of such designs is its ability to work against gravity without the need for an internal wick structure which means that they are relatively low cost. However, due to the complex hydrodynamic and thermodynamic internal coupling effect, the fundamental design methods are not fully understood and further research is required [36].

2.1.4 Variable Conductance Heat pipe

Although HPs in general are classified as passive heat transfer devices, the Variable Conductance Heat Pipe (VCHP) can passively control heat transfer and maintain a given temperature at varying operating conditions. It operates similarly to the CHP with the addition of a reservoir of non-condensable gas (NCG) typically located at the condenser section. Under shutdown / low load periods, the NCG occupies the vapour space. No condensation of the working fluid will occur within the NCG region. As the system is activated and heat load at the



evaporator end increases, the resultant vapour temperature and pressure increases, sweeping and compressing the NCG towards the reservoir and increasing the active area of the condenser, as shown in Figure 2-3. This increases the overall thermal conductivity of the heat pipe and hence reduces the temperature of the evaporator.

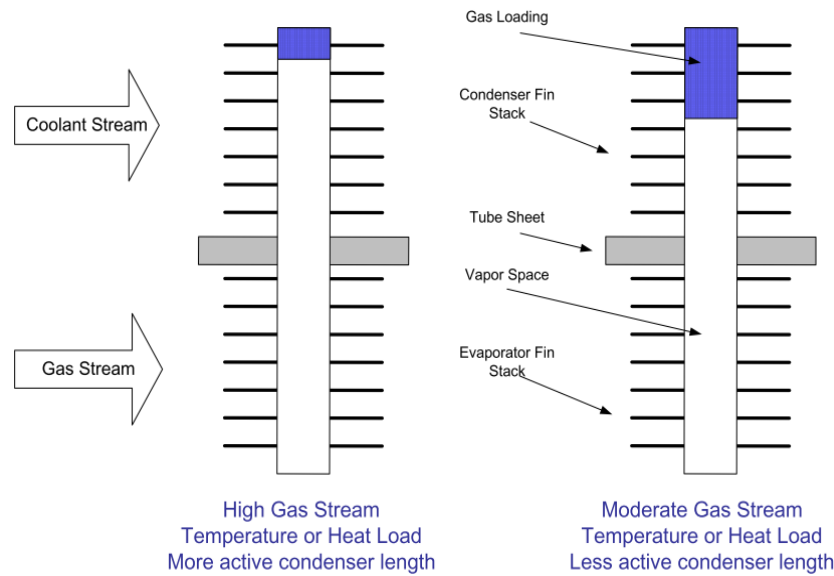


Figure 2-3. Variable Conductance Heat Pipe schematic, figure reproduced from [37].

Conversely, under low evaporator loads, the resultant internal vapour pressure is lower and the NCG would occupy a larger space thus reducing the active area of the condenser. This will result in a lower thermal conductivity and retain more of the heat at the evaporator end. The design's advantages over traditional actively controlled systems include no additional control systems, sensors, actuators, or additional power / parasitic losses which all result in reduced risk of failure, maintenance issues and decreased system efficiency. The flexibility in integration of the design could also be improved thus resulting in reduced volume and pressure drop across the system. With it first being developed for the spacecraft sector, maintaining an optimal temperature can also be essential for a wide range of terrestrial applications including combustion, fuel cells, thermal storage and heating, and ventilation and air conditioning (HVAC) systems [38]. The possibility of passively utilising the wasted heat is also significant in improving system efficiency.



2.1.5 Vapour Chamber

The concept surrounding vapour chambers, also known as flat-plate heat pipes, is equivalent to that of a CHP, although the overall design is planar with a small aspect ratio, as shown in Figure 2-4.

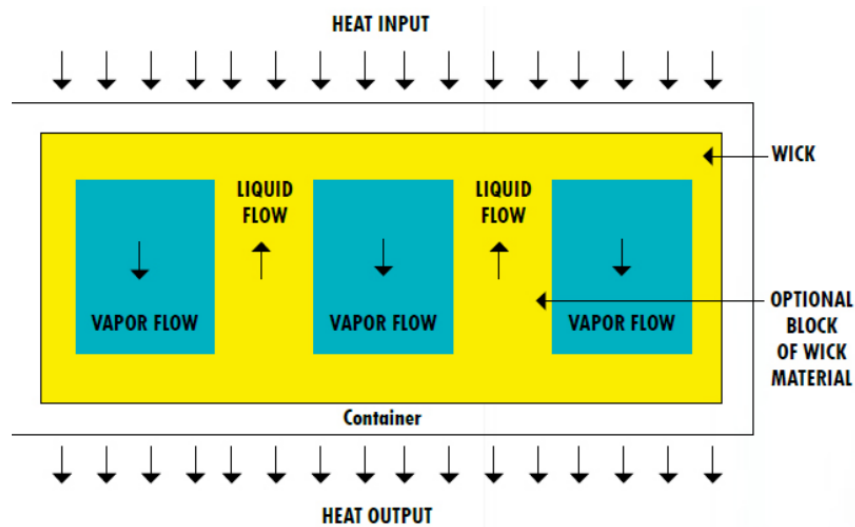


Figure 2-4. Schematic of Vapour Chamber, figure reproduced from [39].

This results in the vapour chamber's ability to transport heat in 2 dimensions, contrary to the heat pipes linear heat transfer characteristics. Depending on the application and designed orientation, a wick may not always be required in the condenser section if it is positioned above the evaporator. However, to prevent dry-out within the evaporator, a wick must be used. Vapour chambers are often used for high heat flux electronic cooling applications as they operate in two- and three-dimensional space unlike the CHP. Through careful design, a vapour chamber can achieve a highly uniform temperature gradient along with greater relative power densities as a result of the increased surface to volume ratio [15]. The conventional fabrication process of a vapour chamber, like that of a heat pipe, is labour intensive. With possibilities of the wick being manufactured separately or integrated into the container and the need to weld the end caps on, the process can be both time consuming and costly [40].

2.2 Wicking Structures

As mentioned in Section 1.2, to achieve a full working fluid cycle and successfully operate against gravity, numerous techniques are used to transport the fluid back to the evaporator section. The more traditional method utilises the differential density of the vapour and liquid



phases to allow the liquid to return to the evaporator through means of gravitational forces. This design, often referred to as a thermosyphon, is limited in system orientation as the condenser must be positioned at an elevated level compared to the evaporator and cannot be operated against gravity.

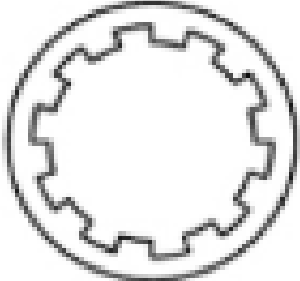
2.2.1 Traditional Wicking Structures

To combat this issue, numerous techniques have employed capillary pressure to drive the liquid back to the evaporator through a wick structure and achieving the fully passive cycle. Capillary pressure is effective due to the forces of adhesion between the liquid and wall particles, cohesion between the liquid molecules, and surface tension between the working fluid and the complex curved geometry of the wick structure [31]. Optimal heat pipe performance requires high permeability to maintain low flow resistance and low capillary radius to achieve high capillary pressure, essential for applications where gravity is of concern. Unfortunately, a trade-off is required as lower pore radius tends to result in lower permeability.

In addition to supplying the capillary forces which allow a heat pipe to work in multiple orientations, the wick structure also effects the boiling process by offering additional nucleation sites and thereby aiding in bubble formation. Common wick structures include axial groove, fine fibre, screen mesh and sintered, each with their own advantages and disadvantages as shown in Table 2-1.



Table 2-1. Comparison of wick structure, data collated from [39, 41, 42].

Wick Structure	Advantages	Disadvantages
<p data-bbox="316 439 459 465">Axial Groove</p> 	<ul style="list-style-type: none"> • Good thermal conductivity. • Low thermal resistance. • Simple fabrication. • High permeability. 	<ul style="list-style-type: none"> • Poor capillary performance. • Poor flow against gravity. • Non-uniform circumferential liquid distribution.
<p data-bbox="331 797 443 824">Fine fibre</p> 	<ul style="list-style-type: none"> • Good Capillary Performance. • Suitable for smaller applications. 	<ul style="list-style-type: none"> • Low permeability. • Low thermal conductivity. • Not effective under partial wick drying conditions.
<p data-bbox="312 1155 459 1182">Screen mesh</p> 	<ul style="list-style-type: none"> • Inexpensive compared to other methods. • Low pressure drop. • Moderate capillary action. • High permeability 	<ul style="list-style-type: none"> • Low thermal conductivity. • Poor wettability after evaporator dry-out.
<p data-bbox="331 1536 443 1563">Sintering</p> 	<ul style="list-style-type: none"> • High performance. • Moderate pressure drop. • Excellent flow against gravity. • Operates effectively under partially dried wick conditions. 	<ul style="list-style-type: none"> • Random dispersion of pores. • Relatively high-pressure losses.



The choice of wick structure is essential and is heavily dependent on the operating conditions, orientation, application and cost. The high permeability associated with axial grooved wicks allows for high volume of fluid and hence high heat to be transported over larger distances. However, due to reduced nucleation sites as seen in sintered wick, axial grooved wicks receive less power from the source. During the manufacturing of sintered wicked heat pipes, an axial rod needs to be placed through the heat pipe as a support structure for the un-sintered powder. This results in thicker wick structures and hence greater thermal resistance within the heat pipe. This also creates fabrication and quality issues during the process [15]. As is discussed, with careful consideration throughout the design stage and the use of additive manufacturing, the required supporting structures may be eliminated further enhancing the heat pipe's potential as effective heat transfer devices.

Deng et al. and Tang et al.'s investigations into sintered-grooved hybrid-based wick designs [43, 44] aimed to combine the benefits of multiple wick structures by characterising the capillary performance through permeability and capillary rate-of-rise tests. Tests indicated that such composite design resulted in improved permeability and capillary performance (+20%), when compared to standard sintered wicks, while also exhibiting larger capillary pressure than standalone grooved wicks. Furthermore, the capillary pressure was increased by 2-4 times compared to the grooved wick. Tests conducted with various powder sizes determined that, unlike capillary pressure, both permeability and capillary performance increased with increased particle size. This shows a trade-off between capillary pressure and permeability, both of which are major considerations in the design of a wicked heat pipe. The experimental work also looked at the effects that the sphericity of the powder had on various parameters, as shown in Figure 2-5.



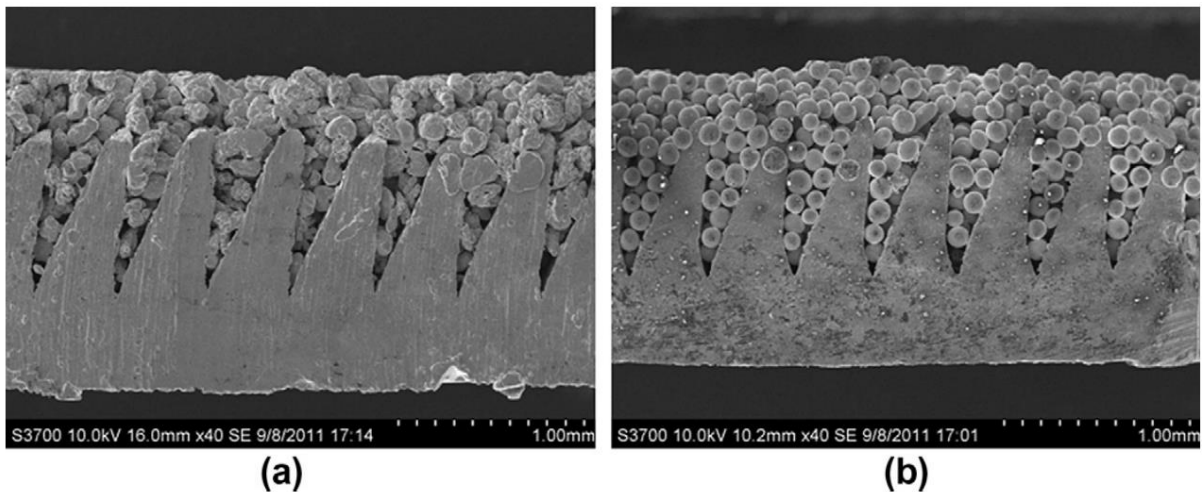


Figure 2-5. SEM images of composite wick with two kinds of sintered powder (a) irregular powder (Sample: CI75-110); (b) spherical powder (Sample: CS75-110), figure reproduced from [43].

It was concluded that in terms of both permeability and capillary rate-of-rise, irregular powder showed superiority over its spherical counterpart since more interconnecting pores exist for the irregular case. This research shows great potential for the integration of AM to design a hybrid-based wick structure tailored for the conditions at each section of the heat pipe.

2.2.2 Biomimetic Wicking Structures

Biomimicry is a method used to mimic natural structures, that have been optimised over millions of years of evolution, to enhance design performance. Efficient capillary action is often seen throughout nature, such as trees and cacti in arid ground conditions transporting water at low pressure from the roots and stems to the rest of the plant as well as the movement of water through sand and the release of fluid from tear ducts.

This was investigated by Wang et al. [45] to enhance heat pipe wick structures. The work looked at characterising the parameters of both surface wetting and capillary effects often seen in nature. Through their research, a bi-porous sintered wick structure was proposed for the evaporator section with smaller pores on top in a grooved pattern, as shown in Figure 2-6. This aids in varying the surface roughness throughout the heat pipe thus improving capillary pumping force and surface wetting.



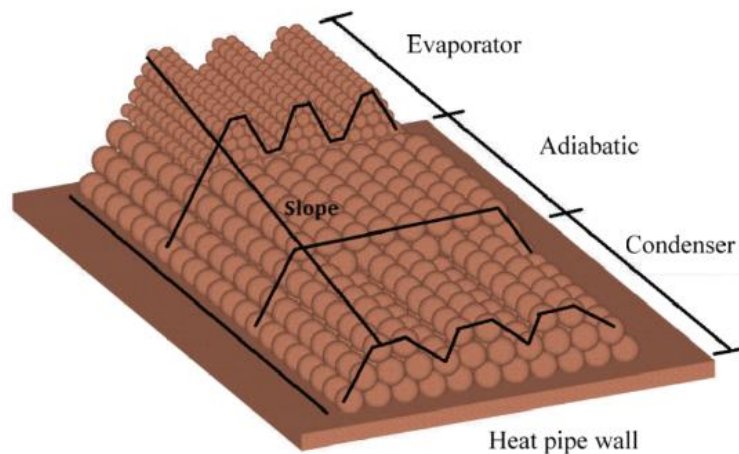


Figure 2-6. Novel biomimetic-based heat pipe wick design, figure reproduced from [45].

The grooved wick structure seen in the evaporator and condenser sections provide a continuous longitudinal layer of liquid, while the sintered wick reduces the risk of non-uniform circumferential liquid distribution which is a prominent issue in grooved wick structures. Furthermore, neglecting the grooved design for the adiabatic section reduces the overall surface area and hence reduces heat loss from the section.

A further study by Putra et al. [46] investigated the use of coral biomaterial as a wick structure for a heat pipe-based Central Processing Unit cooling system. Through comparison with a sintered copper wick heat pipe of similar mean pore diameter, the simulator plate temperature was reduced by as much as 44.25°C. Further research is required to determine whether the improvement in thermal dissipation seen by the coral wick is due to the geometric structure, material properties or a combination of both. Nevertheless, this shows great interest and potential for biomimetic wick structures that may be produced through additive manufacturing.



2.3 Working Fluids

The choice of working fluid used in a heat pipe is dependent on the operating temperature of the application together with design material compatibility. There are many working fluids, including, but not limited to: water, acetone and ammonia as well as a range of alkali metals and refrigerants, each with various properties as shown in Table 2-2.

Table 2-2. Thermophysical Properties of various working fluids, data collated from [35, 47, 48].

Working Fluid	Melting Point (°C)	Boiling Point at atmospheric pressure (°C)	Latent heat of vaporisation (KJ/kg)	Surface Tension at 25°C (N/m)	Useful Range (°C)
Ammonia	-78	-33	1360	0.0280	-60 to 100
Methanol	-98	64	1093	0.0220	10 to 130
Ethanol	-112	78	503	0.0220	0 to 130
Acetone	-93	56	552	0.0237	0 to 120
Water	0	100	2260	0.0720	30 to 200
Potassium	64	762	1938	0.1170 (at 77°C)	500 to 1000
Sodium	98	878	3913	0.2080 (at 141°C)	600 to 1200
Lithium	179	1317	19700	0.3960 (at 179.2°C)	1000 to 1800

These properties contribute to towards the fluid's ability to transfer heat in addition to improving wick wettability for increased capillarity. In accordance with the Young-Laplace Equation, shown in Equation (2-1), the delivered capillary pressure (p_c) is directly proportional to the surface tension (σ) and the cosine of the contact angle (θ), and inversely proportional to the radius of curvature of the surface.

$$p_c = \frac{2\sigma\cos\theta}{r_c} \quad (2-1)$$



Theoretically, a heat pipe has capabilities to operate throughout the fluid’s range from the triple point through to its critical point. As an example, this would be between 0.01 °C and 373.9 °C for water, as shown in Figure 2-7. However, its capabilities are drastically reduced near these limitations. In reality, the typical useful range for water as a heat pipe working fluid is limited to approximately 30 – 200 °C.

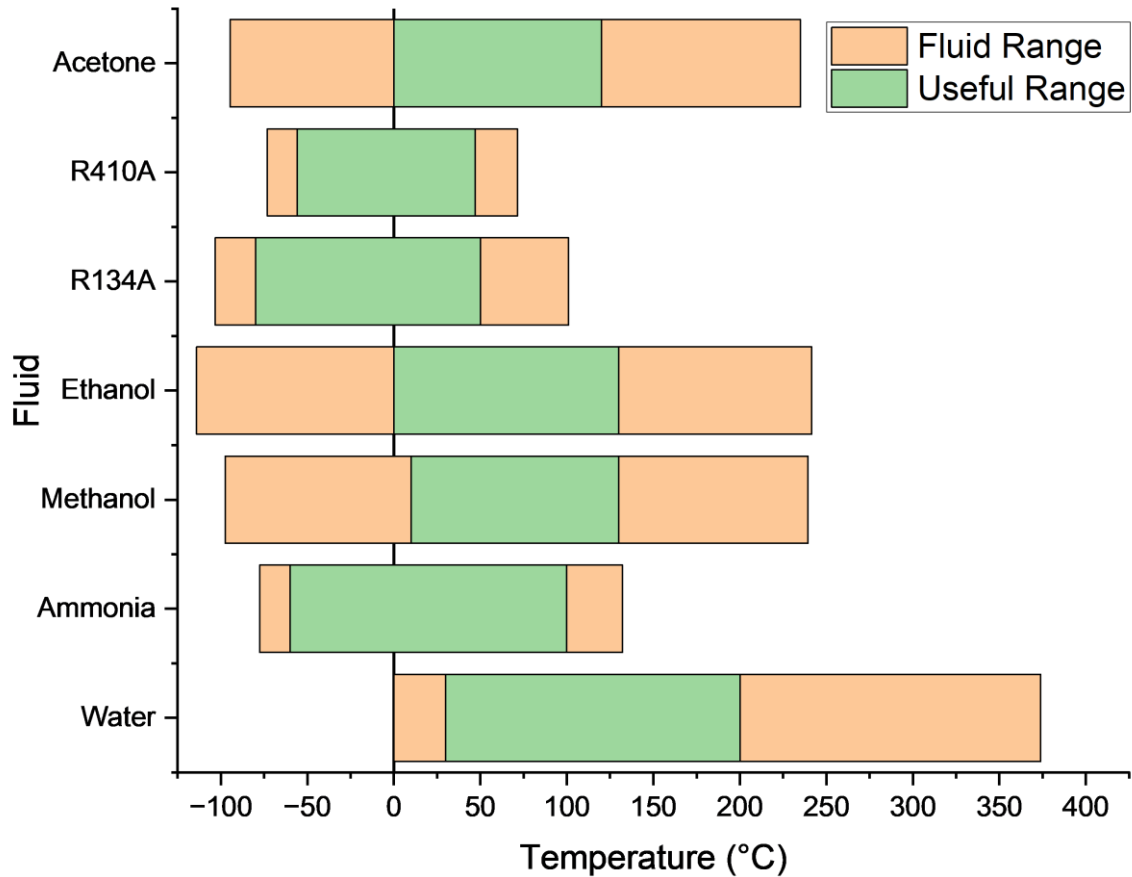


Figure 2-7. Triple and critical temperature point and useful temperature range for various heat pipe working fluids.

As can be seen, in some cases the useful temperature range of the selected fluid is drastically reduced and is dependent on a number of factors including vapour pressure, heat transfer capabilities, thermal stability and wettability [49].

A term often used to quantify the fluid’s capabilities at varying temperatures is the merit number or figure of merit, M, shown in Equation (2-2).

$$M = \frac{\sigma_l h_{fg} \rho_l}{\mu_l} \quad (2-2)$$

Where σ_l , h_{fg} , ρ_l and μ_l are the surface tension, enthalpy of evaporation, density and dynamic viscosity, respectively.



This is frequently considered with respect to the capillary limit, as discussed in Section 2.5, when vapour pressure loss and gravitational head can be neglected. With this in mind, the merit number evaluates the working fluid's properties that contribute to the maximum heat transport [50]. Figure 2-8 shows how the merit number changes with temperature for a range of typical heat pipe working fluids. The various fluid properties for Figure 2-7 and Figure 2-8 were collected with the use of CoolProp library [51] and implemented into a specially designed Matlab script with python integration, shown in Appendix 12.2.

As can be seen, the selection of working fluid can be essential for the effective heat transfer within heat pipes. Through consideration of the merit number, water is shown to be the most effective heat transfer fluid over a wide temperature range but also ineffective at the lower temperature range, where depending on factors such as material compatibility, acceptable vapour pressure limits and environmental impact, other working fluids may be preferred.

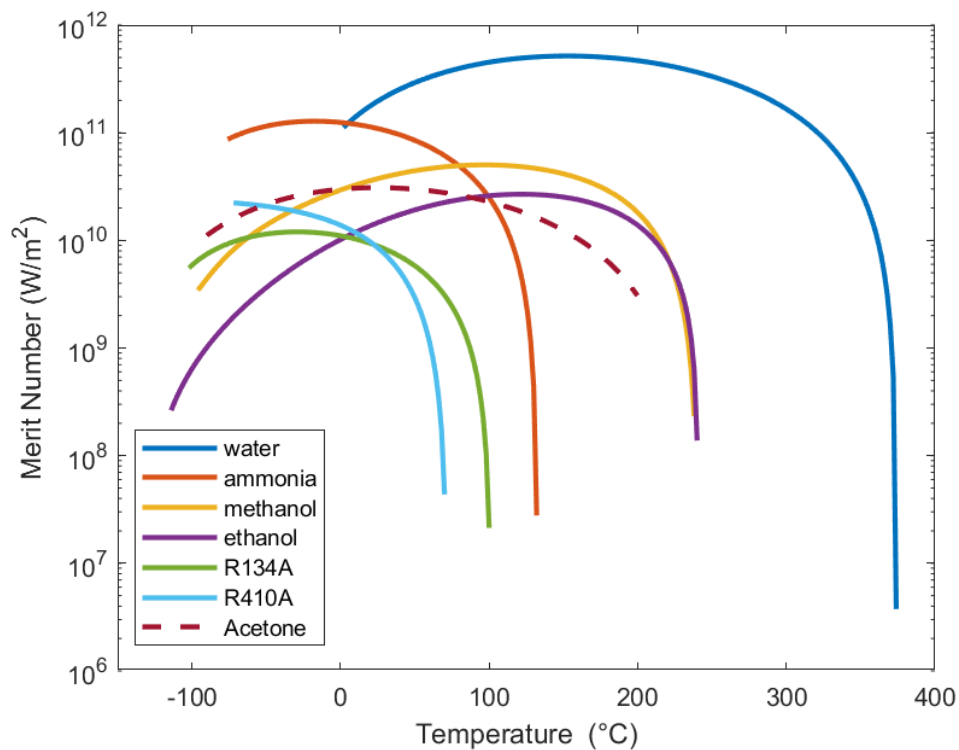


Figure 2-8. Merit number for a range of typical heat pipe working fluids at varying temperature with logarithmic scale.



The compatibility of the working fluid and utilised structural materials is essential in the design of an effective heat pipe capable of safe long-term use. Table 2-3 shows the compatibility of a range of different working fluids and wicking material combinations.

Table 2-3. Compatibility of various working fluids and wick materials at low temperatures, data reproduced from [52].

Wick Material	Working Fluids					
	Water	Acetone	Ammonia	Methanol	Dow-A	Dow-E
Copper	RU	RU	NR	RU	RU	RU
Aluminium	GNC	RL	RU	NR	UK	NR
Stainless steel	GNT	PC	RU	GNT	RU	RU
Nickel	PC	PC	RU	RL	RU	RL

RU, recommended by past successful usage; RL, recommended by literature; PC, probably compatible; NR, not recommended; UK, unknown; GNC, generation of gas at all temperatures; GNT, generation of gas at elevated temperatures, when oxide is present.

Of the materials considered, copper is shown to be the most versatile material for heat pipes for lower temperature applications with ammonia the only fluid not recommended for its use. It can also be seen that acetone is the most multifaceted in terms of material compatibility, although it should be noted that further research needs to be undertaken for its recommended use with stainless steel and nickel.

In addition to the working fluids evaluated here, a mixture of multiple fluids may also be used, dependant on the application and operating conditions, such as a water-toluene blend for low temperature applications typically in the range of 20-200°C [30]. A recent development in heat pipe technology is the use of nanofluids which include nanometre-sized oxide or metallic particles suspended within the fluid. Through including a small amount of nano-particles in the fluid, it's possible to enhance the heat transfer rates by up to 30% thus reducing system volume and mass [53]. Due to the high Global Warming Potential and intended phase-out of commonly used hydrofluorocarbon-based refrigerants, they will not be considered as working fluids for this project.



2.4 Contact Angle

As shown in Equation (2-1), a high contact angle, resulting in hydrophobic behaviour, can be detrimental for the performance of a heat pipe, drastically reducing the effectiveness of the delivered capillary pressure with p_c tending towards zero as the contact angle (θ) tends towards 90° . Through considering the energy balance between the wetting and non-wetting phase on a solid surface, it can be determined that the equilibrium position, and hence contact angle, can change with surface tension. This is shown in Figure 2-9, and derived with a horizontal force balance in Equations (2-3) and (2-4), which is also known as the Young Equation.

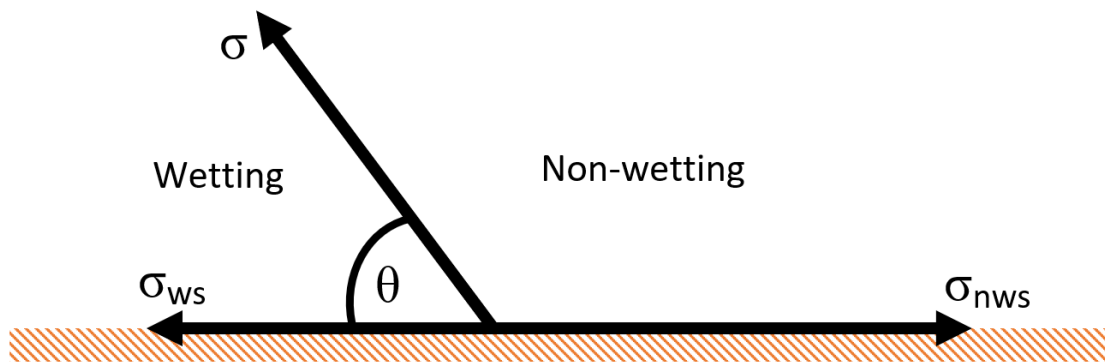


Figure 2-9. Horizontal force balance of a two fluid phase system on a solid surface, where σ , σ_{ws} and σ_{nws} represent the liquid surface tension, wetting-solid interfacial tension and non-wetting-solid surface energy.

$$\sigma_{nws} = \sigma_{ws} + \sigma \cos \theta \quad (2-3)$$

$$\cos \theta = \frac{(\sigma_{nws} - \sigma_{ws})}{\sigma} \quad (2-4)$$

For a high wetting surface, the surface energy attracts the liquid droplet to spread along the surface. For this to occur, the surface energy must be larger than the liquid surface tension which attempts to keep the liquid molecules together in droplet form. Contrary, for a low wetting surface, the surface tension of the liquid drastically overcomes the surface energy, resulting in a low interfacial tension and high contact angle. Wettability can be affected by several other factors, including surface roughness. The consideration of the impact of surface roughness on the wetting characteristics was first proposed in 1936 by Wenzel [54] and later extended by Cassie and Baxter [55], as shown in Figure 2-10.



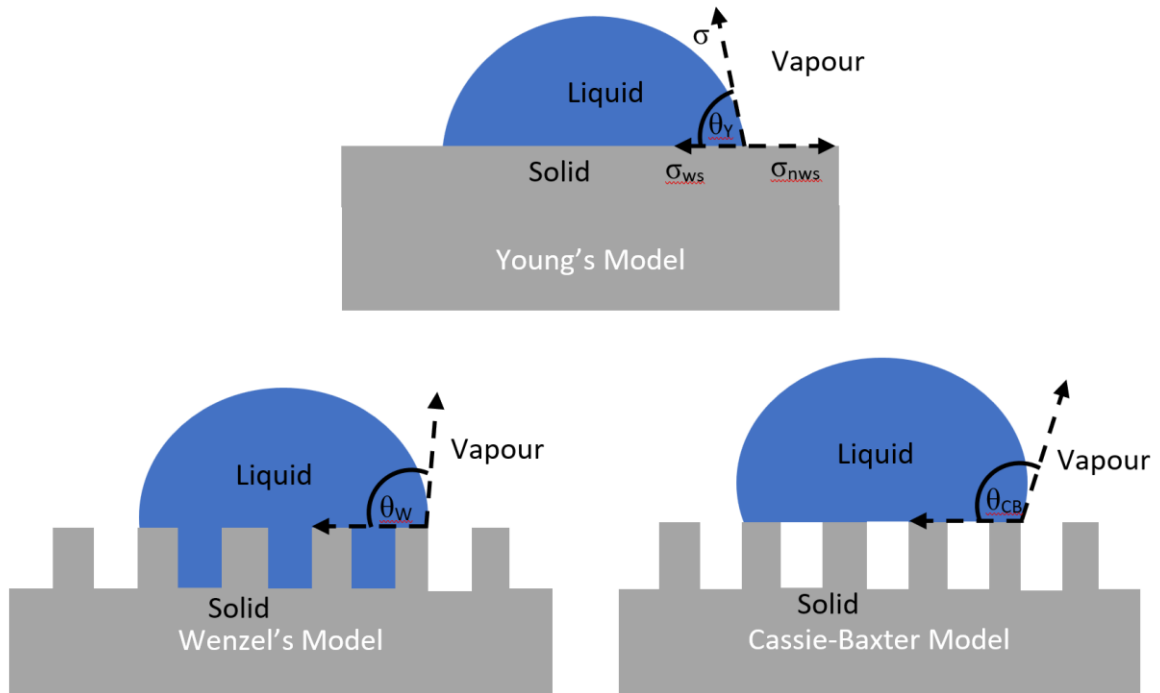


Figure 2-10. Schematic of Young's model (top), Wenzel's Model (bottom-left) and the Cassie-Baxter Model (bottom-right).

As stated by Kim et al. [56], a droplet placed on a hydrophilic surface will generally be in the Wenzel state. In contrast, a hydrophobic surface will generally result in the droplet being in the Cassie-Baxter state. These two states can also coexist while transitioning from one to another [57].

2.4.1 Wenzel State

Wenzel proposed that liquid would fill the grooves left by the topography of a rough surface [54, 58, 59]. The relationship between Young's contact angle and that modelled by Wenzel is based on the increase in actual surface area compared to that of a perfectly flat surface, as shown in Equation (2-5).

$$\cos \theta_W = r \cos \theta_Y \quad (2-5)$$

Where θ_W and θ_Y are the Wenzel and Young contact angles, respectively, and r is the surface roughness ratio, as shown in Equation (2-6).

$$r = \frac{A_r}{A_0} = \frac{\cos \theta_W}{\cos \theta_Y} \quad (2-6)$$



The surface roughness ratio can be associated to both the actual surface area, A_r , and the geometric surface area, A_0 . Equation (2-6) states that an increase in surface roughness can enhance both the hydrophilicity of a hydrophilic surface and the hydrophobicity of a hydrophobic surface. As described by Azizian and Khosravi [58], for surfaces with high roughness values, or those with porous surfaces, the right side of the Wenzel equation can be greater than unity which hinders the effectiveness of the correlation. For such instances, the Cassie-Baxter model should be implemented.

2.4.2 Cassie-Baxter Regime

The alternative Cassie-Baxter (CB) regime allows for the suspension of a liquid droplet on a highly rough surface. This increased roughness enables air to be trapped between the liquid-solid interface, enabling the formation of liquid droplets through minimising the contact area between the liquid-solid surface, as shown in Figure 2-10. The CB Equation is shown in Equation (2-7).

$$\cos \theta_{CB} = f_{sl} \cos \theta_Y - (1 - f_{sl}) \quad (2-7)$$

Here, f_{sl} and θ_{CB} represent the solid-liquid surface area ratio and Cassie-Baxter contact angle, respectively.

In addition to impacting the contact angle and the resultant delivered capillary pressure, implementing the CB regime poses further challenges. In terms of heat transfer for heat pipe and heat exchanger applications, the resultant air pocket between the solid and liquid interface would allow for additional thermal resistance within the system due to the low thermal conductivity of the vapour [60].



2.4.3 Wettability in Natural structures

Both hydrophobic and hydrophilic structures are often seen throughout nature. Such examples of hydrophobicity and super-hydrophobicity in nature is the leaves of plants, such as the *Hosta* and *Salvinia Molesta* plants, shown in Figure 2-11 and Figure 2-12, respectively.



Figure 2-11. Example of hydrophilic nature of a *Hosta* plant.

Here, a large contact angle between the *Hosta* leaf and water is clearly present. The surface of *Hosta* plant leaves, like many others, consists of a hydrophobic wax-like microstructure enhancing the hydrophobicity of the structure. In addition to repelling water, this characteristic, also referred to as the lotus-effect, serves as a self-cleaning process, removing microorganism and other contaminants from the leaf surface [61, 62]. The findings emphasise the significance of microstructure analysis.

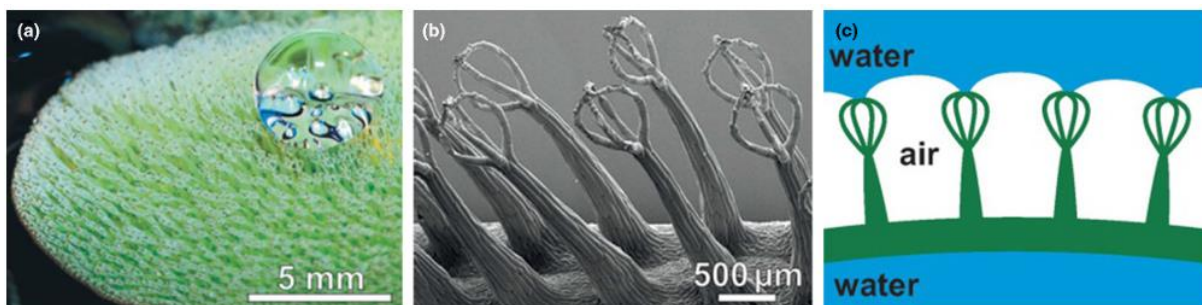


Figure 2-12. Superhydrophobic nature of *Salvinia Molesta* at different magnifications, figure reproduced from [63].



The presence of the whisk-shaped pillars of the *Salvinia Molesta* plant, shown in Figure 2-12, allow for the air to be trapped underneath, reflecting that of the Cassie-Baxter regime, enabling the plant leaves to stabilise air levels underwater for several weeks [63].

The Namib desert beetles are capable of thriving in arid environments through collecting water from the limited humid air at night [64]. The insects achieve this through a combination hierarchical multi-phased hydrophilic areas to capture the water and hydrophobic patches to transport the water along their backs towards their mouths.

In terms of heat pipe application, reducing the associated surface roughness may aid in reducing the liquid contact angle, allowing for possibilities to enhance the delivered capillary pressure. Furthermore, a reduction in internal pressure losses experienced within the wick may be achieved. Achieving this would enhance the wick's permeability performance, allowing for greater transfer of fluid and hence enhanced heat transfer capabilities. However, considerations should also be made of the impact on the structure's capillary characteristics. For instance, over polishing could not only smooth the surface but also attack the bulk material resulting in surface pitting, significantly increased pore size and hence reduced capillary pressure capabilities [29]. Therefore, ensuring an effective post processing method to reduce the surface roughness could be key to further advancing the performance of AM heat pipes.



2.5 Operating Limits

There are five operating limits governing a heat pipe's thermal performance as summarised below and shown in Figure 2-13.

Viscous Limit: Occurs at the lower end of a temperature range of a heat pipe, where the vapour pressure difference between the condenser and evaporator may not be enough to overcome the viscous forces. These viscous forces slow down the vapour flow within the heat pipe. Should flow from evaporator to condenser stop, no latent heat is transported.

Sonic Limit: Typically, the vapour approaches velocities near the speed of sound. However, the flattening of a heat pipe, utilising bends or variations in the heat input, can reduce vapour passage and result in lower vapour speed. Heat increase leads to higher vapour speed thus building a larger pressure difference between the evaporator and condenser, restricted by the slower vapour in front.

Entrainment limit: Where the vapour flow strips liquid from the wick if there is insufficient vapour passage. This will reduce the amount of liquid returned to the evaporator reducing the heat pipe performance. Flattened and bent heat pipes are particularly affected by this. Through the integration of additive manufacturing, possibilities arise to eliminate this limitation through printing a solid surface between the wick and vapour space throughout the adiabatic section. This would ensure that all the working fluid flows from the condenser back to the evaporator. However, challenges relating to powder removal may be experienced.

Capillary Limit: Capillary action occurs within the wick due to the forces of cohesion and surface tension which forces the liquid to propagate in all orientations. This capillary action needs to overcome gravity and all other pressure losses in the system to enable the transport of liquid through the wick back to the evaporator. Along with the difference in capillary pressure across the liquid-vapour interface, this is the main limiting factor for heat pipes operating at lower temperatures [15].

Boiling Limit: Evaporation needs to occur on the wick's surface. If boiling occurs within the wick, it will prevent the return of liquid back to the evaporator. If no liquid returns to the evaporator, there is no continuous boiling which would result in a failure of the heat pipe. This typically occurs at the highest operating temperature range of a heat pipe and heat inputs should not exceed the boiling limit.



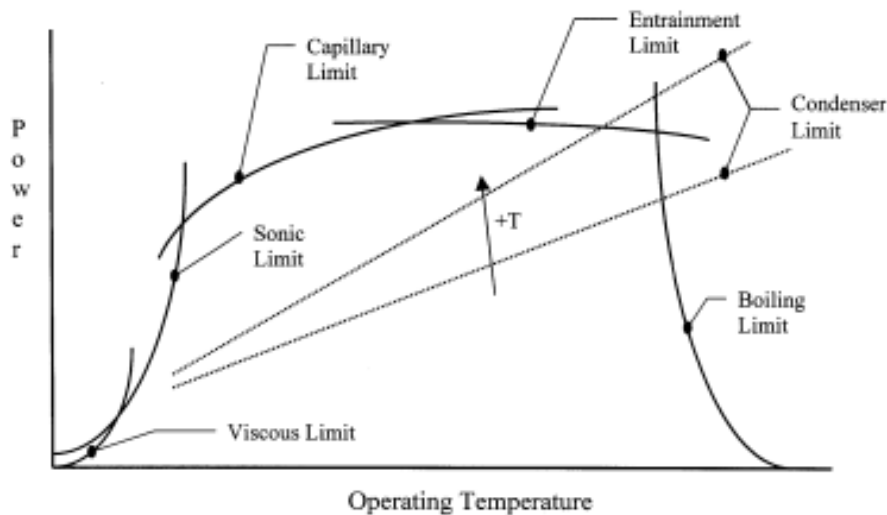


Figure 2-13. Typical heat pipe performance map, figure reproduced from [65].

2.6 Applications

With the advancements in the fundamental understanding of the heat pipe, and the ability to cover a wide temperature spectrum, the list of applications is expanding and may be used for effective heat dissipation and regulation. Applications may be categorised as low or high-temperature and can be an excellent alternative to other cooling methods such as jet impingement cooling, liquid cooling and phase change storage media. This section will emphasise high-value heat pipe applications most suited for additive manufacturing whilst considering its limitations in terms of dimensional constraints and material selection.

2.6.1 Electronic Components

Thermal management of electrical components and systems may be the most widely used application of the copper-water heat pipe, with possibilities to manage microprocessors and power electronic devices effectively and reliably. They are an ideal solution for applications with high heat flux requirements and limited space for additional cooling components, including laptops and tablets. Through the incorporation of bends and flattening of the heat pipe, an effective thermal pathway from source to sink may be achieved. The heat may be dissipated from the condenser to ambient through forced convection via a cooling fan, such as the applications shown in Figure 2-14.



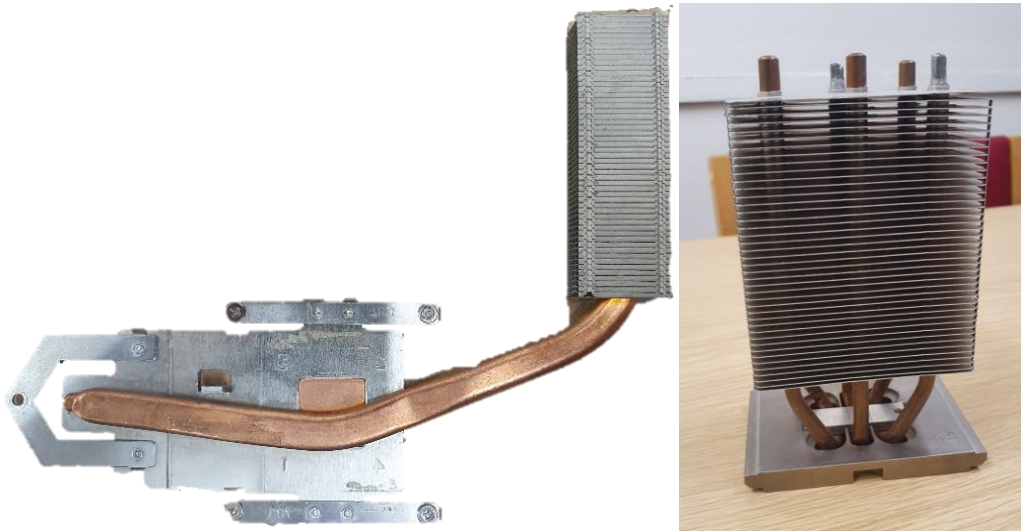


Figure 2-14. Flattened and bent heat pipe for forced convection laptop thermal management (left) and CPU heat pipe cluster heat exchanger (right).

Through utilising such systems, the heat pipe equalises the temperature of the condenser fins, and hence eliminates the large conductive losses that are often experienced with standard heat sinks. Alternatively, should the heat pipe length, area and heat flux be sufficient the heat may be dissipated along its length into the structure of the device and into the environment [66]. This further reduces device volume and improves efficiency through eliminating the need for additional cooling fans.

With the increase power demand of modern electric motors, the thermal dissipation requirement is also increased to maintain motor performance and lifetime. Numerous studies have examined the integration of heat pipes for this purpose. The heat pipes may be placed inside the motor housing, contained within the shaft or positioned on the surface of the motor housing, as investigated by Putra et al. [67]. The study altered a 0.5HP prototype electric motor with the rotor and coil replaced with a cartridge heater to replicate the heat generated at various operating conditions. Through using the motor fan to dissipate the heat from each of the copper-water heat pipes, the surface temperature was reduced by 33.8°C from an initial baseline temperature of 102.2°C . In terms of further system enhancements, additive manufacturing may be used for integrating the heat pipes and body into a single unit. This will aid in reducing the interfacial thermal resistance due to eliminating the need for thermal compounds or welds between the pipe and body. Furthermore, the improved design freedom may result in a more novel, thermal efficient design while locating the heat pipe evaporators nearer to local hotspots.



An investigation by Sun et al. [68] investigated the possibilities of enhancing the cooling strategy of a water-cooled 54kW DC electric motor with the use of heat pipes. The 3 dimensional heat pipes employed a hybrid wick structure with sintered copper powder attached to the inner microchannels, similar to the work of Deng et al. [43] and Tang et al. [44] previously discussed in Section 2.2. The heat pipes are located within the gap between the winding and casing while employing potting silicon gelatine to fix the pipes in position (HP + P-M). The results were compared to the standard motor (O-M) and a motor without the potting silicone gelatine (HP-M). Results showed a significant winding temperature reduction of 22.9°C for the HP + P-M motor compared to the O-M motor. Only a 10°C reduction was seen for the HP-M motor. However, both motors significantly improved the temperature distribution while the HP + P-M motor extended the running time from 84.4 s to 135 s under peak loads. It should be noted that, as often seen in literature, the use of off-the-shelf heat pipes may pose further challenges in terms of thermal and electromagnetic compatibility. In this case, utilising heat pipes for winding thermal management may result in additional power losses being generated in their bodies and requires further study [69].

2.6.2 Spacecraft Technology

With the need to minimise weight and reduce parasitic losses and maintenance periods, heat pipes have proven to be a suitable candidate for a wide range of satellites, including small satellites (100 – 500 kg), Microsatellites (20-100 kg) and Nanosatellites (1 – 10 kg). Generally, the larger the satellite, the higher the requirement to dissipate waste heat from the onboard electronic devices [12]. The interest in further development of heat pipes for satellite and spacecraft thermal management is growing, as illustrated in Figure 2-15.

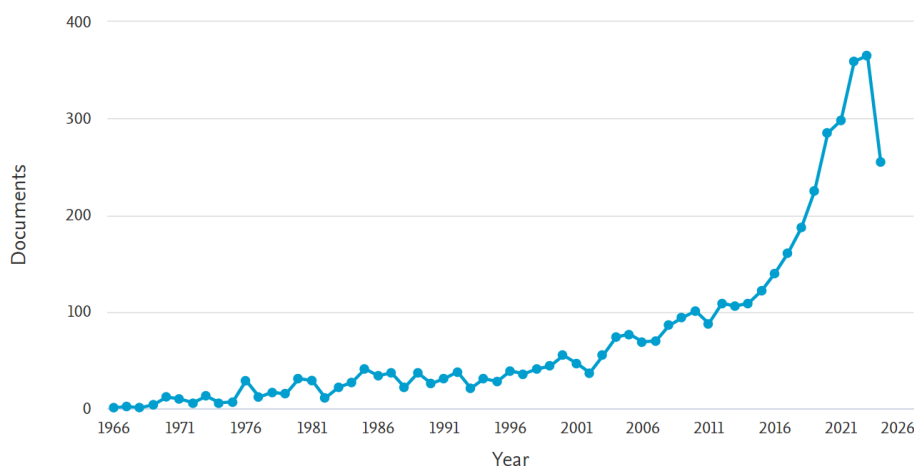


Figure 2-15. Scopus search analysis with keywords: ("heat pipe" OR "heat pipes") AND ("satellite" OR "satellites" OR "spacecraft"), data collected 29/08/2024.



A significant increase of annual published papers can be seen in the last decade with figures for 2024 expected to increase further by the end of the year. As no convection will occur in space, heat rejection through radiation is the main mode of transfer for satellites, as shown in Figure 2-16.

Component heat rejection may also be achieved via conduction through the satellite body or insulation and into subsidiary cooling systems. The smaller sized satellites face several thermal management challenges including:

- low thermal mass which increases their susceptibility to any change in environmental conditions,
- limited volume which increases thermal coupling between tightly packed internal components, and
- limited external surface area which results in restricted area for solar cells, radiators and overall radiative area for heat rejection.

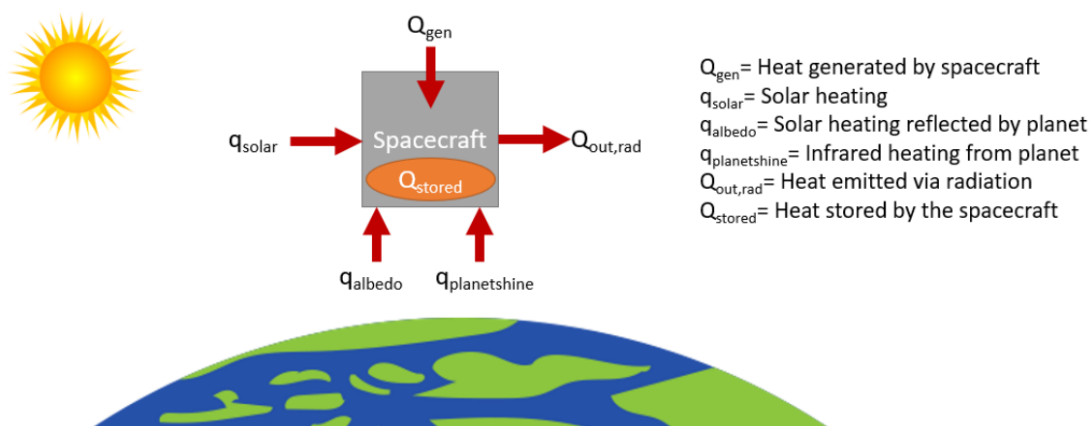


Figure 2-16. Orbiting spacecraft heating simplified overview, figure reproduced from [70].

The large variation in ambient temperatures experienced in space poses many thermal and engineering challenges when designing a thermal management system. With possibilities of high frequency freeze-thaw cycles, the choice of working fluid and heat pipe material is essential. Most spacecraft applications utilise ammonia, methanol, ethanol or water as the working fluid [53]. However, as water freezes it expands by around 9%, it is therefore critical to accommodate this expansion by either preventing the working fluid from overcooling via additional heaters or allowing for the expansion within the heat pipe structure [71]. Failure to do so may result in critical damage to the internal wick structure should the selected material have insufficient yield strength.



Heat pipes have been used for decades within the space industry with NASA commissioning Grumman Aerospace Corporation to investigate the potential uses of heat pipes aboard the space shuttle orbiter [72]. A total of 11 areas of interest were identified with the top 5 being:

- Heat pipe augmented cold rail
- Avionics heat pipe circuit
- Heat pipe / phase-change material modular sink
- Air-to-pipe heat exchanger
- Heat pipe radiating panel for compartment temperature control

In-depth analysis including physical design details, performance data and baseline comparisons were presented for each concept. A further concept of utilising heat pipes in space radiators for waste heat rejection showed great potential and was decided to be explored further under a separate project. Although this report is fairly dated by now, it identified the required research for further heat pipe-based aerospace development.

The GEOS-II satellite was the first to incorporate heat pipe technology as an integral part of the thermal system in 1968. The design effectively transported 64W of heat between two onboard transponders whilst operating with a small temperature gradient over the observed 145-day period. In comparison with the system's predecessor, GEOS-I, the maximum temperature of the transponder was reduced from 138°F (58.9°C) to 79°F (26.1°C) with the incorporation of the heat pipe [73]. Numerous satellites and spacecraft have utilised heat pipe technologies as part of their thermal management systems over the years, as outlined in Table 2-4. One key area of interest is the integration of multiple heat pipe configurations into one system. As developed by Advanced Cooling Technologies [74], the constant conductance heat pipes are embedded into the electronics boxes/modules and aid in effectively transferring the heat to the loop heat pipe evaporator. This integration aims to use the CCHP's higher heat capacity to reduce the thermal gradient at component level and then exploit the LHP's ability to transfer the heat over larger distances to the surrounding radiators.



2. Theoretical foundations and Literature Review

Table 2-4. Brief outline of heat pipe deployment in spacecraft and satellites.

Spacecraft Configuration	System Configuration	Company (Year)	Reference
GEOS - II	Aluminium 6061 T6 (1" OD, 0.065" wall) 120 – wire mesh wick Freon – 11 64 W HT rates	Applied Physics Laboratory (1968)	[73]
Bi-Spectral Infrared Detection (BIRD) 0.2m ³ 94kg Microsatellite	Constant Conductance grooved wick	(2001)	[70, 75]
TacSat 4 Micro-satellite 5-700W heat load	Aluminium / Ammonia loop heat pipe Nickel primary wick (<1.5µm), screen composite secondary Embedded constant conductance heat pipe	Naval Research Laboratory & Advanced Cooling Technologies (2009)	[74]
SDS-4 40kg Microsatellite	Flat-Plate Heat Pipe	JAXA (2021)	[70]
TechEdSat-10 6U CubeSat	FlexCool conformable micro heat pipe Copper	Redwire (2020)	[70]
Spacecraft or planetary surface vehicle	Heat pipe power system Sodium HPs to transfer heat from reactor uranium core to generate electricity via Stirling or Brayton cycle converters	Los Alamos National Laboratory	[76]
Space Shuttle Endeavour	High Temperature stainless steel/NaK heat pipe (482°C)	National Aeronautics and Space Administration	[66]
SAFE-400 (Safe Affordable Fission Engine)	Molybdenum heat pipe (880°C)	National Aeronautics and Space Administration	[66]
HOMER-15 (Heat pipe Operated Mars Exploration Reactor) 15-kW thermal unit	Stainless steel/sodium heat pipes structurally and thermally bounded to the fuel pins. OD 16mm, L 1.06m	National Aeronautics and Space Administration	[66]

In addition to the previously mentioned satellites, heat pipes have also been used for spacecraft applications including on the Space Shuttle Endeavour and in the SAFE-400 and HOMER-15 reactors. As a result of the high temperatures, alkali metals are often required to transfer the heat from the reactor to generate electricity via a subsidiary cycle such as the Stirling or Brayton cycles. Lee et al. [77] investigated a titanium water heat pipe radiator for a small fission Kilowatt system operable in the range of 1 to 10kW_e. The design incorporated



alkali metal heat pipes to transfer the heat from the nuclear reactor to Stirling convertors, as shown in Figure 2-17.

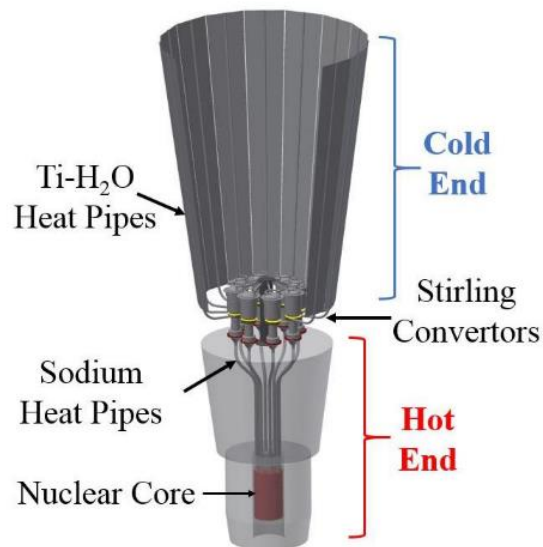


Figure 2-17. Kilopower system conceptual design and the thermal management system, figure reproduced from [77].

Separate specially designed titanium ware heat pipes were used to transport the waste heat from the convertors to the radiators which included a bi-porous screen evaporator and a screen-groove hybrid wick for the adiabatic and condenser sections. This enabled the system to operate under zero-gravity conditions, as well as against-gravity and below freezing temperatures.

2.6.3 Fuel Cells

There have been numerous studies researching the use of heat pipes for the thermal management of fuel cells. Sarraf et al. [37] designed a passive temperature control for a diesel fuel cell reformer. The rapid changes in fuel cell electrical load and reactant flow rates posed challenges for a standard valve-controlled thermal management control system. The design's advantages over traditional valve-based control systems include reduced ancillary equipment such as valves, sensors, actuators, or additional power which all result in reduced risk of failure due to maintenance issues. The flexibility in integration of the design has also improved, resulting in reduced overall reformer volume and reduced pressure drop across the heat exchanger.



Faghri and Guo [14] explored the possibility of integrating heat pipe technology into the bipolar plates of a proton exchange membrane fuel cell (PEMFC). Two designs were proposed, the first utilising micro heat pipes into bipolar plates for stack thermal control while another design used flat heat pipes, as shown in Figure 2-18. Having an efficient and effective heat pipe-based cooling system can reduce stack failure from overheating, in addition to simplifying the design and manufacturing process and improve power density and efficiency. It was also noted that utilising waste heat recovery for reactant preheat, pre-vaporisation, combined cycle operation or cogeneration is also beneficial.

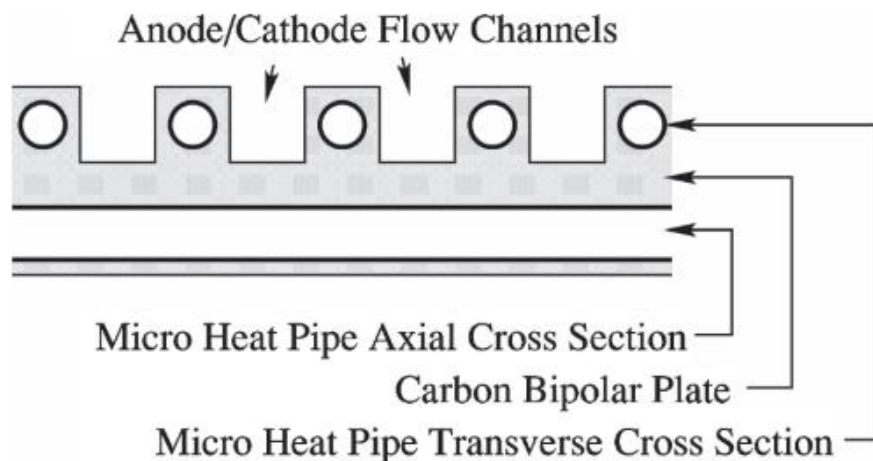


Figure 2-18. Micro-heat pipe embedded in a bipolar plate, figure reproduced from [14].

The proposed design shown in Figure 2-18 consists of a standard bipolar plate with additional holes where a separate heat pipe may be inserted and sealed together. However, this method would incur additional thermal resistance resulting in lower heat transfer within the device. Bipolar plates are manufactured from either graphitic or metallic materials such as stainless steel and titanium, or composites. However, for the purpose of this literature review, composite materials will not be considered. Each material has its own attributes and limitations as shown in Table 2-5.

Due to the possibilities of manufacturing PEMFC bipolar plates out of metallic materials, an opportunity arises to implement AM to develop a fully integrated heat pipe design and is of keen research interest. Furthermore, novel reactant flow paths may be developed to further enhance the FC efficiency.



2. Theoretical foundations and Literature Review

Table 2-5. Comparison of graphite and metallic material for bipolar plates, data collated from [78].

Material	Advantages	Disadvantages
Graphite	<ul style="list-style-type: none"> • High electrical conductivity • High thermal diffusivity • High corrosion resistance 	<ul style="list-style-type: none"> • Poor mechanical strength • Brittle • Poor production processing • High cost
Metallic	<ul style="list-style-type: none"> • High mechanical strength • High electrical conductivity • Simpler production process 	<ul style="list-style-type: none"> • Low corrosion resistance • Oxide layer formation increases resistivity • Coating generally required

Further studies [79, 80] have looked at the possibilities of including a separate flat-plate type heat exchanger within the fuel cell stack. The first study was undertaken by NASA as a means of passively cooling an acid-based PEMFC to reduce system complexity and parasitic losses. The design resulted in a titanium heat pipe with a thermal conductivity of 20,000 W/mK and a density of approximately 2.6 g/m³. This can be compared to the thermal conductivity of solid titanium alloys of around 5.5 – 25 W/mK and a density of 4.5 g/cm³ [81].

The former study followed a similar concept, as presented in Figure 2-19, and showed that flat plate heat pipes could benefit the PEMFC in terms of energy savings and simplification. Although the design in Figure 2-19 dissipates the heat into the environment, further development opportunities could make use of the waste heat for reactant preheating to further improve system efficiency. However, the proposed flat plate heat pipe design had an overall thickness of 1.5mm and manufacturing such thin structures with the fine internal wick structure geometry may prove difficult through MPBF technology.

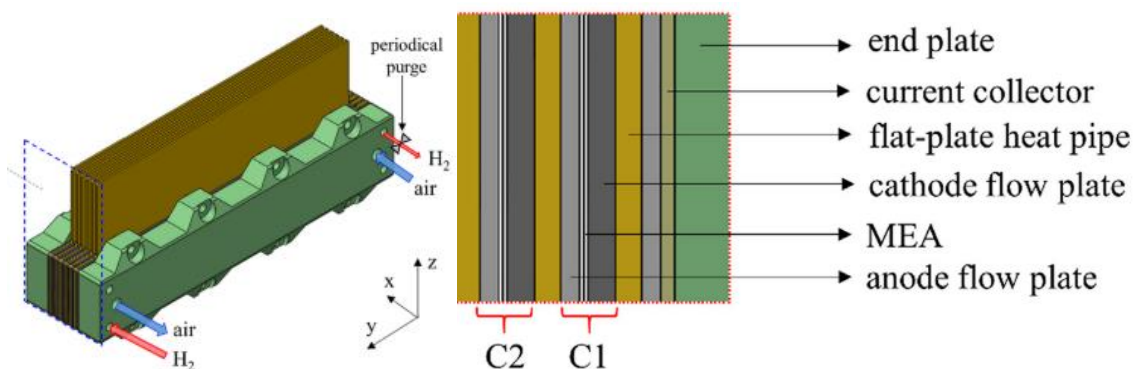


Figure 2-19. PEMFC stack cooled by flat-plate heat pipes, figure reproduced from [80].

An earlier study by NASA Glenn Research Centre [82] looked at dissipating the waste heat of a unitised regenerative fuel cell system to the surface of hydrogen and oxygen tanks with



the use of a looped heat pipe system. The condenser section was coiled around the tanks with a thin layer of thermally conductive carbon composite to spread the heat away from the pipe and across the entire tank. This resulted in mass reduction and system simplification through integrating the fuel tanks and radiator and shows great potential for future hydrogen-powered aerospace applications. Further potential for AM includes the design and manufacture of the evaporator section to both increase thermal transfer between the FC and heat pipe as well as enhancing its internal wick structure.

2.6.4 Additional Applications

There have also been several other applications mentioned in literature from concept to commercialised stages, each with varying technology readiness levels [49, 66, 83-85]. These applications include:

- Phase Change Material energy storage
- Nuclear reactor / waste storage facilities
- Chemical reactors
- Waste heat recovery from process for preheating combustion reactant / air
- Turbine cooling / isothermalisation
- Heat pipe turbine – power from low grade heat



2.7 Heat Pipe and Additive Manufacturing Integration

As discussed, AM is a rapidly evolving technology with the surrounding research at record levels, as shown in Figure 2-20. Evidently, there is significantly more research for additive manufacturing compared to that surrounding heat pipes, let alone the integration of both AM and HP technologies.

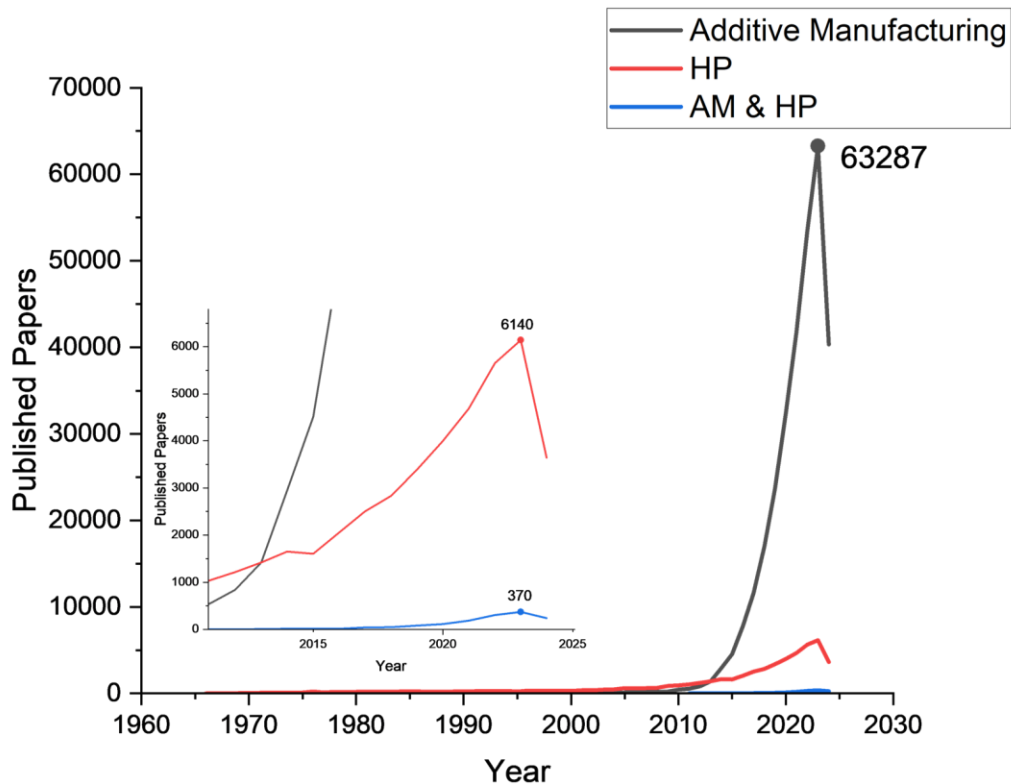


Figure 2-20. Scopus results for ("Additive Manufacturing" OR "3D Printing"); ("Heat Pipe" OR "Heat Pipes"); [("Additive Manufacturing" OR "3D Printing") AND ("Heat Pipe" OR "Heat Pipes")], data collected 17/06/2024.

Interestingly, the sudden surge in research surrounding AM began around 2010, and up until 2013 a greater number of papers were published annually for HP compared to AM. Numerous studies have been undertaken relating to the optimisation of HPs through AM technology.

As mentioned, the most common traditional wick structure is the sintering style, typically copper. Sintering of aluminium alloys can be exceedingly difficult due to the thermodynamically stable oxide layer on the powder surface caused by the presence of atmospheric oxygen or water vapour. To combat this, the oxygen partial pressure must be reduced to $<10^{-50}$ atm at 600°C which cannot be achieved during the conventional sintering process [86, 87]. AM can therefore play a key role in the manufacturability and development of aluminium heat pipes, bridging the gap between low temperature copper heat pipes and their higher temperature stainless steel counterparts.



Ameli et al. [88] was believed to develop the first SLM manufactured sintered-style aluminium heat pipe with ammonia as the working fluid. The work investigated a range of heat pipe parameters including porosity, permeability and pore size as well as density, hardness and vibration resistance. Optimal heat pipe performance requires high permeability to maintain low flow resistance and low capillary radius to achieve high capillary pressure, essential for applications where gravity is of concern. As discussed, a trade-off is required as lower pore radius tends to result in lower permeability. Two successful functional samples were obtained which proved the feasibility of SLM to manufacture heat pipes. Due to the novelty of the aluminium sintered-style heat pipe, economic comparison and justification was believed to be irrelevant. However, the prohibitive costs associated with AM may make the components more viable for high-performance and low volume applications. It should be observed that since the start of this work, advancements in AM have made larger volume productions more justifiable and viable. It was noted that high-performance applications may benefit from the manufacturability of the complex wick structures and optimisation possibilities for said application. However, in practice, the removal of any loose, non-melted powder within the wick structure has been found to be a key issue affecting performance, a problem throughout the additive manufacturing industry. This study found a profound difference between the theoretical and experimental values of permeability and pore size, believed to be down to an ineffective powder removal strategy. Furthermore, traces of titanium contamination were detected in the AlSi12 samples believed to have been from poor material changing process from previous builds and lab environment.

Traditionally, heat pipes with wicks manufactured through powder sintering have the drawback of pore randomness which can result in irregular liquid-vapour interface that in turn impacts the permeability resulting in unsteady fluid thermal behaviour. Esarte et al. [33] designed a prototype SLM manufactured loop heat pipe cooling system for an 80W LED streetlamp. The study resulted in a geometrically consistent component and achieved a pore radius of $80\mu\text{m}$, permeability of $1.25 \times 10^{-12} \text{ m}^2$ and 17% porosity manufactured from stainless steel grade 316.

Advanced Cooling Technologies (ACT) also studied the possibilities of manufacturing the evaporator section of a looped heat pipe through AM [89-92]. The aims were to reduce manufacturing cost and lead times that are associated with conventional labour-intense



methods of evaporator fabrication whilst achieving a pore size in the range of 1-10 μm to attain the required high capillary pressure. LHP evaporators are limited in length as they are reliant on an interference fit between the wick and body during assembly. Any misalignment can damage components and result in increased wastage, time and costs. The utilisation of AM would eliminate this issue as the wick and body is manufactured as a single component. Furthermore, AM eliminates the need for a knife edge seal as the components may be welded directly to the evaporator part.

Through an iterative process, a sub-5 μm pore size was achieved for the primary wick with a maximum value of 4.9 μm which was measured through the bubble point test in accordance with ASTM E128 standards [93]. In this study, porosity was achieved through altering the machine parameters to prevent the powder from fully melting. However, several samples failed the bubble point test due to the samples not being completely porous through out the length of the wick, together with the internal formation of cracks resulting from the incomplete sintering of the metal powder. It was noted that to achieve an even smaller pore size, more representative of traditional LHP wick structures, smaller powder size would be required. However, such powders are not yet commercially available. Findings also identified Hot Isostatic Pressing (HIP) as an effective post-production method of reducing pore size resulting in a 18% reduction. HIP is a process that is frequently used throughout the additive manufacturing industry and is considered effective in increasing component density as well as improving the component's microstructure homogeneity. However, further investigation is required as subsequent post-HIP heat treatments such as annealing may reopen pores and result in a "blistering" effect for near-surface pores [94]. The secondary wick, which aims to maximise permeability and liquid flow from the compensation chamber to the primary wick was identified as having an ideal pore size in the region of 30 - 50 μm . This was achieved using lattice structures, although challenges arose in terms of file size and machine/hardware capabilities. Due to this, and the large pores achieved, the feasibility of using defined lattice structures for full-scale LHP secondary wick was affected. However, further research into the management and processing of such large files may improve its viability in future.

Wick optimisation through AM has also been explored by Jafari et al. [95], which characterised the performance of various stainless steel wicks manufactured through AM in terms of porosity, effective pore radius, liquid permeability and capillary performance. It was



noted that gravitational effect resulted in slower capillary rising of the 3D-printed wick, compared to alternative conventional types such as sintered powder, screen mesh and composite wicks. A further study by Jafari et al. [96] explored the characteristics of a multi-scaled 316L stainless steel wick structure for a flat heat pipe. The design featured large pore structures manufactured through LPBF with laser-sintered micro-pores on top. The phase-change characteristics of the design was defined with a developed test rig and resulted in enhanced evaporative heat transfer. This shows immense potential for further developments of 3D printed wick structures.

Robinson et al. [97] developed a novel additively manufactured AlSi10Mg flat heat pipe. Through only varying the hatch distance between 0.6 and 1.0mm and maintaining the laser power at 370W and scan speed at 1300mms⁻¹, porosities of 43-59% and capillary performances of 0.27-0.45μm were achieved for the wick structures. Results indicated that increasing the hatch spacing resulted in both higher porosity and capillary performance.

A detailed study by Elkholy et al. [98] investigated the manufacturability, porosity and capillary performance of various AlSi10Mg LPBF lattice-based wicking structures for heat pipe applications. These included body-centred cube (BCC), face-centred cube (FCC) simple cube (SC) and Voronoi lattice designs while altering the strut thickness to control porosity. A mass-based capillary rate-of-rise experiment was undertaken with ethanol as the working fluid. Although the evaporative effects were reduced by capping the liquid opening, the authors fail to account for the evaporation of ethanol from the wick surface as it rises. The SC structure of 0.30mm strut thickness was identified as the highest performing structure with porosity and capillary performance values of 53.9% and 0.53μm, respectively.

Groth et al. [99] presented a new methodology for stochastic biomimetic designs also identified as well suited to the additive manufacturing sector. Through applying a Gaussian distribution and standard deviation to control the randomness, the methodology was able to create a truly biomimetic array of unit cells while randomising a range of parameters. Although heat pipes were not specifically mentioned in the paper, such integration of the design methodology may prove beneficial in future developments and should be investigated further.



2.8 Surface Roughness Enhancements in the Additive Manufacturing Industry

As previously identified, the inherently high surface roughness of additively manufactured components may have mixed results on their performance, depending on the application in mind. A review by Kaur and Singh [100] identified that inherent surface roughness is a key consideration across numerous heat exchanger types. Furthermore, this can contribute to significant dimensional deviation from the intended design. This is especially prevalent when approaching manufacturing limitations, as is the case with the lattice structures evaluated throughout this study.

Runyon et al. [101] investigated the effects of surface roughness on additively manufactured generic gas turbine swirl burners. Here, two AM Inconel 625 swirlers were manufactured, with one undergoing grit blasting as an additional post-processing step to reduce the R_a value by 40%, compared to the raw component. Increasing surface roughness was shown to increase turbulence near the burner exit. This along with the increased residence time resulted in enhanced flame stability and reduce NO_x emissions.

Numerous techniques have been conducted for surface enhancements of AM components including electropolishing (EP) [102-104], electrochemical polishing (EC) [105, 106], chemical polishing (CP) [102, 106-110], mechanical / abrasive [101, 111] and laser polishing (LP) [112, 113]. Each technique has its advantages and disadvantages which vary its suitability for each application. One of the key considerations for this study is the techniques' ability to penetrate the complex lattice geometries and provide isotropic removal of material throughout the component. Although a promising technique, LP requires line-of-sight between the optics and the surface [112] and therefore proves inadequate for use in this current study. Mechanical and abrasive methods such as milling, grinding, shot peening and sandblasting would again either require line-of sight or would produce uneven polishing of the surface through the lattice structure [114]. Utilising shot peening or sand blasting techniques also runs the risk of particles getting stuck within the structure which could drastically impact its performance.

A study by Tyagi et al. [102] investigated the effects of both CP and EP on the roughness of AM internal surfaces. The work showed CP to be effective in simultaneously reducing the surface roughness on complicated internal and external stainless-steel surfaces. The arithmetic mean areal surface roughness, S_a , was reduced to 2.10 and 5.22 μm for EP and CP, respectively, from an unpolished value of 13.88 μm . Interestingly, sub- μm cavities were



identified for both methods, covering only 1.3% of the EP surface whereas the entire surface of the CP sample was impacted. The study showed that electropolished samples reduced the contact angle of water on the sample from 90° to 45° , while no significant change on the chemically polished sample was identified. EP therefore appears to be a promising method for the reduction of surface roughness while also enhancing the capillary pressure through increasing the hydrophilicity of the surface/fluid. However, the complex nature of lattice-based wicking structures could cause issues for placing the counter electrode at a close enough proximity to the surface to be polished, which was identified as an important consideration by Tyagi et al. This phenomenon is further identified by Acquesta and Monetta [103] who identified a greater decrease in surface roughness at locations closer to the cathode. Further identified was EP's reduced effectiveness for internal surfaces due to the electrolyte's low conductivity.

Ferchow et al. [104] investigated the effects of EP on a complex stainless steel SLM component consisting of internal surfaces and lattice structures. Three different EP techniques were evaluated: direct current, pulse/pulse reverse current and pulsed current while varying current density and processing time. The direct current technique showed to have most effect on the lattice structure, however it should be noted that geometric features of the designed lattice structures were, at a minimum, an order of magnitude larger than that expected sufficient for heat pipe wick structures.

A review into the influence of post-processing techniques on AM lattice structures conducted by Majeed et al. [115] identified the possibility of utilising CP as a method to dissolve the semi-attached powder particles without altering the surface chemical composition. However, caution should be taken with processing time, as treating for too long can create surface porosities, reduce strut diameter and lower strength and stiffness.

Similarly, Chmielewska et al. [116] examined the effects of CP to remove semi-sintered agglomerated powder particles from the surface of a NiTi skeletal fixation plate. Here, three solutions containing varying concentrations of Hydrofluoric acid (HF), Nitric acid (HNO_3) and Water were used in an ultrasonic bath at room temperature for between 3 and 10 minutes. As stated, HF was used as a dissolvent while the HNO_3 passivated the surface, increasing the surfaces' corrosion resistance. Due to the aggressive nature of HF, it was deemed essential to reduce the HF concentration and increase the HNO_3 to optimise the polishing process.



Sharma et al. [108, 109] investigated CP of AlSi₁₀Mg AM cuboid components in a bid to improve overall surface quality. A solution containing 800ml Phosphoric acid (H₃PO₄), 100ml Hydrochloric acid (HCL), 100ml Water and 40g of Potassium Nitrate (KNO₃) at 95°C was used. The treatment occurred in two stages: the first where the peaks begin to dissolve and settle into the trenches achieving a smoother surface with minimal dimension loss. The second stage resulted in the metal surface beginning to degrade and overall sample height reducing. In both studies, it was identified that the greatest reduction in surface roughness occurred at the earlier stages. Results showed a reduction in Ra values from 19.37 to 3.39µm over a 15minute period. With consideration of AlSi₁₀Mg AM lattice structures, it is anticipated that the desired results will occur within the first 10 minutes, without overly impacting the bulk geometric dimensions. Interestingly, the solution showed no change in the surface chemical composition of the samples pre and post polishing.

Scherillo et al. [110] performed a similar study with the use of different chemical solutions. This methodology utilised two stages: chemical machining consisting of a solution of HF, HNO₃ and water, and chemical brightening consisting of a solution containing HF, HNO₃, H₃PO₄, H₂SO₄ and CuSO₄. The chemical machining step showed to have reduced the arithmetic mean height, Sa, from ~25 to ~15µm, while the chemical brightening stage further reduced Sa down to ~7µm. The study further noted the ability of the chemical machining stage to provide a constant etching rate, allowing for accurate material removal predictions. Both steps had no change on the composition of the alloy. Although the study by Scherillo et al. showed promising results, like that of Sharma et al., the use of HF poses additional risks and hazards that should be thoroughly considered.

In addition to altering the surface topography of AM structures, chemical polishing has been widely observed to be vastly superior for improving fatigue properties compared to both stress relieving and hot isostatic pressing due to the removal of the attached powder yielding a smoother surface [114, 117]. Numerous studies have investigated the use of chemical polishing for lattice structures [107, 116, 118]. However, these were all titanium-based alloy scaffold structures. Further studies into AlSi₁₀Mg solid bulk geometries have also been investigated [108-110, 119]. To the best of the author's knowledge, no studies investigating the effect of chemical polishing on AlSi₁₀Mg micro-lattice structures, and its influence on heat pipe performance, have been conducted.



2.9 Review Summary & Opportunities

In conclusion, heat pipes have been shown to be highly efficient and effective heat transfer devices that could play a significant role in aiding to improve system efficiency, performance and reducing parasitic losses. Such applications of interest include the thermal management of fuel cells, electronic components, power electronics and particularly aerospace and spacecraft-based systems. The heat pipe's advantages of having practically no maintenance requirements make it particularly suited for these applications with long operational lifetimes and limited access once in operation.

Numerous wick structures are available including axial groove, fine fibre, screen mesh and sintering. Additive manufacturing has an opportunity to produce new and novel wick structures which could imitate and enhance the characteristics seen within sintered wick designs while also overcoming the associated pore-randomness often associated with sintered structures. Further enhancement of the local wick characteristics of each section of the heat pipe to improve both mass transport and thermal properties is also possible. The implementation of additive manufacturing could eliminate the entrainment of the fluid from the wick before it returns to the evaporator section. This may be achieved through manufacturing a solid wall along the liquid-vapour interface within the adiabatic section.

Further research is needed to ascertain the most effective method for generating fine porous structures via additive manufacturing. Altering the machine parameters to replicate a sintering process may prove beneficial in achieving smaller pore sizes and simplifying the design stages. Utilising defined lattices will provide greater control and repeatability within the process, in addition to enhanced modelling opportunities, but do suffer from larger file sizes which limit the size of printable components. Investigation of data management and processing is key for future additively manufacture heat pipe progression.

Several heat pipe designs, including the conventional, loop, pulsating, variable conductance heat pipes and the vapour chamber have an opportunity to further enhance the thermal management of such applications. The integration of a variable conductance heat pipe could prove to be beneficial for thermal management at varying loads or ambient conditions. A loop-based heat pipe may reduce system complexity and simplify integration with opportunities for additive manufacturing to improve heat transfer within the evaporator and condenser section as well as enhancing the primary and secondary wick structure.



Increased surface roughness has been identified as an inherent factor of additive manufacturing. Both EP and CP have been utilised throughout literature to effectively reduce the surface roughness of additively manufactured components. However, due to the nature and complexity of lattice structures, EP may not effectively treat the internal surfaces. With limited literature identified, higher surface roughness could be detrimental to the fluidic performance of lattice-based wicking components as the fluid's contact angle, and hence hydrophobicity of the structures, could be increased severely impacting the structure's ability to deliver sufficient capillary pressure. The lack of literature investigating surface roughness modifications of $\text{AlSi}_{10}\text{Mg}$ lattice structures was identified as a clear opportunity for further research. Therefore, as key parameters in the design of heat pipes, the effects of surface roughness, and surface roughness enhancements, on both capillarity and permeability should be further investigated.

2.10 Objectives

The following objectives have been identified for this study addressing the limited research for the effects of surface roughness on additively manufactured heat pipe wicking structures identified throughout this chapter:

1. Examine the influence of varying the design parameters and build orientation of Body-Centred Cubic (BCC) lattice structures on geometric accuracy and printability.
2. Develop a 2D geometry analysis tool, to improve workflow efficiency and effectiveness while validating against other tools and methods.
3. Optimise porous wick structures to maximise capillary performance and permeability.
4. Determine the relationship between capillary performance, wick pressure drop and pore size to establish the most effective design for specific applications.
5. Investigate the influence and effectiveness of surface roughness modification on wick geometry and performance.



3. Experimental Design and Theoretical Frameworks

This Chapter outlines the underlying methodologies and necessary theory required to achieve the research objectives previously set out. It will cover the initial design stage through to the various experimental campaigns and analysis.

3.1 CAD Preparation

Based on the extensive industrial knowledge and expertise of HiETA Technologies Ltd. / Parker Aerospace, the parameter limitations, shown in Table 3-1, were chosen.

Table 3-1 Sample build limitations.

Lattice Type	Body-Centred Cubic (BCC)
Cell Size Range (mm)	0.70 - 1.00
Strut Diameter Range (mm)	0.15 - 0.30
Geometry Varieties	12
Total Samples	24 (12 Horizontal & 12 Vertical – See Section 3.2)

Both cell size and strut thickness ranges were determined by considering machine limitations, powder size, and available machine parameters to achieve a reliable build. A streamlined and highly effective workflow methodology was devised for generating the complex lattice geometries using a visual 3D modelling tool. The methodology specifically developed by the author for this study leverages advanced parametric capabilities to allow for rapid iterations and design adjustments, significantly reducing time spent on manual modifications and improving overall efficiency. Due to the proprietary nature of the work and the intellectual property involved, further technical details and specific implementations remain confidential and beyond the scope of this study. A detailed identification of parameters for each sample with the relevant identification is shown in Table 3-2 with parameters illustrated in Figure 3-1.



3. Experimental Design and Theoretical Frameworks

Table 3-2 Sample build Parameters.

Sample ID	Unit Cell Size (mm)	Strut Thickness (mm)
1	1.00	0.30
2	0.90	0.30
3	0.80	0.30
4	0.70	0.30
5	1.00	0.20
6	0.90	0.20
7	0.80	0.20
8	0.70	0.20
9	1.00	0.15
10	0.90	0.15
11	0.80	0.15
12	0.70	0.15

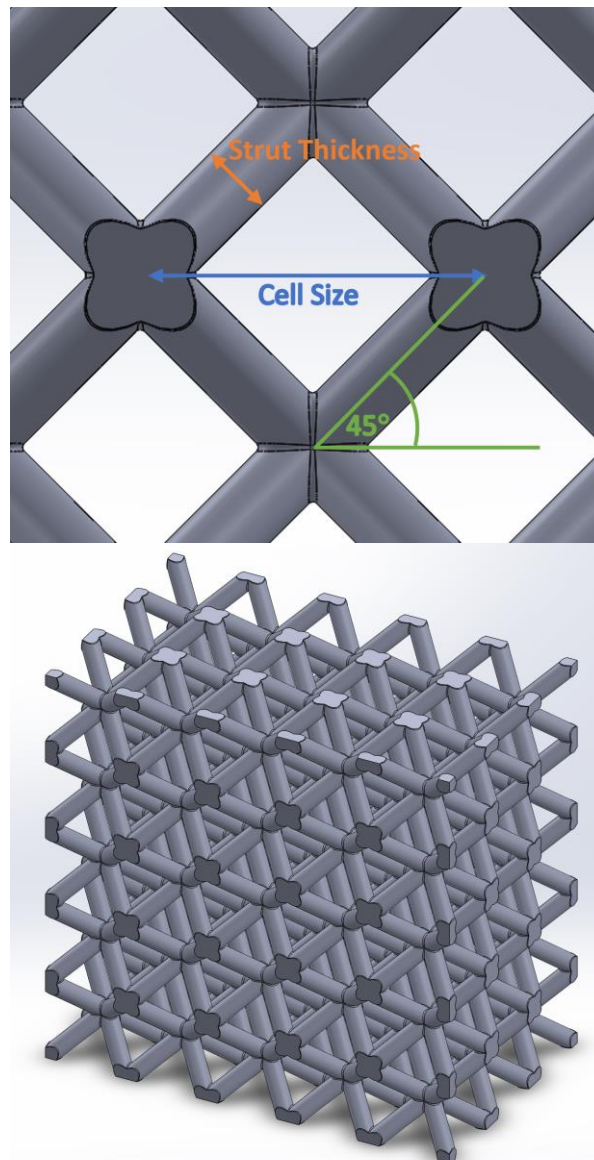


Figure 3-1. Lattice geometry parameters (Top) and 3D trimetric view (bottom)



3.2 Manufacturing

Samples were manufactured from aluminium alloy, AlSi₁₀Mg via LPBF by HiETA Technologies Ltd. / Parker Aerospace. The raw aluminium powder used for this study had a median diameter of approximately 40µm with a typical distribution of 20-60µm. The machine of choice was the Renishaw RenAM 500Q, printed with a 30µm layer thickness to capture as much detail as possible and achieve the desired net shape designs. The RenAM 500Q has 4 x 500W lasers of 1070nm wavelength and 80µm spot diameter [120]. Each sample geometry was printed in both horizontal and vertical orientation, as illustrated in Figure 3-2.

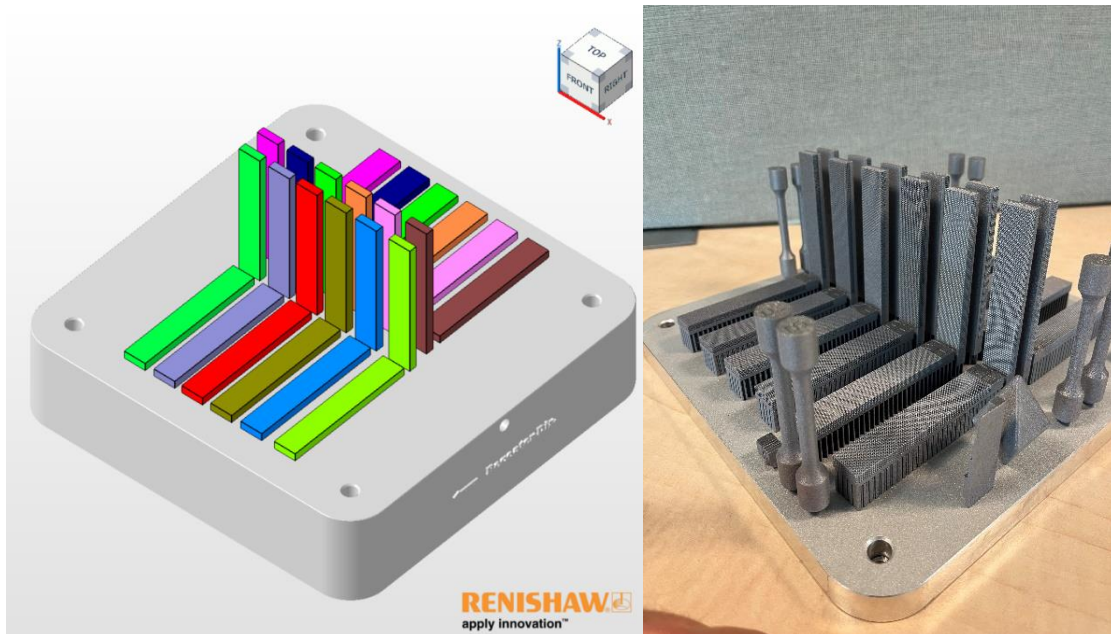


Figure 3-2. Proposed Build plate layout (Left) and printed components with traveller samples (Right).

As can be seen in Figure 3-2, each sample was attached to the build plate with specially designed breakaway supports. The build had a total of 3251 layers and used a total of 121.8cm³ of powder with a total build time of 17 hours. Following removal of the build substrate, the majority of unfused powder was removed inhouse at HiETA Technologies Ltd., prior to delivery of samples. This process included a multi-axis stage, with varying vibratory frequencies and amplitude. Following this, the samples had undergone a thorough purging step with compressed air where the majority of remaining residual powder was removed. As a precautionary measure, samples were soaked in a bath of Isopropanol Alcohol (IPA) and treated in an ultrasonic bath for 15 minutes before testing began.



3.3 Porosity Measurements

As discussed, porosity is a key factor in the development of heat pipes and other devices reliant on both heat transfer and fluid flow. Porosity can be presented in numerous forms including apparent, true, and trapped porosity [121]. Apparent porosity compares the apparent density of the wick to the theoretical value of the material, in this case, AlSi₁₀Mg has a density of 2.67 g/cm³ [122], as shown in Equation (3-1). This porosity method considers any loss of mass from internal microporous defects and closed off pores.

$$\varepsilon_a = 1 - \frac{m_w}{V_w \rho_s} \quad (3-1)$$

Where ε_a , m_w , V_w and ρ_s are the apparent porosity, mass, bulk volume, and density, respectively. Due to the samples including a mixture of wicking lattice structures and supporting material, it was necessary to disaggregate the mass into the unnecessary bulk material and actual mass of the lattice section for the calculations. This was attained through measuring the mass of the entire sample, m_s , and subtracting bulk mass, as shown in Equation (3-2).

$$m_w = m_s - (V_B \rho_s) \quad (3-2)$$

Bulk volume, V_B , was based on the geometric dimensions of the original CAD drawing, which aligns well with the printed bulk geometry. True porosity only considers the main pore space and disregards any defective trapped porosities. This was calculated following Archimedes' method through using a wetting liquid to fully saturate the wick while recording the total mass of liquid as explained in Equation (3-3).

$$\varepsilon_t = \frac{1}{1 + \frac{m_w \rho_l}{m_l \rho_s}} \quad (3-3)$$

Where m_l and ρ_l equate to the penetrated mass and density of the wetting liquid, respectively. However, a disadvantage of using both methods is the assumption of solid density values, which can decrease the reliability of results for smaller porosity structures [123].

As discussed by Jafari et al. [95], a volatile liquid should be used and the mass recorded as the level of liquid falls beyond the pores. For this study, acetone of density 0.79g/cm³, was



used as the saturating liquid for its volatility and enhanced wettability characteristics compared to water. Acetone was infiltrated into the wick with a 1ml syringe which allowed precise dropwise application. For all porosity measurements, each test point was repeated three times with averages and variations calculated, as discussed in Section 5.4.

3.4 Geometry Validation

Validation of geometry is an essential stage to determine the reliability and robustness of experimentally based results. Numerous techniques such as 2D/3D microscopy, Scanning Electron Microscopy (SEM), and X-ray Computed Tomography (XCT) have been utilised throughout this work to characterise the complex and fine geometry incorporated into the design of AM heat pipe wick structures. Each technique comes with its benefits, limitations, and challenges which is discussed further throughout this section. Existing test methods such as standard and micro X-ray Computerised Tomography (XCT / μ -XCT) and SEM can be costly processes throughout the initial design stage and often require subcontracting to external partners thus inducing additional lead times and risks [124]. On the other hand, traditional 2D digital microscopy can often be completed in-house at lower cost but may require additional time for analysis, especially considering that of complex lattice geometries. Another possibility is Mercury Intrusion Porosimetry (MIP). As there have been reports of performance characterisation of additively manufactured heat pipes with the use of MIP [125], due to the incompatibility and potential harsh reaction between mercury and aluminium and the small test volume, this method was not chosen for further analysis in this study. For this thesis, a specially designed non-proprietary software, Lattice Analysis Tool (LAT), was developed to effectively assess 2D scans of lattice geometries, as further described in Chapter 4.

3.4.1 3D Profilometry

Due to the steep inclines and relatively large distance between the peaks and troughs of the cells in the z direction, 2D microscopy proved to be ineffective in providing clear, in-focus images. Here, the Sensofar S Mart non-contact 3D optical sensor, shown in Figure 3-3, was used for both still imaging and surface roughness analysis. Numerous parameters, both areal and profile based, are available for surface topology characterisation of additively manufactured components.





Figure 3-3. Sensofar S Mart 3D optical sensor. Figure reproduced from [126].

Historically, styli-based profilometers, classified under ISO 4287 [127], have been the most widely used method and are still ubiquitous throughout industry to date [128]. However, for the purpose of analysing complex and porous additively manufactured components, such as lattice structures, styli-based measurements prove to be impractical and could lead to damage of the component and apparatus [29, 129].

The sensor has the option of three different measuring techniques [126]:

- Confocal – to measure surface height of both smooth and rough surfaces while providing the highest lateral resolution of all techniques with special sampling down to $0.10\mu\text{m}$.
- White Light Interferometry – to measure surface height of smooth to moderately rough surfaces and provides nanometre vertical resolution.
- Focus Variation – tailored for large surface roughness samples. This technique can offer up to 86° sloped surfaces, high measurement speeds, and an increased vertical range.

Due to the inherent large surface roughness often associated with AM parts and its higher measurement speeds, focus variation was chosen as the measuring technique for the analysis of AM lattice structures. Focus variation allows the objective lens to focus a beam of white light onto the surface, which is then projected onto a planar detector. A series of in-focus images are captured throughout the z-axis between the minimum and maximum planes of



focus for the sample [128]. Equipped with a 10x Objective and a coaxial and ring light, the Sensoscan, alongside the SensoVIEW software [130], can effectively determine a range of useful features including surface roughness, topography characteristics and surface profile as shown in Figure 3-4.

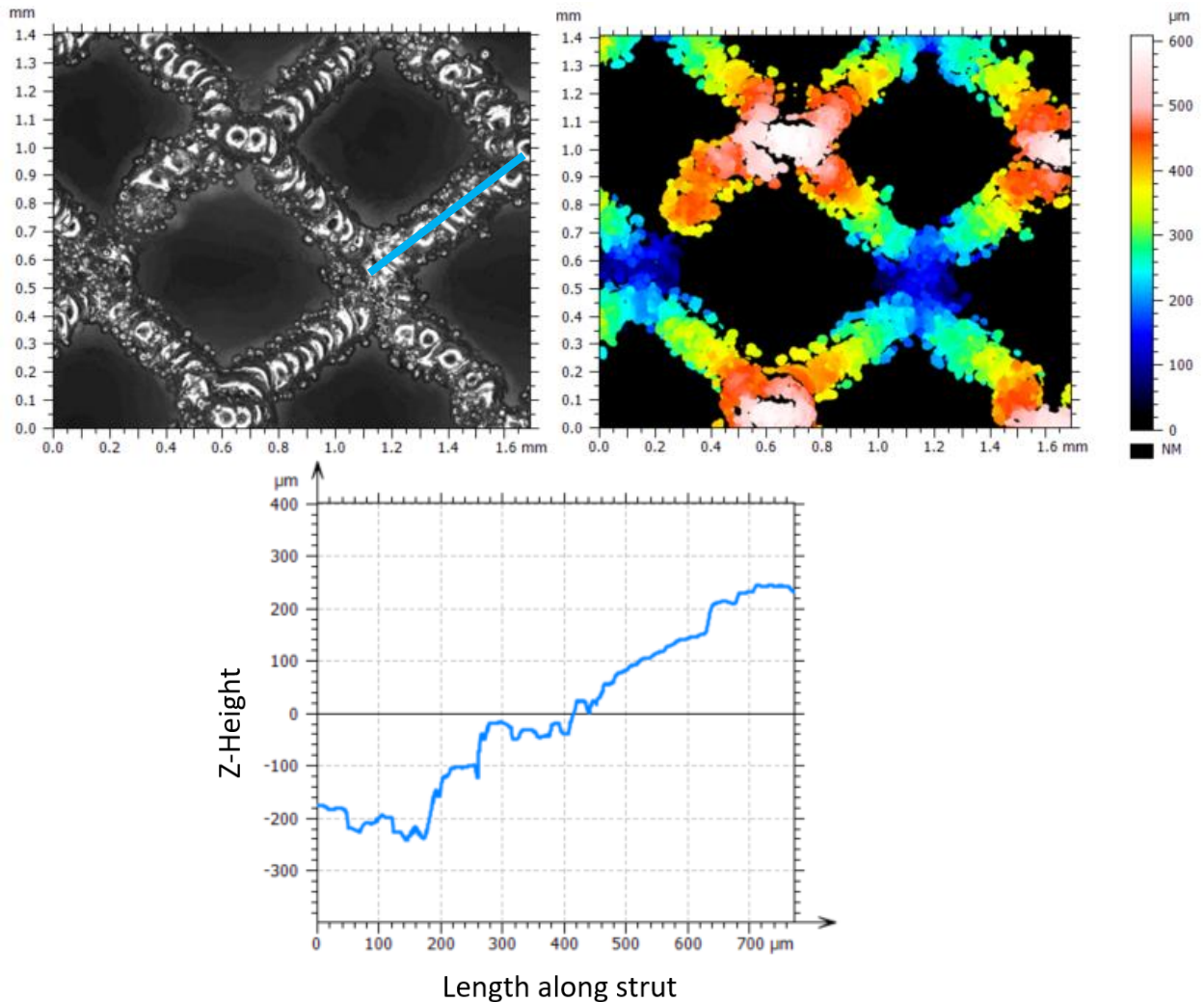


Figure 3-4. Example 3D Optical scan of unit cell lattice structure: Stacked image (top left), Topography (top right) and extracted profile of a single strut (bottom).

Here, the agglomeration of partly melted particles during the printing process is clearly visible on the strut surface and is discussed further throughout this study. Furthermore, the stair-stepping effect is clearly visible, which in conjunction with other factors, can impact the surface roughness of the structures and deviate away from the intended net shape design. The effect of layer height on the overall structure can be visualised in Figure 3-5.



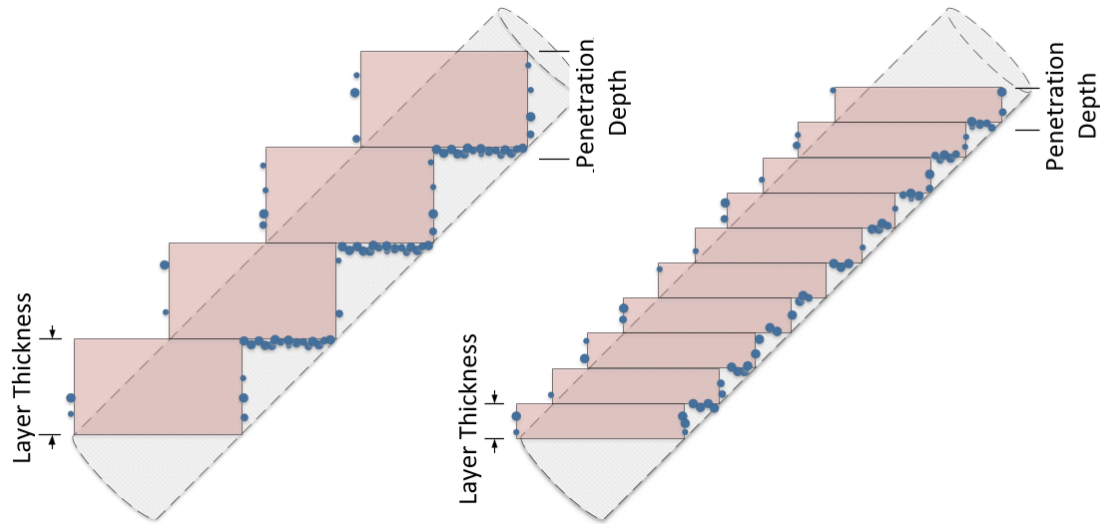


Figure 3-5. Comparison of large (left) and small (right) layer height on the overall intended design.

The areal height parameters to be considered for this research include the arithmetic mean height (S_a), root mean square height (S_q), maximum peak height (S_p), maximum valley height (S_v) and maximum height (S_z) as described in Equations (3-4) to (3-8).

$$S_a = \frac{1}{A} \iint_0^A |Z(x,y)| dx dy \quad (3-4)$$

$$S_q = \sqrt{\frac{1}{A} \iint_0^A |Z^2(x,y)| dx dy} \quad (3-5)$$

$$S_p = \max_A X(x,y) \quad (3-6)$$

$$S_v = \min_A X(x,y) \quad (3-7)$$

$$S_z = S_p + S_v \quad (3-8)$$

One key consideration for surface topography evaluation through non-contact methods, such as that of focus variation, is the preprocessing of the data and selection of the filter nesting indexes as per ISO 25178 [131]. Data preprocessing included form removal, levelling and restoring non measured points. The surface filters may be categorised as: form removal (F-Operator), high-pass filter (L-Filter) and low-pass filter (S-Filter). With a combination of



such filters and operations, the primary surface may be adapted to determine the roughness surface (S-L) and waviness surface (S-F), as depicted in Figure 3-6 and Figure 3-7.

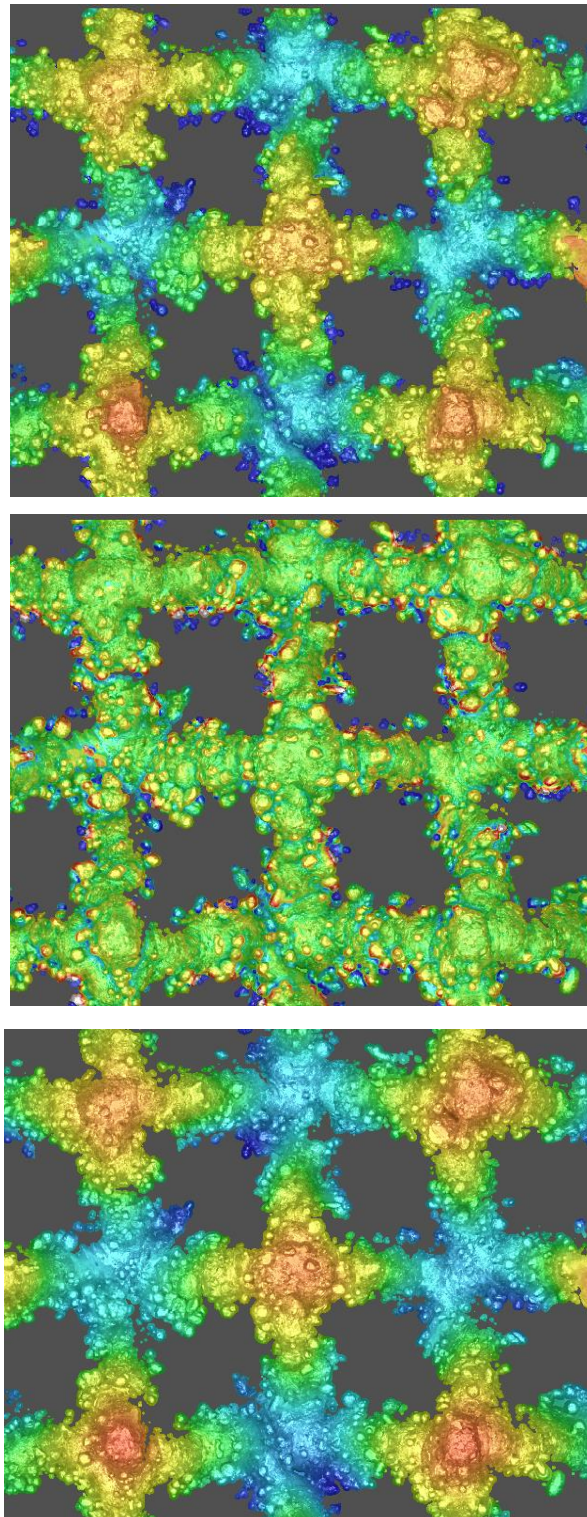


Figure 3-6. Example image of areal Primary Surface (top), Roughness Surface (middle) and Waviness Surface (bottom).



3. Experimental Design and Theoretical Frameworks

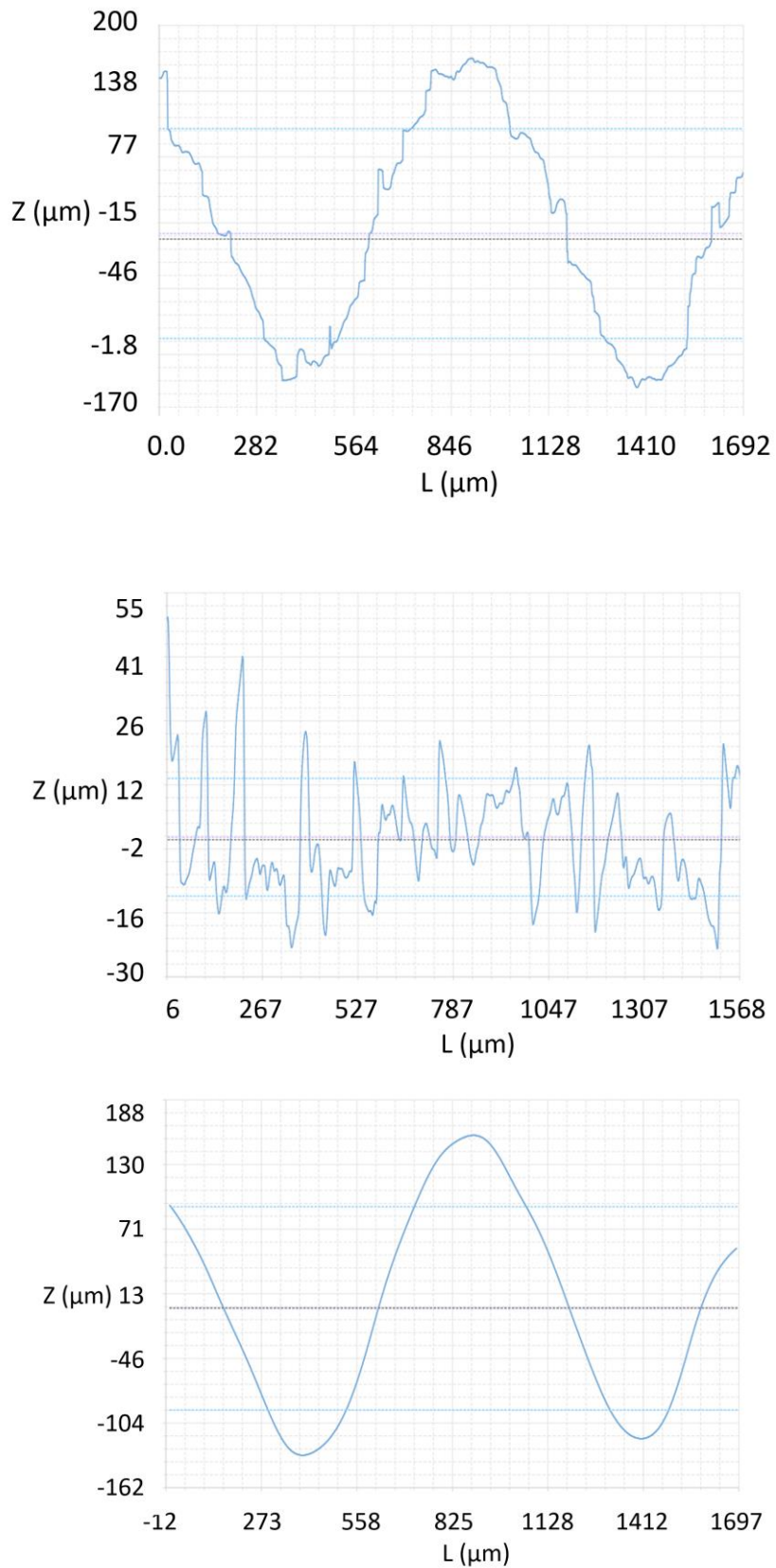


Figure 3-7. Example image of profile Primary Surface (top), Roughness Surface (middle) and Waviness Surface (bottom) along approximately one-and-a-half-unit cell.



For the purpose of this research, the roughness surface is used to determine the height parameters previously stated in Equations (3-4) to (3-8). The default filter of choice, in accordance with ISO 25178, is a gaussian filter which is employed throughout this research. The low-pass (S-Filter) is often utilised as a noise filter and typically has less impact on the results compared to its high-pass counterpart. For this study, the smallest standard value within the software of $8.000\mu\text{m}$ was chosen for the S-Filter nesting index, allowing for removal of process induced noise while maintaining sufficient sample detail.

As recommended by ISO 25178, the L-Filter nesting index is typically *“five times the scale of the coarsest structure of interest”* [131]. For this study, and often for other AM components, the coarsest structure of interest is the agglomerated, semi-sintered particles of powder. A total of 5 samples were evaluated with twenty particles measured on each with an average diameter of 0.030mm . Therefore, the L-filter nesting index was set to 0.150mm . Additionally, levelling, thresholding and restoring algorithms were applied to each sample allowing for the removal of any major discrepancies and restoration of small non-measured locations. Three measurements have been taken on the front face of each sample at the top, middle and bottom. Capturing surface roughness measurements at the top, middle and bottom locations of the samples allowed opportunities to determine the effect of build height and any warpage experienced within the samples. However, further analysis was undertaken on the side faces of several horizontal samples, corresponding to the vertical build z-axis, reflecting that of the front face of the vertical samples. This allowed for comparison between the various build planes of the samples. Measurements were concentrated on the front faces due to time constraints and increased amount of dislocated and damaged cells appearing on the side faces, resulting in limited measurement capabilities.



3.4.2 Scanning Electron Microscope

High magnification Scanning Electron Microscope (SEM) images were captured on the ThermoScientific Phenom Desktop SEM [132], with main components shown in Figure 3-8. Detailed visualisation of a sample's surface is achieved by utilising a focused beam of high-energy electrons produced with an electron gun. The emitted electrons are captured by detectors, which convert these signals into a form that can be processed to create an image. Differing to standard microscopy techniques, SEM offers increased resolution and enhanced depth of field along the optic axis (typically 100 times larger than that possible by light microscopy [133]), making it ideally suited for the analysis of intricate lattice structures.

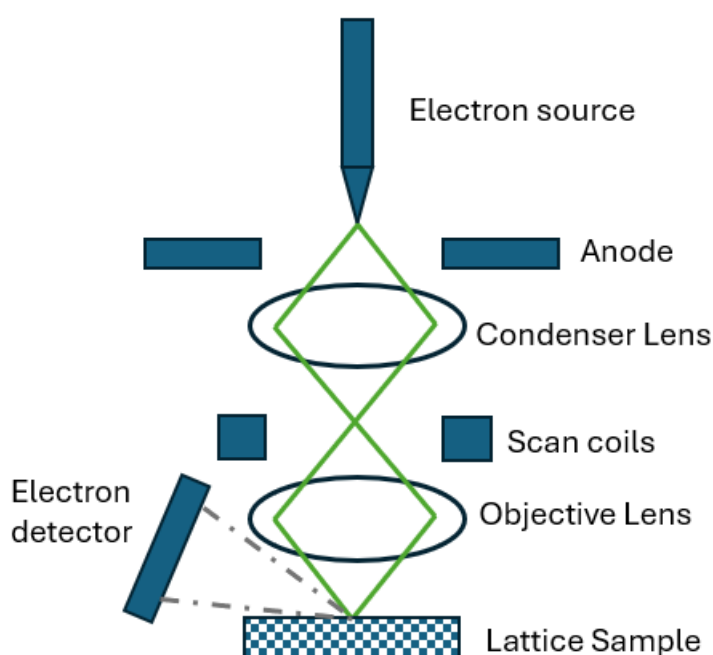


Figure 3-8. Main components of SEM process, figure adapted from [132].

The SEM's additional Energy Dispersive X-ray Spectroscopy (EDS) functionality was also used to quantify any change in elemental composition of the samples following the chemical polishing procedures. When the electron beam from the SEM interacts with the sample, it can eject inner-shell electrons from atoms, causing the emission of X-rays. These X-rays have energies that are characteristic of specific elements, allowing the EDS detector to identify and quantify the elements present in the sample. For this study, a 15kV accelerating voltage was used for both SEM and EDS data collection.



3.4.3 X-ray Computed Tomography (μ -XCT)

As a non-destructive analysis technique, μ -XCT can aid in analysing internal structures in addition to supporting a more effective method to identify specific regions of interest. XCT analysis enabled further quantification of porosity, pore, and strut diameter distribution in addition to identifying any internal defects or irregularities. XCT operates based on the principle of exposing a sample to a stream of X-ray radiation, capturing the ensuing absorption X-ray image, and iteratively collecting these images as the sample undergoes rotation. The obtained X-ray absorption images, referred to as projections, offer diverse perspectives of the sample from various angles, revealing internal details as a result of X-ray penetration.

The data was captured within the Nikon Metrology “High Flux” bay at the Henry Moseley X-ray Imaging Facility [134], shown in Figure 3-9. The Nikon system voltage and current were set to 150kV and 90 μ A, respectively. Together with the 2024 x 2024-pixel detector and 6358 projections at an angular step of 0.05662°, the system achieved a reconstructed voxel resolution of 13.986 μ m with a volumetric aspect ratio of 1. To attain the achieved voxel resolution, a narrower field of view of 28.31mm was used. Although this limited the analysis of distribution through the length of the samples, ensuring superior resolution was of greater importance.

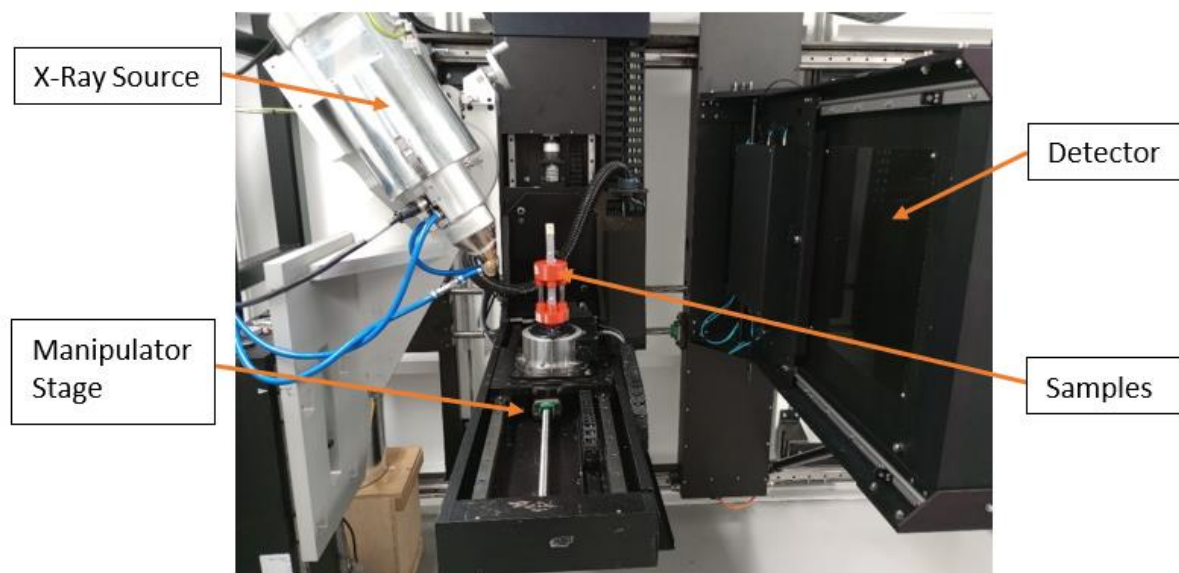


Figure 3-9. Nikon Metrology “High Flux” Bay

To fully exploit the machine’s allotted scanning time, minimise sample setup time, and improve overall workflow efficiency, three samples were placed back-to-back with an additional set of three located above with each set taking approximately 3 hours to complete



the scan. Each sample was separated with approximately 1mm thick packing material to simplify the data separation during the post-processing stage. To achieve a high resolution, a rigid and compact supporting rig was required. Additionally, including low density materials allowed the X-rays to easily pass through toward the region of interest, enabling a low X-ray attenuation. The rig was 3D printed, via Fused Deposition Modelling (FDM), out of Polylactic Acid (PLA) with hollow acrylic supporting rods of density 1.24 and 1.18 g/cm³ [135, 136], respectively. As the diagonal X-ray paths had more material to penetrate, reducing the amount of material in this direction was essential to further improve the scan quality. Therefore, the supporting rods were located perpendicular to the front/back and side faces of the samples. A drawing of the finalised rig is shown in Figure 12-2 in Appendix 12.3.

Following the reconstruction of the scanned data, post-processing and further image analysis were completed using the Dragonfly software [137], in addition to LAT. The overall structure for determining porosity values is shown in Figure 3-11.



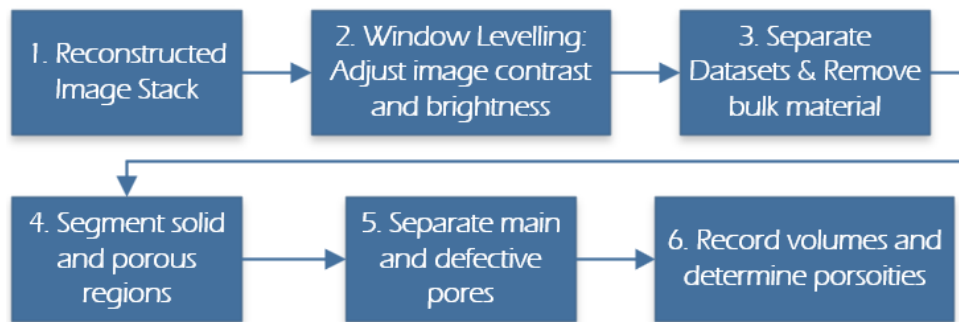


Figure 3-11. Workflow of porosity determination via XCT analysis.

The reconstructed stack for each sample set consisted of 2024 greyscale images in TIF format and sliced in the XY plane. These were directly imported into the dragonfly software whilst cropping out surrounding air space and several of the first and last slices to disregard the ring artifacts, shown in Figure 3-10.

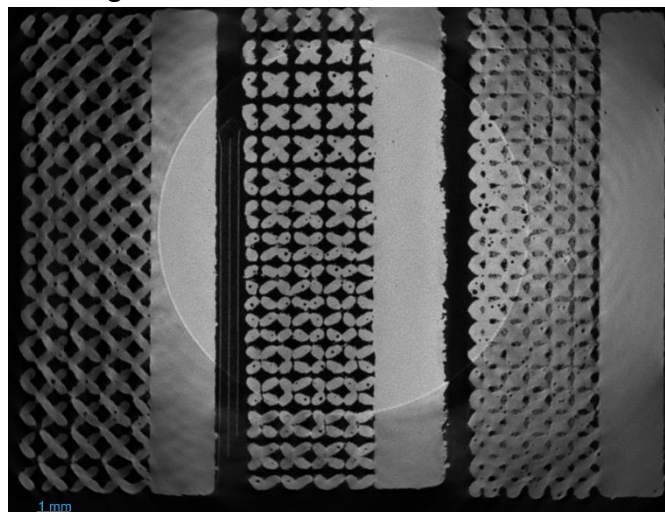


Figure 3-10. Example of ring artifact seen within the reconstructed slices

The ring artifact identified in Figure 3-10 can be seen throughout all sample sets and may be a result of a defective or incorrectly calibrated detector within the CT hardware [138]. Due to the artefacts only being apparent on the outside slices, the likely cause is ineffective use of beam hardening compensation techniques [128, 139]. As discussed by Townsend [128], this is a result of the weak X-rays being more readily absorbed by the structure thus hardening the beam. One such method of beam hardening compensation is with the use of aluminium or copper filters placed in front of the X-ray source. Since collection of data, it has become apparent that no such filters were used for this study. Nonetheless, as the artefact only impacted a few external slices, disregarding these slices had no significant impact on the results.



Through adjusting the window levelling settings, both contrast and brightness may be tailored to emphasise the visibility of specific material classes, i.e. solid metal or surrounding void space. To calculate both apparent and true porosity, it was required to separate each sample and crop out any of the supporting bulk material.

Through evaluation of the greyscale image stack's histogram, two noticeable peaks are present, with the lower and higher density peaks identified in Figure 3-12 corresponding to the porous voids and solid classes, respectively.

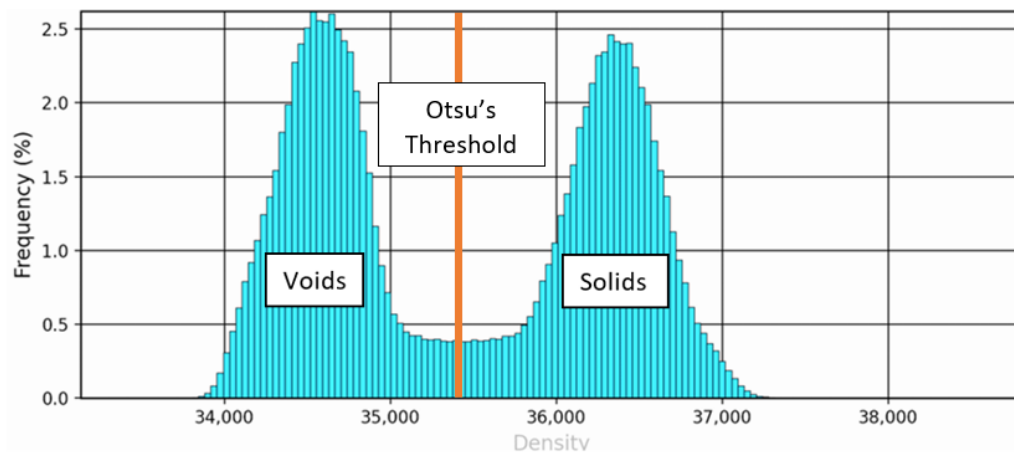


Figure 3-12. Example of histogram identifying the voids and solid classes of sample V1

Due to these distinct peaks, segmentation of the solid and porous phases may be accomplished via Otsu's method [140], with the lower and upper bounds corresponding to the porous and solid regions, respectively. Through further separation of the porous regions, the samples were fully segmented into three classes: solid, main pores and defective pores, as shown in Figure 3-13.

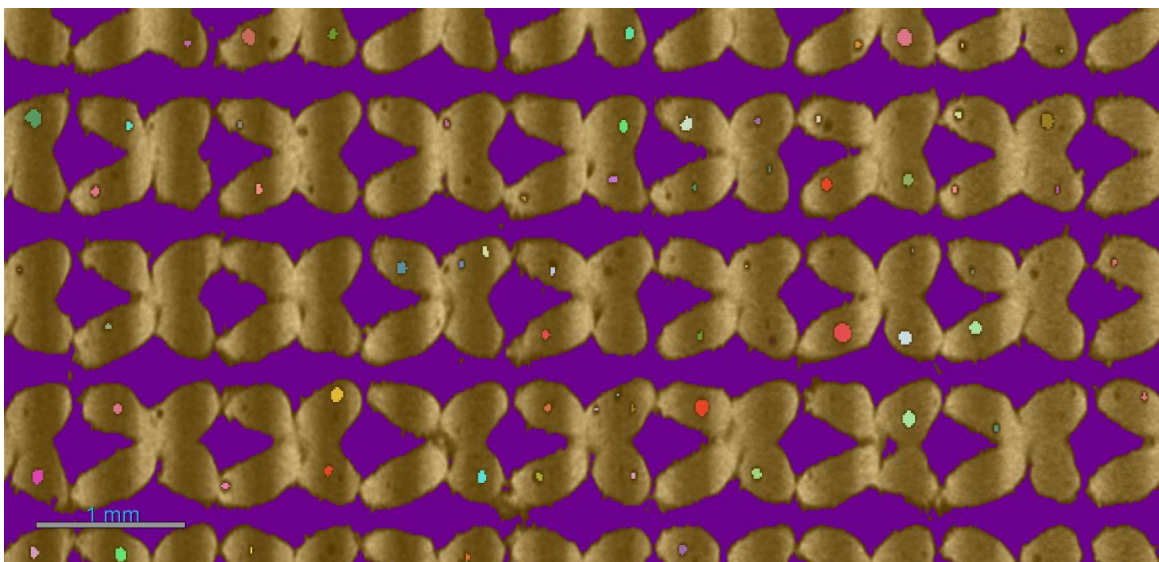


Figure 3-13. Example of fully segmented sample, identifying the Solid (orange), main pores (purple) and defective pores (multicoloured) for sample V1.



To disregard any detection errors within the scans, pore volumes of less than $10,000\mu\text{m}^3$ were removed from the analysis in accordance with similar work carried out by Hazeli et al. [141]. In this case, with a voxel resolution of $13.986\mu\text{m}$ in all three axes, all pores containing less than 4 voxel counts were disregarded. With the fully segmented samples, the volumes of each class may be recorded and both apparent and true porosities calculated in accordance with Equations (3-9) and (3-10).

$$\text{Apparent Porosity (\%)} = \frac{\text{Pore Volume}_{\text{main}} + \text{Pore Volume}_{\text{Defective}}}{\text{Volume}_{\text{Total}}} \times 100 \quad (3-9)$$

$$\text{True Porosity (\%)} = \frac{\text{Pore Volume}_{\text{main}}}{\text{Volume}_{\text{Total}}} \times 100 \quad (3-10)$$

Through following this methodology, the validity of the experimentally derived apparent, and true porosities were determined, as is further discussed in Section 5.4.



3.5 Experimental Campaign

Each AM wick design underwent a range of experiments to characterise the wick's capillary action and permeability, both of which are key performance indicators in the design of efficient and effective heat pipes. As mentioned, capillary pressure and permeability are two conflicting characteristics with capillary pressure increasing with a reduction in pore size whereas permeability tends to decrease.

3.5.1 Capillary Rate-of-Rise

As previously highlighted, the capillary limit is generally the limiting factor in a heat pipe operating at standard conditions, where the maximum capillary-limited heat load is typically determined through Equation (3-11) [142].

$$Q_{capillary\ limit} \approx 2 \left(\frac{\rho_l g h_{fg}}{\mu_l} \right) \left(\frac{A_w}{L_{eff}} \right) \left(\frac{K}{r_{eff}} \right) \quad (3-11)$$

Where $(\rho_l g h_{fg})/\mu_l$ is the merit number of the working fluid, A_w represents the cross-sectional area of the wick, L_{eff} is the effective length of the heat pipe, K the permeability and r_{eff} is the effective pore radius.

Therefore, characterising the K/r_{eff} parameter, also known as the capillary performance, is a key factor in the design of heat pipes and determination of the capillary limit. To increase the capillary pressure, a reduced pore size may be beneficial. Consequently, reduced permeability will also be experienced. Therefore, exploiting the capillary performance reflects the balance between these two opposing factors.

The capillary rate of rise experiment was conducted to determine this parameter in addition to the wick's maximum rise height working against gravity. Numerous techniques have been trialled throughout literature for detecting and measuring the liquid rise within capillary structures, including:

- Infrared (IR) thermography which can track the rise due to the difference in emissivity between the working fluid and wick material [95]. However, challenges and discrepancies can occur due to conductance at elevated temperatures and evaporative cooling through the material can alter the results and reduce reliability.



- High-speed videography to track the rate of rise [142, 143]. This is particularly effective in capturing and evaluating the early stages of the experiment where the rate of rise is seen to be much greater than the intermediate and latter periods. However, detecting a noticeable difference between the solid and liquid phases can be difficult.
- Ultraviolet (UV) fluorescent doping which has been used in conjunction with the high-speed recording method to enhance the contrast between the saturated and unsaturated regions [144]. This method requires the addition of a fluorescent dye mixed with the working fluid and using a UV light source of a specific activation wavelength. Typically, a filter is used in front of the camera to block UV wavelengths and allow all visual light through. The addition of fluorescent dye can influence fluid properties, including viscosity and surface tension, both of which can directly influence its wettability and hence the capillary performance of the wicking structure.

Mass-based measurements eliminate any discrepancies that are often seen when analysing the liquid front for typical height-based rate-of-rise experiments. However, further abnormalities may occur as additional mass is drawn forming a meniscus surrounding the edges of the sample, illustrated in Figure 3-14.

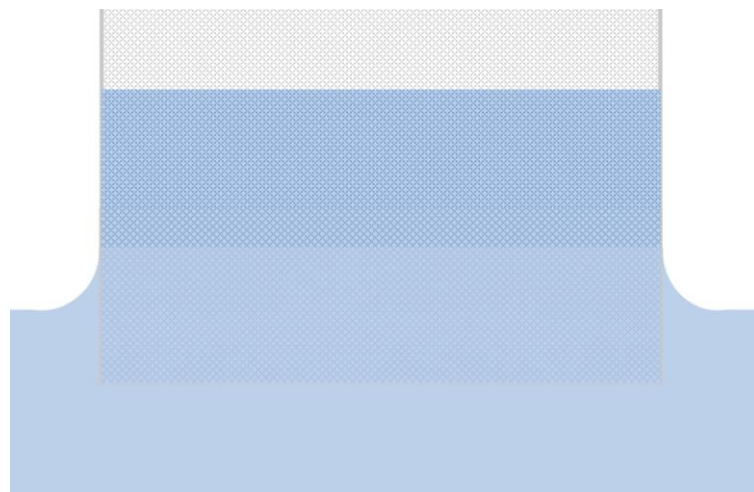


Figure 3-14. Formed meniscus surrounding sample during capillary rise experiment.

Further identified concerns include the capture rate and stabilisation time of the apparatus, as discussed further in Section 3.5.1.2.



3.5.1.1 Capillary Theory

For effective capillary rise, the overall system pressures must be in balance. As previously stated, the capillary pressure (P_c) is governed by Young-Laplace, again shown in Equation (3-12), where the pore radius (r_p) may be replaced by the effect capillary radius (r_{eff}), as shown in Equations (3-13) and (3-14).

$$\Delta P_c = \frac{2\sigma \cos\theta}{r_p} \quad (3-12)$$

$$r_{eff} = \frac{r_p}{\cos\theta} \quad (3-13)$$

$$\Delta P_c = \frac{2\sigma}{r_{eff}} \quad (3-14)$$

Additional system pressures include the hydrostatic pressure (P_h) and the internal frictional pressure losses (P_f) within the wicking structure, as shown in Equations (3-15) to (3-16).

$$\Delta P_h = \rho gh \quad (3-15)$$

$$\Delta P_f = \frac{\mu\varepsilon}{K} h \frac{dh}{dt} \quad (3-16)$$

For this study, with capillary pressure acting against gravity, the capillary pressure was opposed by the internal frictional losses within the wick and the hydrostatic pressure drop, as shown in Equations (3-17) and (3-18).

$$\Delta P_c = \Delta P_f + \Delta P_h \quad (3-17)$$

$$\frac{2\sigma}{r_{eff}} = \frac{\mu\varepsilon}{K} h \frac{dh}{dt} + \rho gh \quad (3-18)$$

Through rearranging Equation (3-18), the capillary performance may be determined via linear regression, as shown in Equations (3-19) and (3-20).

$$\frac{dh}{dt} = \frac{2\sigma}{\mu\varepsilon} \frac{K}{r_{eff}} \frac{1}{h} - \frac{\rho g K}{\mu\varepsilon} \quad (3-19)$$



$$y = \frac{2\sigma}{\mu\varepsilon} \frac{K}{r_{eff}} x - \frac{\rho g K}{\mu\varepsilon} \quad (3-20)$$

Where $y = dh/dt$ and $x=1/h$.

Through determination of the gradient, the capillary performance may be calculated in accordance with

$$\frac{K}{r_{eff}} = m \frac{\mu\varepsilon}{2\sigma} \quad (3-21)$$

Where m represents the slope of the curve.

Jurin's law [145, 146] which is often used to formulate the time-independent maximum equilibrium rise height of a liquid column, is determined as per Equation (3-22).

$$h_{max} = \frac{2\sigma \cos \theta}{\rho g r_{eff}} \quad (3-22)$$

Here, it is noticeable that the height of the rising column is inversely proportional to the effective radius. Jurin's law is based on the rise height within a capillary tube or between two parallel plates. As would be expected with all derived formulations, they become less applicable as the model deviates from the initial assumptions. In terms of comparison to the utilised additively manufactured lattice structures, Jurin's law does not consider any internal pressure drop within the wick and the complex interconnectivity of the pore structure is a significant deviation from the assumed geometry characteristics. A further assumption of Jurin's law is that the tube radius is much smaller than the capillary length, which is denoted by Equation (3-23).

$$L_c = \sqrt{\frac{\sigma}{\rho g}} \quad (3-23)$$

The capillary length is a characteristic length scale where the forces of gravity and surface tension are in equilibrium and calculated as 1.75mm and 2.72mm for both acetone and water at 20°C, respectively. This may be further expressed in consideration of the dimensionless quantity, Bond number (Bo), as expressed in Equation (3-24).



$$B_o = \frac{\rho g L^2}{\sigma} \quad (3-24)$$

The Bond number describes the ratio of gravitational forces to surface tension impacting the system and may be linked to the capillary length with Equation (3-25).

$$B_o = \left(\frac{L}{L_c}\right)^2 \quad (3-25)$$

Where L represents the characteristic length, which in the case of capillary rise is represented by the pore radius. This indicates that for pore radii significantly smaller than the capillary length (i.e. $B_o \ll 1$), surface tension dominates. Contrary to this, gravity has greater significance on the hydraulic characteristics if the pore radius is larger (i.e. $B_o \gg 1$). As discussed with relation to Jurin's Law, the applicability of Bond Number may deviate for complex lattice geometries from assumed capillary tube due to factors such as pore interconnectivity, surface roughness and contact angle. Nevertheless, consideration and evaluation of such formulations are invaluable to future AM-based wicking structures.



3.5.1.2 IR Capillary Setup

A thorough consideration of all methods, with initial trials for both UV and IR-based data collection, was undertaken. With the available equipment, it was clear that the detection of the liquid front was much more distinguishable through the IR setup, which is schematically depicted in Figure 3-15.

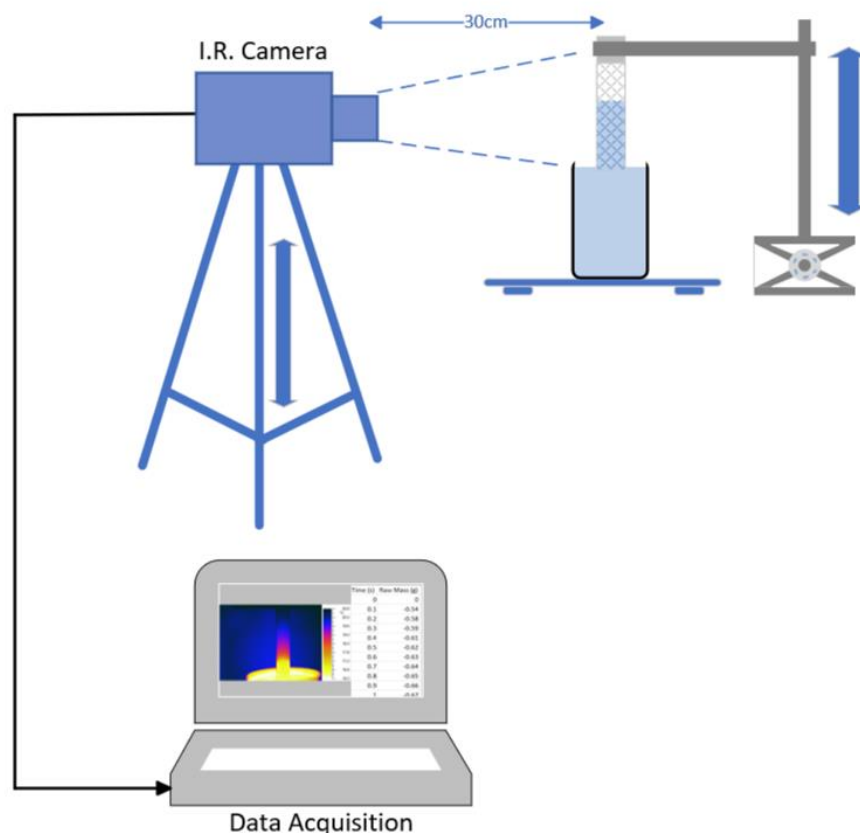


Figure 3-15. Capillary Rate-of-Rise experimental setup

The NEC Avio H2630 IR camera [147] used had a temperature detection range set at -40 to 120°C with a stated temperature resolution of 0.08°C and accuracy of $\pm 2^{\circ}\text{C}$ or $\pm 2\%$, whichever is greater. The thermal camera was calibrated by adjusting the emissivity to eliminate the deviation between the known ambient temperature of a black surface and the recorded temperature. However, having an exact temperature reading of the liquid within the wick was not of vital importance and priority in hardware set up was given to enhancing the contrast between the solid and liquid phases. Trials were originally conducted in conjunction with a Sartorius Entris II mass balance to capture the rate of rise on a mass basis [148]. However, results were shown to be inaccurate and not aligning with expectations. This was due to the relatively high measurement and stabilisation time of the available apparatus, making it



unsuitable for transient applications. Live IR data was recorded with the use of the Thermography Studio package [149]. The IR data was captured at a framerate of 10 fps and exported as JPEG images of dimensions 824 x 480 pixels and a pixel resolution of 0.17mm. The samples were held on a specifically designed PLA holder, shown in Figure 12-1 in Appendix 12.3 and 3D printed via FDM and connected to a stand clamp. The laboratory stand was connected to a laboratory jack to allow for precise and smooth lowering and raising of the samples into the liquid. Data was captured for a total of 60s, or until the liquid reached a stable maxima.

3.5.1.3 Minimum Liquid Entry Pressure

Initial trials with deionised water proved unsuccessful at delivering the desired capillarity for liquid penetration into the wick, as shown in Figure 3-16.

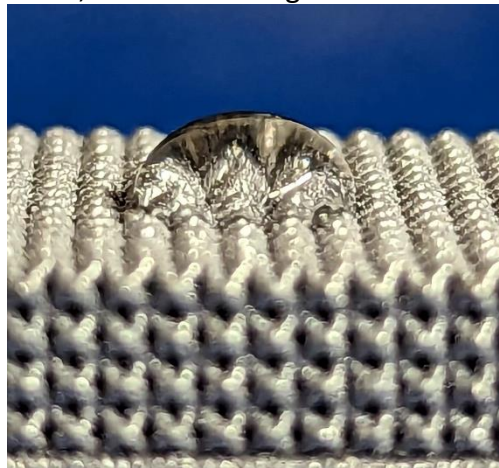


Figure 3-16. Initial trial showing the high contact angle and hydrophobicity of water on the manufactured porous surface.

Due to the hydrophobicity of the structure, liquid is unable to effectively wet the surface. This can be related to the effects of the Wenzel and Cassie-Baxter states, as described in Section 2.4. The concept of minimum Liquid Entry Pressure (LEP) is often used for applications including hydrophobic membranes, soil science, petroleum and hydrology. LEP is based off the Young-Laplace Equation and states the minimum hydrostatic pressure required by the working fluid to penetrate and wet the structure, as shown in Equation (3-26) [150, 151].

$$LEP = \frac{-2B\sigma_L \cos \theta}{r_{max}} \quad (3-26)$$

Here, r_{max} is the maximum pore radius of the wicking structure and B represents a dimensionless geometric factor to account for any irregularities. For perfectly cylindrical



pores, B is equal to 1 and for all other pore geometries lies between 0 and 1. However, this can be difficult to quantify and is often used as an adaptable parameter [151]. As stated by Rezaei et al. [57], with a non-wetting liquid a convex meniscus is formed which impedes the liquid's ability to penetrate the porous structure, closely reflecting that of the *Salvinia Molesta* plant in Figure 2-12. Once the LEP is overcome and penetrating commences, the structure loses its hydrophobicity characteristics, leading to continuous water bridging, as shown in Figure 3-17.

Evidently, Figure 3-17 shows that once sufficient pressure is supplied and wetting commences, the liquid is able to efficiently penetrate the sample passively through capillary action. The points of contact between the liquid-solid interface can be clearly seen in Figure 3-17 (a) where the nodes of the cells are magnified within the water droplet, which, with water's high surface tension, was found to result in an effective pore size significantly larger than that actually measured. This increase resulted in lower capillary pressure to overcome the surface tension of the liquid. The suspension of the liquid on the lattice surface, resulting in air entrapment beneath, closely aligns with the Cassie-Baxter model, albeit at a distinct geometric scale compared to conventional surface roughness features, highlighted in Section 2.4.2. In addition to increasing the effective pore size, the suspension of the liquid on these asperities reduces the available contact area thus reducing the effect of the surface energy which aids in enhancing the wettability of the structure.

Due to the reasons set out, along with the associated long term compatibility of water-aluminium heat pipes, as discussed in Section 2.3, the capillary rise experiment is conducted with acetone as the working fluid. This phenomenon is further discussed in Chapter 6.



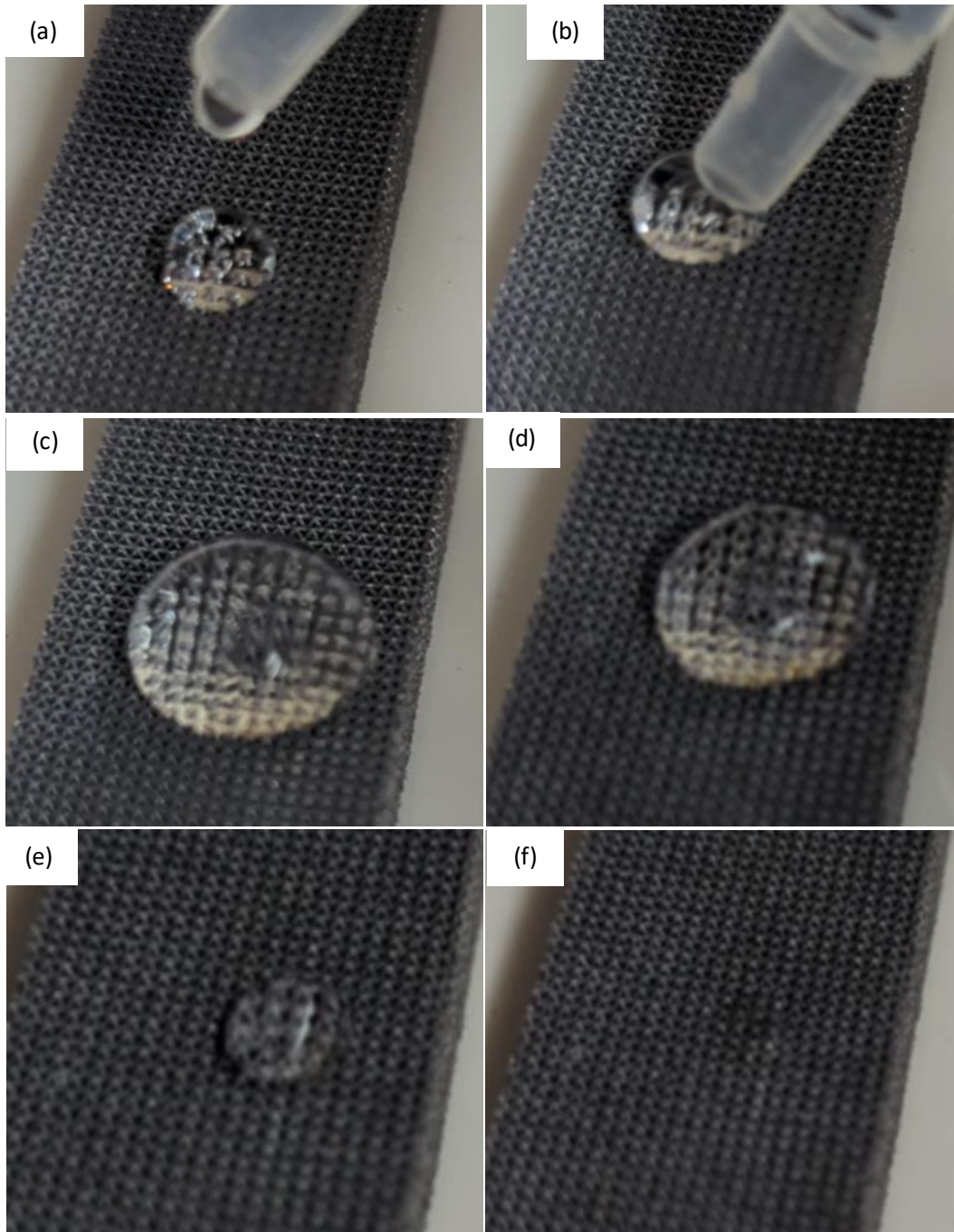


Figure 3-17. Effects over overcoming the LEP with DI water. (a) drop with no forced pressure, (b) applying forced pressure with syringe, (c) $t: 0s$, (d) $t: 0.45s$, (e) $t: 1.50s$ and (f) $t: 1.80s$



3.5.1.4 IR Data Post-Processing and Analysis

To analyse the exported image stack, an interactive Matlab code, shown in Appendix 12.5, was developed allowing for data import, crop and adjust image filtering parameters to maximise contrast surrounding the liquid-dry boundary. Throughout literature, the majority of studies only evaluated a small number of samples while taking manual measurements of a select frame count. For this study, an automated process proved to be a necessity as a total of 24 samples, each with 3 repeated measurements, required analysing. The developed code and analysis of images recorded the instantaneous liquid height of each frame, maximum liquid height, velocity, and acceleration, with results tabulated and plotted. The code is based on converting the cropped image into grayscale and binarising based on a set thresholding value, segmenting the boundaries of the dry and saturated regions, as shown in Figure 3-18. Following this, the *regionprops* function within Matlab was used to detect the white / liquid regions and returning the dimensions of the largest saturated region's bounding box.

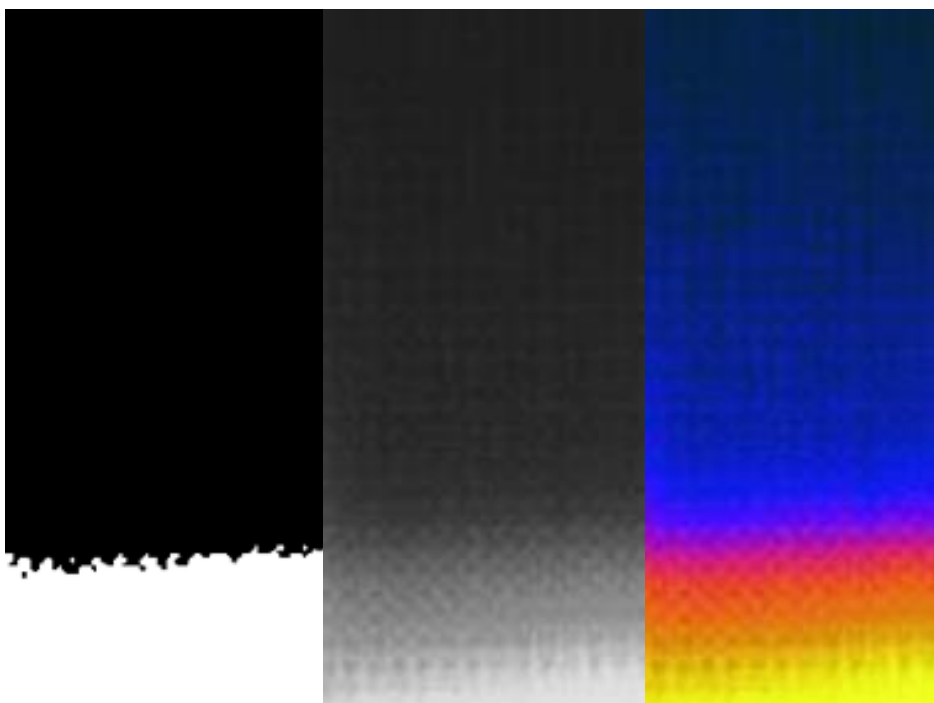


Figure 3-18. Example of code segmentation with raw IR image (Right), greyscale image (centre) and binarised image (Left)

As can be seen from Figure 3-18, the segmentation of the grayscale image aligns well with the visible boundary in the raw IR image. This methodology was placed within a loop to individually and automatically analyse each frame. For the full 60s analysis period, a total of 600 images were captured at a framerate of 10 fps and analysed. To confirm the robustness



and efficacy of the designed image analysis code, several test points were manually analysed with ImageJ [152], shown in Figure 3-19.

As can be seen from Figure 3-19, good agreement is seen between the developed Matlab code and the manual measurements, adding to the value of the developed methodology. Further evaluation of the developed code's effectiveness is shown in Figure 3-20.

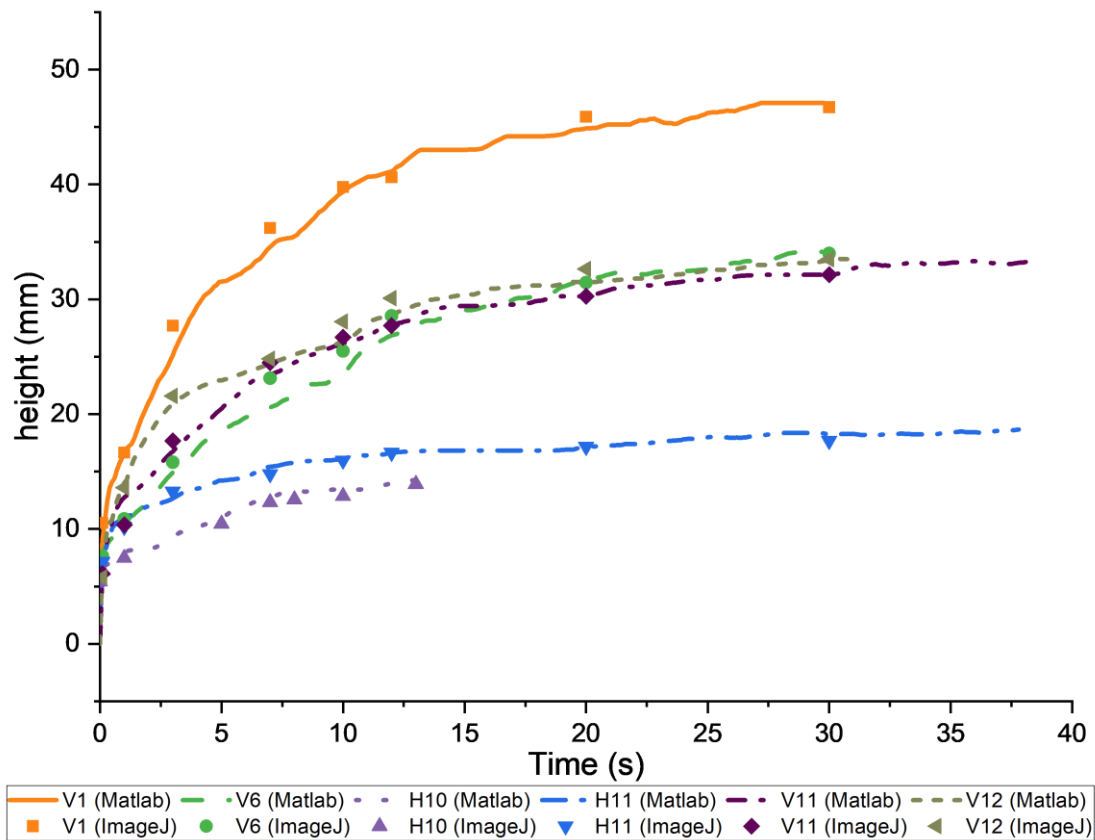


Figure 3-19. Comparison between rise height of developed automatic Matlab code and manual ImageJ measurements.

Clearly, a strong and consistent relationship is presented between the manual and automatic measurements in Figure 3-20, indicating an R^2 value of 0.998 and a Pearson's r value of 0.999. As both values are close to unity, the efficacy of the developed Matlab script is confirmed through indicating high linearity and similarity between the methodologies.



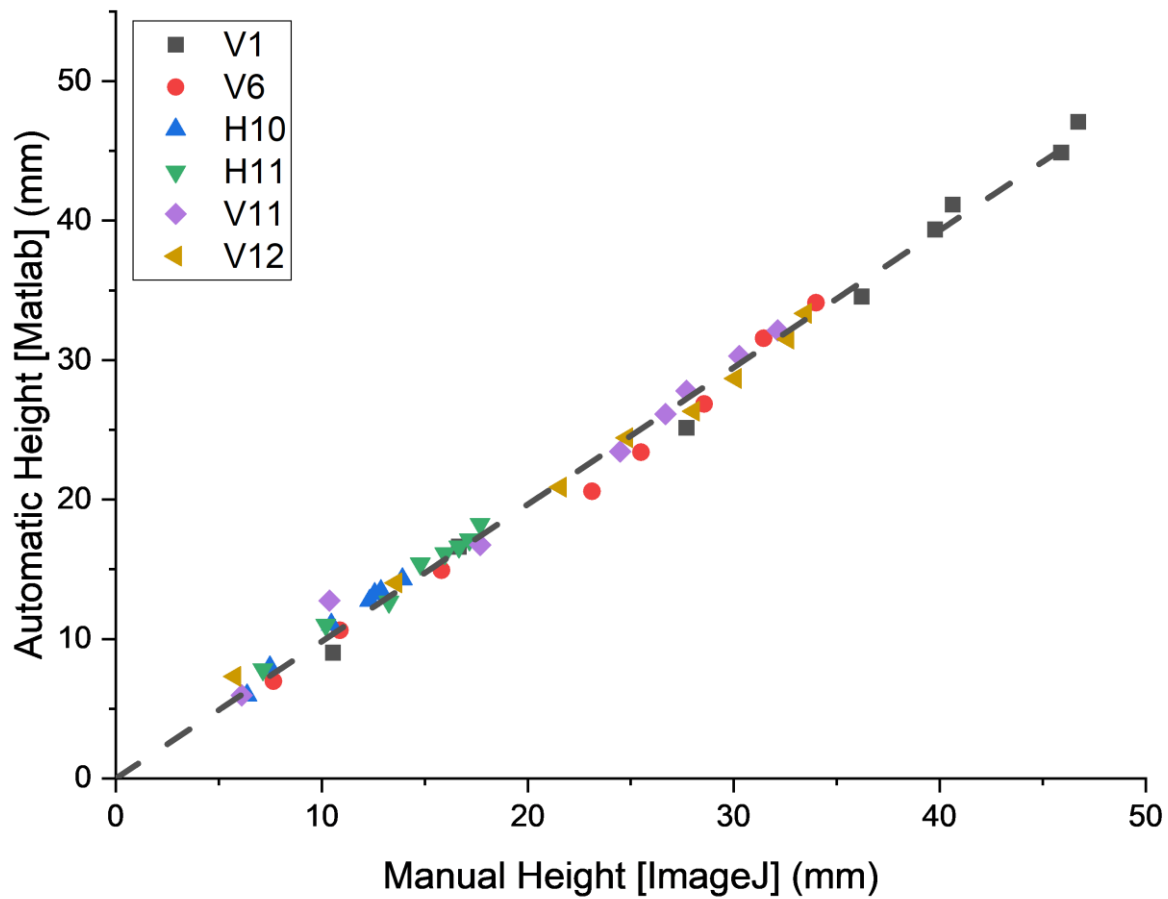


Figure 3-20. Comparison between manual and automatic rise heights of several samples with line of best fit.



3.5.2 Permeability

As a standard experimental method [43, 95], the forced fluid flow test was performed to measure the pressure drop across the wick's length.

3.5.2.1 Permeability Theory

The measured pressure drop, along with recorded flow rate and wick and fluid properties was used to calculate the wick permeability, in accordance with Darcy's Law, shown in Equation (3-27) [95, 153].

$$\frac{\Delta P}{L} = \frac{\mu}{K} v \quad (3-27)$$

Where ΔP , L , μ , K and v are the measured pressure drop, effective length, dynamic viscosity, permeability and superficial fluid velocity calculated by Equation (3-28).

$$v = \frac{\dot{m}}{\rho A} \quad (3-28)$$

Where \dot{m} , ρ and A are the measured mass flow rate, fluid density and wick cross sectional area [95]. For Darcy's law to hold true, inertial effects may be negated, on the assumption that the flow velocities are adequately small.

As meticulously described by Jafari et al. [95], should flow velocities be sufficiently high, to the point where drag becomes relevant, the Forchheimer correction, shown in Equation (3-29), may be used for evaluation of permeability and pressure drop.

$$\frac{\Delta P}{L} = \underbrace{\frac{1}{K_1} \mu v}_{\text{Darcy Term}} + \underbrace{\frac{1}{K_2} \rho v^2}_{\text{Forchheimer Term}} \quad (3-29)$$

Where the first term of the RHS is referred to as the Darcy term containing the Darcyan permeability coefficient, K_1 , and the second term relates to the Forchheimer term containing the non-Darcyan permeability coefficient, K_2 . Similar to that used through the capillary rate-of-rise experiment, linear regression may be used to determine both K_1 and K_2 terms, as shown in Equation (3-30).



$$\frac{\Delta P}{Lv} = \alpha + \beta v \quad (3-30)$$

Where α (Intercept) and β (Gradient) equate to Equations (3-31) and (3-32), respectively.

$$\alpha = \frac{\mu}{K_1} \quad (3-31)$$

$$\beta = \frac{\rho}{K_2} \quad (3-32)$$

The transition from Darcyan flow, is dependent on the internal flow regime, as determined by the permeability-based Reynolds number Re_K [154], as per Equation (3-34).

$$Re_K = \frac{\rho \sqrt{K} v}{\mu} \quad (3-33)$$

At low flow rates, typically where $Re_K < 1$, the flow is in the Darcyan regime where flow is governed by viscous forces showing a linear relationship between pressure drop and flow velocities. As Re_K starts to increase, typically around 1 – 10, inertial forces become more influential and deviations from the linear darcy relationship start to develop [95]. At Re_K values above 10, the flow is considered to be non-Darcyan and fully developed, where quadratic relationship occurs dominated by inertial forces, as shown by Forchheimer in Equation (3-29). However, all actual transition points may deviate from these factors slightly and is dependent on the permeability, wick porosity and tortuosity in addition to fluid properties.



3.5.2.2 Permeability Rig Setup

Deionised water (DI) was used to perform the forced fluid flow test, as can be seen widely throughout literature. Safety concerns at elevated pressure were identified as the main reason for choosing this over the use of acetone, as used in the capillary experiment. A pressurised Millipore vessel, maintained at an inlet air pressure of 5 bar, was used alongside a low flow mass flow controller to provide the desired mass flow rates. The Bronkhurst M14 Coriolis mass flow controller could deliver up to 8.33g/s of water with an accuracy of $\pm 0.20\%$ and repeatability of $\pm 0.05\%$ [155]. The fluid delivery line additionally consisted of an isolation valve, 15 μm filter, thermocouple, and a static pressure transducer, while the downstream line consisted of an additional static pressure transducer and a ball valve to provide additional back pressure onto the system, as shown in Figure 3-21.

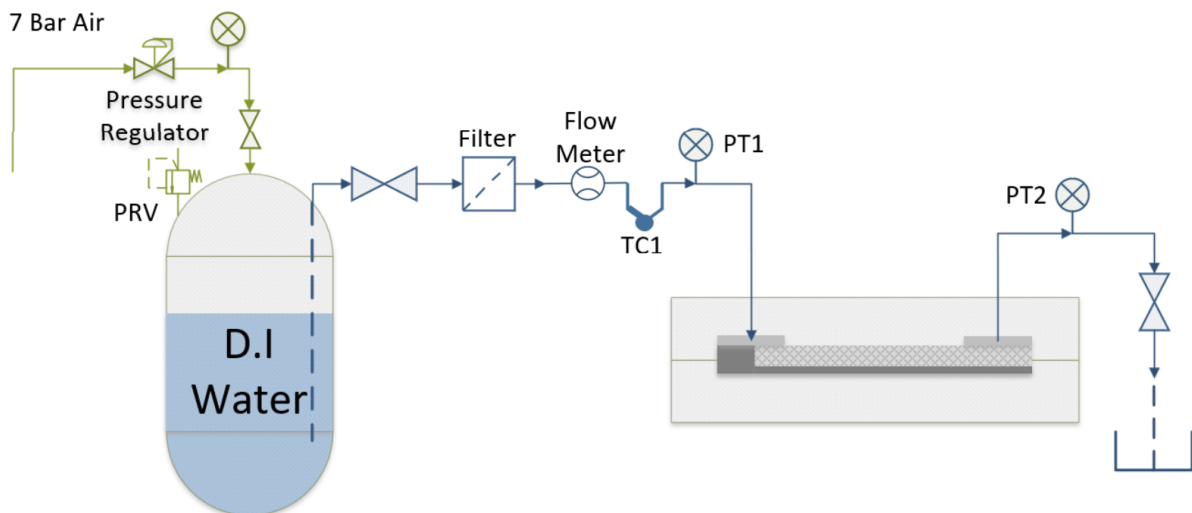


Figure 3-21. Designed setup for permeability test.

The 4-20mA Druck pressure transducers had a static pressure range of 0 – 10bar and a full scale best straight line accuracy of $\pm 0.2\%$ taking into account the combined effects on non-linearity, hysteresis and repeatability [156]. The back pressure valve was deemed a necessity for the experimental setup to maintain a high enough pressure to drive fluid into the pressure transducers and allow for efficient bleeding of the system. For the experimental campaign, this back pressure was maintained within a range of $\sim 100\text{-}300\text{mbar}$. As water is considered an incompressible fluid, maintaining the small amount of back pressure on the system was shown to have negligible impact on the overall pressure drop across the sample, as shown in Figure 3-22.



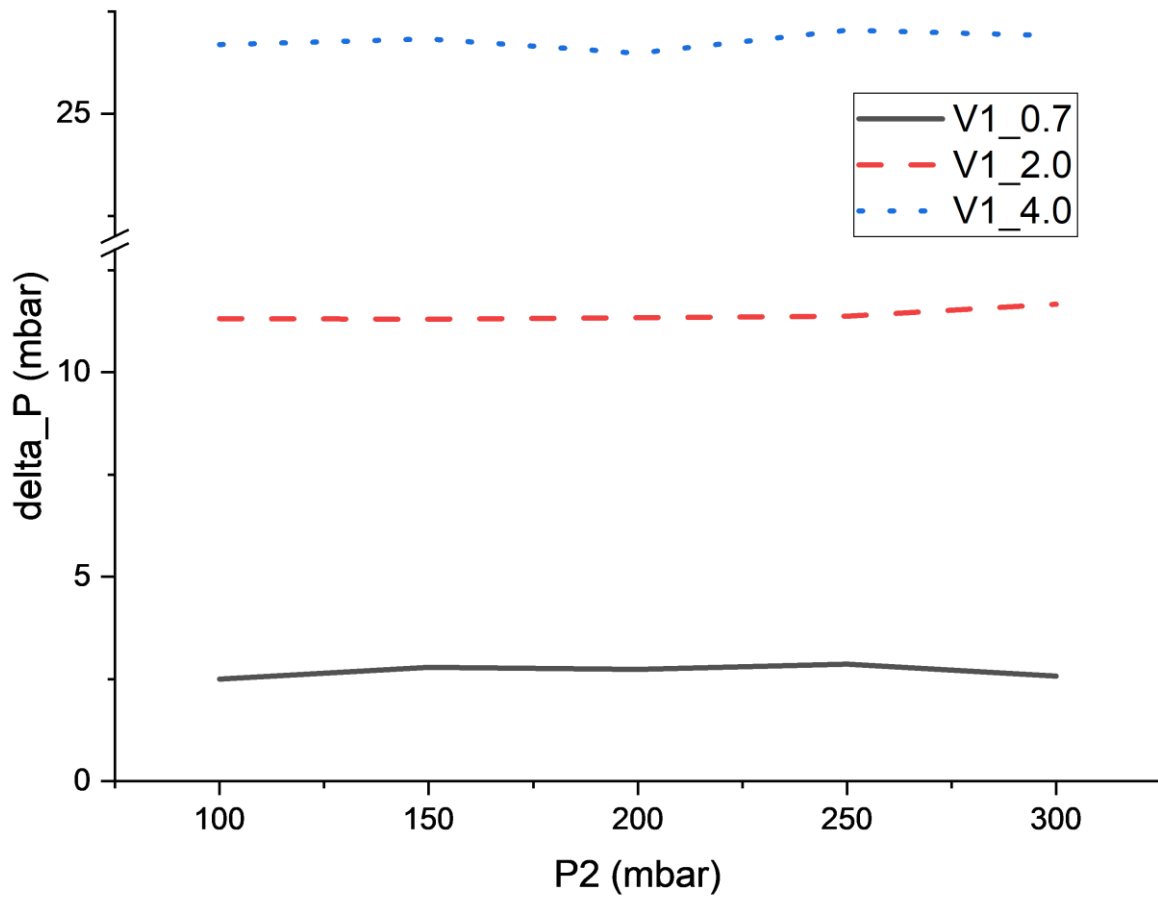


Figure 3-22. Impact of back pressure on measured differential pressure across a range of flow rates.

Over a large pressure range, viscosity is shown to be impacted by increasing pressure, as shown in Figure 3-23. However, as can be seen in the enlarged region of interest of Figure 3-23, at the lower pressure range viscosity is shown to be stable through all temperatures. As a result, it is possible to conclude that the viscous effects associated with a small increase in back pressure is negligible.



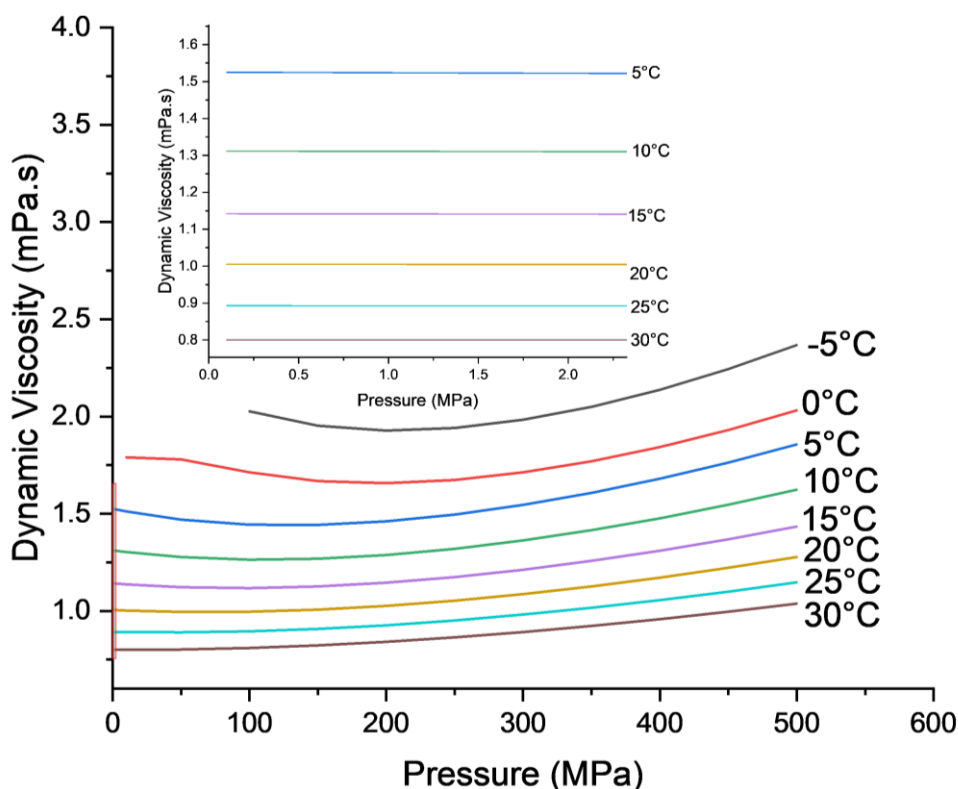


Figure 3-23. The effects of both temperature and pressure on the resultant dynamic viscosity with an enlarged view, data collected with CoolProp [51].

3.5.2.3 Sample Sealing

Ensuring adequate sealing around the sample was essential to direct flow through the desired porous flow space. Numerous methods have been used throughout literature including RTV silicone [43, 157], O-rings [95] and rubber gasket seals. Although no issues were reported with these methods in literature, concerns were raised as to the effectiveness of these methods, especially for sealing the side faces at higher flow rates.

For this reason, it was decided to cast a rubber seal, covering the side, end, and bottom faces, as one component. Doing this and including a tolerance allowing for rubber compression, eliminates the allowable bypassing pathways for the liquid. The rubber of choice was the Polytek PT Flex 60 Liquid Rubber [158]. This was chosen for its intermediate shore hardness of A60, and small shrinkage rate of 0.0025mm/mm. Both the test rig and casting moulds were manufactured out of solid aluminium with tapered location cones positioned in each corner. The upper half of the casting mould included 4 risers with a tapered



angle of 5°, as seen in Figure 3-24. The casting rubber came in two parts, requiring a 50:50 mass-based mix of both parts. The contact faces of the moulding were sprayed with a release

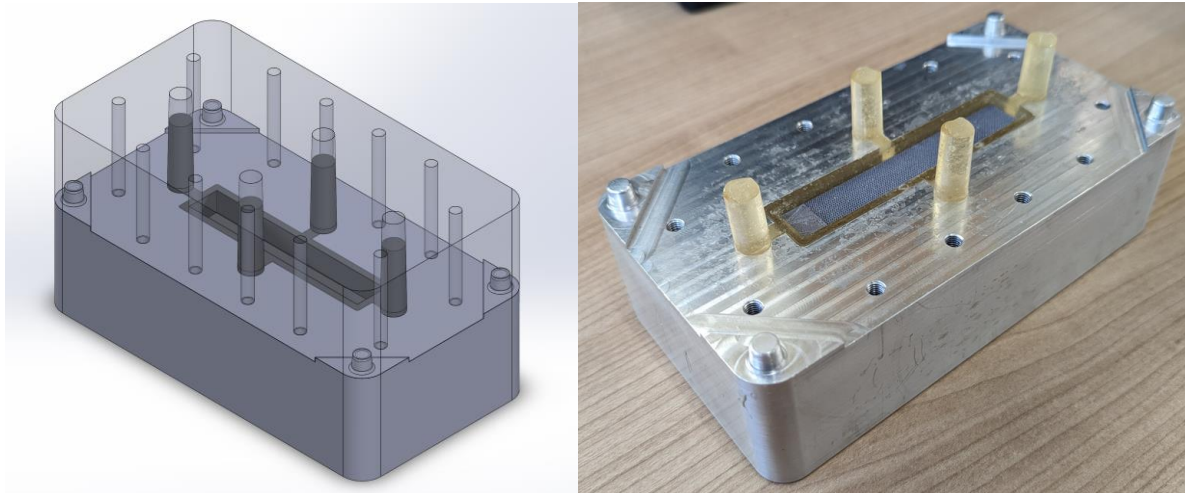


Figure 3-24. Image of designed casting mould assembly (Left) and manufactured seal with sample (Right).

agent to aid demoulding and reduce the chances of damage to the components.

Due to the tight tolerances and designed compression, the risers were also incorporated to supply additional hold for sample removal between each test point. To seal the top face of the wick and the interface between both halves, rubber gaskets were waterjet cut with a sheet of polycarbonate placed above and below the sheets to provide additional support during manufacturing.



3.5.2.4 Permeability Data Acquisition

The thermocouple and pressure transducer data was recorded with a central National Instruments data acquisition system. A graphical user interface control monitor was set up within FlexLogger [159], as shown in Figure 3-25.

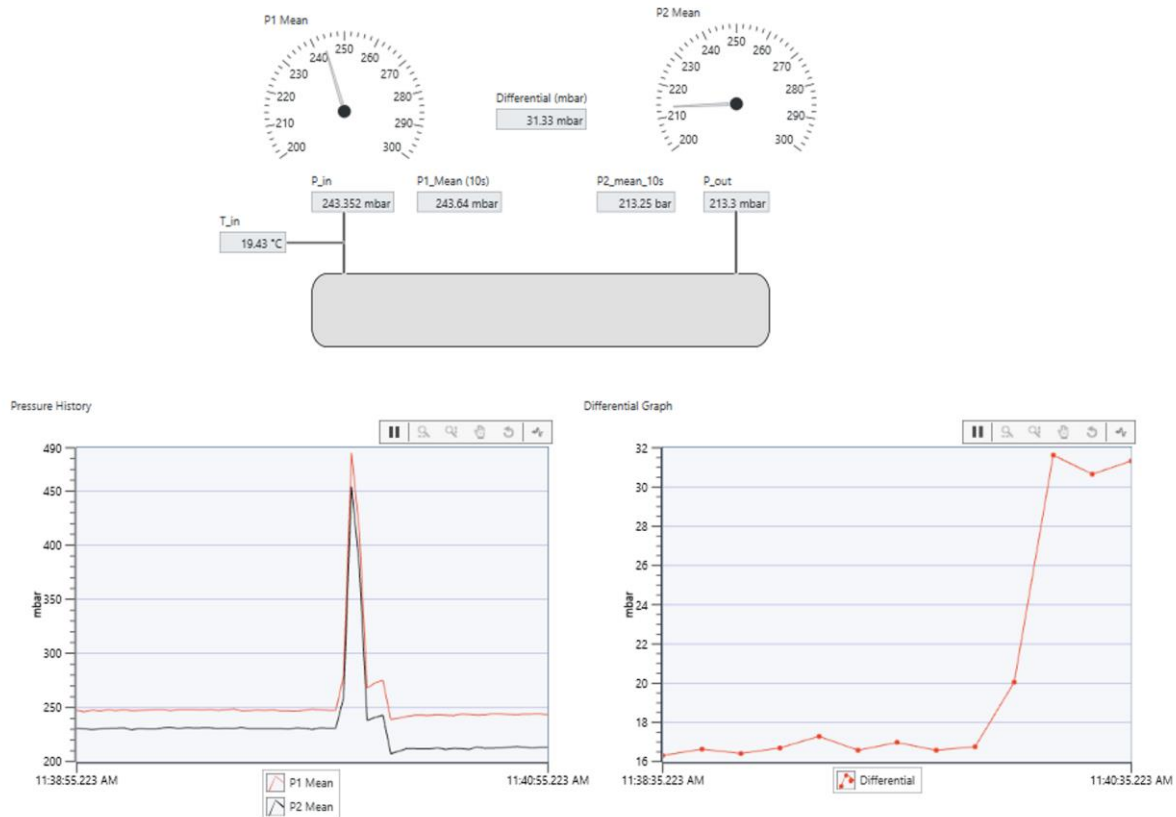


Figure 3-25. Developed FlexLogger graphical user interface.

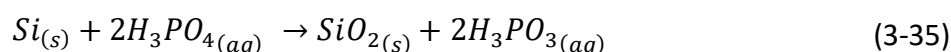
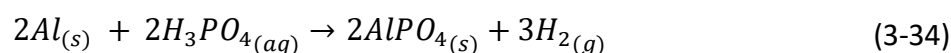
Here live pressures, temperature and flow rate data can be visualised in addition to the pressure differential, required for permeability calculation. Prior to recording, each sample was purged with DI water at 4.00g/s for 120s, ensuring no air was trapped within the samples. Following this, data was captured for a total of 60s with each test point exported into separate files in the native National Instruments file format (.TDMS). The recorded pressure differential was captured at mass flow rates of 0.50, 0.70, 1.00, 1.50, 2.00, 3.00 and 4.00g/s for each sample allowing for effective identification of transition from Darcyan to non-Darcyan flow regime. As a total of over 400 test points were recorded, a Matlab code was developed to efficiently analyse each test point. The developed code determines various parameters including, the minimum, maximum and average pressure for each transducer in addition to the differential and combined standard error of the mean. This is further discussed in Section 6.2.



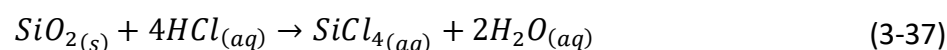
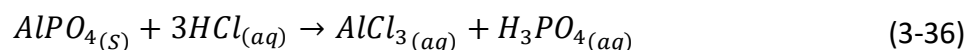
3.5.3 Chemical Polishing

As discussed in Chapter 2, surface roughness can have a significant impact on hydraulic performance within additively manufactured heat exchangers and the lattice-based geometries investigated in this research. To further evaluate this, samples were chemically polished as an additional post-processing action. Chemical polishing was chosen over other surface treatments due to its ability to penetrate and dissolve the internal irregularities of the structures. As discussed in Section 2.8, it was concluded that techniques such as laser milling and grit blasting would only impact the visible outer surface geometries and electropolishing could have an inconsistent result throughout the depth of the structure.

Based on the findings of the conducted literature review, materials utilised and resultant roughness improvement it was decided to base the methodology on that of Sharma et al. [108, 109]. Due to the presence of Si and Mg in the alloy, an appropriate choice of chemicals was needed for the solution. The solution of choice consisted of 80% phosphoric acid, 10% hydrochloric acid and 10% water in addition to 40 grams of Potassium Nitrate. The etching would occur in a two-step process, the first being with the phosphoric acid, shown in Equations (3-34) and (3-35).



Here, it is clear that phosphoric acid alone would be insufficient to effectively remove the material from the surface due to the formation of solid aluminium phosphate and silicone dioxide (silica). For this reason, hydrochloric acid was chosen to be incorporated into the solution with the main reactions shown in Equations (3-36) and (3-37).



This reaction facilitates the transformation of the solid aluminium phosphate and silicone dioxide into aqueous aluminium chloride and silicon tetrachloride. Due to the hydrophobicity of the samples, an additional 0.1g of Sodium Dodecyl Sulphate was used as a surfactant to



reduce the overall surface tension of the liquid and enable effective etching of internal structures. The etching solution was maintained at a temperature of $85^{\circ}\text{C} \pm 3^{\circ}\text{C}$, with an incorporated magnetic stirrer to agitate the flow. The samples were suspended in the chemical bath with a specially designed PTFE holder, shown in Figure 3-26, held at 25mm above the base of the beaker to allow space for the PTFE coated magnetic follower. No metal fittings were used for the wet components of the jig, and all threads and connections were manufactured directly into the PTFE components, chosen for its excellent chemical compatibility [160].

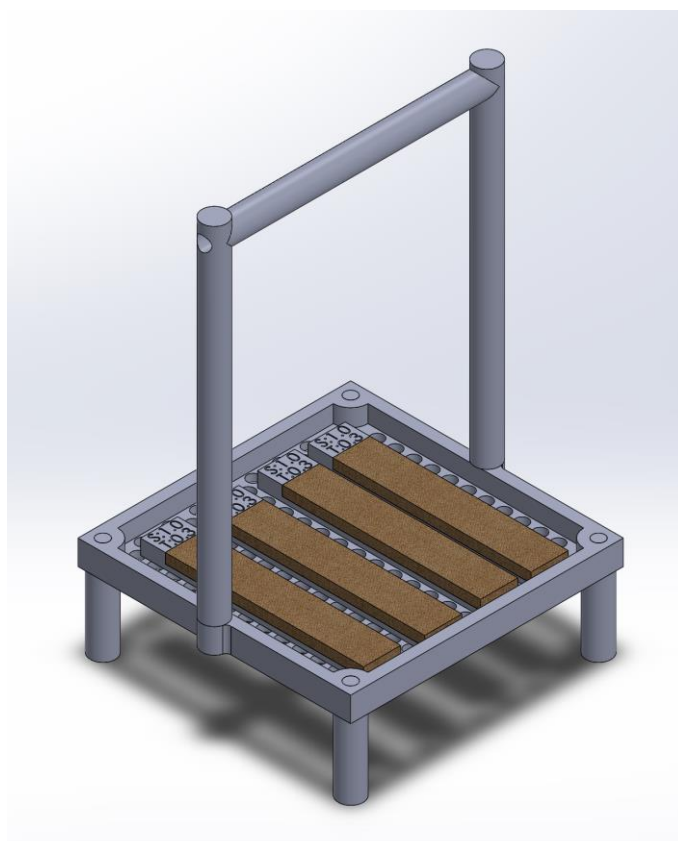


Figure 3-26. Sample holder for chemical polishing.

3.5.3.1 Initial Trials

Based on literature results, Sharma et al. [108, 109] determined that the greatest effect on surface roughness occurred during the first 5 minute period, with significant dimensional losses after 10 minutes of etching. For this reason, initial trials were conducted for 3 minutes with the specified etching solution. Although results proved successful in terms of removal of agglomerated particles and enhanced hydrophilicity, following on from Energy Dispersive X-ray (EDX) analysis, it became clear that an oxygen and phosphorus-rich layer was present



across the surface of the samples. This layer is likely to be aluminium phosphate – the insoluble reaction product between aluminium and phosphoric acid. Although this was taken into account in Sharma et al.'s methodology with the inclusion of hydrochloric acid [108, 109], the concentrations utilised were shown to be ineffective for this current study.

Ideally, further parameter studies would be conducted identifying the most effective concentration of hydrochloric acid. However, for the purpose of this research, an additional etching stage of 10% concentration hydrochloric acid was conducted and is discussed further in Section 7.1.

Following on from the etching process, sample rinsing and soaking using DI water was carried out until no visible reaction gasses were present, ensuring minimal reaction rates as a result of any residual acids. This was followed by ultrasonic cleaning with both DI water and isopropyl alcohol (IPA) for 10 minutes each. Using IPA as the final cleaning technique ensured enhanced sample infiltration due to its lower surface tension in addition to its evaporative characteristics resulting in improved sample drying.



4. Lattice Analysis Tool (LAT)

As mentioned above, the post-analysis of 2D microscopy for heat pipe wick analysis can prove to be inefficient and time consuming. Porosity and average pore diameter are two essential parameters in the design of an effective wick structure. Therefore, improving the workflow efficiency and effectiveness of techniques employed for the sector is vital for future progression.

Presented within this section is the development of a Lattice Analysis Tool (LAT) which has been tailored for additively manufactured heat pipe wick structures and published at the *Joint 21st International Heat Pipe Conference and 15th International Heat Pipe Symposium* in Sydney, Australia [161]. Although falling outside of the scope of this specific research, further case studies of the potential applications of LAT is shown in Appendix 12.4. These include the analysis of a Ti-6Al-4V AM lattice coupon, AM heat exchanger channels, the deterioration of a screen meshed wick nanofluidic heat pipe and defect characterisation of an AM counterflow burner cooling nozzle.

It was essential that such a tool could quickly and efficiently determine scaled measurements of the planar porosity, diameter, area, perimeter and centroid of each porous region to offer possibilities for further geometry analysis. LAT was specifically developed for this study to overcome the challenges surrounding heat pipe lattice-based wicking structures. It was released as an open-source software licensed under the GNU General Public License, version 3 [162] (available for download at <https://github.com/llywelynughes/LAT>) and was designed through Matlab's App Designer feature [163]. LAT consists of over 2500 lines of code capable of presenting tabulated results which can be shown in heatmaps and histograms for visual representation. With its simple user interface, shown in Figure 4-1, key lattice geometric parameters are quickly and methodically determined, as per Figure 4-2.

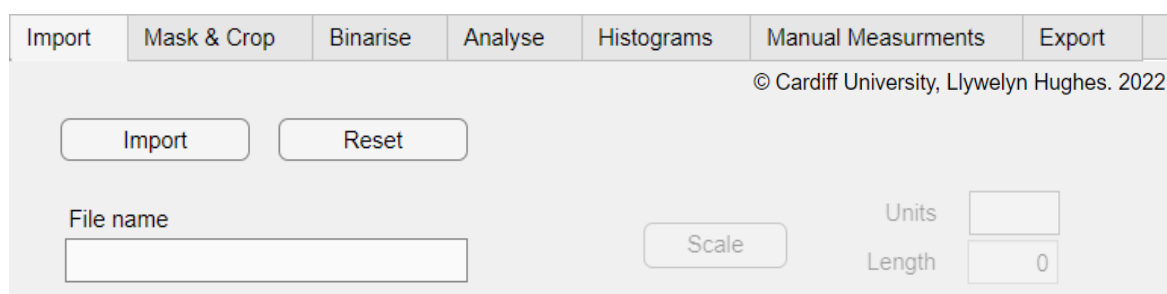


Figure 4-1. LAT User Interface



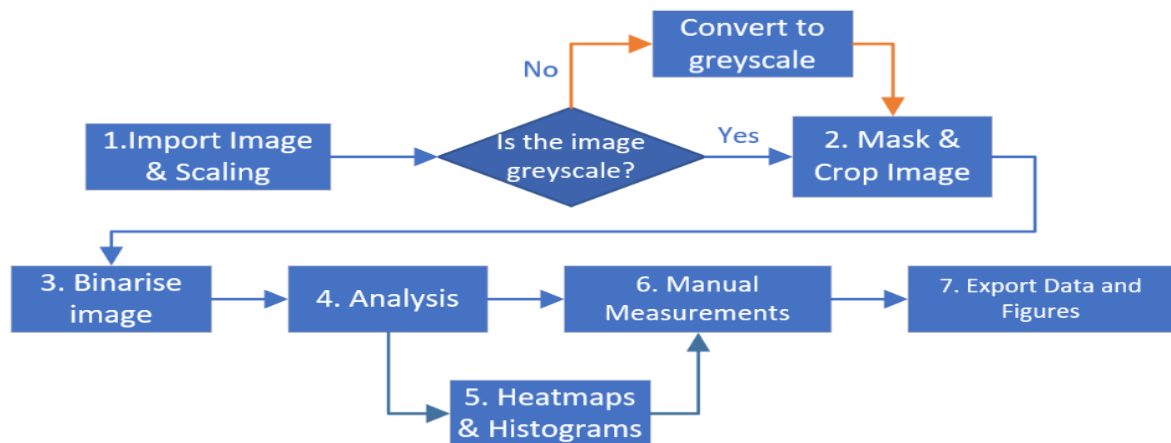


Figure 4-2. LAT Workflow

4.1 File Import & Scaling

LAT supports a range of image file formats including BMP, TIFF, PNG and JPEG making it ideally suited for analysing the lattice-based geometries used throughout this research. The image may be analysed with generic pixel count or scaled to appropriate units of choice with a scaling bar or known measurement, as shown in Figure 4-3.

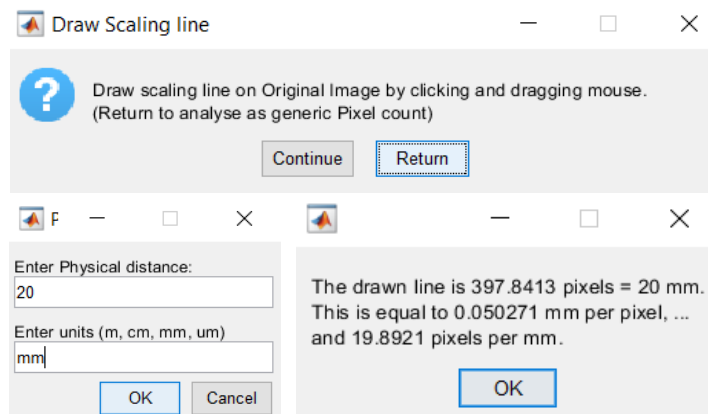


Figure 4-3. Scaling user interface example. Initial instruction window (Top), user input (Bottom-Left) and scaled results (Bottom-Right).

Scaling is achieved by measuring the pixel length of a drawn line using Pythagoras' theorem with the start and end points of the line comprising the x and y coordinates, as shown in Equation (4-1).

$$pix_dist = \sqrt{(x_2 - x_1)^2 + (y_2 - y_1)^2} \quad (4-1)$$

With the physical distance and known units, LAT calculates the length of each pixel and pixels per unit length. This conversion factor is then used throughout the application for



effective scaling of measurements. For the purpose of this research, all acquired images were in JPEG file format with a pixel resolution of 2400dpi (10.58 μ m).

4.2 Mask & Crop

Once scaled, the image may be cropped with a circle, rectangle, polygon or freehand mask, as shown in Figure 4-4. Any region which falls outside of the masked area are set to a pixel intensity value of 255 (white) and are discounted from further analysis. Through incorporating a range of masking options, the tool accounts for both simple and complex geometries. It also means imperfections in the image or component can be avoided and only specific regions of interest considered. The rectangular cropping feature was used for this study, allowing for exclusion of the bulk material from further analysis.

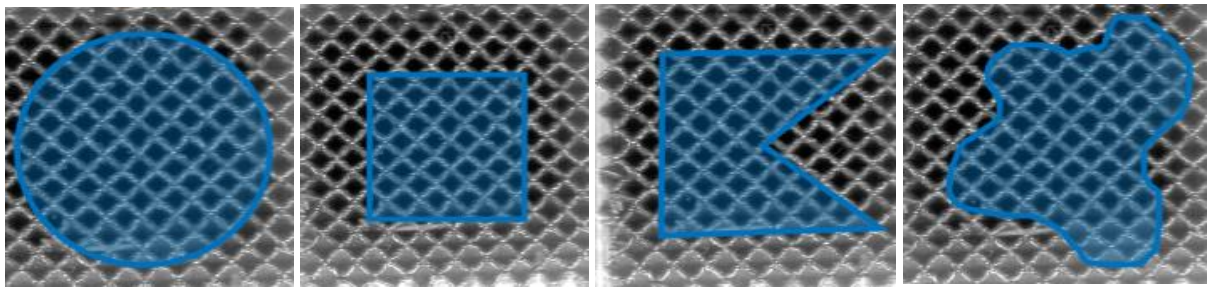


Figure 4-4. 2D scanned images of lattice coupons identifying masking options. From left to right: Circle, rectangle, polygon and freehand.

4.3 Binarise

Automatic image processing techniques have been built into the tool including the wiener2 function which is a 2D adaptive noise-removal filter that preserves image detail [164]. This function is used to estimate the local mean (μ) and variance (σ) surrounding each pixel of a specific neighbourhood size (M, N), as shown in Equations (4-2) and (4-3), respectively.

$$\mu = \frac{1}{N \cdot M} \sum_{n_1, n_2 \in \eta} a(n_1, n_2) \quad (4-2)$$

$$\sigma^2 = \frac{1}{N \cdot M} \sum_{n_1, n_2 \in \eta} a^2(n_1, n_2) - \mu^2 \quad (4-3)$$

Following this, the algorithm then creates a pixel-wise Wiener filter using these local statistics, as shown in (4-4).



$$b(n_1, n_2) = \mu + \frac{\sigma^2 - v^2}{\sigma^2} \cdot (a(n_1, n_2) - \mu) \quad (4-4)$$

Where v^2 is the noise variance. The adaptive wiener2 filter preferentially smooths areas of low variance, preserving edges and details better than a standard linear filter.

However, to alleviate any further noise or slight imperfections within the image, a 2D Gaussian smoothing kernel filter with a standard deviation of 2 is overlaid, as shown in Figure 4-5.

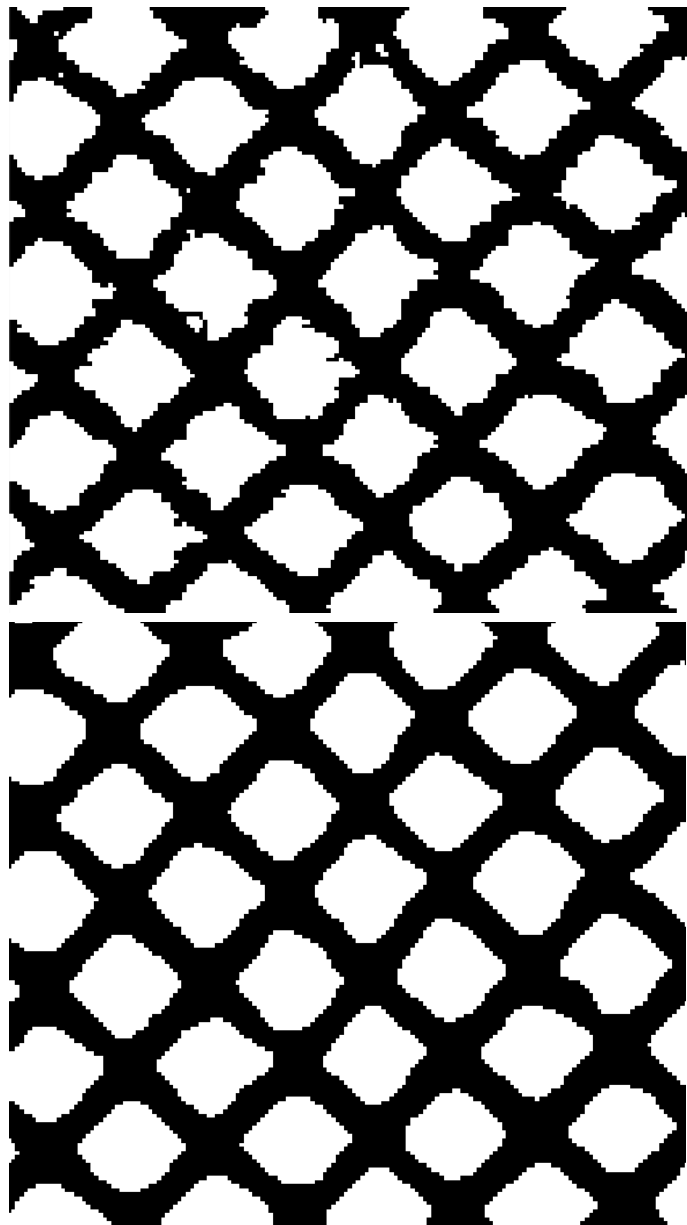


Figure 4-5. Binarised image with a Gaussian filter standard deviation of 0.01 (Top) and 2 (Bottom).



The tool has been developed to identify and analyse dark or light regions of the grayscale image, dependant on the geometry and image being analysed. Both automatic and manual thresholding options have been utilised. Otsu's method is employed for the automatic thresholding through the inbuilt Matlab function, *graythresh*. For the manual option, an adjustable slider is included to control the threshold of the binarised image. The analysis of light regions takes into consideration the pixel intensities greater than the set threshold value, whereas the dark analysis setting considers pixels less than the set threshold value. In the instance of the lattice coupon shown in Figure 4-4, the analysis is undertaken for the dark regions as the interest lies within the porous makeup. Through displaying the histogram, shown in Figure 4-6, in conjunction with the output binarised image, effective control of the threshold and smoothing values was achieved.

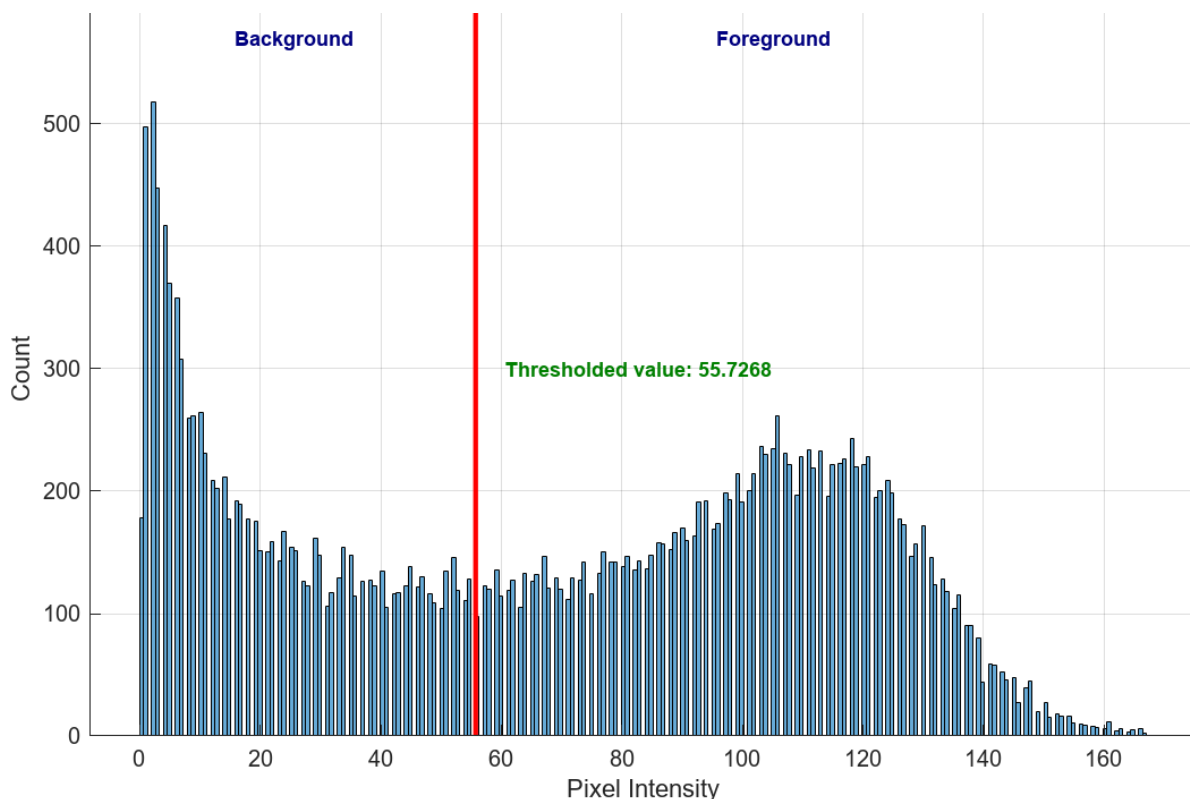


Figure 4-6. Histogram of greyscale image.

Confirmation of acceptable threshold level is achieved through masking the region boundaries onto the greyscale image, as shown in Figure 4-7. For greater accuracy it should be ensured that the boundary is lined up as closely as possible to the edges of the greyscale image.



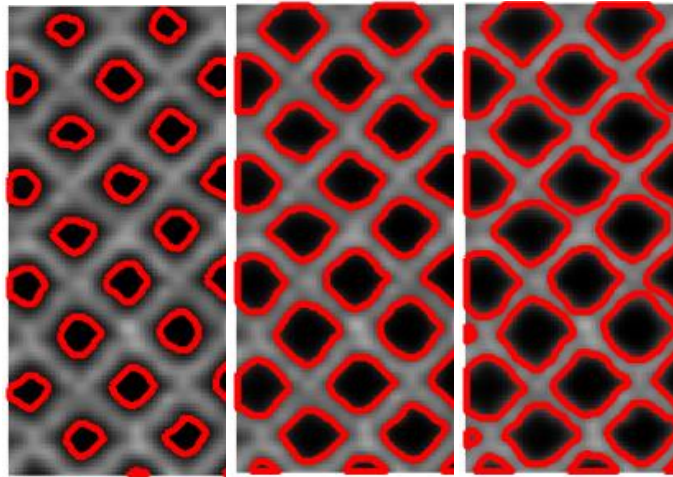


Figure 4-7. Threshold level: too low (Left), acceptable (Centre), too high (Right) for lattice structure.

A binarising threshold level set too low will reduce the size of the detected porous regions and total planar porosity value, whereas a level set too high will result in greater pore size and porosity values. To achieve reliable and repeatable results, this was evaluated for every analysed image.

4.4 Pore Analysis

The code returns a set of properties for the given regions within the boundaries of a binarised image. As shown in Table 4-1, the properties are automatically calculated for each region, which may be cross-referenced to the displayed image in Figure 4-8.

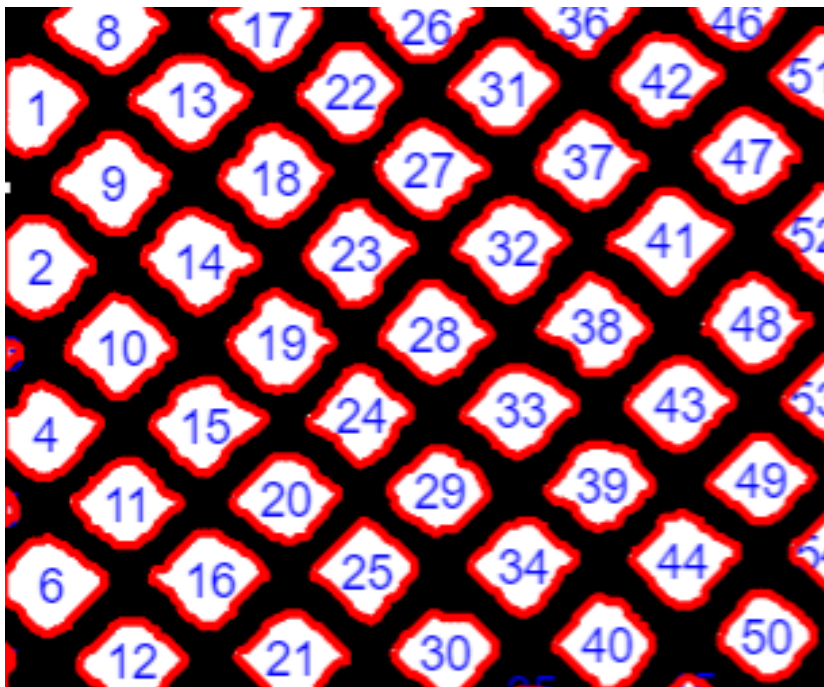


Figure 4-8. LAT pore identification



Table 4-1. Example of pore analysis for a lattice structure.

Region	Mean Intensity	Area (mm ²)	Perimeter (mm)	Centroid (mm)		Diameter (mm) --
				x	y	
13	25.80	0.0470	0.812	0.500	0.268	0.245
14	26.46	0.0499	0.842	0.523	0.687	0.252
15	26.83	0.0456	0.803	0.541	1.121	0.241
16	28.92	0.0466	0.809	0.551	1.524	0.244
17	24.54	0.0355	0.715	0.705	0.800	0.213
18	25.01	0.0473	0.800	0.721	0.468	0.246
19	26.38	0.0469	0.804	0.738	0.906	0.244
20	26.68	0.0423	0.744	0.752	1.315	0.232
21	31.34	0.0423	0.758	0.768	1.730	0.232
22	26.87	0.0437	0.762	0.920	0.247	0.236

The diameter is calculated as its equivalent value, which equates to the diameter of a circle with the same area, as shown in Equation (4-5).

$$D_{eq} = \sqrt{\frac{4A}{\pi}} \quad (4-5)$$

Where D = equivalent region diameter and A = region area.

An area threshold slider is also presented to disregard any smaller pores, irregularities or outliers within the image that have not already been automatically filtered out by the software. Further automatic analysis displayed in the tool include calculating the total number of porous regions, total area, average area and diameter as well as the planar porosity of the cropped image, along with various standard deviations which were all exported into a single file.



4.5 Heatmaps & Histograms

To simplify and display the distribution of the variations in area, diameter and perimeter of each region, results were graphically represented in the form of histograms and heat maps, as shown in Figure 4-9. This function was particularly useful in this study by identifying the effects of warpage on the pore size distribution of the horizontal samples, as is discussed in Section 5.2.3.

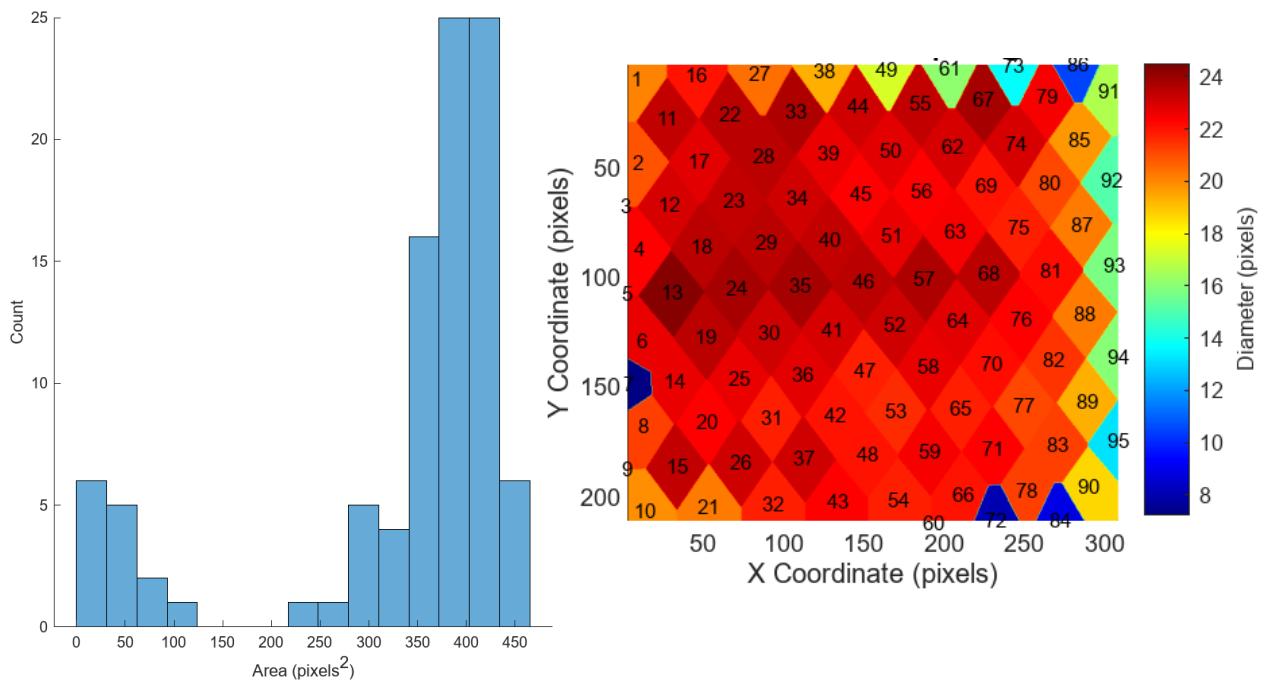


Figure 4-9. Area histogram (Left) and diameter heatmap (Right).

This was achieved by interpolating the data to its nearest neighbour and plotting as a filled contour containing the values of the specified parameters along with the x and y coordinates, exemplified in Figure 4-10.

```
x = linspace(min(app.t2Corr(:,1)),max(app.t2Corr(:,1)),500);
y = linspace(min(app.t2Corr(:,2)),max(app.t2Corr(:,2)),500);
[X,Y] = meshgrid(x,y);
F=scatteredInterpolant(app.t2Corr(:,1),app.t2Corr(:,2),app.t2Corr(:,5),"nearest");
contourf(app.diaHM_UIAxes,X,Y,F(X,Y),100,"LineColor","none");
```

Figure 4-10: LAT diameter heatmap function example Matlab code.

Through utilising this method and sectioning the components at various planes, patterns and irregularities were identified, as is discussed further in Section 5.2. Such patterns include the distribution of pore size at particular sections of the plane, or pore size increasing or decreasing through the z-axis. This may be a result of the anisotropic heat dissipation from the component, unoptimized machine parameters, or simply the effect of gravity.



Evidently, the smaller areas identified in the histogram of Figure 4-9 are a result of the cropping of the original image with partial pores being included in the analysis. Nonetheless, this is required for the porosity calculation of the entire cropped image. This method has proven to work well with ordered porosities such as the lattice structures examined in this research project.

4.6 Strut Analysis

In addition to the above-mentioned pore analysis, the solid struts of the additively manufactured lattice structures were also analysed. A series of lines were overlaid on the binarised image covering the features to be measured, as shown in Figure 4-11. The efficiency of analysis is improved by allowing for multiple struts to be analysed across a single line. In this case, the strut diameter can be measured by drawing lines at $\pm 45^\circ$. The underlying analysis code and methods utilised is similar to those used for the pore analysis. Each line drawn is converted into a mask with all pixels that fall outside of the mask set to white and disregarded from further analysis.

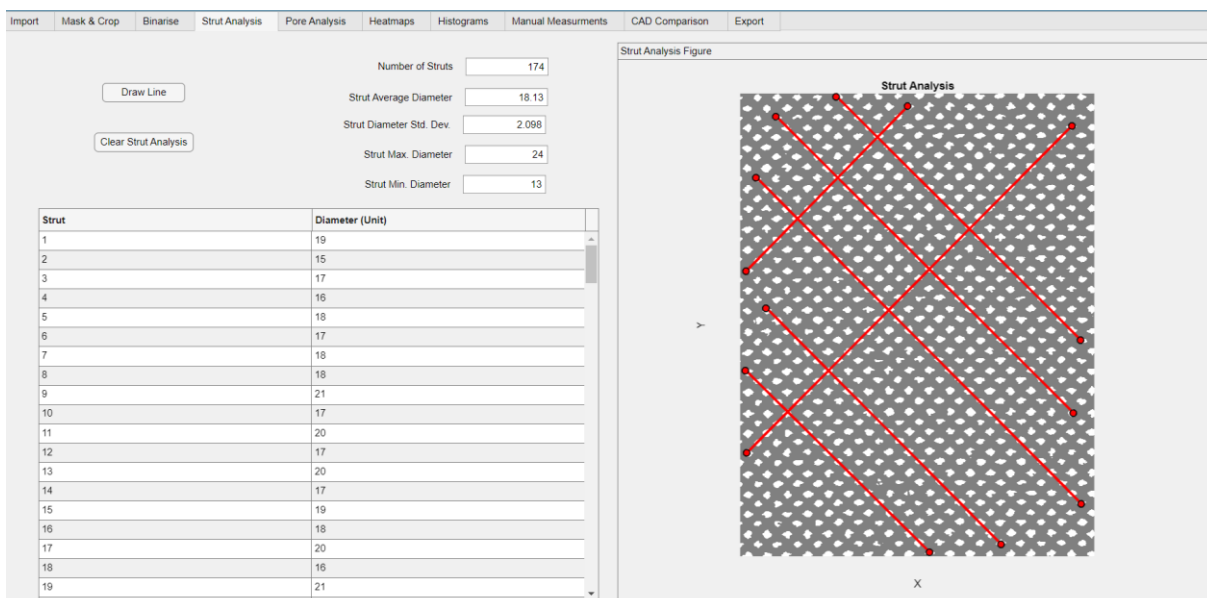


Figure 4-11 Strut analysis example of an additively manufactured lattice structure with units generalised to pixel count.

As the drawn lines are of one pixel width, illustrated in Figure 4-12, the area was calculated with the *regionprops* function to effectively represent the diameter of each strut section. As can be seen from Figure 4-11, LAT has successfully analysed 174 separate struts over 7 drawn lines in multiple orientations while also returning useful parameters such as average, standard deviation, maximum and minimum strut diameter.



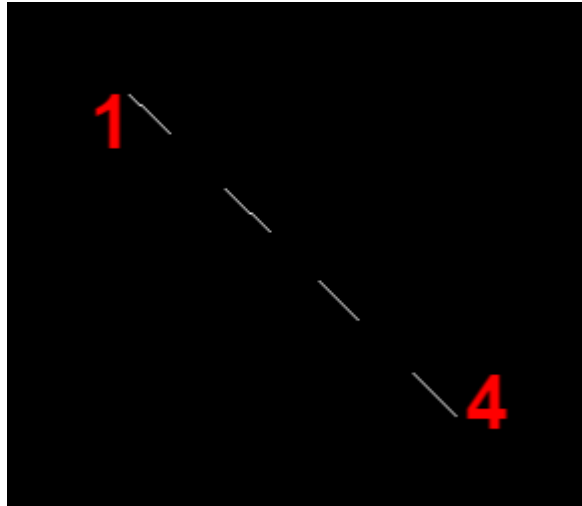


Figure 4-12 Example of inverted image with struts detected (white) and pore space (black)

4.7 Manual Measurements

The *canny edge detection* method within Matlab offers greater detail for manual measurements than the *regionprops* method previously mentioned. This algorithm detects the edges by looking at the local maxima of the image. Through using both a strong and weak threshold, the canny method is less susceptible to noise, as opposed to other solutions [165]. The threshold level is easily altered with the use of a variable slider from 0 to 1, to clear any remaining noise, as demonstrated in Figure 4-13.

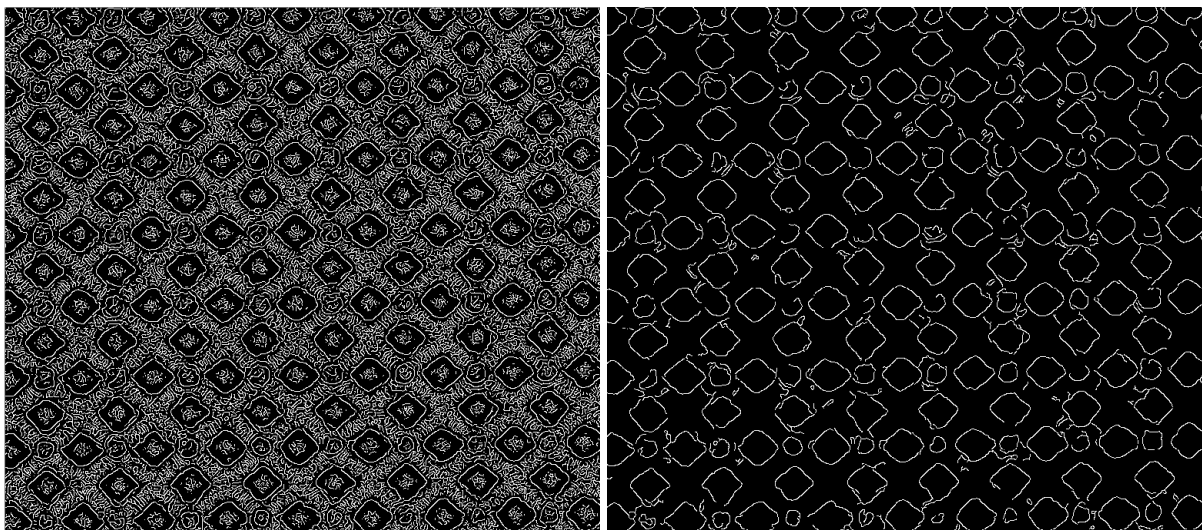


Figure 4-13. Canny Edge Detection example of analysed lattice structure with thresholding values of 0 (left) and 0.5 (right).

The *drawline* function was used to analyse a wide range of lattice geometric features, including strut thickness, cell size, and pore size. The pixel length of the line is calculated



(Equation (4-1)) and then converted to the physical distance. Similarly, the results are tabulated, and shown in a separate figure, as shown in Table 4-2 and Figure 4-14 respectively. This function is set within a loop with the table automatically updated with each new measurement iteration.

Table 4-2. Example of Manual measurements user interface for lattice structure.

Line	Length (Pixels)	Length (mm)
a	22.84	0.57
b	23.31	0.58
c	40.96	1.03
d	40.43	1.01
e	8.42	0.21

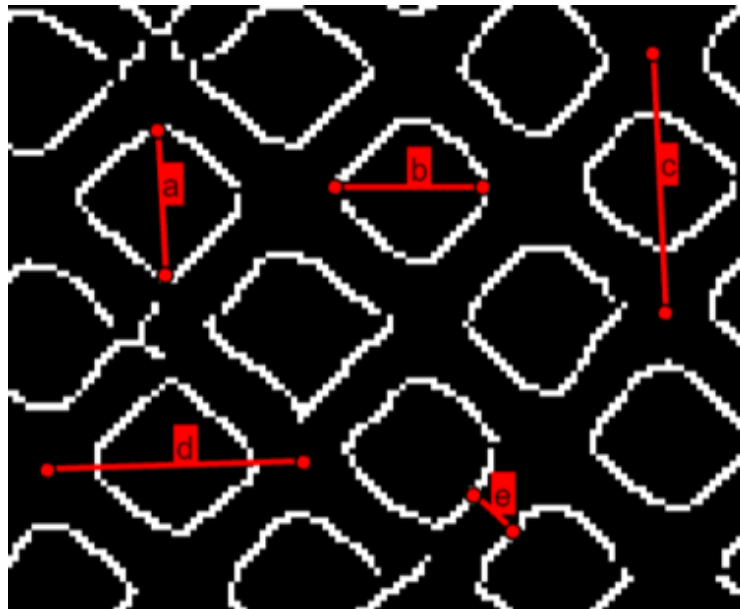


Figure 4-14. Example of edge detection and manual measurement feature.

As shown, LAT's manual measurement feature has the capabilities to measure pore size (a and b), unit cell size (c and d) in both horizontal and vertical orientation as well as strut thickness (e).



4.8 CAD Comparison

Through importing a captured image of the CAD file, LAT has been developed to rescale and overlay the detected boundaries of the microscope image onto the imported CAD image, as shown in Figure 4-15. With the use of two sliders representing both x and y direction, the boundaries may be accurately positioned on the image for precise analysis. The CAD comparison callback developed within LAT enables quick identification of defective regions of the lattice structure.

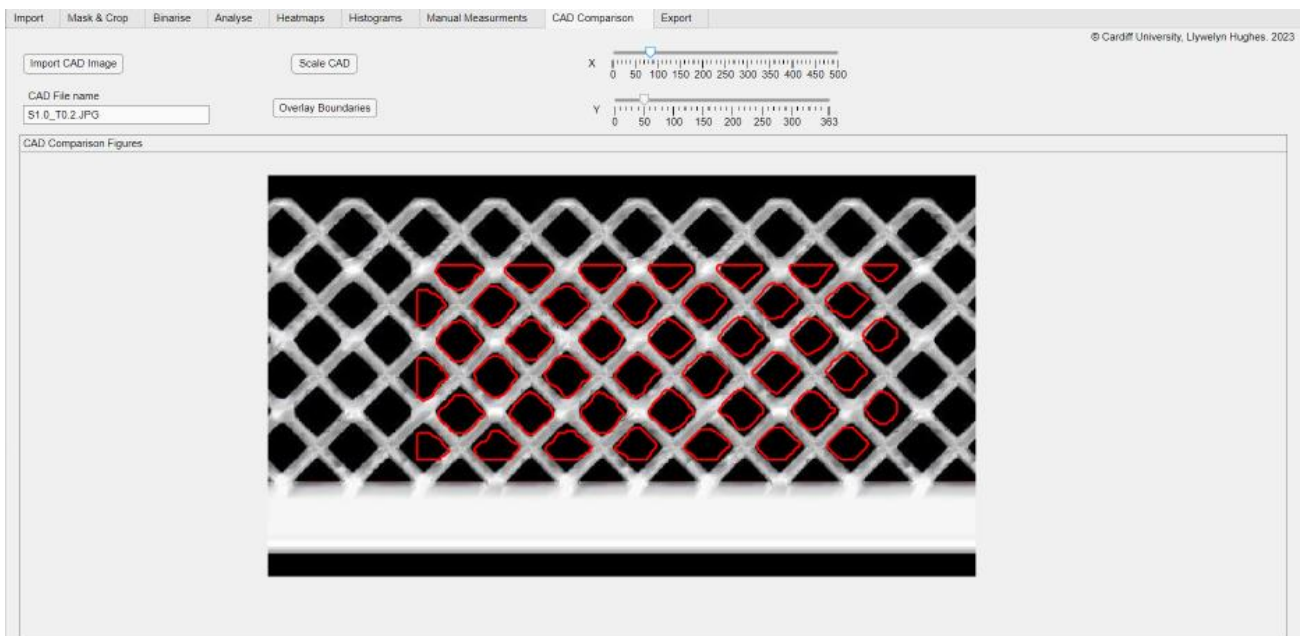


Figure 4-15: Example of CAD Comparison function where the red lines represent the detected boundary of microscope image.



4.9 LAT Robustness and Accuracy

Validation of analysis is essential for confidence in results. The measured parameters within LAT are affected by factors such as the quality of the scan, the binarisation threshold and the presence of agglomerated powder. The robustness of the analysis tool has been quantified with the use of a SensoSCAN S-mart 3D profilometer utilising focus variation techniques [166]. Compared to other techniques such as Confocal and White Light Interferometry, focus variation is well suited for the analysis of lattice structures and offers improved accuracy for larger surface roughness, increased inclination angles, high measurement speeds and an increased vertical range [167].

Four separate scans were taken on the SensoSCAN along the length of the front face of the sample. A 10X magnification objective covering field of view of 1.69 x 1.41mm was used to intentionally achieve greater detail, meaning the number of pores and struts available for evaluation in each scan were restricted, as shown in Figure 4-16.

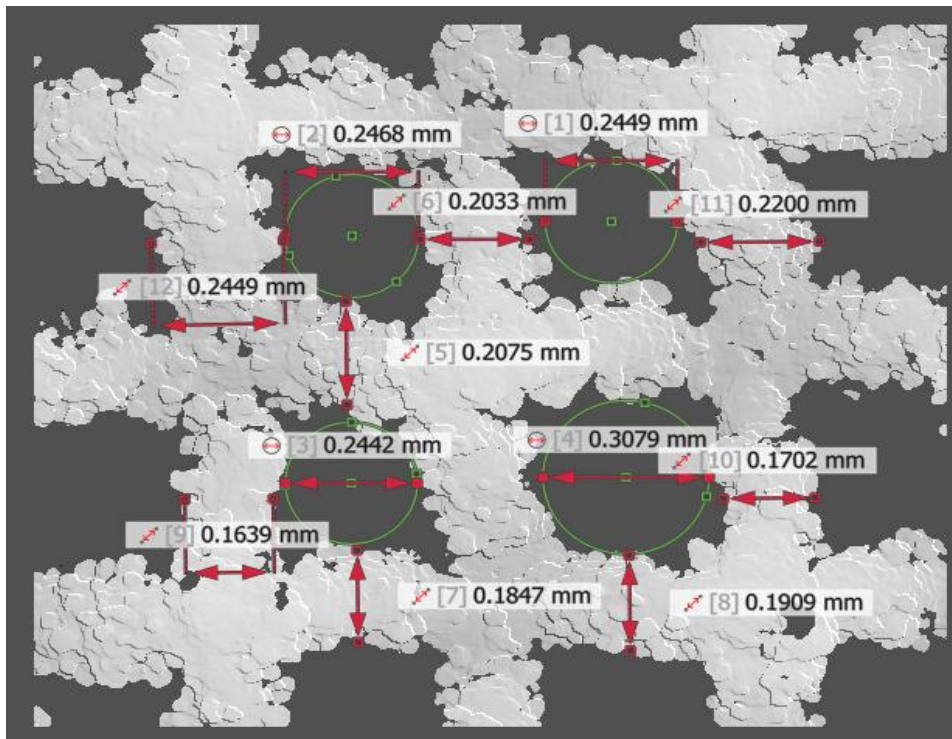


Figure 4-16. Example of manual measurements performed via profilometry.

For this sample a total of 26 pores and 55 struts were measured. This is a significant reduction compared to the 4375 pores and 277 struts analysed with LAT for the same surface. The averaged measurements for both LAT and SensoScan have been shown in Figure 4-17.



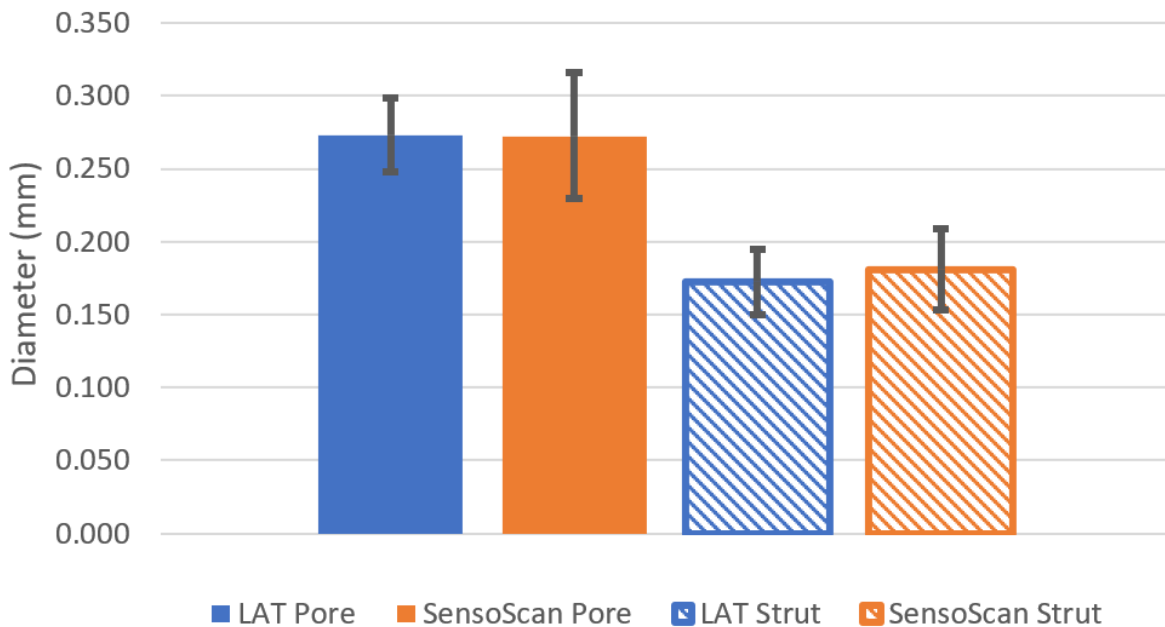


Figure 4-17 Measurement comparison between LAT and SensoScan.

Evidently, both measurement techniques have a strong agreement with a measured ~ 0.27 mm pore diameter and 0.17 and 0.18mm strut diameter for LAT and SensoScan, respectively. However, the SensoScan measurements have a noticeably larger standard deviation, represented by the error bars in Figure 4-17, in addition to having a limited number of measurements due to its reduced field of view. Therefore, utilising LAT has proven to be an effective method for geometric characterisation across the whole sample. Furthermore, this has shown that utilising the equivalent diameter, as opposed to the circle diameter within the pore, has a negligible effect for Body-Centred Cubic lattice structures.



5. Geometric Validation

Ensuring a suitable and accurate methodology for geometric validation of the lattice structures is an essential step prior to evaluation of their wicking performance. This chapter will therefore delve into the geometric accuracy of the printed samples, utilising methods discussed in Chapters 2.10 and 4, in addition to quantifying their printability in both horizontal and vertical orientation. This fundamental work is essential to the full understanding and quantification of later work packages carried out in Chapters 6 and 7.

5.1 Visual Inspection

Initial visual inspection identified numerous discrepancies between the horizontal and vertical samples both in terms of quality and aesthetic difference. It was evident that the entire set of horizontal samples had become warped (bowing in the centre) during the print process, as exemplified in Figure 5-1.

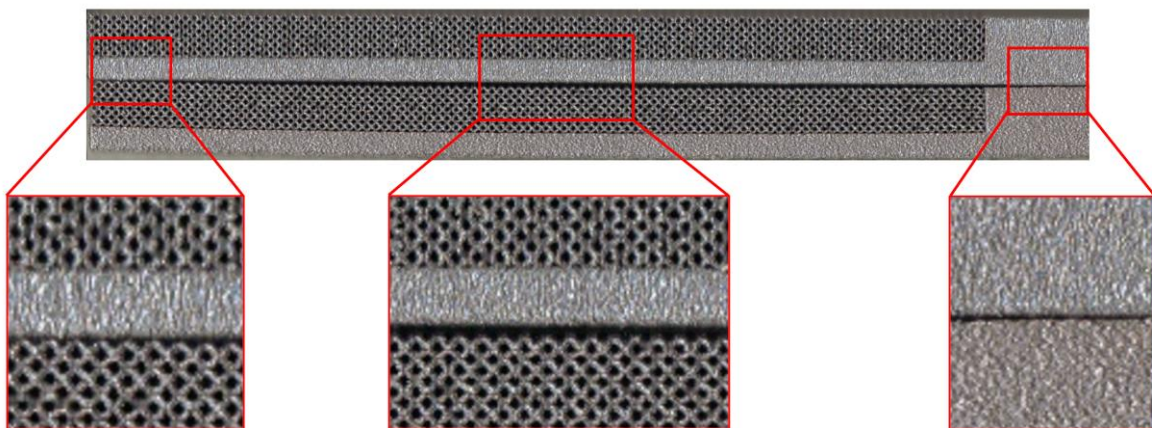


Figure 5-1. Samples 7 Horizontal (Bottom) and vertical (Top), identifying the severity of warpage in the horizontal sample, with magnified sections each section.

As observed, with both sides of the horizontal and vertical samples in contact, the horizontal samples exhibit a proclivity to sag along the build plane leading to elevated compressive and tensile stresses along the upper and lower surfaces, respectively. The severity of warpage varies from sample to sample. The point of maximum deviation within each sample is approximately 2 – 4mm to the left of the centre of their length. This was demonstrated with feeler gauges between the top of the lattice surface and a flat plane, with results shown in Table 5-1.



Table 5-1. Warpage of horizontal samples.

Sample I.D.	Warpage (mm) \pm 0.05mm
H1	0.35
H2	0.35
H3	0.30
H4	0.25
H5	0.30
H6	0.20
H7	0.35
H8	0.35
H9	0.30
H10	0.25
H11	0.40
H12	0.35

As can be seen, the extent of warpage varies from 0.2mm (H6) to 0.4mm (H11). However, as the feeler gauges were around 5mm in width, any small deviation in a single strut could have a significant impact on the measured warpage value. These values should therefore only be used as a guide for the actual deviation.

Also noticeable is an increased number of dislocated struts on the horizontal samples compared to their vertically printed counterparts, as shown in Figure 5-2. The dislocated struts are identified as the darker out of focus regions.



Figure 5-2. Example of dislocated struts on sample H12 (bottom) compared to V12 (top), where the large dislocation (circle) is shown and the differing colours highlighted on the labels (square).

Figure 5-3 shows a more detailed SEM image of large dislocation represented by the red circle in Figure 5-2.



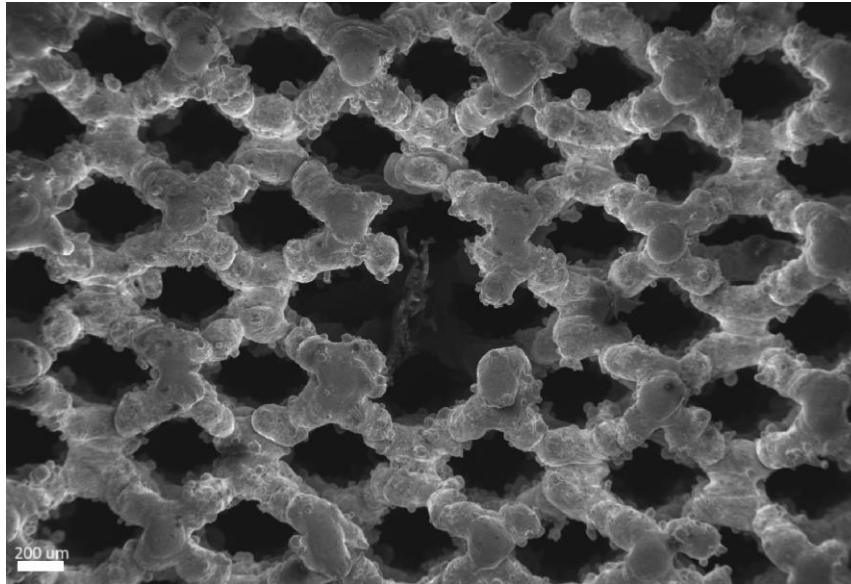


Figure 5-3. SEM Image of sample H12 showing dislocated struts at centre of front face.

The increased amount of strut dislocation on the horizontal may be attributed to excessive thermal stress induced warpage. This sagging nature would result in the highest compressive stresses being on the front surface of the structures, while the back surface in contact with the support structures would undergo the highest tensile stress. Minor dislocations were also present across the vertical 0.15mm strut diameter samples, which experienced no visible warpage. This may be a result of the available machine parameter settings within the build file having been optimised for 0.16mm strut diameter.

Upon further inspection, samples 3 and 4 – both horizontal and vertical variants, were restricted when examining the line of sight through their side faces. This is due to excessive blockage of the pores owing to the combination of reduced designed pore sizes and particle agglomeration on the strut surface. This is discussed further throughout and quantified with the use of XCT analysis in Section 5.5.

Interestingly, the final print layer of each sample was of darker colour to the side faces, as can be seen in Figure 5-2. This may be down to the differences in microstructure resulting in varying optical properties across each face which may be affected by several factors including:

- The final layer of the component likely undergoing a single melt, whereas the side faces experience multiple melting and solidification dynamics as the laser penetrates through the layers resulting in different thermal and cooling regimes.



- Varying rates of thermal gradients and residual stresses possibly experienced between various surfaces due to the rapid melting and cooling of the melt pool.
- The top surfaces of LPBF structures often undergo an additional re-melting which has the benefits of improved surface finish, enhanced microstructure and reduced oxidation and impurities.

These factors frequently exhibit interdependence and reciprocity, making it challenging to pinpoint a singular cause.

5.2 Dimensional Accuracies

The following analysis was done using LAT and images were scanned with a resolution of 2400 dots per inch (dpi) which is equivalent to a pixel size of $10.58\mu\text{m}$.

5.2.1 Strut Analysis

Through utilising LAT's strut diameter feature, as exemplified and described in Chapter 4, accurate and reliable measurements were obtained. The struts were analysed on the external front face at the top, middle and bottom of each sample, as show in Figure 5-4. Following this method allows for simple identification of any trends within the distribution of strut diameters along the length of the samples.



Figure 5-4. Measurement locations of strut analysis

Figure 5-5 shows the results of the analysis for both horizontal and vertical samples. The number of struts analysed for each sample location varied from $\sim 120 - 290$ allowing for accurate average and standard deviation values.



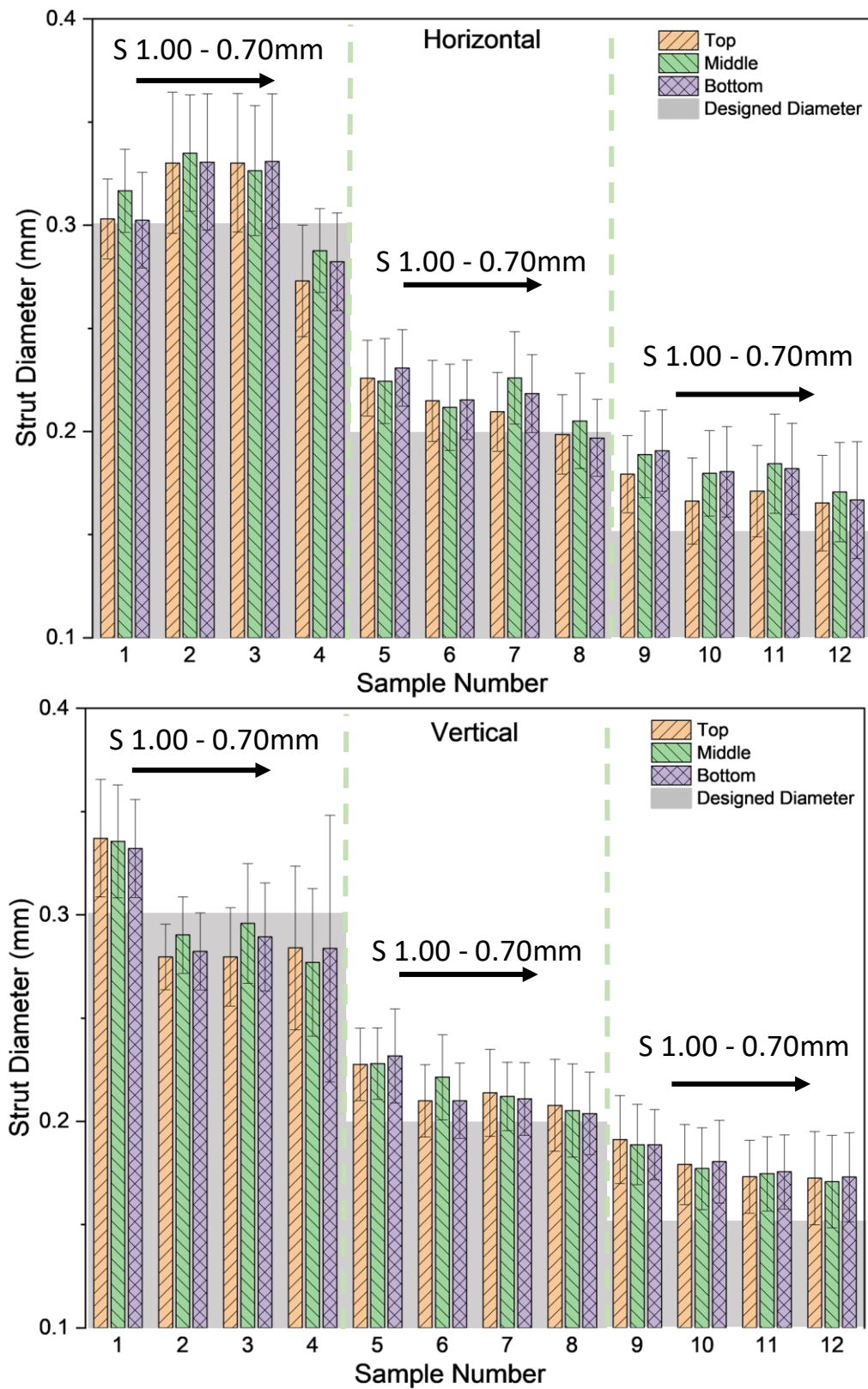


Figure 5-5. Comparative analysis of measured strut diameters at various positions along their lengths for both horizontal (Top) and vertical (Bottom) samples with error bars representing the standard deviation.



Through evaluation of Figure 5-5, it is evident that no clear trend is present within the distribution of strut diameters across the length of the samples and that the distribution reflects a stochastic nature, as expected. This indicates that neither build height of the vertical samples, or the associated warpage of the horizontal samples had any meaningful impact on the printed strut diameter. However, through evaluation of the normalised results in Figure 5-6, overall, the percentage deviation from the mean, otherwise known as the Relative Standard Deviation (RSD), as per Equation (5-1), increases with a reduction in both designed strut diameter and cell size.

$$RSD = \frac{Std.Dev}{Mean} \times 100 \quad (5-1)$$



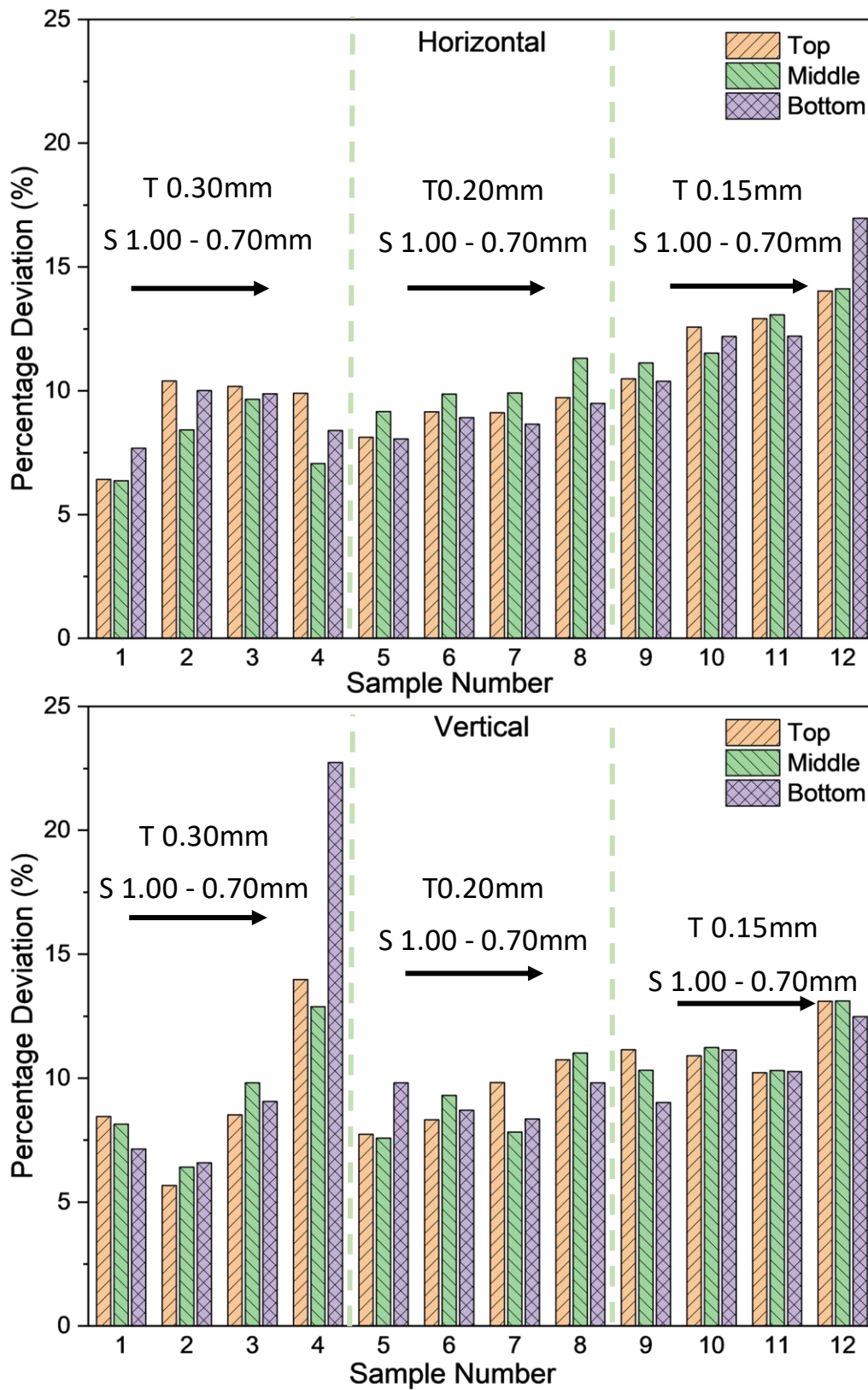


Figure 5-6. Strut Diameter percentage deviation from mean for both horizontal (Top) and Vertical (Bottom) samples.



This shows that as both designed strut diameter and cell size decrease, the resultant diameters of struts become more deviated as the designs approach the manufacturing limitations. As previously mentioned, samples 4 in both horizontal and vertical orientation showed minimal visible porosity, with no clear line of sight through the component. This is further explained with the increased percentage deviation of strut diameter, shown in Figure 5-6, resulting in a less consistent pore size distribution, as is further discussed in Section 5.2.3. To further analyse and display these results, Figure 5-7 shows the comparison between the designed and printed strut diameters averaged across the front face.

This shows a consistent trend between the horizontal and vertically printed samples, apart

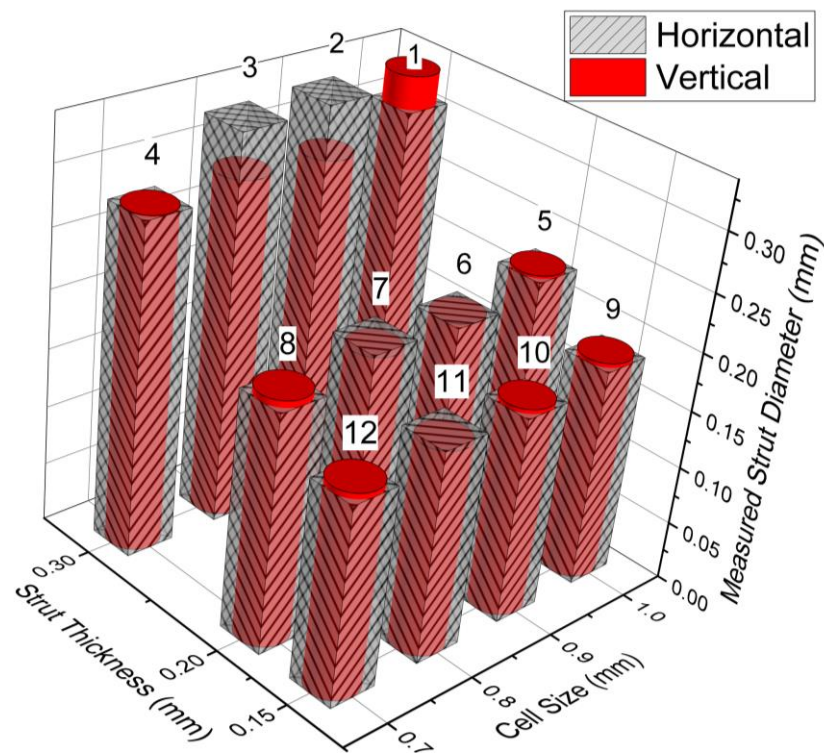


Figure 5-7. Comparison between desired and measured average strut diameter.

from the samples of 0.30mm strut thickness and cell size larger than 0.80mm. Again, this reflects the reduced printability and quality of these samples previously discussed. Notably, little difference is shown between the measured strut thicknesses of the 0.15mm and 0.20mm sample sets, as further displayed in Figure 5-8.



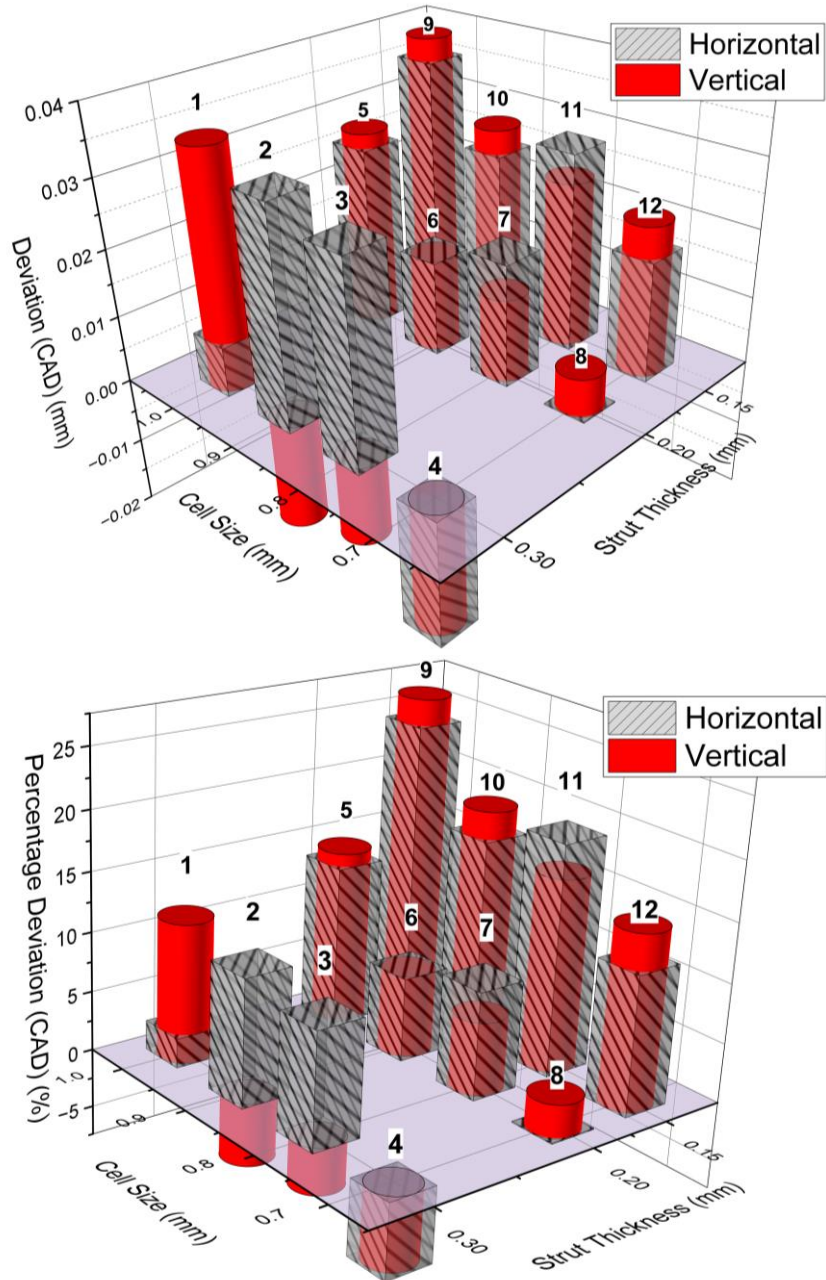


Figure 5-8. Deviation (Top) and normalised percentage deviation (Bottom) of the measured strut diameters from the designed CAD.

Most samples exhibited strut diameters larger than the desired values with a maximum deviation of 26.4% for sample V9 (S1.0, T0.15). However, half of the desired 0.3mm strut samples (H4, V2, V3, V4) resulted in the average measured strut diameter being ~5% smaller than intended. It is clear that the percentage deviation of the measured strut thicknesses compared to the intended CAD design generally increases with a reduction in designed strut thickness. Again, this is due to the design approaching the inherent limitations of the apparatus and agglomerated semi-sintered powders having a greater influence at these lower



strut diameters. Should smaller diameter powder be used for the build, the size and influence of the resultant agglomerations would reduce. Furthermore, as previously stated, the available build parameters used for the 0.15mm strut thickness samples had been optimised for designs of 0.16mm thickness while aiming for a mean diameter of 0.15mm.

A thorough review into defects associated with LPBF-based lattice structures by Echeta et al. [117] identified a wide range of deviations in strut thicknesses from the intended design. Of the analysed literature, deviations ranged from -45% up to +128%. The maximum deviation found in this study (Sample V9 S1.00 T0.15mm) was shown to be 26.4% larger than intended with only one of the reported studies evaluated by Echeta et al. showing smaller deviations.

5.2.2 Cell Size Analysis

Similar to that undertaken for the strut analysis in Section 5.2.1, unit cell size analysis was performed on the top, middle and bottom sections of the front faces, with 10 measurements taken for each sampling location. This enabled the effective identification of any trends relating to the build height of the vertical samples or the associated warpage of the horizontal counterparts, as shown in Figure 5-9.

Differing to that previously shown for the strut thickness analysis, it should be noted that the sample order of Figure 5-9 have been grouped into their respective designed cell size sets, as opposed to their corresponding sample number. Clearly, no consistent trend is present between the sampling locations on both horizontal and vertical samples, indicating a more stochastic distribution of cell sizes across the samples, as expected. Through considering the standard deviation of the measurements, as depicted by the error bars in Figure 5-9, it's clear that the overall measured cell sizes across each sampling location align well with the intended design parameters. This deviation from the mean, calculated with Equation (5-1), is further exemplified in Figure 5-10.



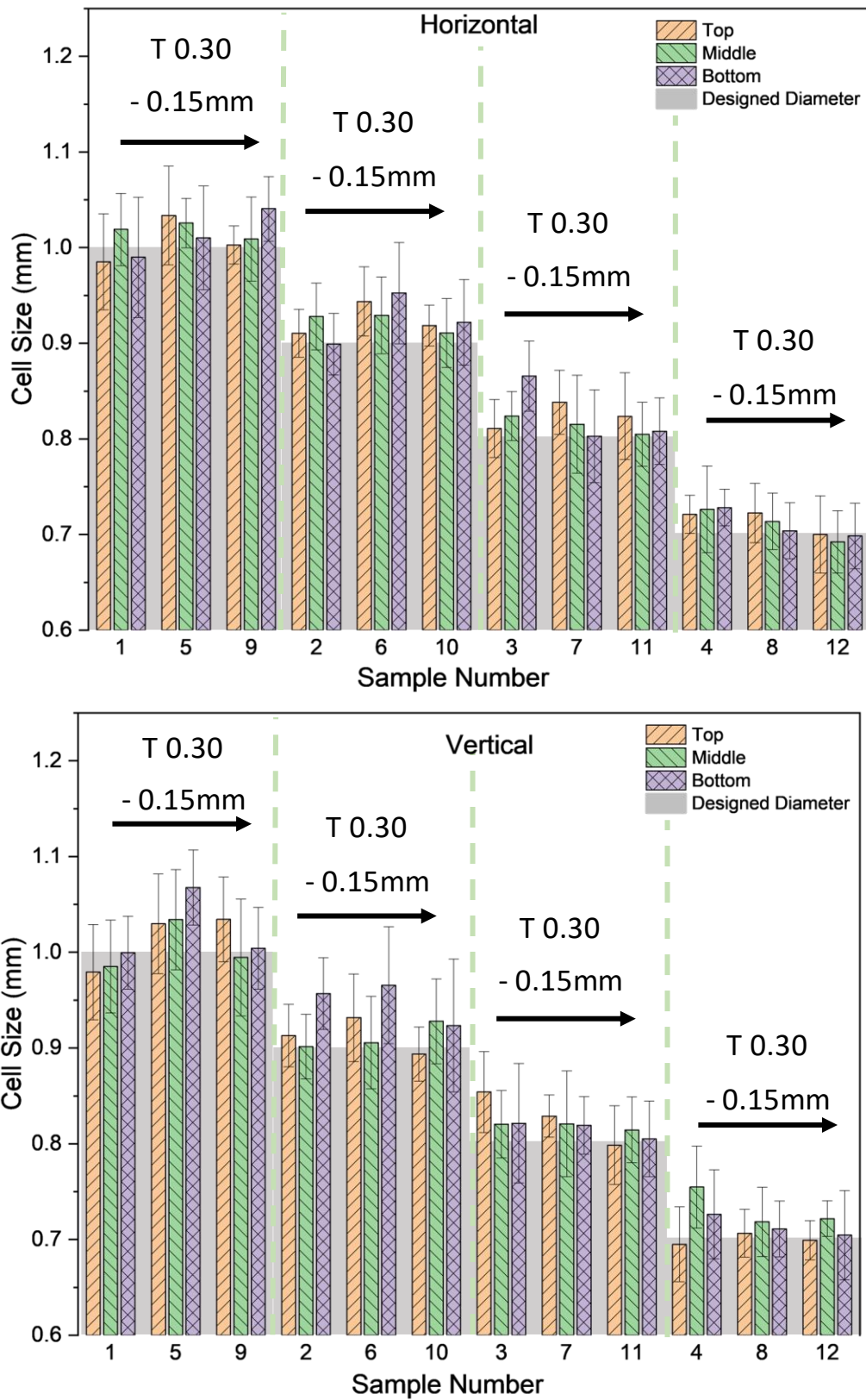


Figure 5-9. Comparative analysis of measured cell sizes for horizontal (top) and vertical (bottom) sample sets, with the standard deviations represented by the error bars.



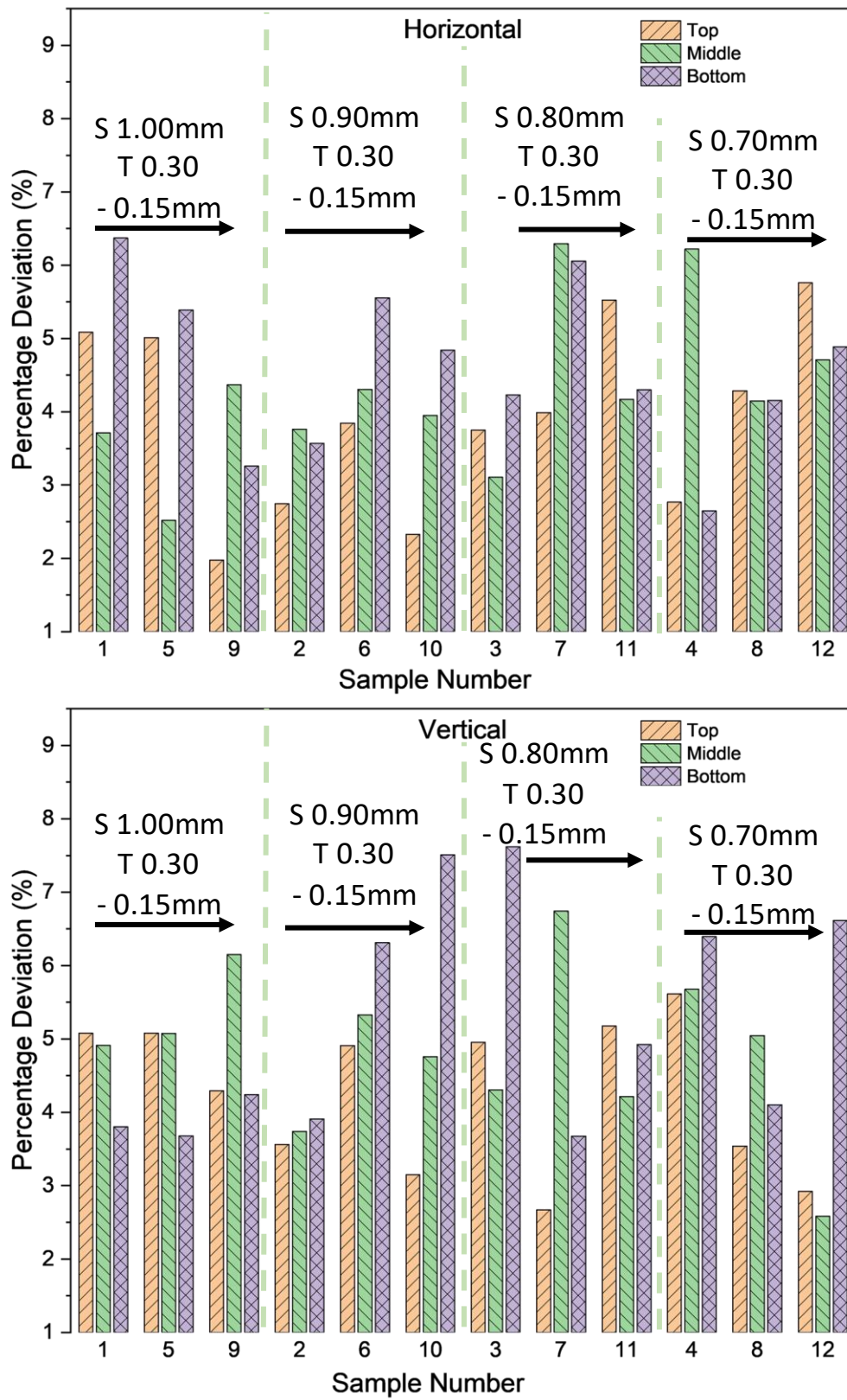


Figure 5-10. Cell Size percentage deviation from mean for both horizontal (top) and vertical (bottom) samples.



Here, the overall stochastic nature of the percentage deviation across each sampling location indicates no consistent influence of build height or warpage on the distribution of the printed lattice unit cell sizes. Figure 5-11 shows the evaluation of the effects of print orientation on the average cell sizes for both horizontal and vertical orientations.

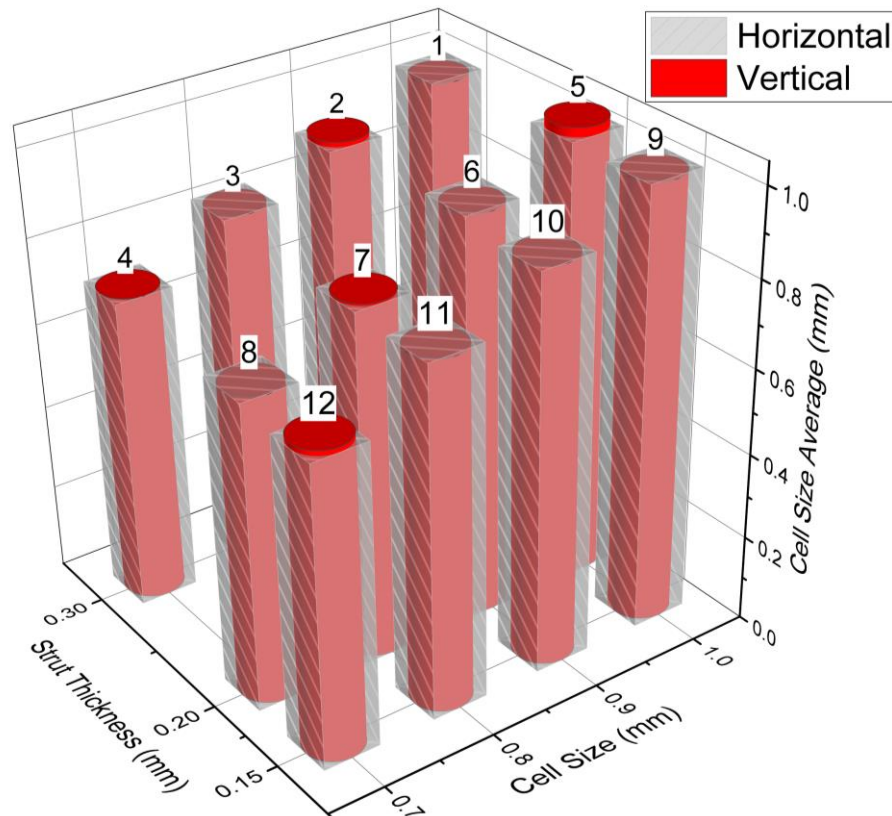


Figure 5-11. Comparison between desired and measured average cell size.

Through evaluation of the average cell sizes in Figure 5-11, it is clear that little discrepancy is presented between both print orientations. It can be seen that two thirds of the sample sets, apart from samples 2, 5, 7 and 12, show either larger cell sizes in the horizontal orientation, or essentially equal as is the case for sample 4. This deviation from the intended CAD design for both horizontal and vertical samples is further evaluated in Figure 5-12. The relationship between the measured cell sizes and the designed strut thickness is again shown to be stochastic in nature with no clear consistent trends presented. This allows for the determination that the printed cell size is independent of the designed strut thickness.



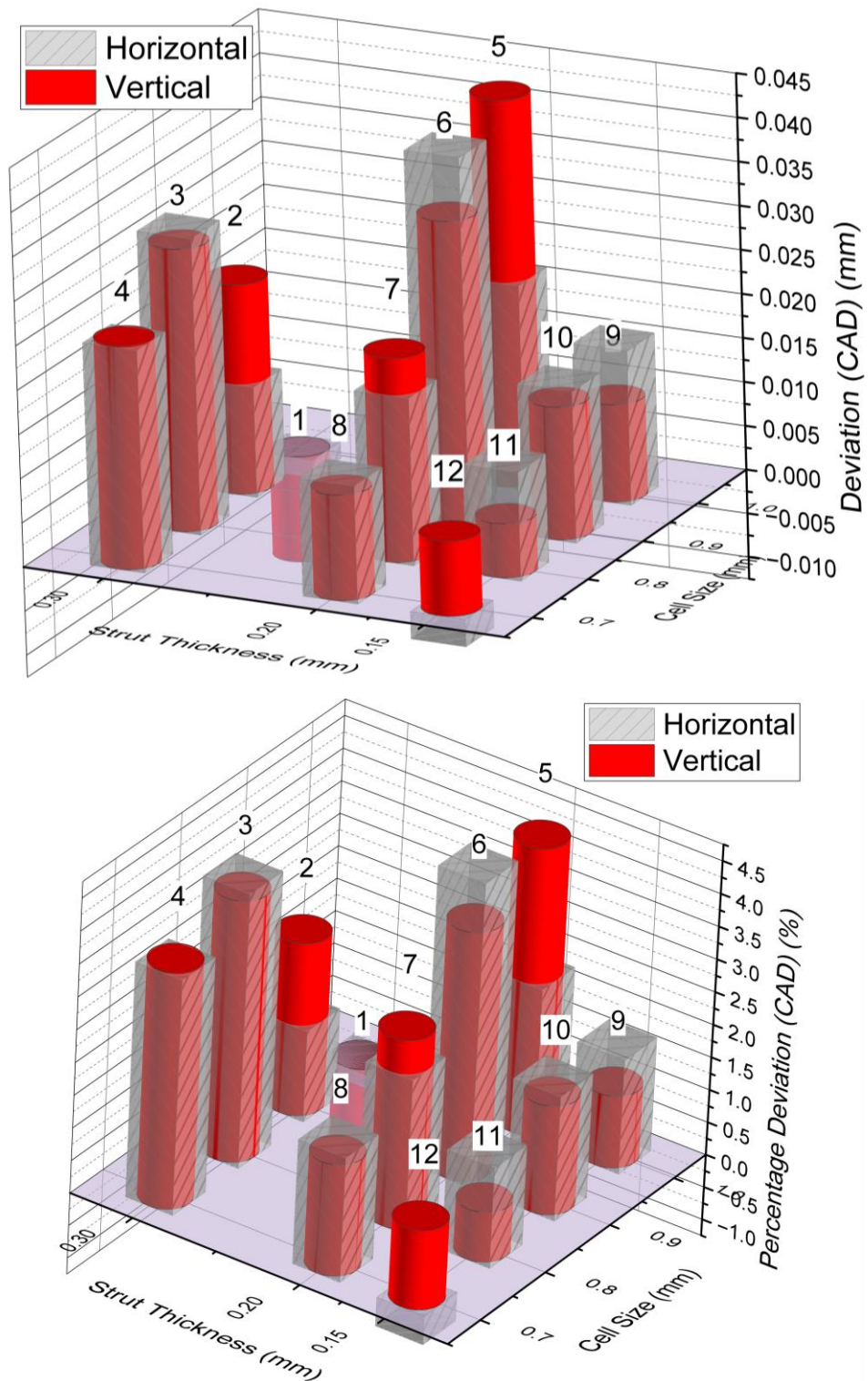


Figure 5-12. Deviation (Top) and normalised percentage deviation (Bottom) of the measured cell sizes from the designed CAD.



5.2.3 Pore Analysis

With the use of LAT's pore diameter feature, over 100,000 pores were automatically detected and analysed across the 24 samples. This serves well to characterise the geometric features and distribution of pores visible on the external surfaces. Analysis was undertaken on the external surfaces of the front, left and right faces of each sample to identify any trends or defects resulted from the build orientation, as shown in Figure 5-13.

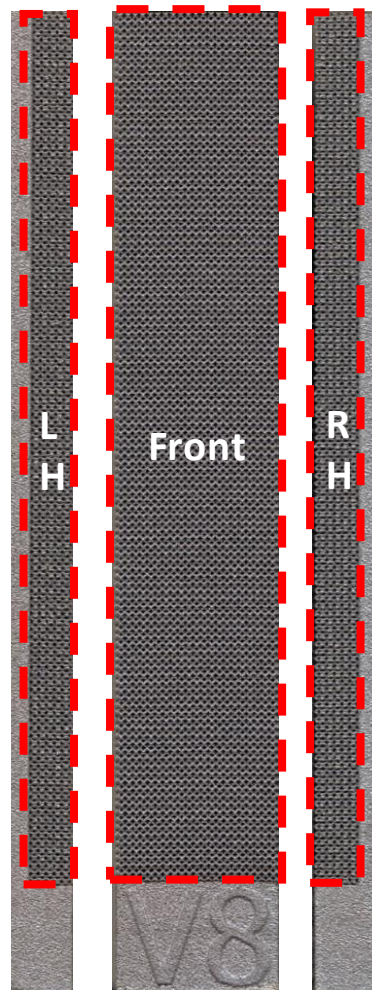


Figure 5-13. Investigated surfaces for pore analysis. LH (left), Front (middle) and RH surface (right).

This methodology differs to that previously undertaken for strut and cell size analysis due to the enhanced automation of the pore analysis process allowing for improved analysis efficiency. By meticulously assessing the average pore diameter across each face, as shown in Figure 5-14, it becomes clear that the resultant pore diameter increases with a decreased strut diameter and decreases with a reduction in designed unit cell size, aligning with expectations.



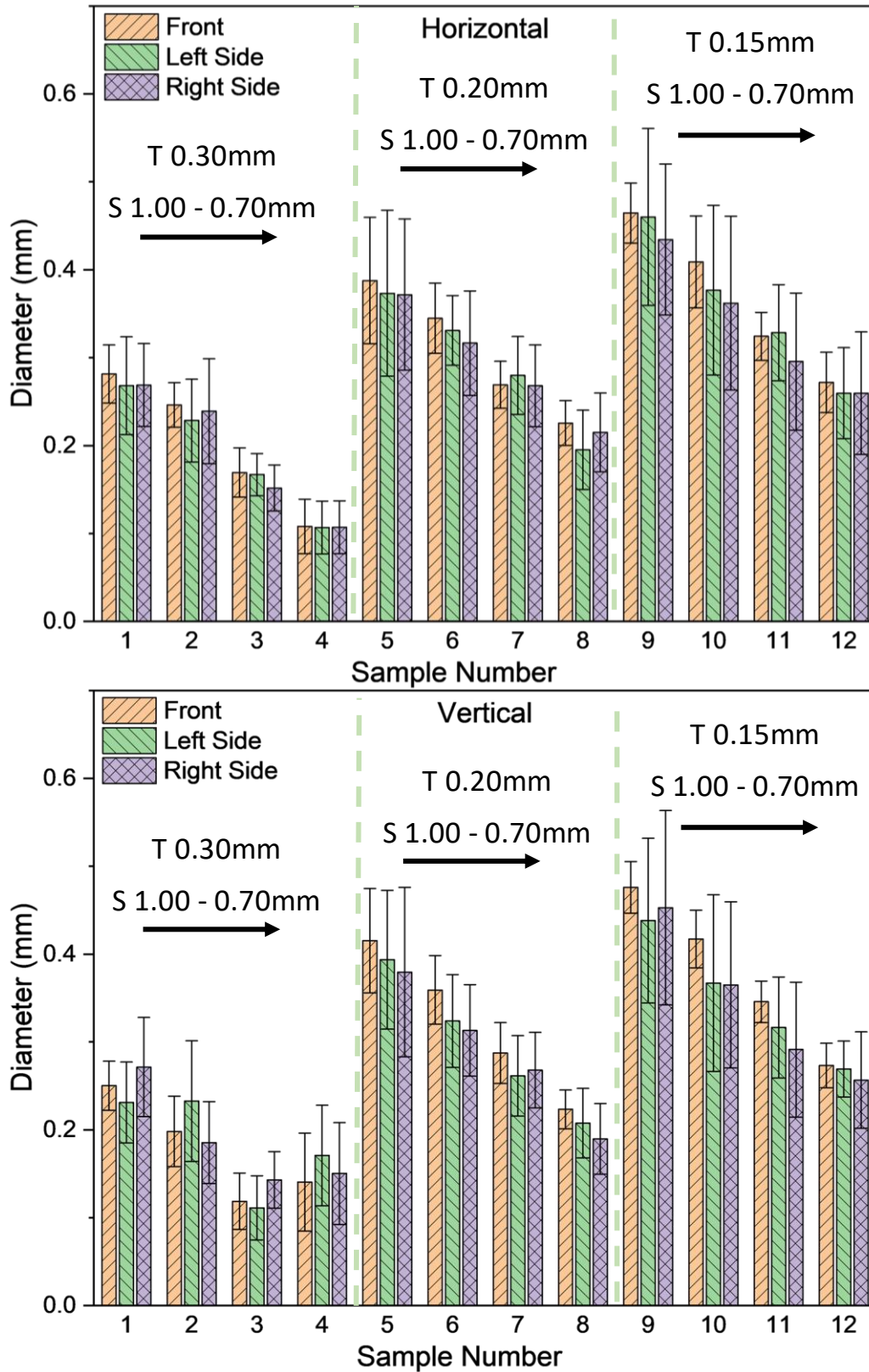


Figure 5-14. Average measured pore diameter for the front, left and right faces of both horizontal (Top) and vertical components (Bottom), with standard deviation represented by the error bars.

Evidently, the spatial variation of pores across the surfaces shows a generally favourable stochastic nature, with minimal variation observed among the faces. Analysis of the standard



deviation in pore diameters reveals a congruent distribution across the faces. Generally, the pore sizes are shown to be marginally larger on the front face as opposed to the side faces. It is important to note that the number of pores analysed on the front face was significantly larger due to its greater surface area. This has led to a higher standard deviation for the side faces, as shown by the error bars in Figure 5-14. Consequently, the average pore size on each face falls well within this margin of error. Due to the small differences between the analysed faces, only analysing the strut thicknesses and cell sizes on the front face was shown to be an acceptable methodology.

A less consistent trend is present for sample V4 showing a pore size unexpectedly larger than V3 which is of a larger designed unit cell size. This discrepancy may be attributed to a combination of machine limitations and the possible incompatibility of the combination of larger strut diameter and smaller unit cell size. Figure 5-15 shows a comparison between average pore diameter of both horizontal and vertical samples.

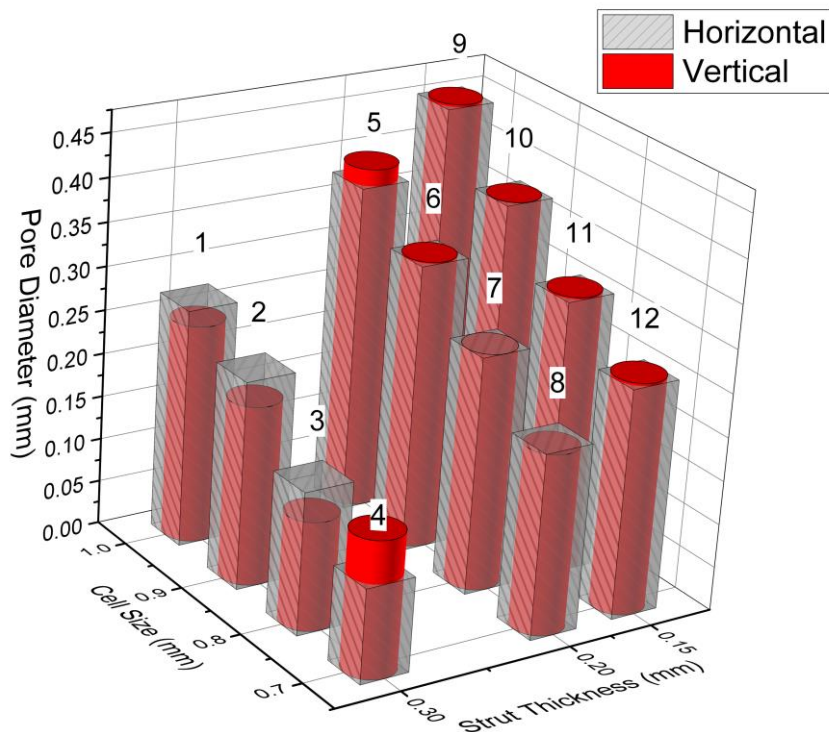


Figure 5-15. Average sample pore diameter.

As expected, the combination of larger strut sizes and reduced unit cell sizes produce smaller pore sizes. Largely, there is little difference between the as-built horizontal and vertical sample pore size. However, for the 0.30mm strut diameter samples, this variation is noticeably greater, with a variation of 13.6, 23.6, -43.4 and -4.9% between the horizontal and



vertical pore diameters for samples 1 – 4, respectively. This contrasts with the 0.15 and 0.20mm samples which showed a maximum difference of only 2.4%. Through analysing the deviation from the CAD model, shown in Figure 5-16, all samples showed pore diameters considerably smaller than the intended design. Adding to the inconsistencies of the 0.30mm strut diameter samples, the percentage deviation in Figure 5-17 shows pore sizes up to 61.2% smaller than intended, whereas the 0.15 and 0.20mm samples have a maximum deviation of 40.7%.

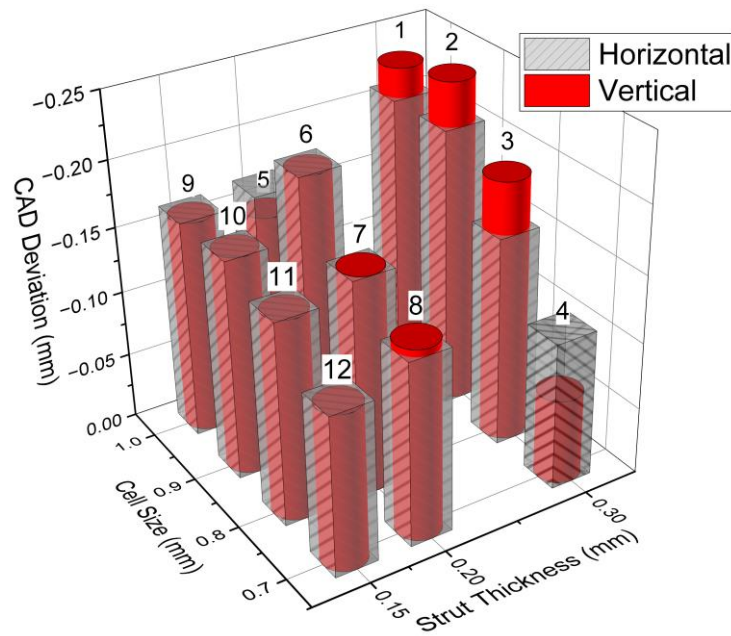


Figure 5-16. Pore size deviation from designed CAD.

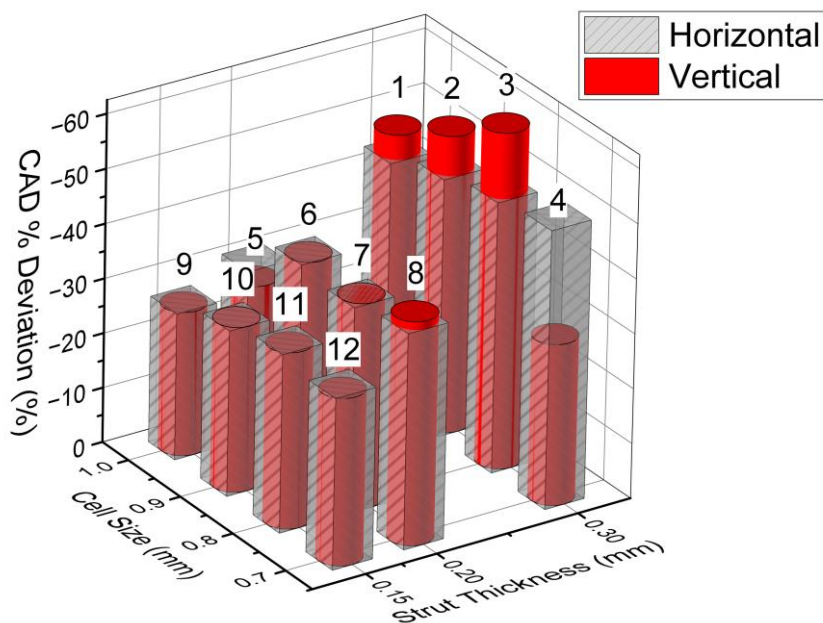


Figure 5-17. Pore size % deviation from designed CAD.



As identified in Figure 5-8, the percentage deviation in strut diameters from the intended CAD design was shown to increase as the designed strut thickness was reduced. This is a contrasting relationship to that identified for pore percentage deviation, shown in Figure 5-17. Furthermore, little variation between the designed and produced cell sizes was seen, highlighted in Figure 5-12. This could therefore be a result of increased node sizes for the 0.30mm strut thickness samples. Through examination of the significantly reduced pore sizes of sample set 3 and 4, couple with the limited line of sight through sample set 4, it is concluded that with the build file parameters and raw material used for this study, a minimum pore size of $\sim 160\mu\text{m}$ is achievable.

As previously discussed, it was clear that the horizontal samples were warped during the printing process. The effect of this is seen within the pores size distribution along their front faces. Through using LAT's heatmap function, this distribution can be visualised, as shown in Figure 5-18. Similar distribution can be seen throughout all 12 horizontal samples.

Through analysis of the vertical samples of Figure 5-18, a more stochastic nature of pore distribution is seen, showing no correlation between pore diameter and build height over the 80mm analysed lattice section. Little difference is generally seen between the average pore diameter of the horizontal and vertical samples, identified in Figure 5-15, when considering their entire length. However, the warped nature and resultant larger pores at the ends of the horizontal samples have reduced the efficacy of the deliverable capillary pressure at these localised regions, resulting in reduced maximum capillary height and capillary performance, as is discussed further in Section 6.1.



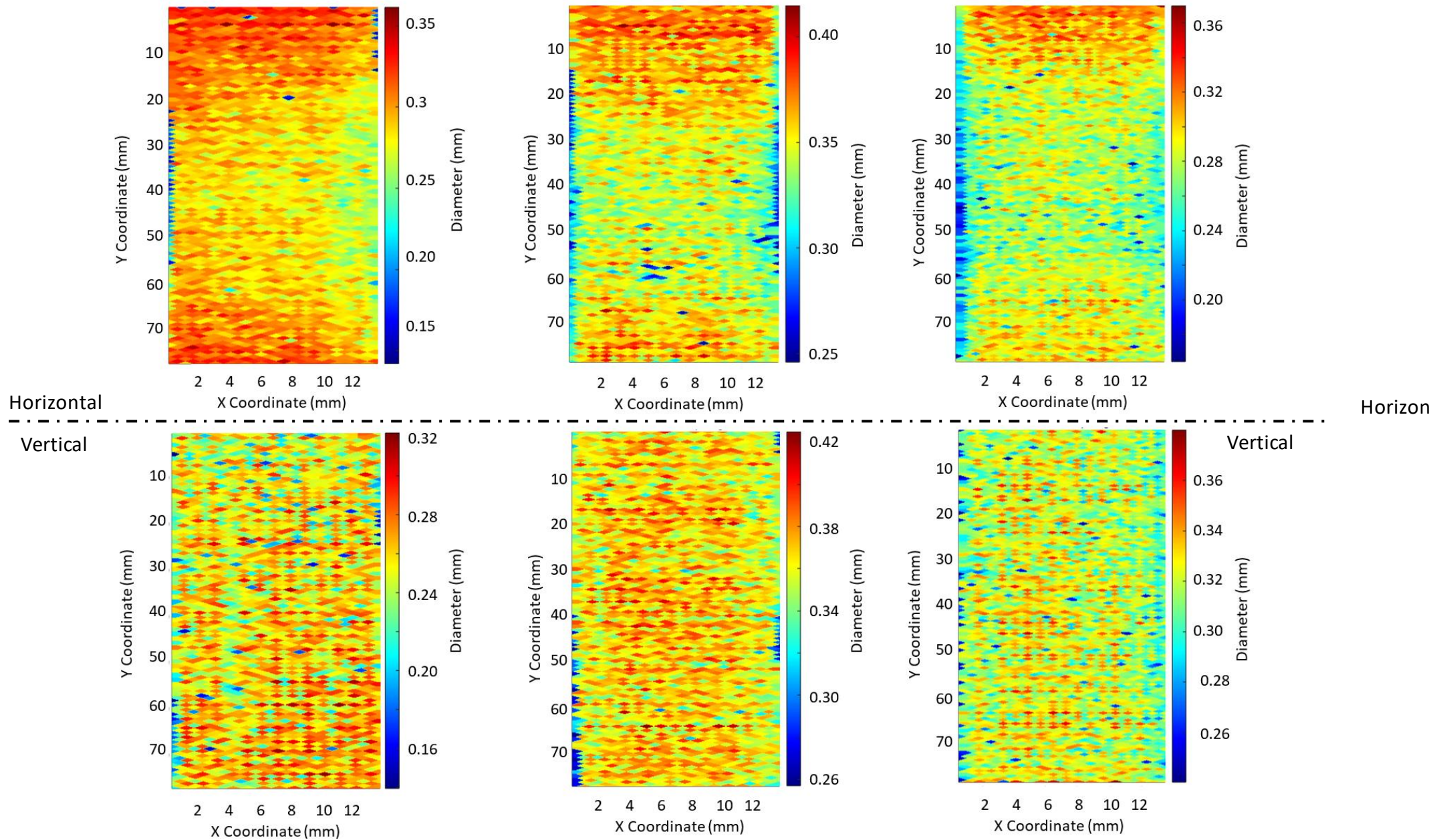


Figure 5-18. Horizontal (Top) and Vertical (Bottom) heatmap pore diameter distribution of samples 1 (Left), 6 (Centre) and 11 (Right)

5.2.4 Dimensional Accuracy Summary

Through evaluation of printed strut thickness, cell size and pore diameter of each sample, numerous conclusions can be drawn emphasising the effect of design parameters, print orientation and effectiveness of AM as a net shape technology. For example:

- The majority of samples exhibited strut thicknesses larger than the intended designs with no clear discrepancies between the average thicknesses of the horizontal and vertical samples.
- As both designed strut diameter and cell size decrease, the resultant diameters of struts become more deviated as the designs approach the apparatus' limitations.
- For the 0.15mm strut thickness, the agglomerated powders on the surface have been shown to have a larger influence on the percentage deviation from the CAD design with a maximum deviation of 26.4%.
- Neither strut thickness, cell size or pore diameter is shown to be affected by the build height for the vertical samples.
- Cell sizes have been shown to align well with the intended designed parameters, showing results independent of the designed strut thickness.
- The pore sizes have all been shown to be up to 61.2% and 40.7% smaller than the intended design for the 0.30mm and 0.20/0.15mm strut thickness samples, respectively. This was shown to be due to the agglomeration of powder resulting in larger strut and node diameters.
- The associated warpage experienced by the horizontal samples has resulted in the compression of the central pores of the front face, visualised with the heatmaps.

5.3 Surface Roughness

Following the methodology previously stated in Section 3.4.1, areal height parameters S_a , S_q , S_p , S_v and S_z have been determined.

5.3.1 Arithmetic Mean Height, S_a

Scans were mainly focused on the front face of each sample with measurements taken at the top, middle and bottom locations. As discussed, further evaluation and considerations of the side faces of several horizontal samples was also be undertaken. These faces correspond to the vertical printing z-axis, reflecting that of the front face of the vertical samples.

Figure 5-19 shows the arithmetic mean height across the top, middle and bottom of the front face of each sample for both horizontal and vertical datasets. Evidently, no clear relationship is present between the measured surface roughness and sampling location on either the horizontal or vertical sample sets. This indicates that neither the build height of the vertical samples or the defective warpage associated with their horizontal counterparts has had a meaningful impact on the characterisation of surface topology when considering the arithmetic mean height. Clearly, the measured S_a values increased as the strut thickness decreased.

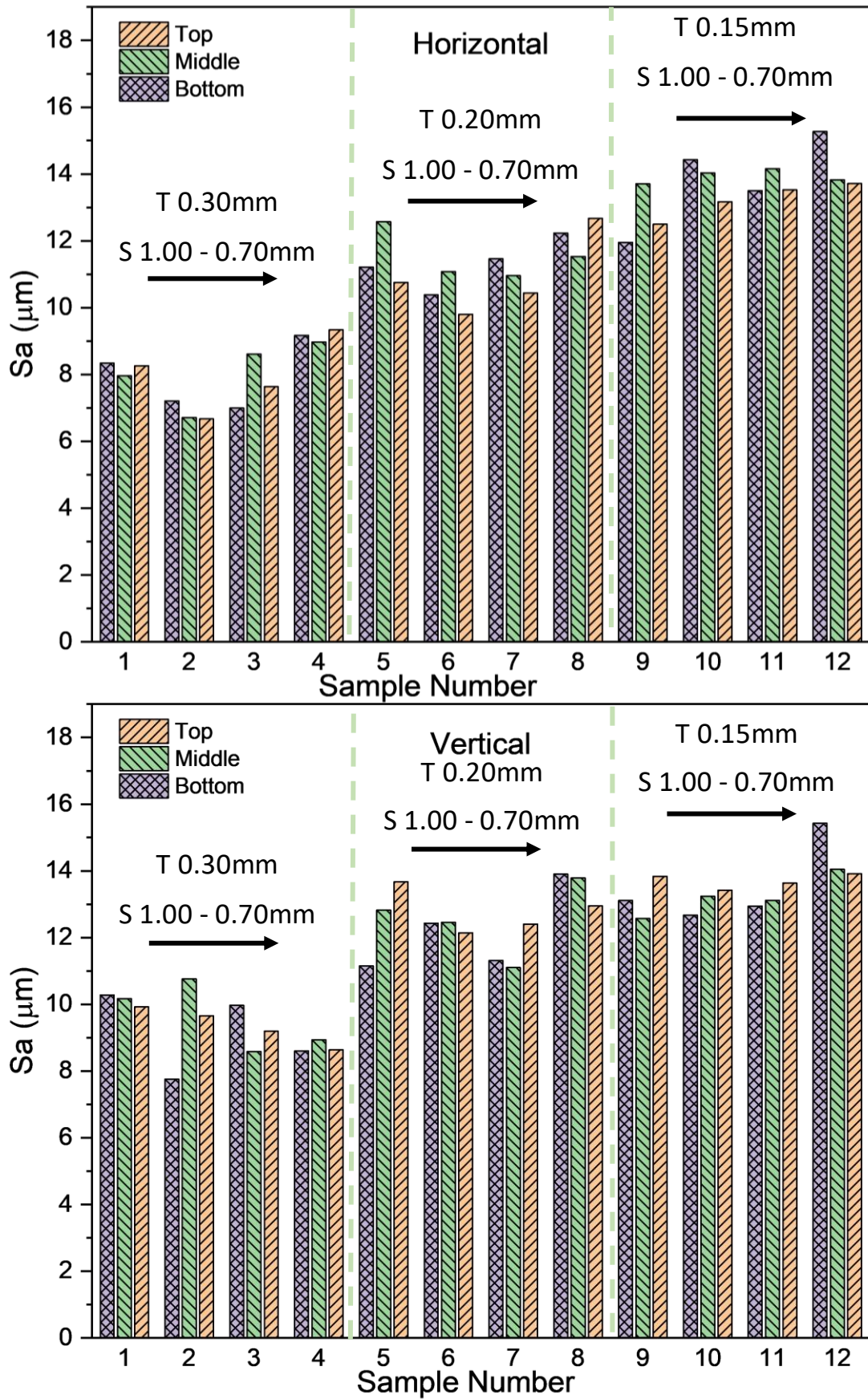


Figure 5-19. Arithmetic mean surface roughness at the top, middle and bottom locations for both horizontal (top) and vertical (bottom) samples.

For clarity and enhanced data visualisation, Figure 5-20 shows the averaged Sa values across the front of each face.

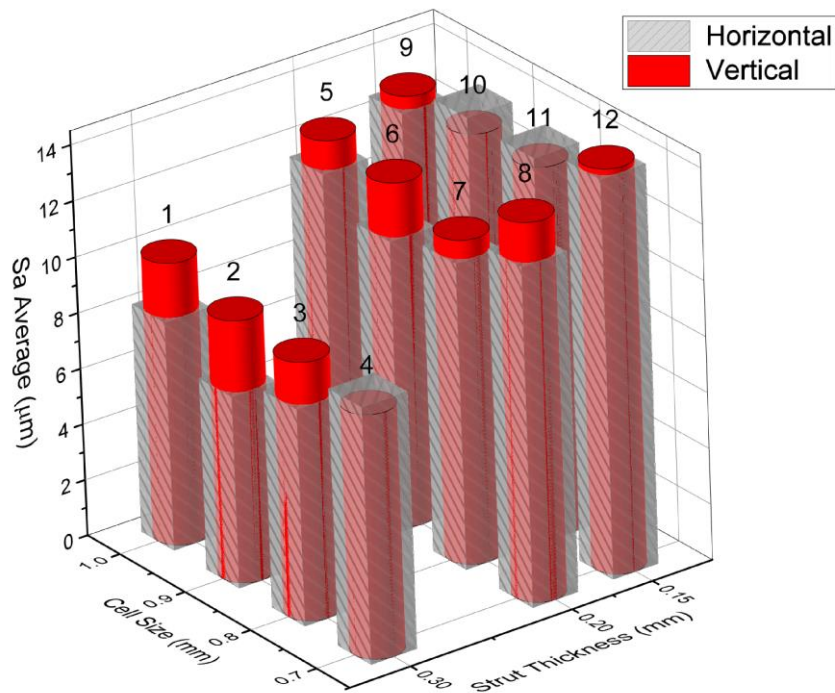


Figure 5-20. Averaged arithmetic mean surface roughness, Sa, for both horizontal and vertical samples.

Through detailed evaluation of Figure 5-19 and Figure 5-20, Sa tends to increase with a reduction in strut thickness for both horizontal and vertically printed samples. This is likely caused by the increased rate of agglomerated particles seen at the lower strut thickness samples. Furthermore, as the strut thickness is reduced, the ratio between the diameter of the attached particles and that of the struts is increased and therefore has a larger influence on the overall mean surface roughness. This trend is reflected in the study of Zeng et al. [168] which saw an increased in both Sa and Sq at smaller strut diameters. This was especially prevalent at strut thicknesses below 0.40mm where powder-size effects were dominant with Sa values ranging from $\sim 6 - 18\mu\text{m}$, closely aligning to that identified within this current study. Therefore, reducing the feed powder diameter could aid in reducing the surface roughness lattice structures of small strut thickness.

A less consistent trend is present when evaluating the effects of cell size on the Sa of the samples. However, through disregarding the defective blocked samples 3 and 4, as the cell sizes of the 0.20 and 0.15mm strut thickness samples decrease, a marginal increase in Sa is seen. As this is only a small increase (typically $1 - 2\mu\text{m}$) compared to the pore diameters, it is

unlikely to have any meaningful impact on the flow dynamics of the permeability forced flow experiments. However, this variation could have a more noticeable impact on the rate of rise experiment, reliant on the passive nature of capillary performance of the structures.

Interestingly, both 0.20 and 0.15mm strut thickness sample sets agree well showing noticeably higher S_a values than the 0.30mm equivalents, which may be attributed to the distribution of designed strut thicknesses. Seemingly, for the majority of samples, with the exception of samples 4, 10 and 11, the vertical samples show consistently larger S_a values than their horizontal equivalents. This is due to the vertically orientated samples experiencing greater rates of agglomerated particles, shown in Figure 5-21. Additionally, on the front faces of the samples the vertically printed samples experienced greater amounts of down-skin surfaces, which is widely reported throughout literature to yield rougher surfaces [117].

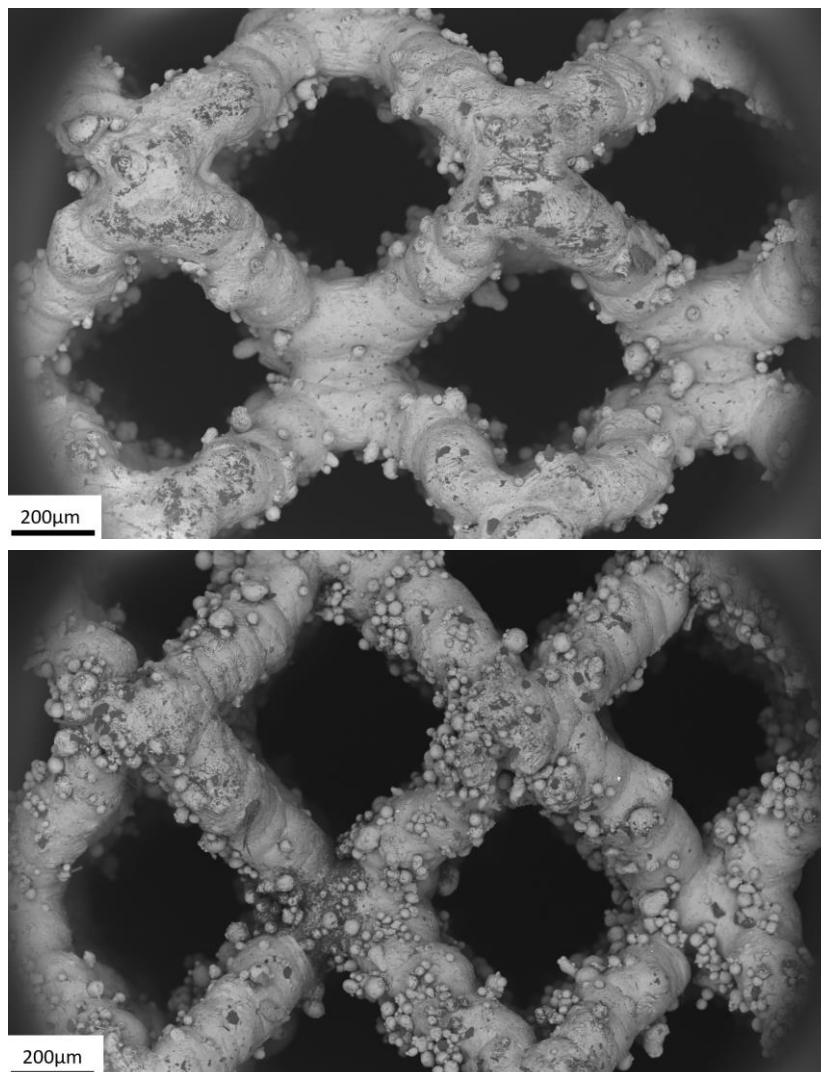


Figure 5-21. SEM Image of sample H6 (Top) and V6 (bottom).

As is further discussed throughout, the extent of agglomerated semi-sintered particles could play an important part on the hydraulic performance of the wicking structures. This may include increasing the overall pressure drop, leading to lower permeability values or possibly acting as micropillars and additional micro flow paths and enhancing the structures capillarity.

5.3.2 Root Mean Square height, Sq

Although Sa is widely used throughout industry to quantify the topological characteristics of surfaces, it does not give an indication of the overall distribution and variation across the surface. Similar to the profile equivalents, Ra and Rq, the arithmetic mean heights of different surfaces can be equal but have drastically different root mean square height values. For this reason, effective analysis of Sq is an essential part in the quantification of these structures. The same methodology was undertaken to determine the Sq values of each sample. Again, no obvious correlation was present between the sample height of the vertical samples, warpage of the horizontal samples and the Sq values, as shown in Figure 5-22.

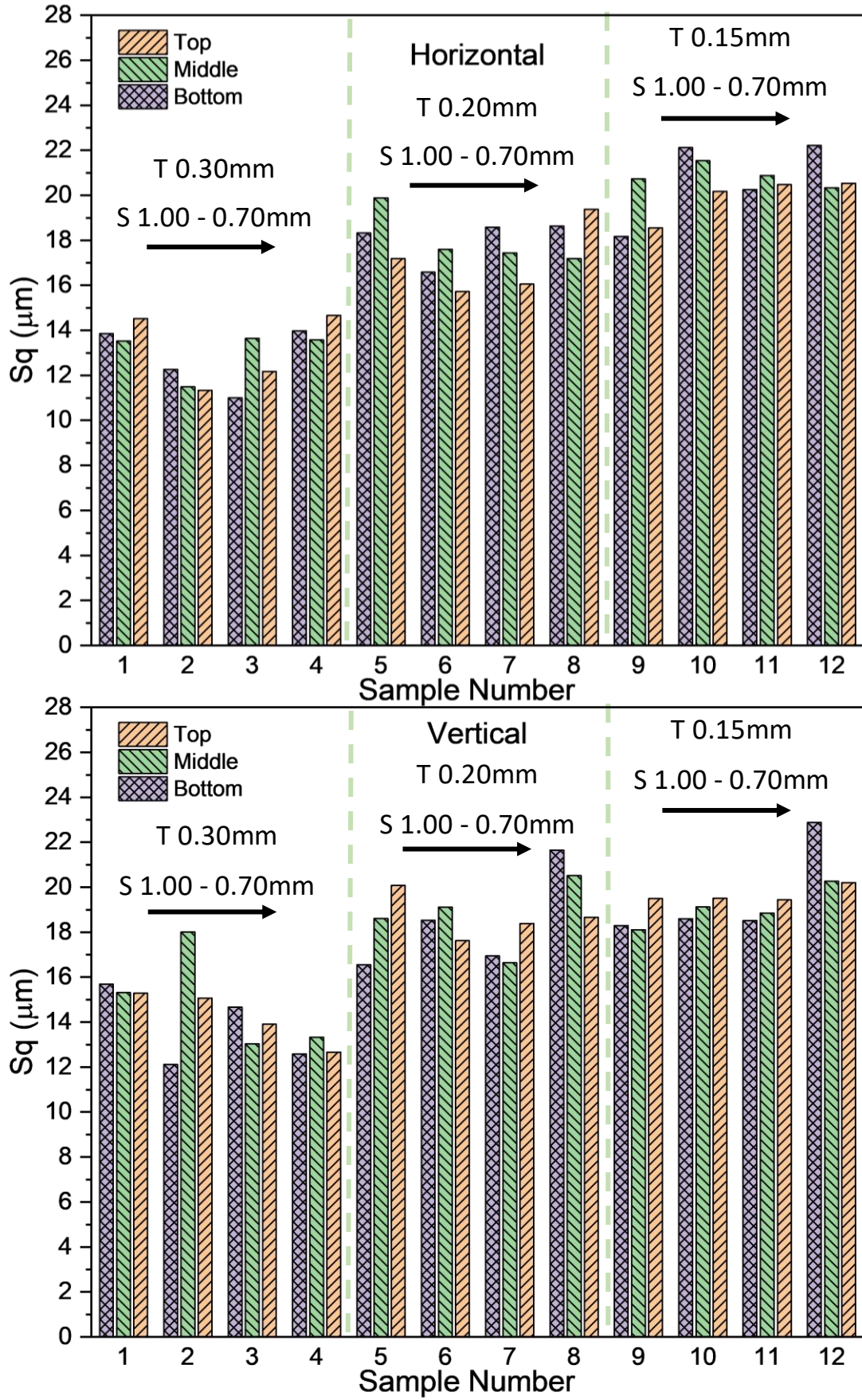


Figure 5-22. Root Mean Square height at the top, middle and bottom locations for both horizontal (top) and vertical (bottom) samples.

The averaged Sq values across the front face in comparison to designed strut thickness and cell size is shown in Figure 5-23.

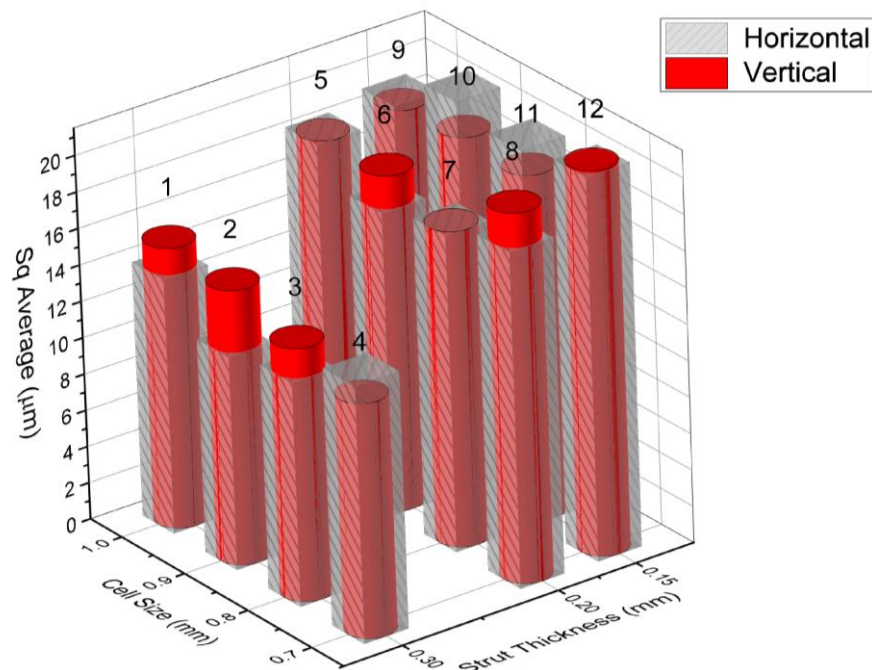


Figure 5-23. Averaged Root Mean Square height, Sq, for both horizontal and vertical samples.

Similar to the relationship of Sa, Sq tends to increase with a decrease in strut thickness with both 0.15 and 0.20mm sample sets being noticeably larger than the 0.30mm counterparts. Again, this may be attributed to the increase in agglomerated particles and ratio of particle diameter to strut diameter exhibited for the lower strut thickness samples. Following the trends previously identified with Sa, cell size is shown to have no consistent trend on the root mean square heights of the samples. When assessing the effects of print orientation, Sq shows a more arbitrary relationship, compared to that of Sa. However, 5 of the vertical samples are noticeably higher than that of the horizontal variants. This is in contrast to only 3 of the horizontal samples showing a visible increase, where the remaining 4 samples show minimal difference. This concludes that the increase in down-skin surfaces of the front face of the vertical sample contributes to a higher deviantisation (Sq) of the surface heights as well as the overall mean height (Sa).

5.3.3 Maximum Peak Heights, Sp

Through evaluation of the maximum peak heights, Sp, across the three recorded measurements, no clear relationship is present between the sampling locations, as shown in Figure 5-24.

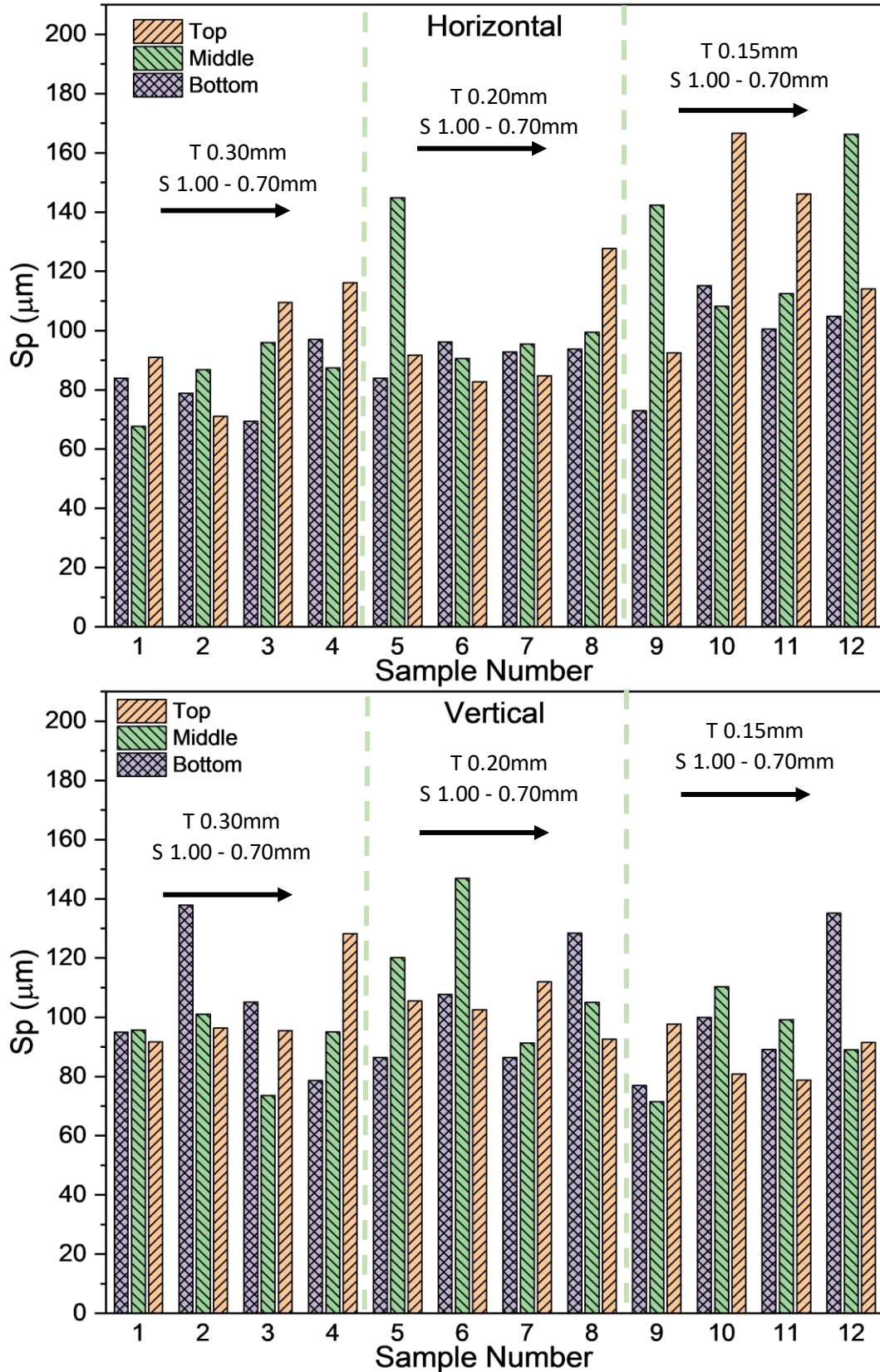


Figure 5-24. Maximum Peak height at the top, middle and bottom locations for both horizontal (top) and vertical (bottom) samples.

Differing to that seen previously, both the maximum peak and valley measurements are single point measurements, compared to the surface integrated values discussed for Sa and Sq. Seemingly, the deviation between the maximum and minimum Sp measurement across all three location is visibly larger than previously discussed for Sa and Sq. This is particularly prevalent for the horizontal samples, especially the 0.15mm strut thickness varieties (Samples 9 – 12), as shown in Figure 5-25.

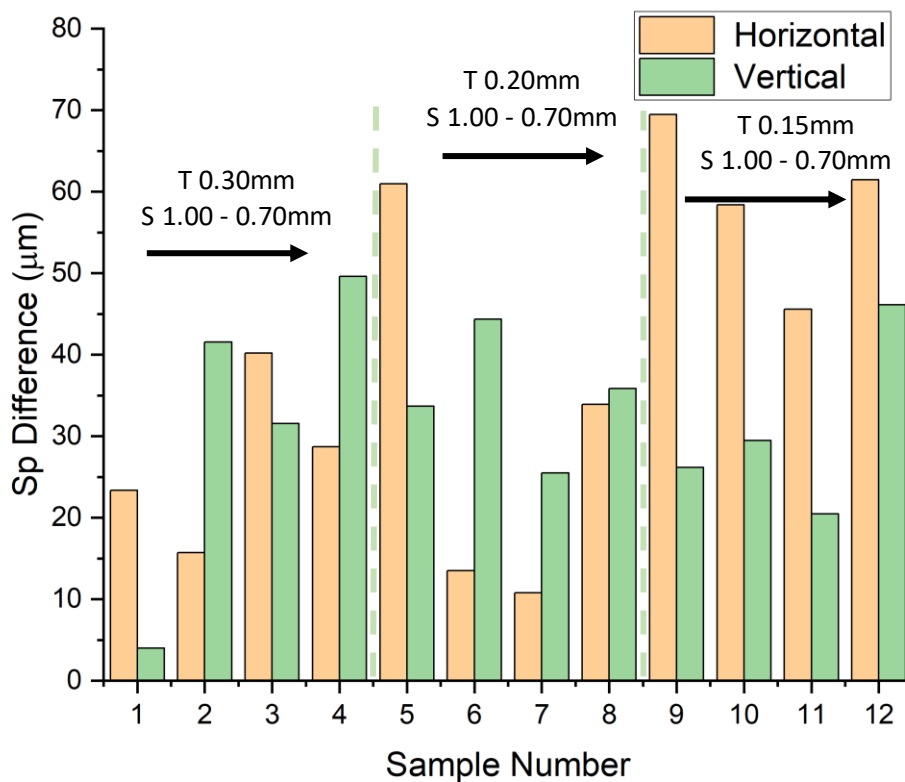


Figure 5-25. Maximum peak height difference.

This correlates with the increased visible cell dislocation and defects on these horizontal samples. The averaged Sp values for each sample are shown in Figure 5-26. Here, it can be noted that the horizontal samples of the 0.15mm strut thickness variants have a consistently larger maximum peak height, compared to the vertical samples. A less consistent trend is present for the 0.20 and 0.30mm strut thickness samples.

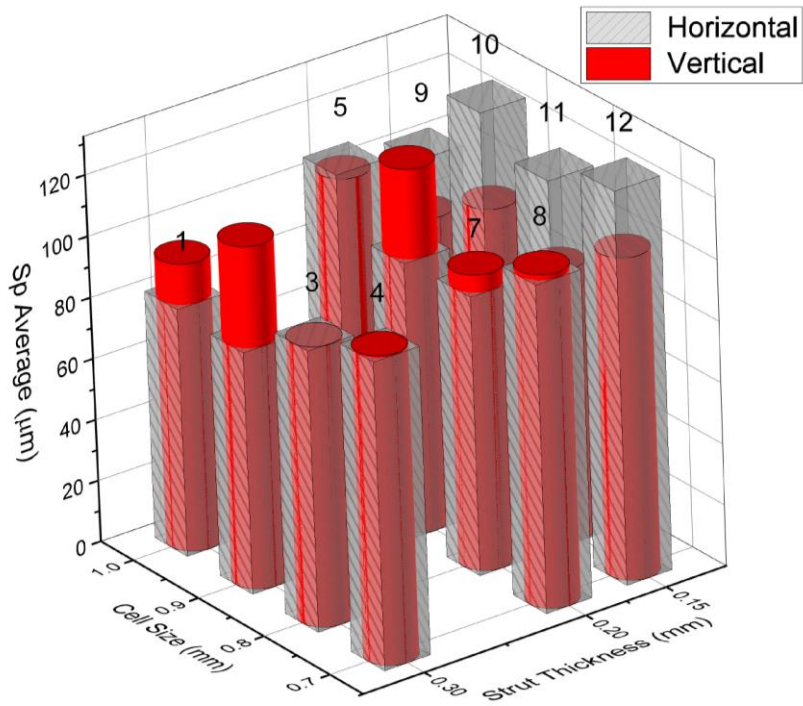


Figure 5-26. Maximum Peak height, S_p , for both horizontal and vertical samples.

5.3.4 Maximum Valley Heights, S_v

Contrary to the higher S_p values exhibited on the 0.15mm horizontal samples, the maximum valley heights for the horizontal samples is shown to be more stochastic with noticeably large face differences for samples 1 and 2 in the horizontal orientation, shown in Figure 5-27 and Figure 5-28.

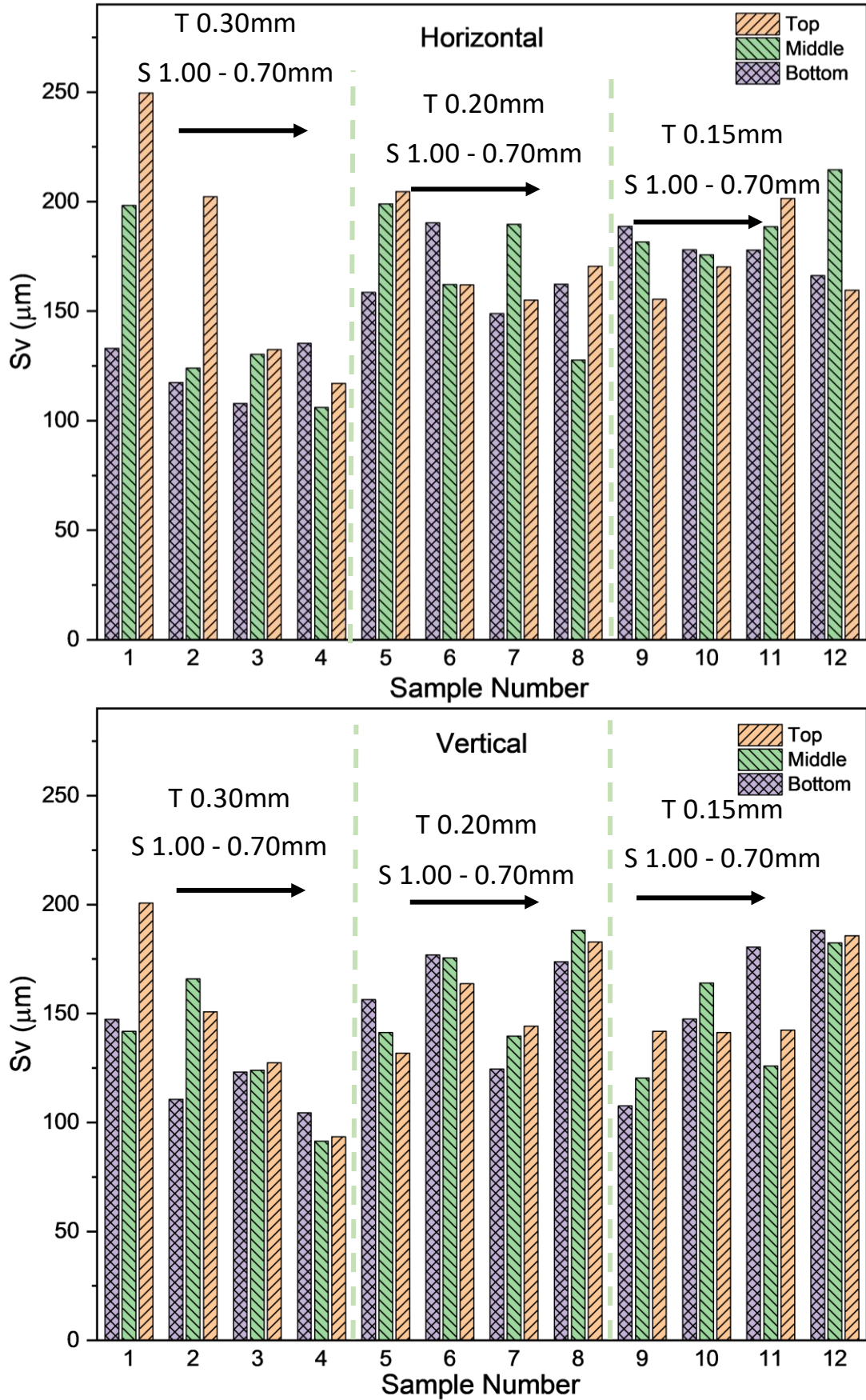


Figure 5-27. Maximum Valley height at the top, middle and bottom locations for both horizontal (top) and vertical (bottom) samples.

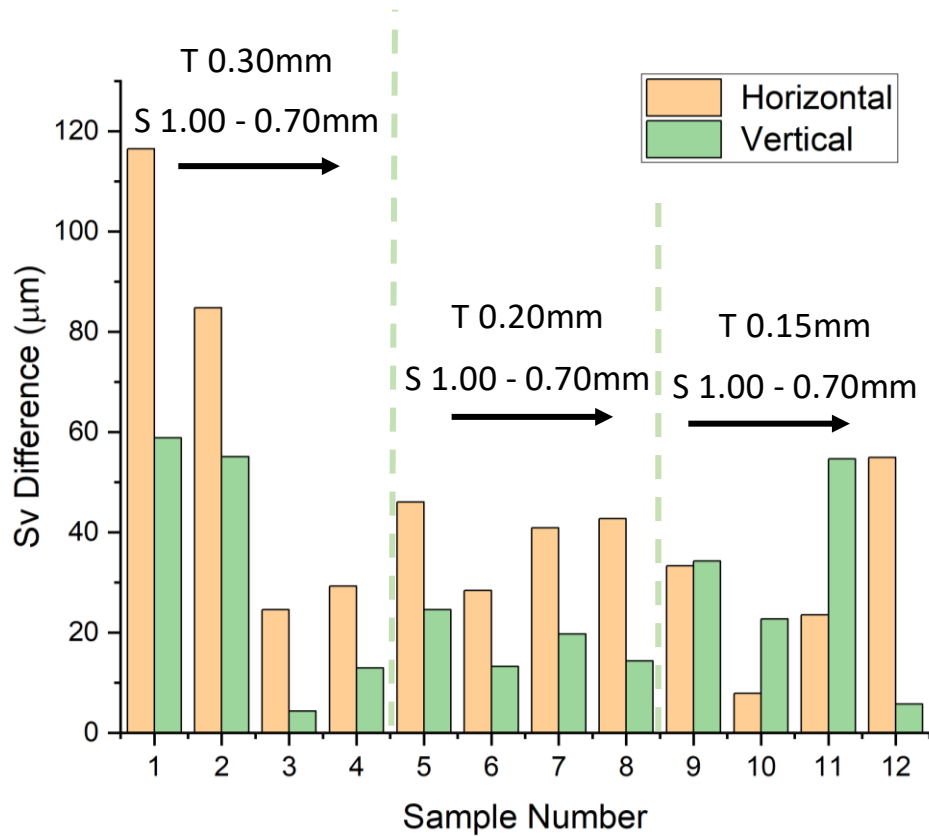


Figure 5-28. Maximum valley height difference between measurement locations.

For the majority of samples, the horizontal variants show a consistently larger maximum difference between sample measurement location compared to their vertical counterparts. This may be a result of the increased rate of dislocated struts and damaged cells exhibited. The averaged maximum valley height across the front face for each sample is shown in Figure 5-29.

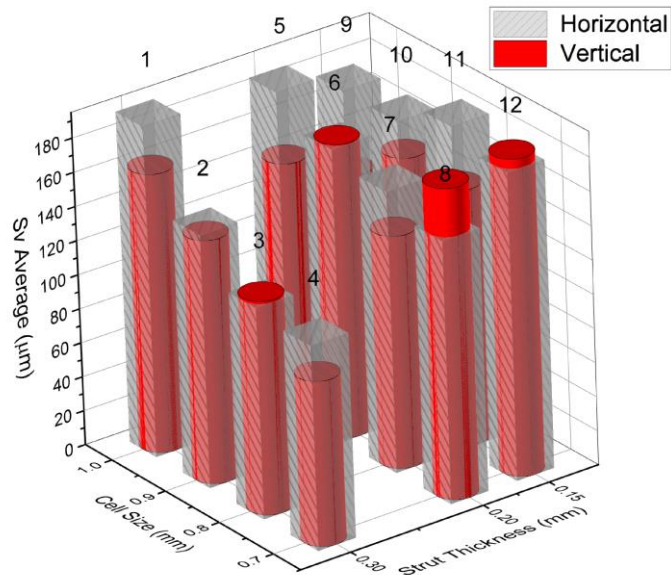


Figure 5-29. Averaged maximum valley height, S_v , for both horizontal and vertical samples.

5.3.5 Maximum Height, S_z

The maximum height, which equates to the sum of the maximum peak and maximum valley heights, can be accounted for in accordance with Equation (3-8). Again, the distribution of measurements across the front face of the samples has been evaluated and shown in Figure 5-30. Similar to the previously analysed height parameters, no clear trend in measurement location is present for either horizontal or vertical samples. However, the horizontal samples exhibited a visibly larger difference between the measuring locations, as shown in Figure 5-31.

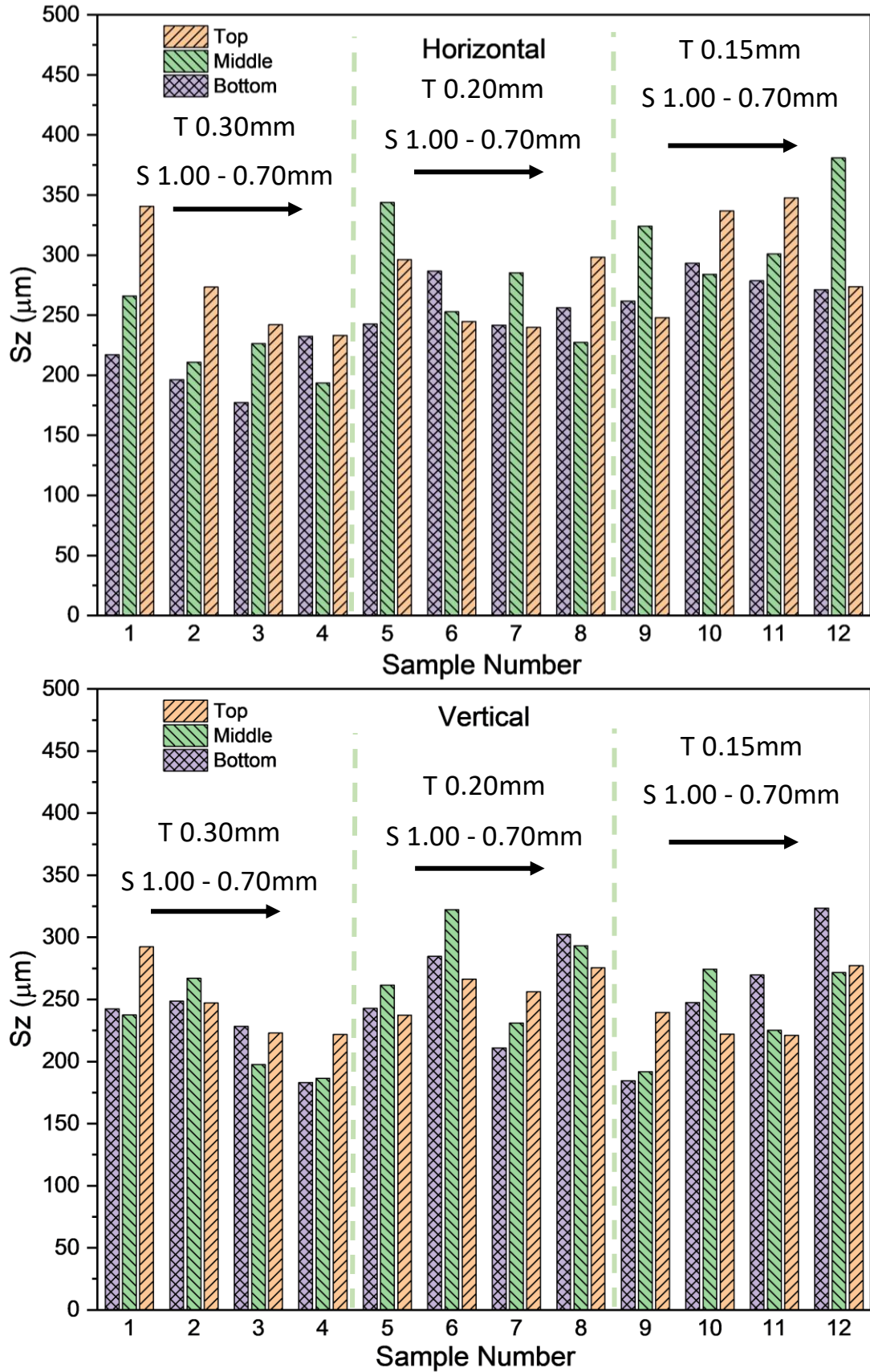


Figure 5-30. Maximum height at the top, middle and bottom locations for both horizontal (top) and vertical (bottom) samples.

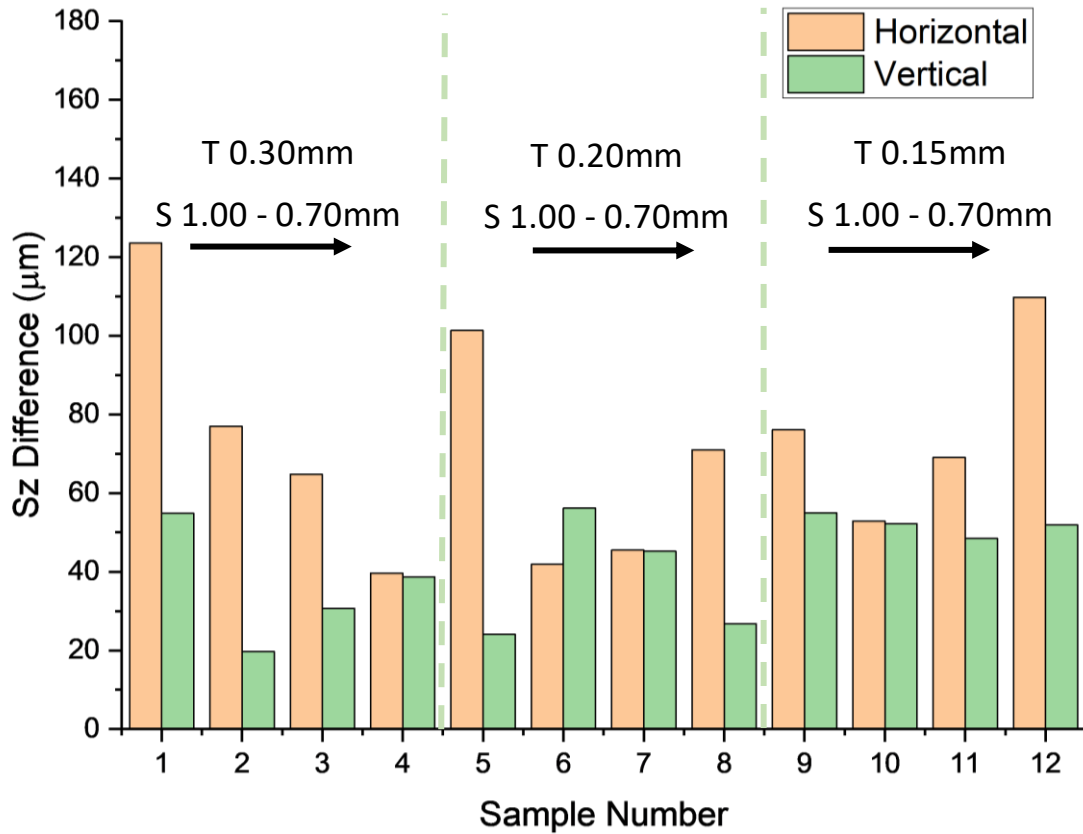


Figure 5-31. Maximum height difference between measurement locations.

The impact of sample location and print orientation can be clearly seen in Figure 5-31 with the horizontal samples showing a maximum difference of 123.61µm, with its vertical equivalent only showing a difference of 54.88µm. The 0.15mm strut thickness vertical samples exhibited relatively steady maximum difference between the measurement locations of around 50µm. The averaged maximum height across the front face of each sample has been shown in Figure 5-32.

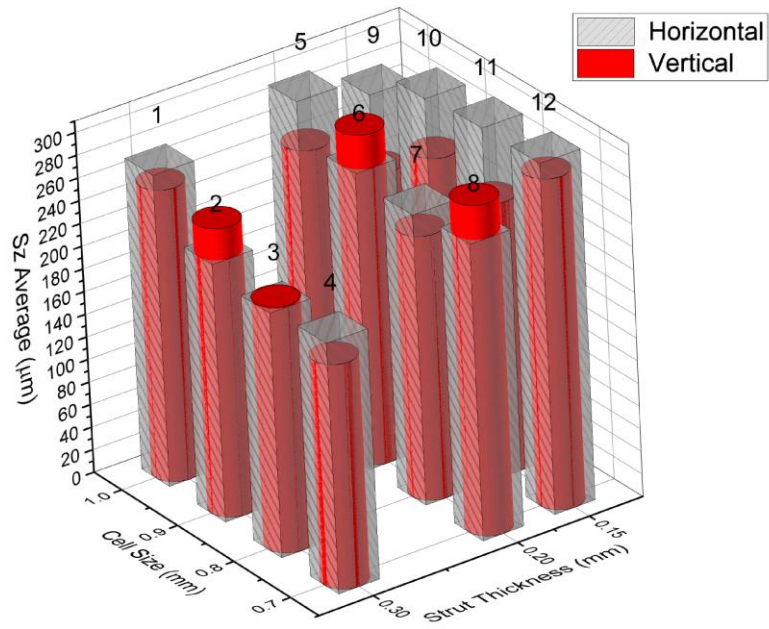


Figure 5-32. Maximum height, S_z , for both horizontal and vertical samples.

5.3.6 Comparison of Horizontal Faces

Printing orientation can have a significant effect on the measured surface roughness of the structures. As a select few samples were chosen for chemical polishing, the rest were used for more detailed raw analysis. The comparison between the front and side faces of these horizontal raw samples in addition to the front face of the vertical samples is shown in Figure 5-33.

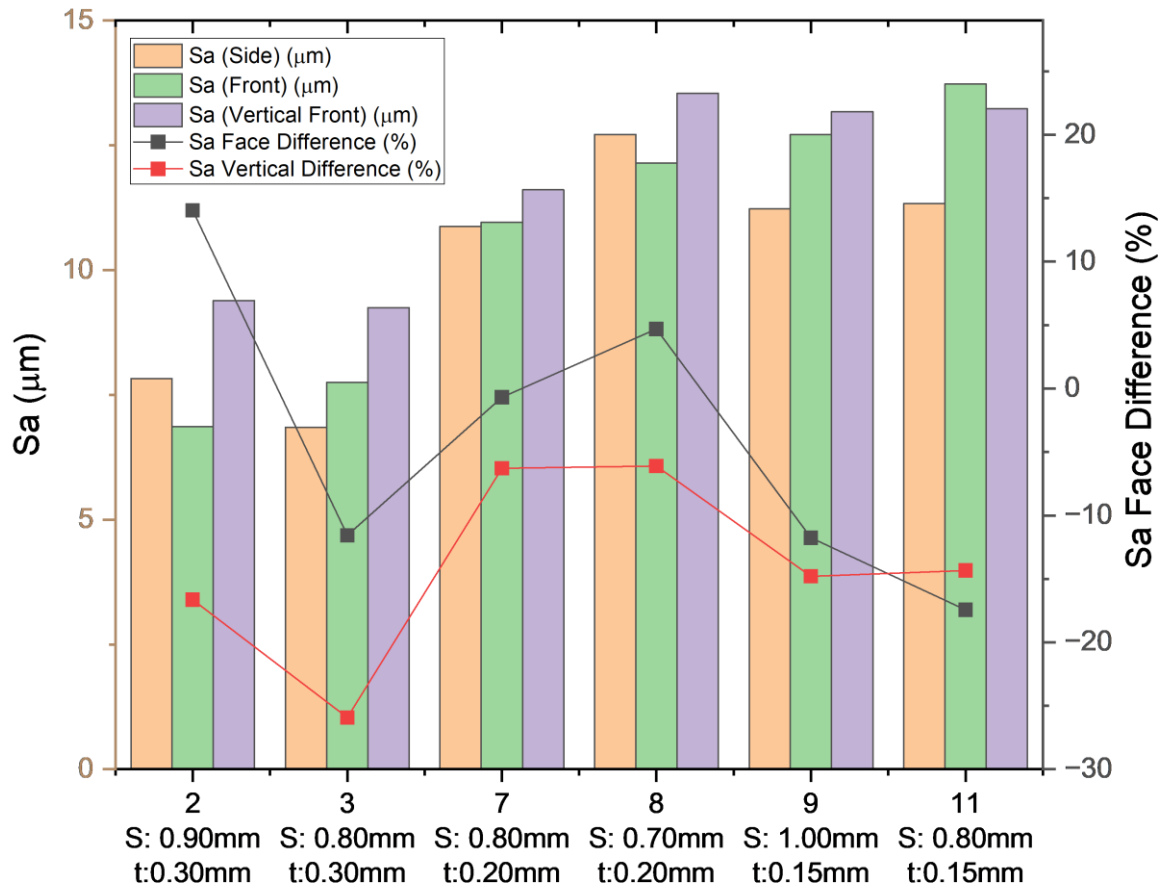


Figure 5-33. Comparison between averaged arithmetic mean surface roughness of side and front faces of horizontal samples and the front face of the vertical samples.

Interestingly, varying results were seen with only samples H2 and H8 showing larger surface roughness on the vertically orientated side faces. This corresponds to the increase in down-skin surfaces on the faces aligning with the vertical z-axis of the build. The remainder of the analysed samples showed lower Sa values on the side faces, contrary to expectations. Despite the varying results, all analysed samples still showed Sa values noticeably lower than their vertical counterparts. This draws to the further conclusion that the heat dissipation within the sample plays a key part in the number of agglomerated particles, and hence Sa measurements. As the vertical samples have a significantly reduced cross sectional surface

area in the XY build plane, they would tend to experience less efficient heat dissipation, leading to localised overheating beyond the laser spot. Furthermore, as the build goes beyond the final layer of the horizontal samples, cooling time between layers is significantly reduced and leads to further heat accumulation. This in turn allows the unmelted powder particles to partially sinter to the strut surfaces. Furthermore, the consideration of heat accumulation and dissipation plays an important part in rationalising the increased rates of partially sintered particles on the lower strut thickness samples. This can be further quantified with consideration of the root mean square parameter, Sq, as shown in Figure 5-34.

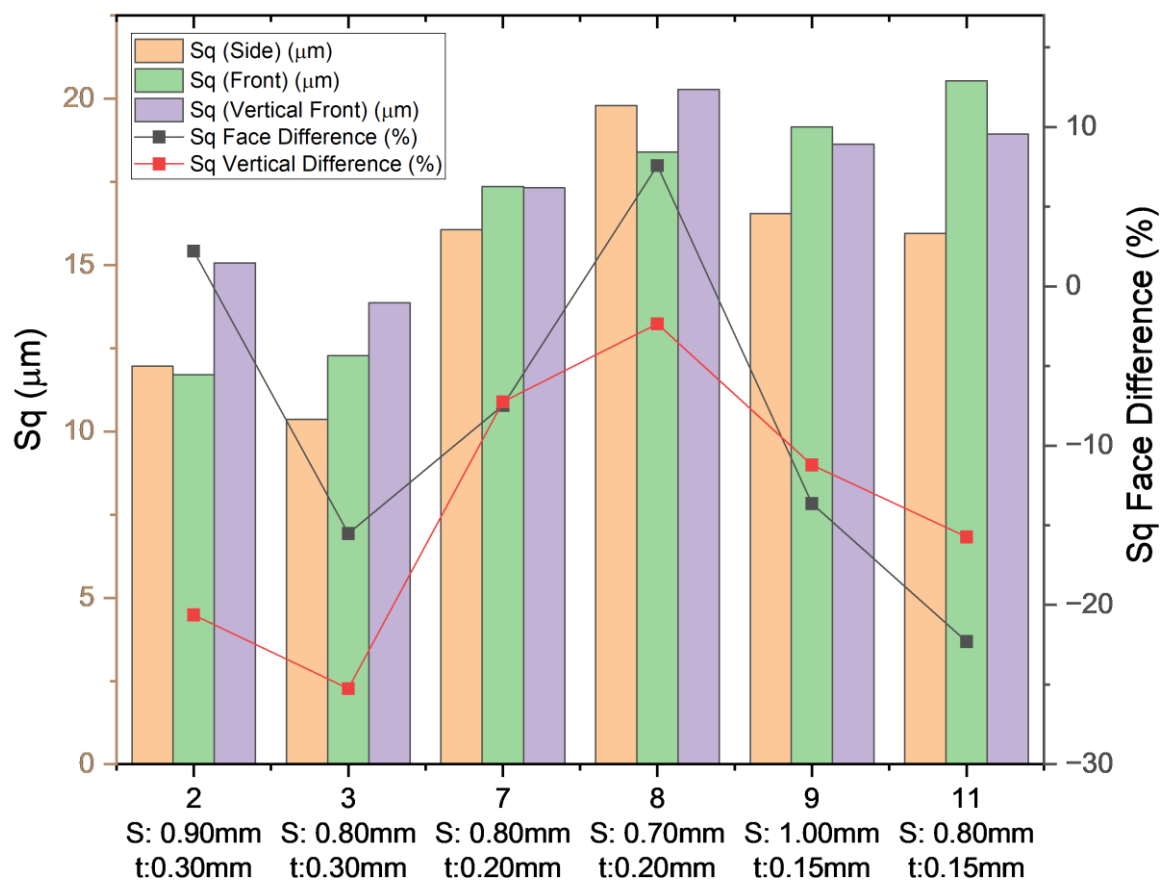


Figure 5-34. Comparison between root mean square height of side and front faces of horizontal samples and the front face of the vertical samples.

As was the case for Sa, only samples H2 and H8 showed larger Sq values on the vertically orientated side faces. Again, this contradicts expectations resulting from the small layer height used for the build file which minimises the staircase effect in the z-axis (previously illustrated in Figure 3-5) and laser scanning strategy optimised well for minimising surface roughness. Furthermore, the identified warpage on the horizontal samples could contribute

to the general higher measured surface roughness on their front faces through resulting in increased rates of micro-deformities. As the top surface of the vertical samples align with the XY build plane, similar trends may also be found. However, such analysis was not possible without sectioning the samples due to the limited z-movement of the Sensoscan profilometer. This falls beyond the scope of this current study but does show potential for future research.

5.3.7 Surface Roughness Summary

The consistent trend between the various roughness height parameters and strut thicknesses along with the less noticeable trends when considering cell sizes may be associated with the following identifiable factors:

1. As the strut thickness is decreased, the dimensional ratio between the roughness features (agglomerated particle diameter) and strut is increased.
2. An increased number of agglomerated particles on the lower strut thickness samples, resulting from increased heat accumulation.
3. The selected build file parameters were tailored to the designed strut thickness, allowing for variations between samples of varying strut diameters.

Generally, the Sa and Sq parameters are higher for the vertical samples with maximum values of 14.46 μm and 21.12 μm , respectively identified on sample V12. This is caused by the less efficient heat dissipation due to their reduced XY cross sectional area and cooling time between layers, compared to the horizontal samples. This allows the powder particles to partially sinter to the struts surface adding to the irregularities and various roughness parameters.

Through further analysis of the side faces of the horizontal samples, aligning with the z-axis of the build, no congruent relationship was identified. Here, only samples H2 and H8 experienced higher surface roughness values on the vertically orientated side faces. Through minimising the variation between faces, the efficacy of the set parameters within the build file with respect to surface roughness is highlighted. Nonetheless, all side faces of the horizontal samples were still noticeably smaller than the analysed vertical samples.

As discussed, Sp, Sv and Sz are all single points measurements across the measured area. Contrary to expectations, all three parameters showed no consistent trend with varying cell size as the depth of scan is altered. These parameters have therefore shown to be less applicable to irregular geometries, such as that of the lattice structures analysed in this study.

5.4 Porosity Analysis

As described in Section 3.3, both apparent and true porosity measurements were taken using the density and Archimedes' methods. Both porosities were measured three times and the average calculated, as shown in Table 5-2. The percentage variation of both apparent and true porosities was calculated with Equation (3-18).

$$\% \text{ Variation} = \left(\frac{\text{Max. Value} - \text{Min. Value}}{\text{Mean Value}} \right) \times 100 \quad (5-2)$$

Table 5-2. Results of experimentally derived apparent and true porosity values for both Horizontal and Vertical samples with the determined percentage variations.

Lattice Sample	Horizontal				Vertical			
	App. Por.	App. % Var.	True Por.	True % Var.	App. Por.	App. % var.	True Por.	True % Var.
(1) S1.00 T0.30	0.5229	0.1592	0.5207	0.5528	0.5510	0.1783	0.5485	0.3817
(2) S0.90 T0.30	0.4405	0.1889	0.4368	1.8610	0.4624	0.0468	0.4602	0.9963
(3) S0.80 T0.30	0.3304	0.5037	0.3231	1.6198	0.3454	0.2530	0.3370	2.3298
(4) S0.70 T0.30	0.2267	0.3672	0.2150	4.0917	0.1979	0.7781	0.1430	19.7376
(5) S1.00 T0.20	0.8087	0.0000	0.8082	0.2009	0.8561	0.0107	0.8495	0.0522
(6) S0.90 T0.20	0.7705	0.0000	0.7659	0.5262	0.8236	0.0404	0.8189	0.3504
(7) S0.80 T0.20	0.7005	0.0000	0.6967	0.9898	0.7470	0.0635	0.7434	0.2446
(8) S0.70 T0.20	0.6326	0.1316	0.6291	0.9235	0.6829	0.0890	0.6812	0.3256
(9) S1.00 T0.15	0.8728	0.1907	0.8707	0.6027	0.9185	0.0254	0.9116	0.0844
(10) S0.90 T0.15	0.8501	0.0979	0.8469	0.9497	0.8898	0.0935	0.8831	0.2457
(11) S0.80 T0.15	0.8040	0.1035	0.8007	1.0127	0.8403	0.0287	0.8351	0.5993
(12) S0.70 T0.15	0.7613	0.2187	0.7606	0.2559	0.7922	0.0452	0.7898	0.4561

5.4.1 Apparent Porosity

The apparent porosity considers both main pore space and defective internal closed porosities, with the results for both horizontal and vertical samples shown in Figure 5-35.

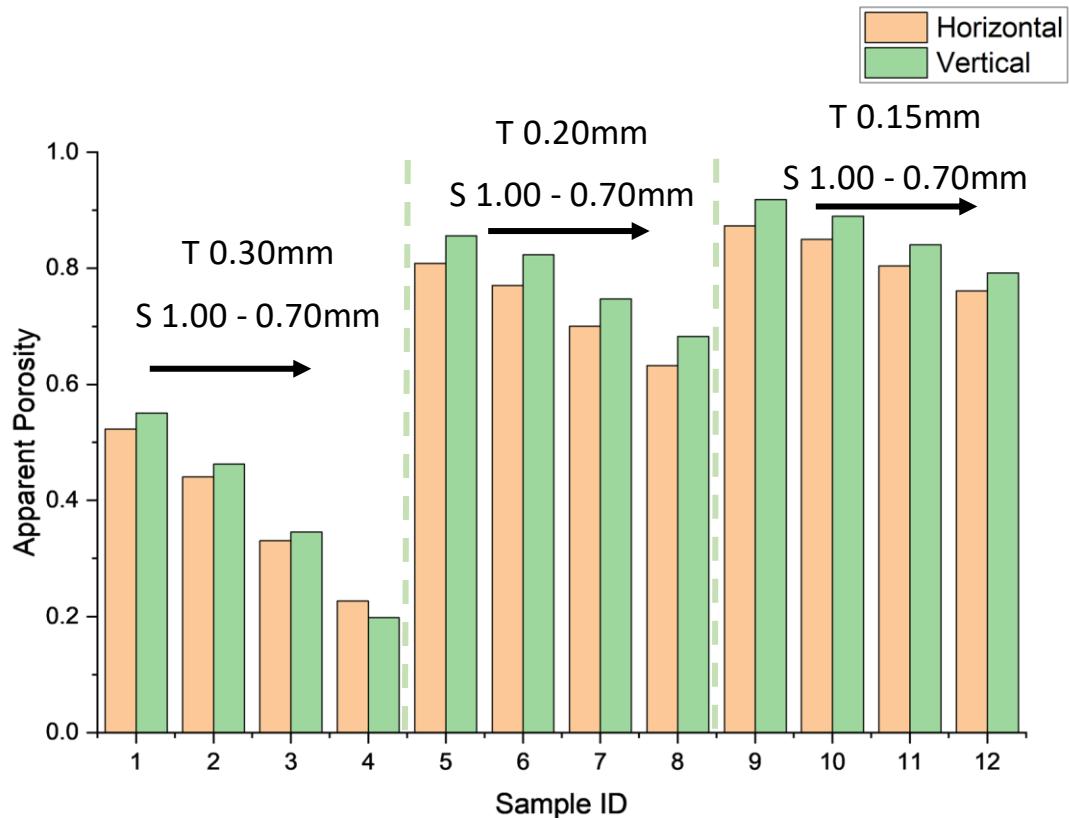


Figure 5-35. Apparent porosities for both horizontal and vertical sample sets.

Here, it is clear that the vertical samples show consistently higher porosity, apart from sample set 4, which has previously been shown to be problematic with no visible line of sight through the sample and further deviation from general trends. As expected, the apparent porosity is shown to increase with a decrease in both designed strut thickness and unit cell size, as further visualised in Figure 5-36. Due to the relatively small difference between the manufactured strut thicknesses of the 0.15mm and 0.20mm samples, previously shown in Figure 5-7, the resultant apparent porosity difference between their equivalent cell size is marginal. This differed to the large increase in porosity seen between the 0.30mm and 0.20mm strut thickness samples.

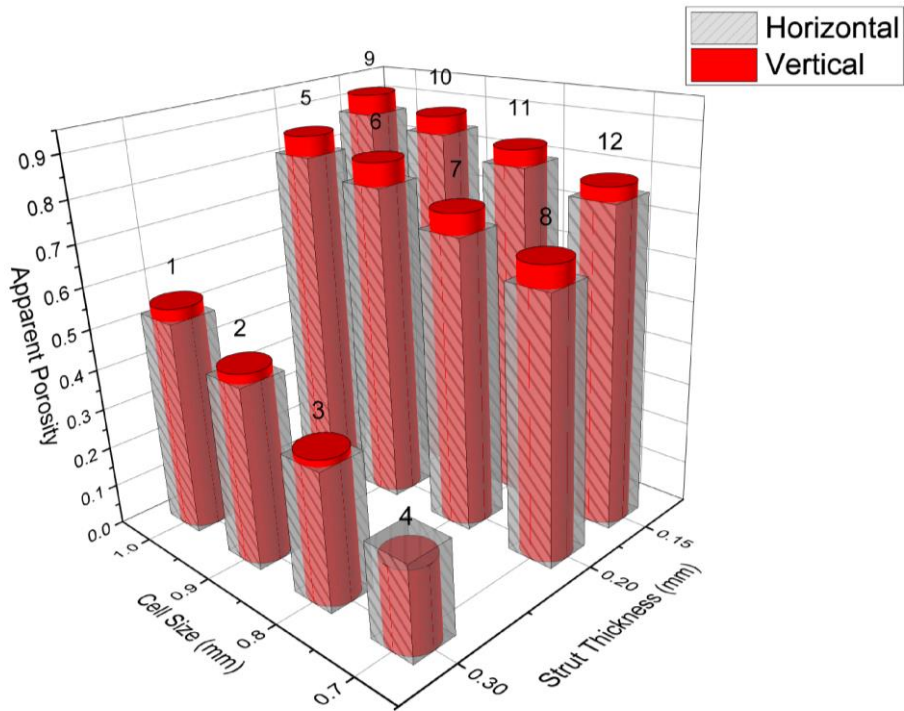


Figure 5-36. 3D plot for apparent porosities of both horizontal and vertical samples.

5.4.2 True Porosity

As discussed, the true porosity measurements only consider the main pore space, infiltrated by the wetting fluid and determined utilising Archimedes' method, with results shown in Figure 5-37.

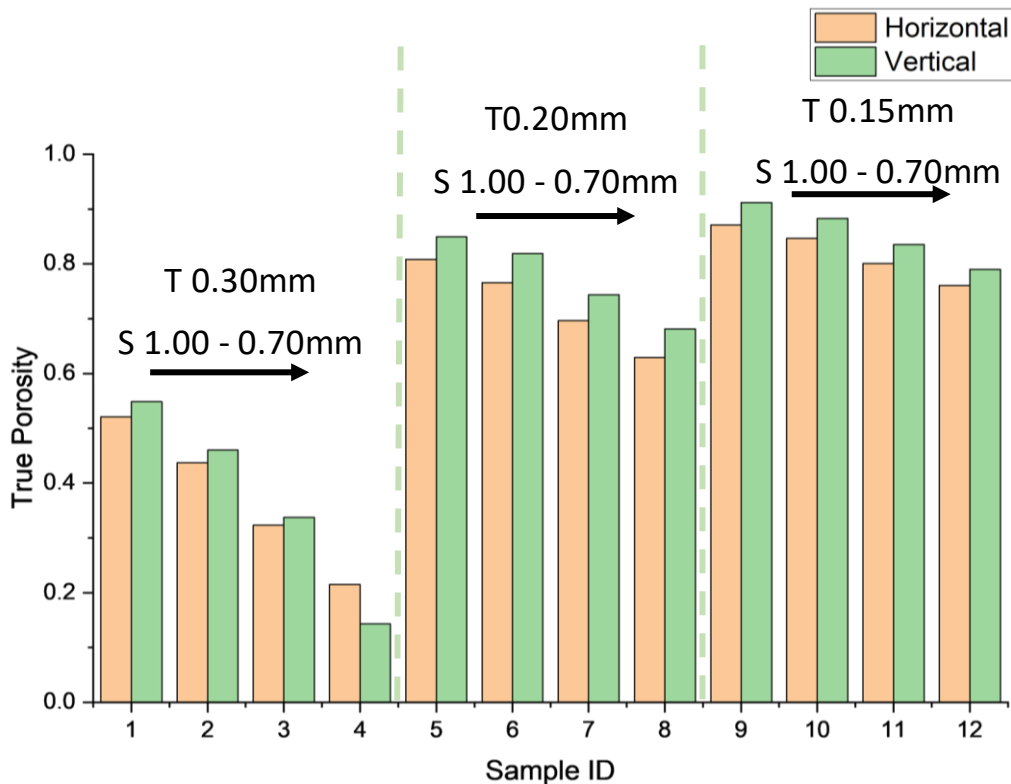


Figure 5-37. True porosities for both horizontal and vertical sample sets.

Evidently, the general trends are comparable to that depicted for the apparent porosities, shown in Figure 5-35. For enhanced visual comparison, the true porosities have been plotted in a 3D chart shown in Figure 5-38.

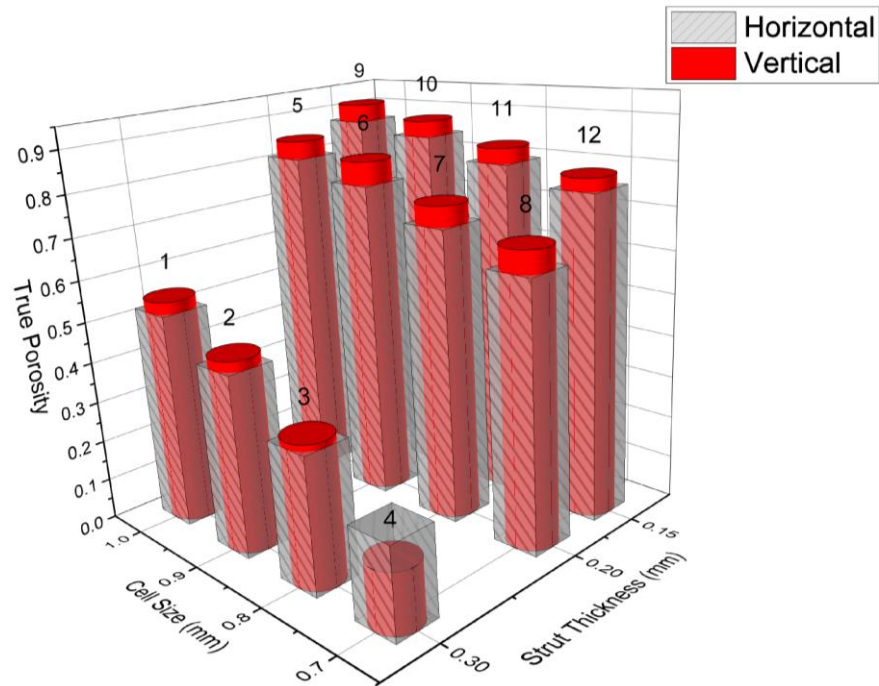


Figure 5-38. 3D plot for true porosity comparison.

Noticeably, the vertical sample of geometry set 4 has a significantly lower true porosity value of 0.143 compared to its apparent porosity value of 0.198. This indicates an increase in trapped porosity.

5.4.2.1 Design Deviation

Achieving porosity values representative of the intended CAD design is essential in the effective design of any heat transfer, fluid dynamic or mechanical based system. Here, the true porosity may be compared to that of the intended design with no porosity defects or irregularities. The designed porosity values were extracted directly from the CAD designs, with each sample's deviation and percentage deviation recorded in Figure 5-39 and Figure 5-40, respectively.

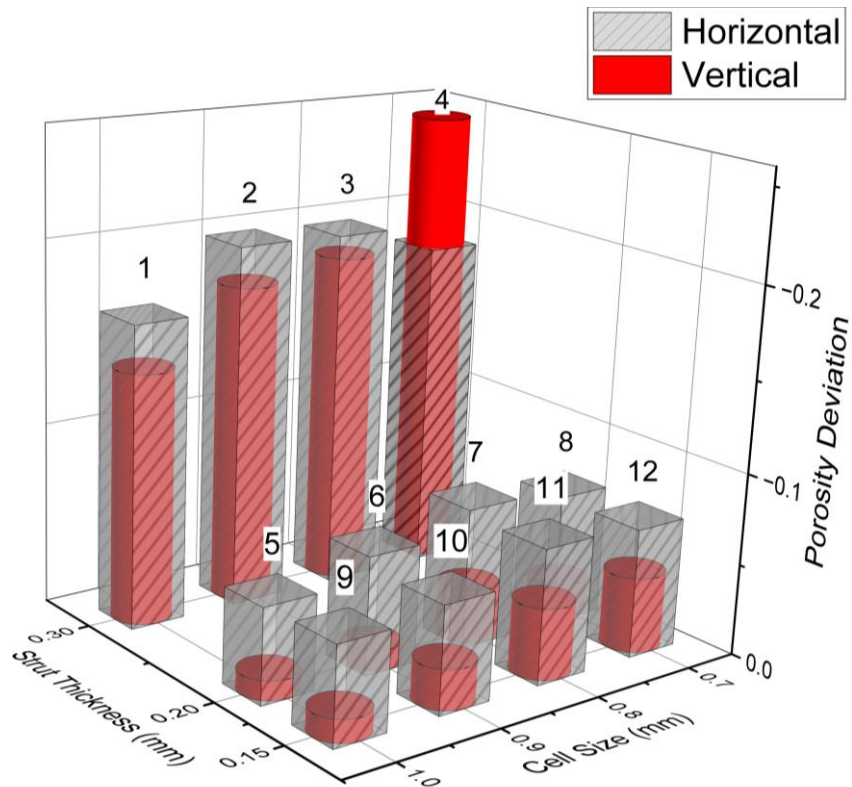


Figure 5-39. 3D plot for porosity deviation from CAD.

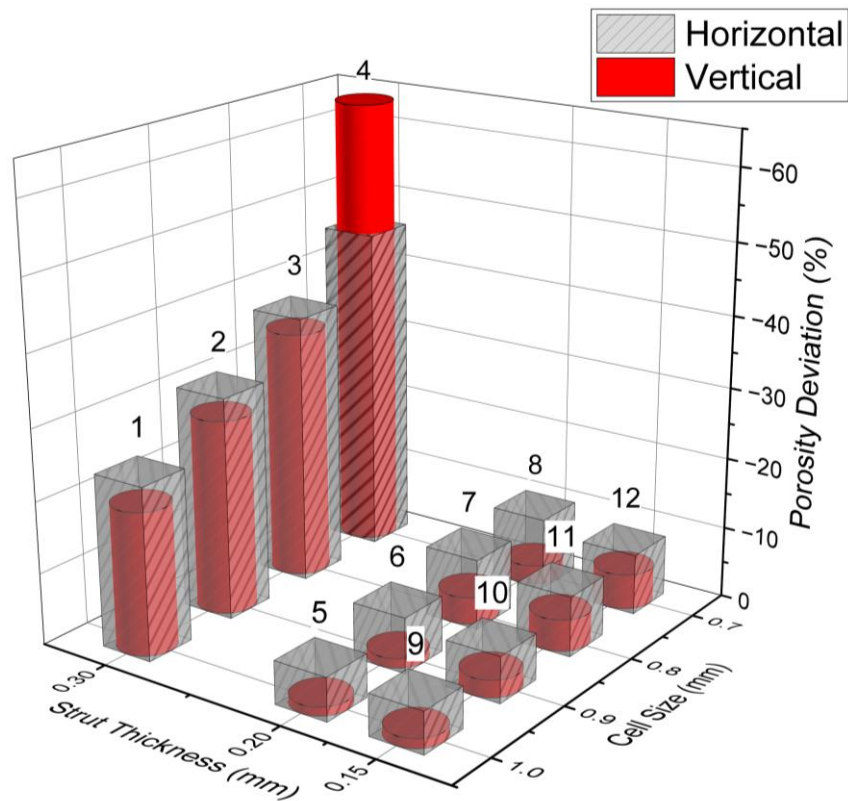


Figure 5-40. 3D plot for porosity percentage deviation from CAD.

Clearly, all samples experienced porosity values less than intended, with the horizontal samples overall showing greater deviation than the vertical counterparts, with the exception

of sample set 4. This deviation from the designed porosities may be attributed to the strut sizes being larger and resultant pores being significantly smaller than intended, previously shown in Figure 5-8 and Figure 5-17, respectively. A clear discrepancy is present for the 0.30mm strut thickness samples showing significantly larger deviations of between -20.04% and -63.97%, compared to both 0.15mm and 0.20 strut diameter sample sets which have maximum deviations of -10.12% and -4.96% with average deviations of -7.85% and -2.78% for the horizontal and vertical samples, respectively. Noticeably, the deviation is found to increase with both increased designed strut thickness and decreased unit cell size. The inconsistency of the 0.30mm samples, especially samples 3 and 4, further indicates the incompatibility of the large strut thicknesses and smaller unit cell sizes.

5.5 XCT Analysis

As previously discussed, XCT analysis has proven to be essential in evaluating internal structures, validating feature characteristics and identifying any internal defects that would otherwise be overlooked with traditional analysis techniques. As discussed, half of the printed samples were analysed with XCT and scanned in four sets of three:

1. V1_H1_V4
2. H4_H5_V5
3. V6_H6_H10
4. V10_V12_H12

A field of view of 28.31x28.31x28.31mm with a voxel resolution of 13.986 μ m was achieved, and analysed within the Dragonfly Software [137], as shown in Figure 5-41.

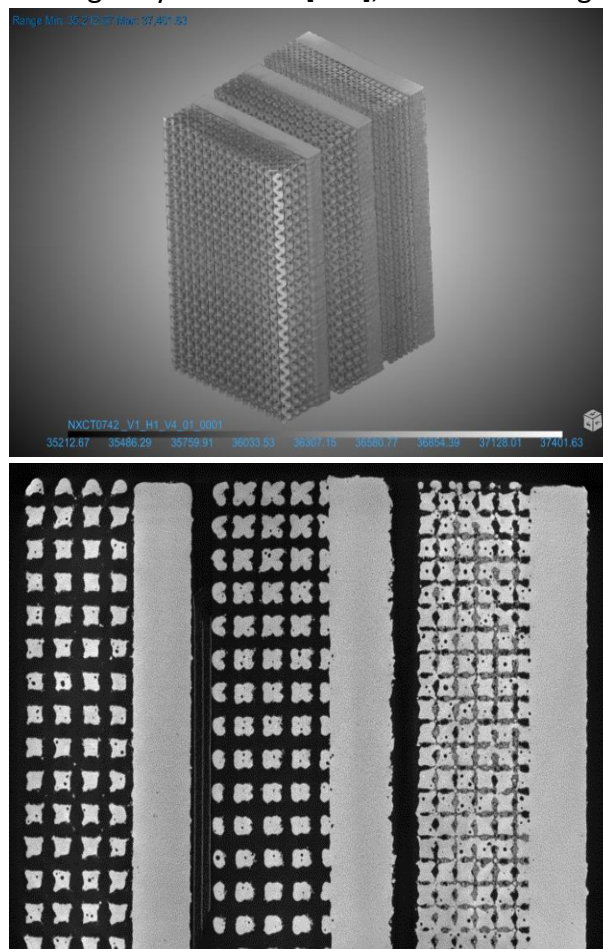


Figure 5-41. 3d reconstruction (top) and sliced example(bottom) of samples V1, H1 and V4 (left – right).

The lower and upper Otsu segmentation boundaries, shown in Section 3.4.3, was found to be effective for most samples. However, the presence of blocked internal powder in Sample V4, as seen in the sliced image of Figure 5-41, required an alternative technique for effective quantification. As seen in the histogram shown in Figure 5-42, three distinct peaks are present, identifying the solid and porous regions, in addition to the additional blocked powder.

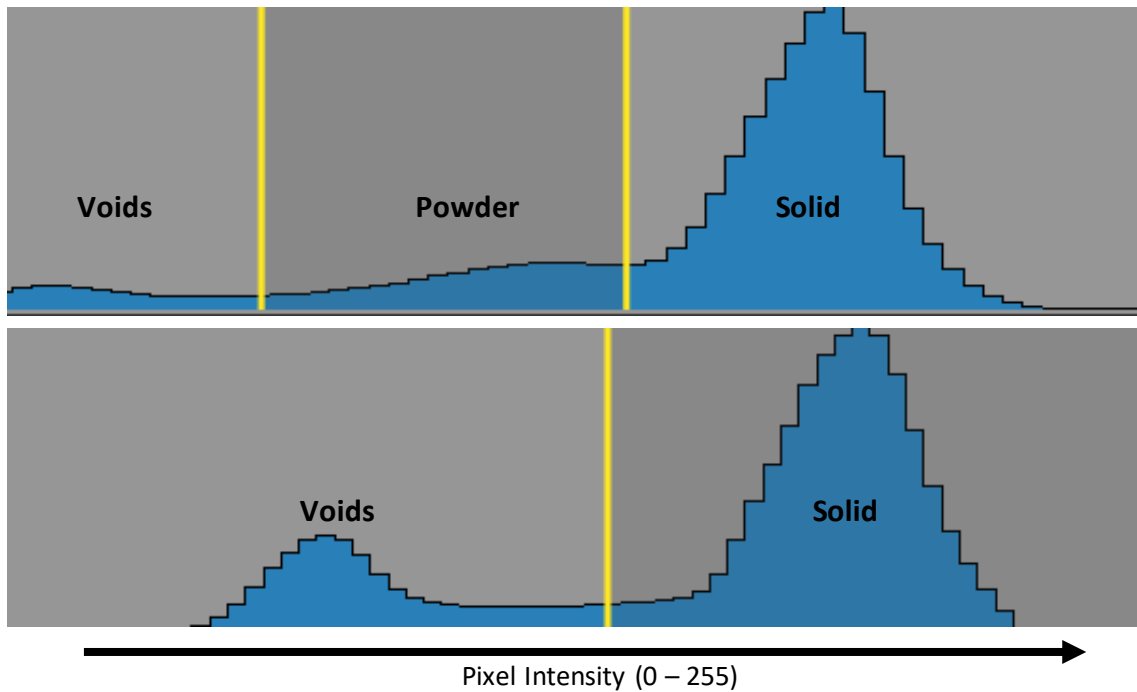


Figure 5-42. Histogram of sample V4 (top) and H4 (bottom).

This contrasts the two distinct peaks presented for all other samples where through thorough visual inspection, Otsu's method was shown to hold true for effective segmentation. Therefore, for the vertical orientation of sample 4, manual segmentation was utilised separating these three distinct regions, with thresholding values shown in Table 5-3 and segmented image in Figure 5-43.

Table 5-3. Segmentation thresholds for sample V4.

Solid	35979.03 – 46166.00
Voids	35079.03 – 35979.03
Powder	33,922.00 - 35079.03

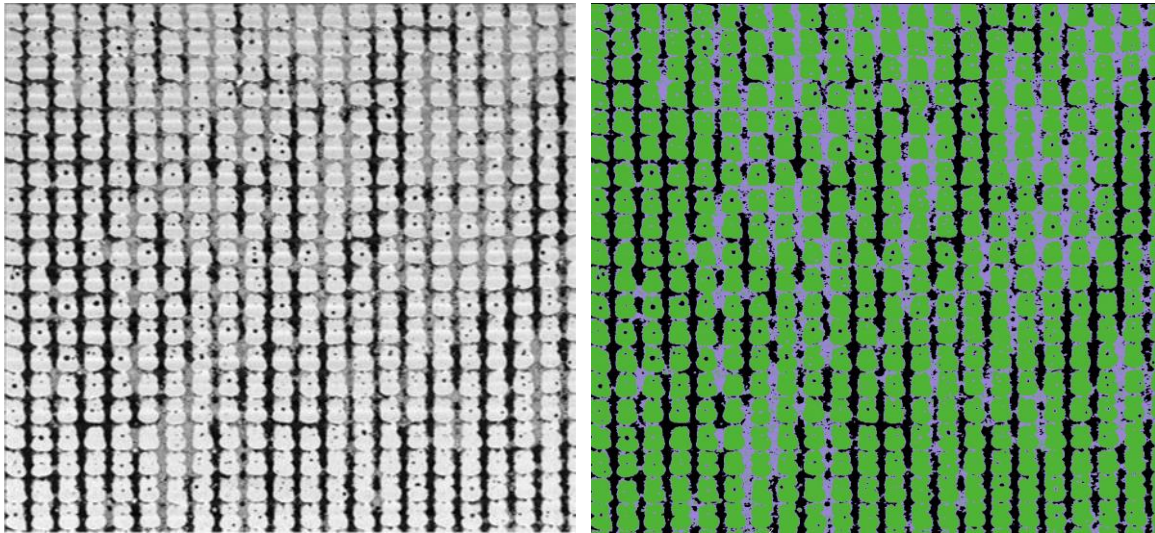


Figure 5-43. Grayscale image (left) and segmented image (right) for sample V4.

Although, this proved successful in terms of image segmentation, further analysis, especially porosity and pore analysis of the sample, proved difficult and unreliable due to the lack of interconnecting pores and overall irregularities throughout. It should be noted that the makeup of the trapped powder is a mixture of solid powder and micro/nano pores. To further analyse this, a higher resolution scan, and hence smaller field of view, would be required. With the 10 largest interconnecting pores shown in Figure 5-44, clearly fluid flow would be heavily affected by the associated defects.

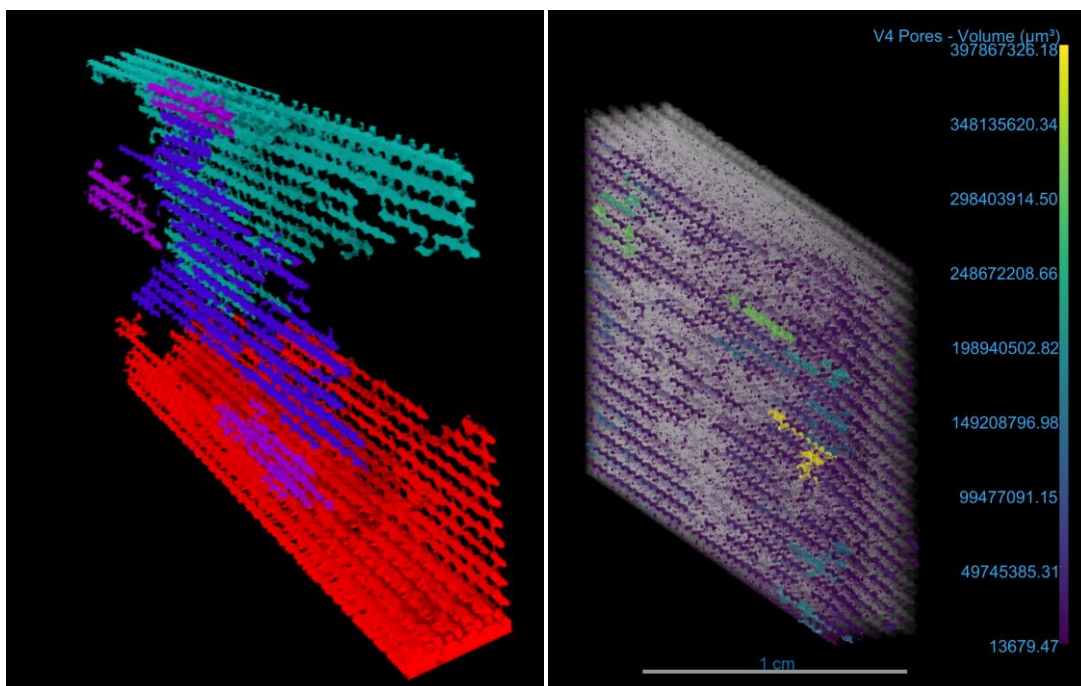


Figure 5-44. 10 largest pores (left) and remaining smaller non-interconnecting pores (right) for sample V4.

Evidently, all 10 of the largest pores identified in Figure 5-44 are the surface channels concentrated around external and mating faces. As can be seen, the overall pore volume for sample V4 is extremely small with an average volume of $0.2421\text{mm}^3 \pm 0.1279\text{mm}^3$. This large standard deviation further indicates the inconsistencies and poor manufacturability of sample V4. Although this value equates to a pore radius of $\sim 0.387\text{mm}$, assuming a perfectly spherical pore, their non-interconnecting characteristics prove ineffective for capillary flow and heat pipe applications. All remaining samples resulted in one singular interconnected main which could easily be separated from the remaining defective pores within the struts, as shown in Figure 5-45.

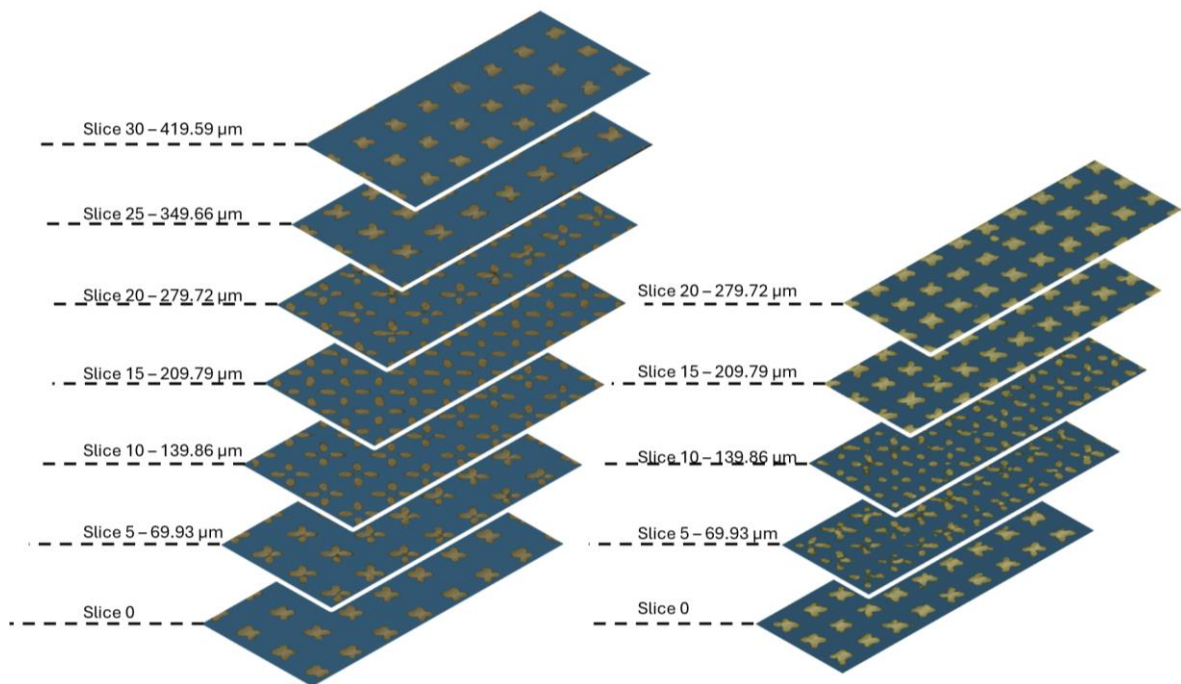


Figure 5-45. Half-cell height evolution for sample V5 (left) and V12 (right)

5.5.1 XCT Porosity Analysis

The apparent and true porosities of all scanned samples was evaluated while validating previously experimentally derived values, as per the methodology set out in Section 3.4.3. Additionally, XCT analysis enabled the quantification of the samples trapped porosity. With the use of XCT, any discrepancies with assuming material density, uneven residual support material and human induced errors has been reduced. The various porosities determined through XCT analysis for each sample is shown in Table 5-4.

Table 5-4. Porosity measurements from XCT data.

	Apparent Porosity	True Porosity	Trapped Porosity
H1	0.5394	0.5368	2.58E-03
H4	0.2670	0.2608	6.25E-03
H5	0.8065	0.8065	8.94E-07
H6	0.7736	0.7736	3.60E-07
H10	0.8456	0.8456	2.31E-07
H12	0.7787	0.7787	2.32E-06
V1	0.5892	0.5861	3.08E-03
V4	0.2427	-	-
V5	0.8024	0.8024	4.52E-07
V6	0.7636	0.7636	4.92E-07
V10	0.8316	0.8316	8.71E-07
V12	0.7393	0.7393	5.33E-07

Due to the non-interconnectivity of the porous makeup and the uncertainty surrounding the permeability of external pores of sample V4, having a reliable measurement of true and trapped porosity proved ineffective and was therefore not included for further analysis. Each measured porosity was compared to that previously physically measured and to the intended CAD design. The apparent and true porosities for both horizontal and vertical samples, along with the associated deviation from experimental and CAD is shown in Figure 5-46 and Figure 5-47, respectively. For clarification, all deviations are calculated with the experimental and CAD values as the reference points.

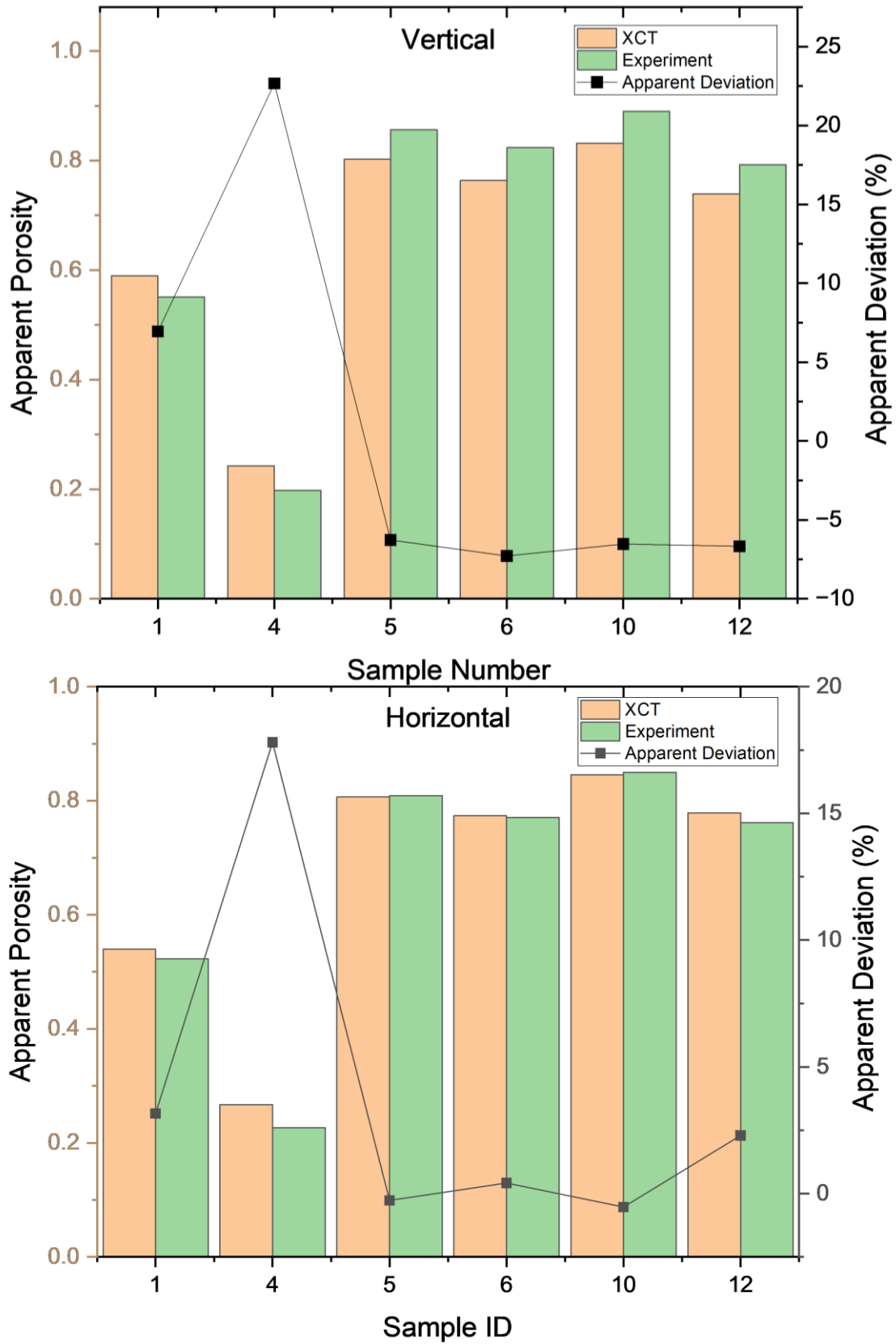


Figure 5-46. XCT Apparent porosity results for vertical (top) and horizontal (bottom) samples.

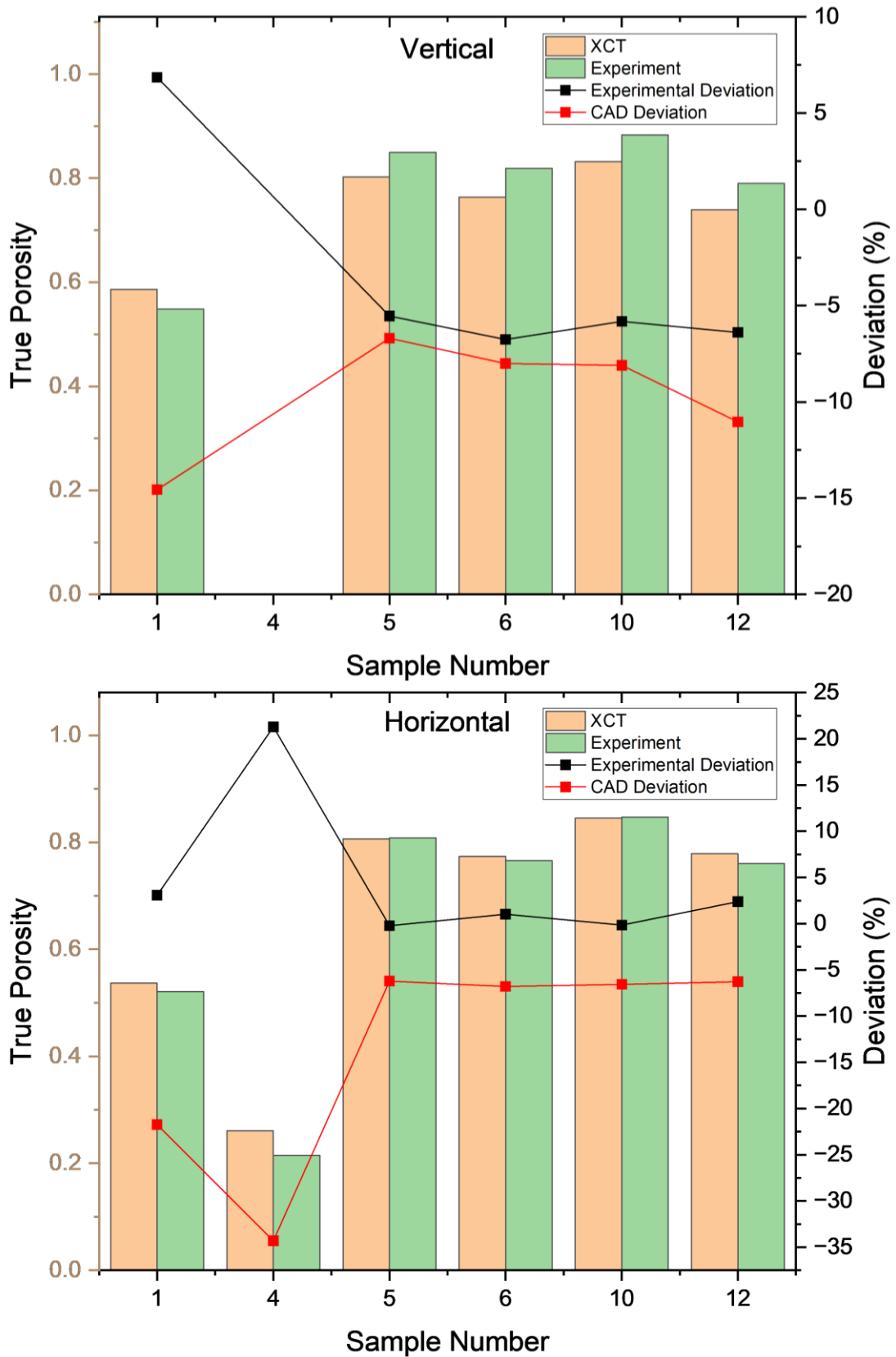


Figure 5-47. XCT True porosity results for vertical (top) and horizontal (bottom) samples.

As can be seen from Figure 5-46, there is generally favourable agreement between the XCT and experimentally determined apparent porosities, especially for samples 5 – 12 in both horizontal and vertical print orientations, showing average deviations of 0.476% and -6.693%, respectively. This contrasts the significantly higher deviation seen for samples 1 and 4 of 0.30mm strut thickness. Due to the relatively small difference between apparent and true porosities of samples 5 – 12, the true porosities follow a very similar trend in terms of comparison to the experimentally determined values. Furthermore, the horizontal orientation of samples 5 – 12 show porosity values closer to that of the intended design with an average deviation of -6.466% compared to an average deviation of -8.459% for the vertical equivalents.

The trapped porosity of each sample has been shown in Figure 5-49. Clearly, set build parameters for the 0.30mm strut thickness of samples 1 and 4 have contributed to a considerably larger trapped porosities within the structure . Samples 5 – 12 of 0.20 and 0.15mm strut thicknesses, showed negligible trapped porosities for the XCT data. This can easily be visualised with the lack of trapped porosities shown throughout stacks of samples V5 and V12 in Figure 5-45 and the noticeable porosities identified for sample V1 in Figure 5-48.

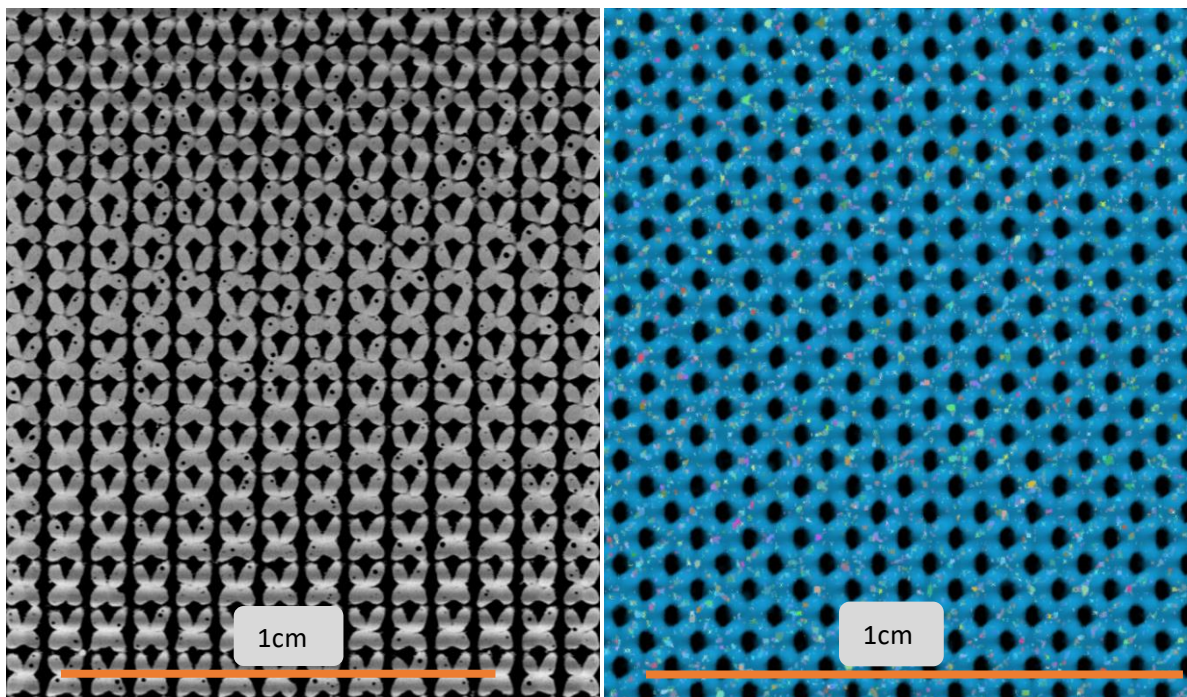


Figure 5-48. Example slice (left) and segmented image (right) of Sample V1.

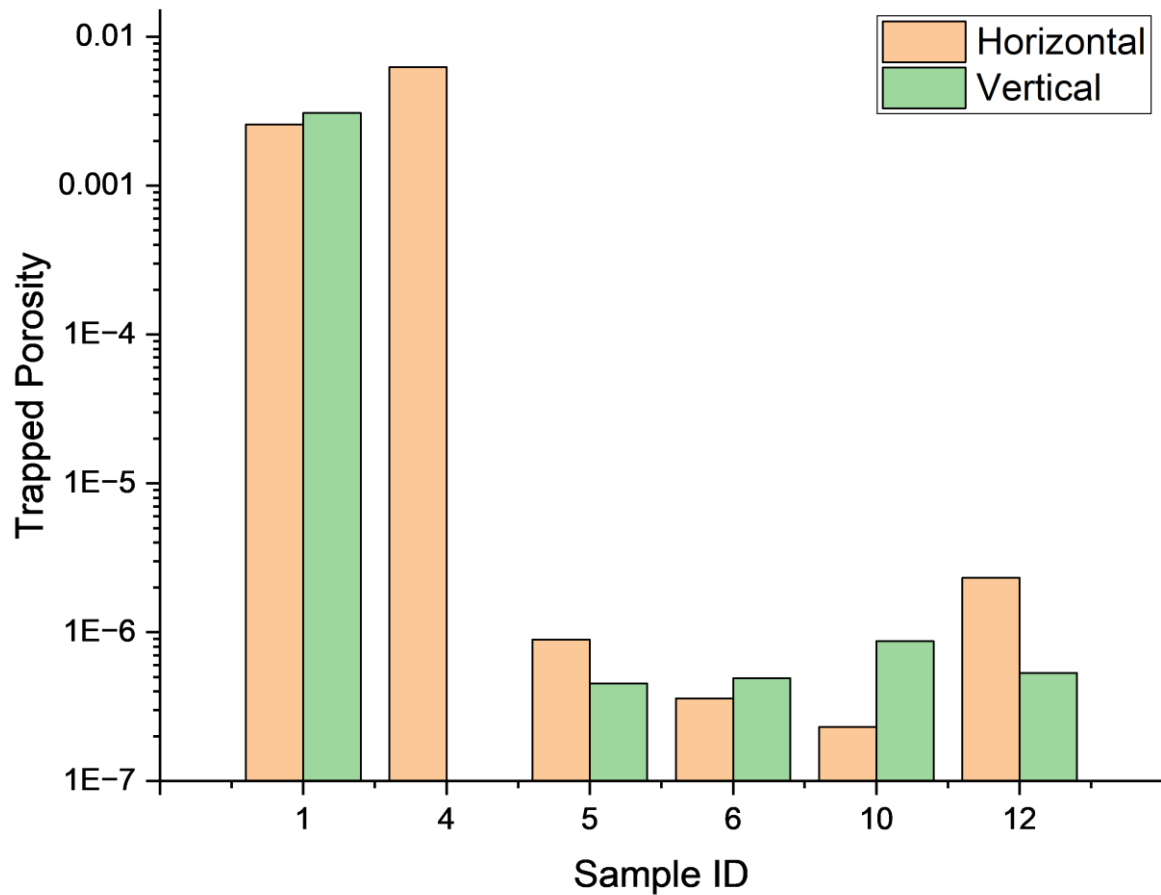


Figure 5-49. XCT Trapped porosity results for vertical (top) and horizontal (bottom) samples.

As only a limited number of samples underwent XCT analysis, confirmation of trends relating to the effects of cell sizes and print orientations on the rate of trapped porosities has not been evaluated in this study.

5.5.2 Internal Defect Identification

XCT presents an opportunity to quantify and characterise the internal defects of the samples which may otherwise go unnoticed. As previously mentioned, and discussed throughout, significant damage, warpage and dislocated struts were identified on the surface of vast amounts of the horizontal samples. This was especially prevalent for the thinner strut diameter samples. Through analysis of the XCT data, it became clear that sample H12 had significant internal defects, such as that shown in Figure 5-50.

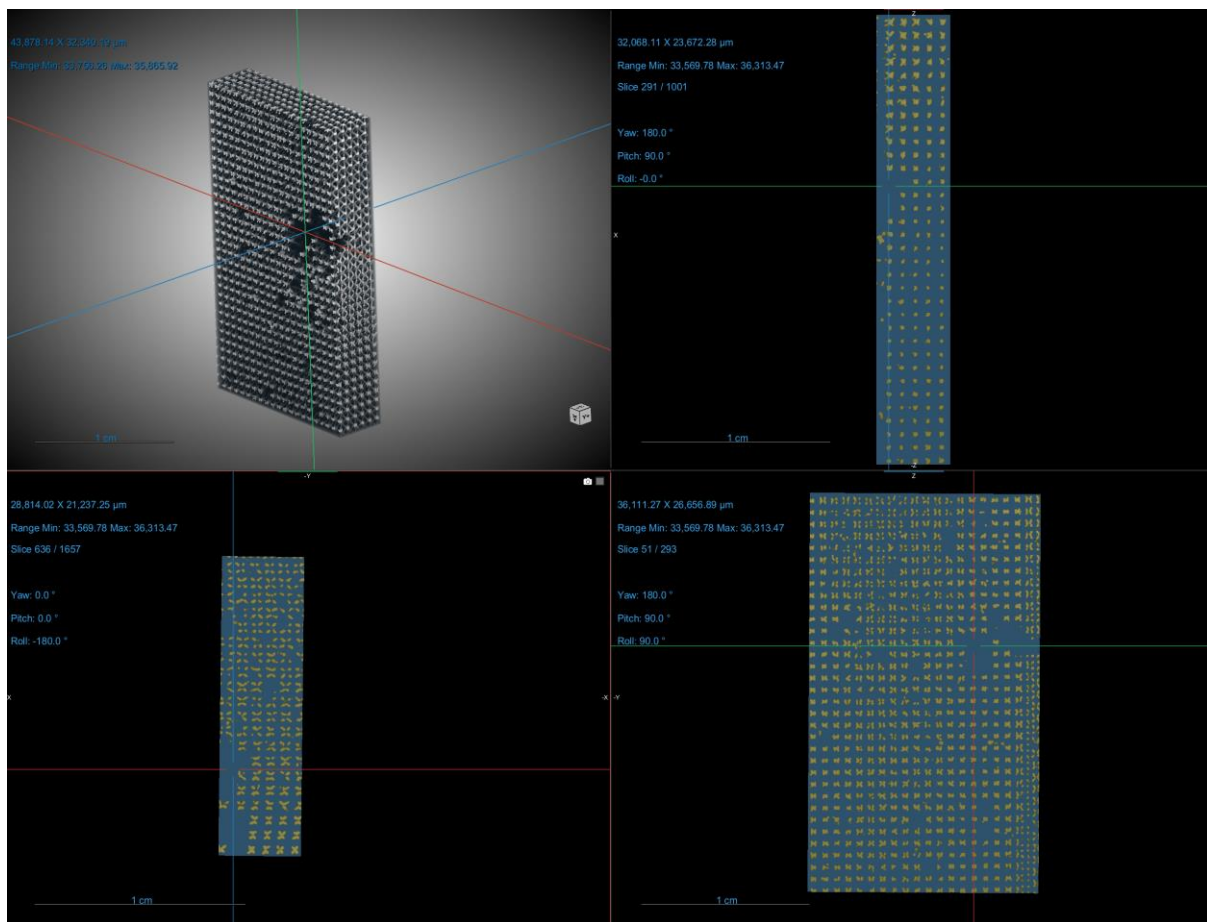


Figure 5-50. Identification of internal damage to sample H12.

Interestingly, the large defect identified in the 3D view of Figure 5-50 is located on the interface between the lattice and bulk material. The extent of the damage on the internal volume of sample H12 can be further seen through cropping it into a single layer of unit cells and an orthogonal image of the 3D view was captured, shown in Figure 5-51.

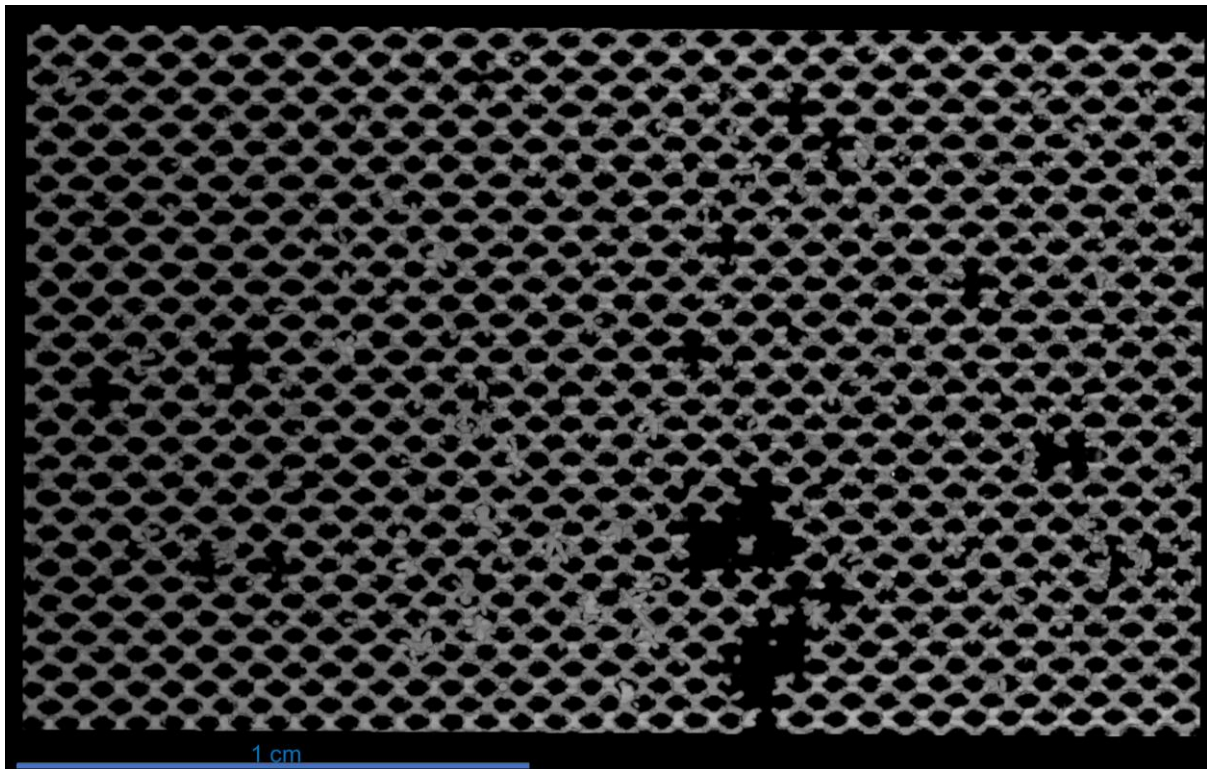


Figure 5-51. XCT image of a single layer of unit cells of samples H12 (top) and V12 (bottom).

In addition to the large defective pore previously identified, numerous smaller defects are also noticeable in Figure 5-51. These include numerous damaged struts resulting in either overlapping of adjacent pores, causing significant blockages, or being completely displaced from the matrix. Sample H12 was the only analysed sample which showed significant internal defects, resulting from the combination of reduced strut thickness and cell size allowing for increased points of failure under the internal thermally induced stresses.

5.6 Chapter Summary

Chapter 5 presents a thorough evaluation of the accuracy and printability of the samples through utilising several analysis techniques including 3D profilometry, standard light microscopy, SEM, μ -XCT and porosity analysis, in addition to analysis using the developed Lattice Analysis Tool outlined in Chapter 4. The following conclusions have been drawn from this work:

- The excessive thermally induced stresses on the horizontal samples resulted in significant strut dislocations and warpage. With the use of the heatmap function in LAT, it was identified that the warpage resulted in the outer layer of central pores of the horizontal samples being compressed. The build height of the vertically orientated samples was shown to have no noticeable effect on the measured strut thickness, cell size or pore diameter.
- The presence of agglomerated particles resulted in strut thicknesses larger than the intended CAD design, leading to reduced pore sizes overall. The deviation of the measured strut thickness from the CAD design was shown to increase with a reduction in both designed cell size and strut thickness as the apparatus' limitations were approached with a maximum deviation of 26.4% for sample V9, outperforming the majority of results found in literature.
- Sample sets 3 and 4 were found to have pores up to 60% smaller than the intended design, with significant internal blockages and limited line of sight through the structure of sample set 4. With the combination of the current build parameters and utilised raw material, an achievable pore diameter of approximately $\sim 160\mu\text{m}$ was found to be achievable.
- Powder size was found to become more influential in terms of both resultant strut thickness and surface roughness as the designed strut thicknesses were reduced. For further enhancements and reductions in strut thickness, utilisation of raw materials of smaller mean diameter and distribution should therefore be considered.
- Strut thickness was shown to be the most influential design factor when accounting for the various surface roughness parameters. This was due to the increased rates of agglomerated surface particles for the smaller strut thicknesses where the dimensional

ratio between the roughness features and struts increasing as the designed strut thicknesses were reduced.

- The vertical samples generally resulted in higher Sa and Sq values as less efficient heat dissipation within the build allowed a greater number of particles to semi-sinter to the strut surfaces. Sample V12 with a value of 14.46 μm was shown to have the highest Sa surface roughness while sample H2 had the lowest at 6.86 μm .
- Consideration of the minimum achievable pore size and trends shown in Figure 5-14 indicated that a further reduction in cell size, down to approximately 0.40 – 0.50mm, is achievable for the 0.15mm strut thickness samples.
- The vertical samples were found to have noticeably higher apparent and true porosities compared to that of the horizontal sample set. Porosity deviation from the intended CAD design was found to be significantly higher for the 0.30mm strut thickness samples.
- μ -XCT was shown to be an effective technique for porosity quantification with both apparent and true values aligning well with that derived through experimental means. The trapped porosities values of the analysed samples were also determined, with noticeably higher values for the 0.30mm strut thickness samples indicating the requirement for further build file parameter optimisation to be explored for the thicker struts.

6. Assessment of Raw AM Components

This chapter presents the results of both capillary rate-of-rise and permeability experiments for the as-printed wicking structures, drawing on the previous findings and relationships identified throughout Chapter 5. Further benchmarking of the samples is undertaken in a thorough literature-based performance comparison in Chapter 8.

6.1 Capillary Rate-of-Rise

As mentioned in Section 3.5.1, due to the hydrophobicity of the as-built samples, capillary action with water as the working fluid proved to be unsuccessful and for this reason, acetone was used for the capillary rate-of-rise experiment. The ineffectiveness of deionised water with as-built samples is further discussed in Section 7.4.3. The experiments were conducted three times with averages and standard deviations of each parameter calculated.

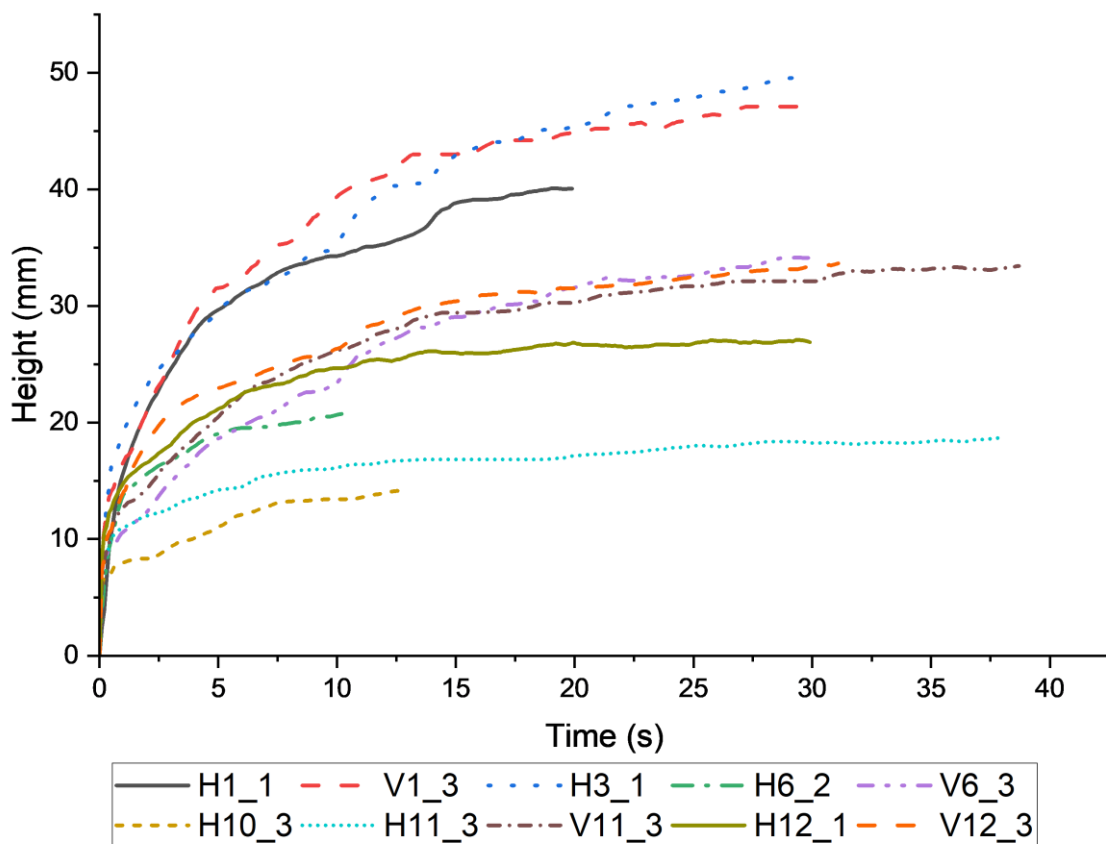


Figure 6-1. Dynamic rise height of several samples

6.1.1 Max Height

With the rise acting against gravity, the maximum equilibrium height can prove to be an effective and simple measure of the wicking structures limitations. Firstly, the maximum height of each sample may easily be determined directly from the processed infrared thermography data, with the average results shown in Figure 6-2.

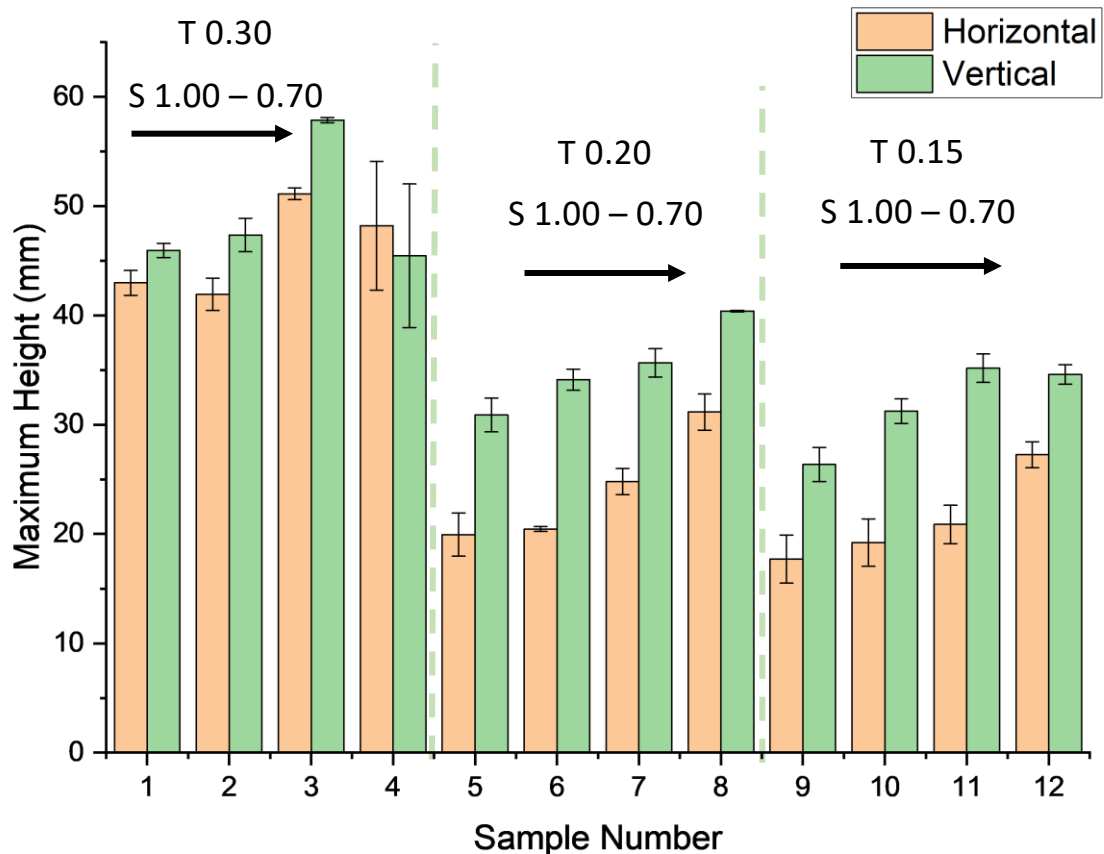


Figure 6-2. Averaged maximum equilibrium rate of rise height for each sample, with the error bars representing the standard deviation of repeated results.

As expected, the equilibrium rise height is generally proportional to the designed strut thickness and inversely proportional to the cell size, as the resultant pore size is reduced. As can be seen, the vertically printed samples consistently outperform their horizontal counterparts with respect to the equilibrium rise height, whilst also showing significantly less deviation between repeated cases. Numerous causes including differences in pore characteristics, porosity, surface roughness and contact angles may be attributed to the discrepancy between the horizontal and vertical samples, as will now be discussed.

As identified in Figure 5-15 of Section 5.2.3, the deviation in average pore size between the horizontal and vertical samples is largely minimal, apart from samples 1 – 4 of 0.30mm strut thickness. Although this is the case, the localised deviation in pore distribution of the warped horizontal samples resulted in the smaller pores being located at the centre of the samples and the larger pores at either end. This discrepancy resulted in local changes in delivered capillary pressure and may be visualised with the lower rise height shown in Figure 6-2. As the maximum horizontal rise height increases, approaching the centre of the samples where the pores are smaller, the deviation between both orientations is reduced, as Figure 6-3 shows.

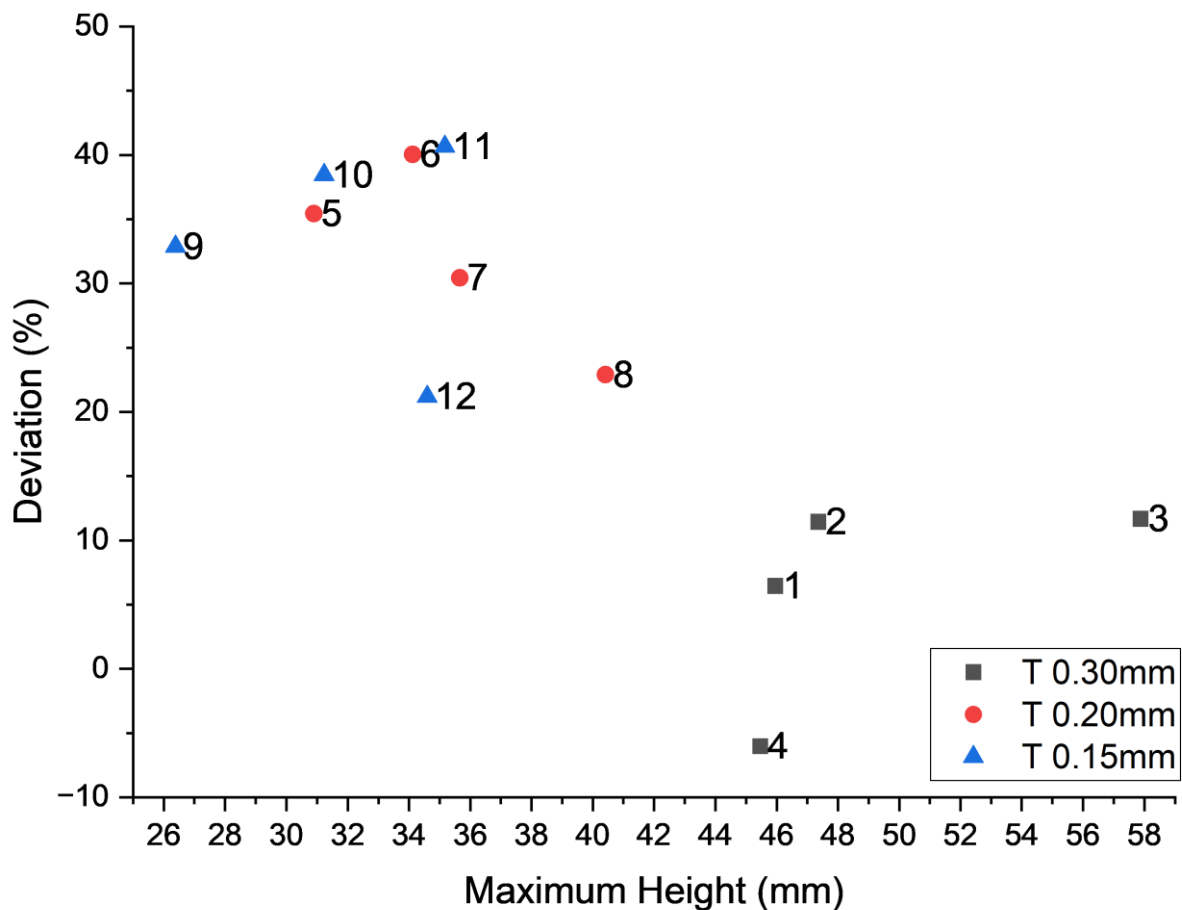


Figure 6-3. Deviation between the maximum rise height of the horizontal samples from the vertical counterpart.

Furthermore, as previously highlighted in Section 5.4.2, the vertical samples consistently had increased true porosities compared to that of the horizontal equivalents, resulting in reduced flow restrictions and lower internal frictional pressure losses, enabling the liquid to rise higher before reaching equilibrium state. As identified in Figure 5-21 of Section 5.3, an increase in agglomerated particles was seen on the vertical samples. The addition of these features may provide additional flow paths through their micropillar-like structures

enhancing the delivered capillary pressure. Furthermore, the additional surface contact area promotes the effect of the material's surface energy, resulting in potential localised variations in the liquid's interaction and greater uptake through the structure. The comparison between pore diameter and maximum equilibrium height is shown in Figure 6-4.

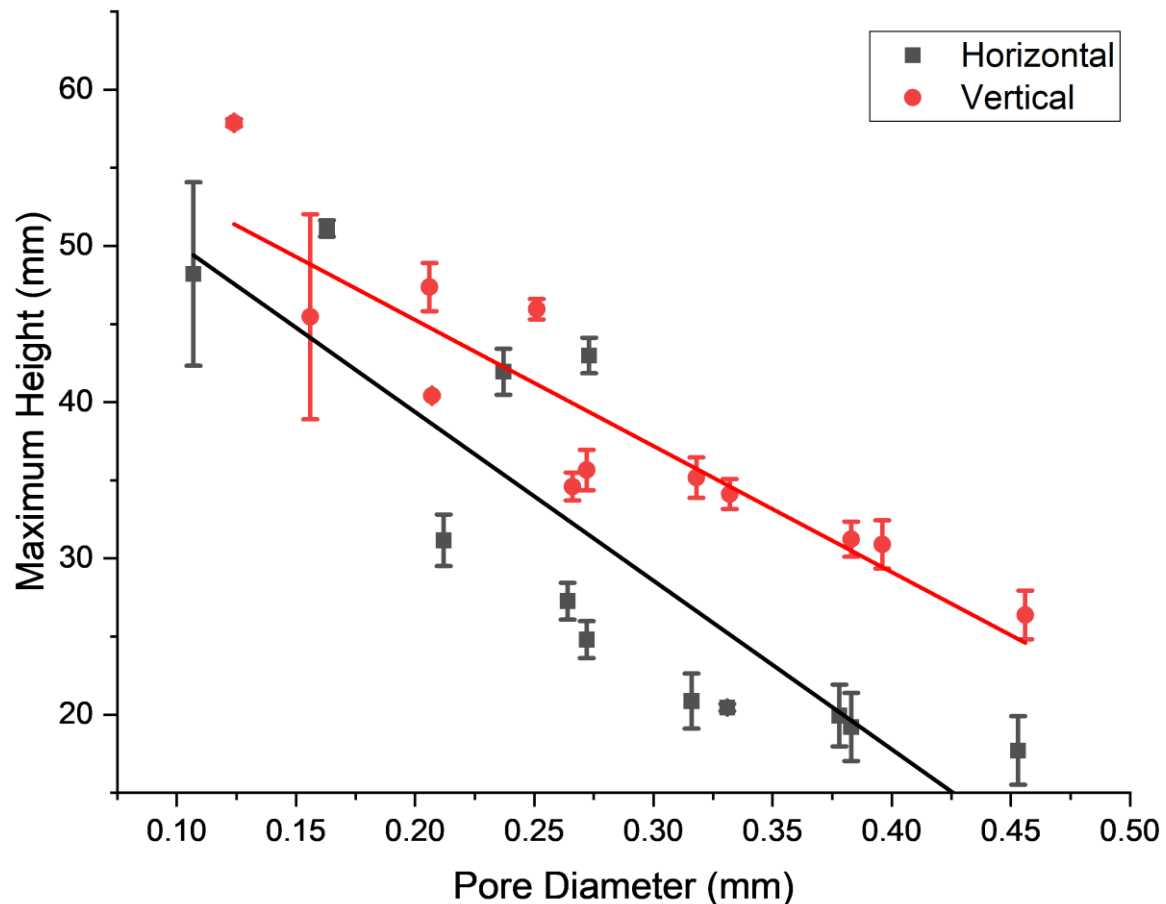


Figure 6-4. The effects of pore diameter on the maximum equilibrium height for all samples showing linear relationship.

The linear tendencies of both orientations align with expectations, in accordance with Jurin's law and stated in Equation (3-22). However, the vertical samples show an increased R^2 value of 0.827, compared to 0.703 for the horizontal samples. However, numerous assumptions are made for Jurin's law for lattice geometries, such as the assumed capillary tube and interconnectivity of the pores, which may not hold true. Jurin's law also fails to consider any internal pressure losses due to surface roughness effects which could also play a key role in their equilibrium rise height. Nevertheless, quantification of the validity of such formulations could be essential for future heat pipe development. Figure 6-5 shows the maximum Jurin's height of each sample in addition to the percentage deviation of the measured height from the theoretical values. Due to the enhanced wettability of acetone and

its near complete wetting characteristics, measuring the static contact angle was proven to be inexact. Therefore, a contact angle of 5° has been used throughout, leading to a resultant cosine factor of 0.996.

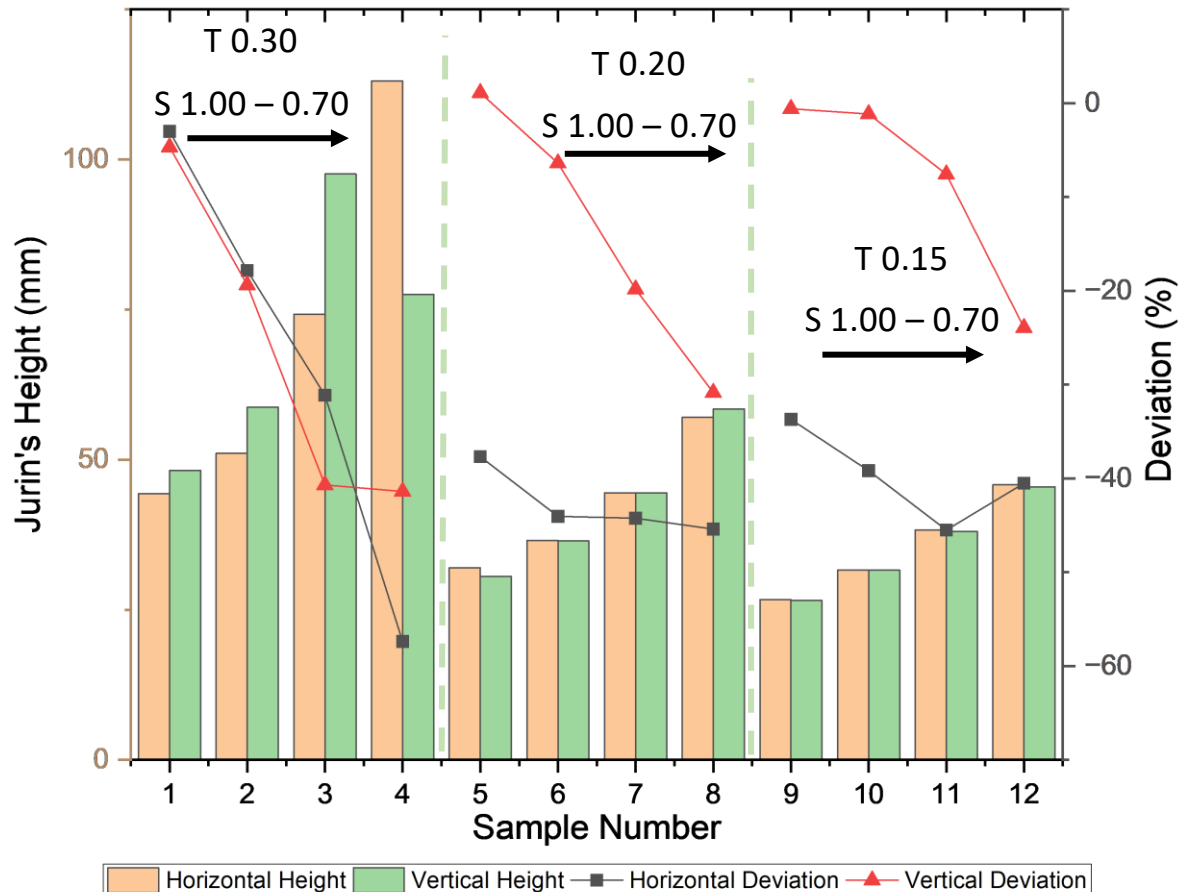


Figure 6-5. Maximum Jurin's height and % deviation of measured rise heights from theoretical values.

Clearly, Jurin's height is shown to increase with an increase in strut thickness and a decrease in cell size, aligning with a reduction in pore size. This decreased cell size amounts to an increase in pore density throughout the sample, adding to further deviations from Jurin's idealised capillary tube experiment. As surface roughness was not shown to be heavily impacted by cell size, factors such as pore interconnectivity and tortuosity are found to be influential in the determination of the structure's theoretical equilibrium rise height. A similar trend is also seen for the deviation of the measured heights of all vertical samples and horizontal samples of 0.30mm strut thickness (Samples 1 – 4). This increased deviation may be attributed to agglomerated particles having an increased effect on the pore characteristics, flow regime and overall internal resistance for the smaller pore sized samples. The deviation of the 0.20 and 0.15mm strut thickness horizontal samples have plateaued at values of around -40% adding to the inconsistencies and general irregularities of the horizontal samples. The

relationship between Jurin's law and the measured deviation from the theoretical values is further examined in Figure 6-6. Here, a clear linear trend is presented for the vertical samples with an R^2 value of 0.800. No clear relationship may be drawn for the horizontal samples.

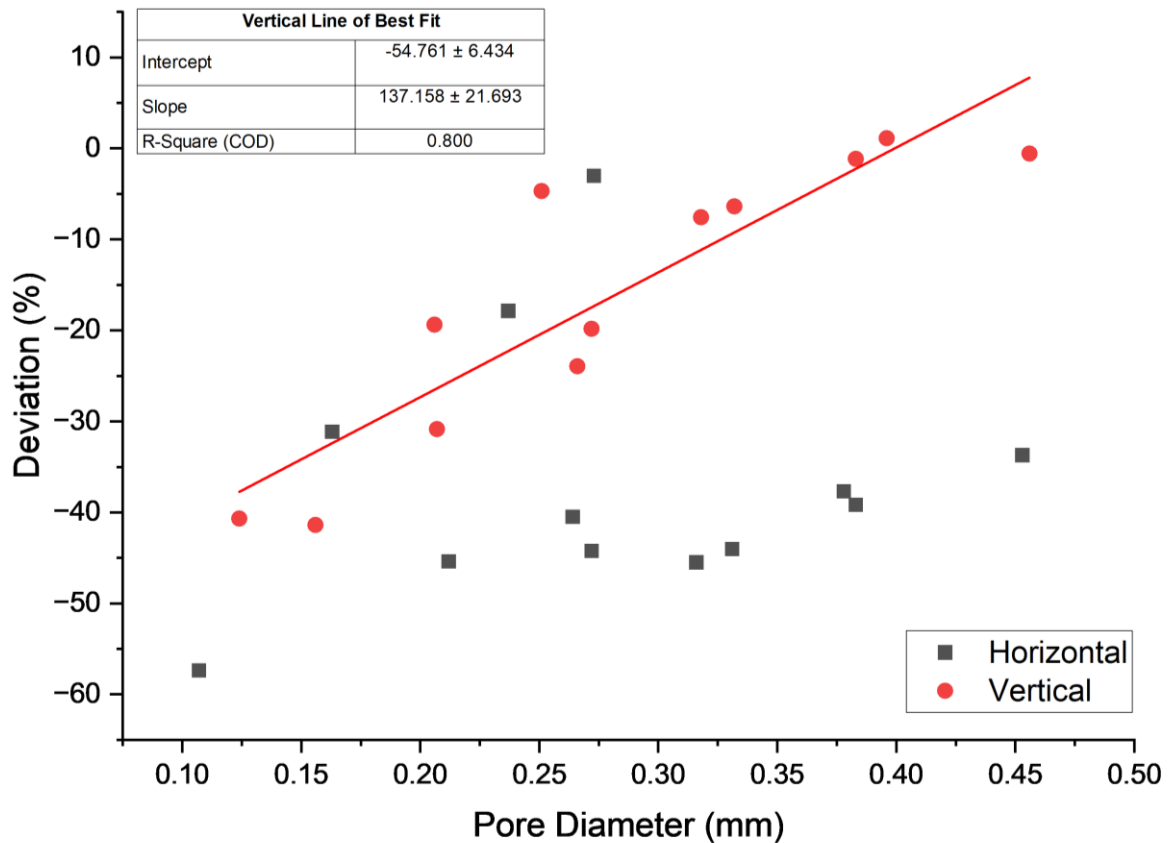


Figure 6-6. The relationship between the measured percentage deviation of the maximum height and Jurin's height with the line of best fit for the vertical samples.

It may be concluded that Jurin's law overpredicts the maximum rise height for the analysed AM lattice structures, especially those of smaller pore dimensions. Assuming a maximum acceptable deviation of -10%, the results indicate Jurin's law holds true for pore diameters larger than ~ 0.35 mm. Furthermore, due to the irregularities presented within the horizontal samples, no clear or consistent trends were observed between the relationship of pore diameter and Jurin's Law.

6.1.2 Capillary Performance

Following the methodology set out in Section 3.5.1, the capillary performance of each sample was determined through linear regression of Equation (3-20), where $x = 1/h$ and $y = dh/dt$. Through extrapolating the gradient of the line of best fit, identified for several test points in Figure 6-7, and inserting into Equation (3-21) the capillary performance may be determined.

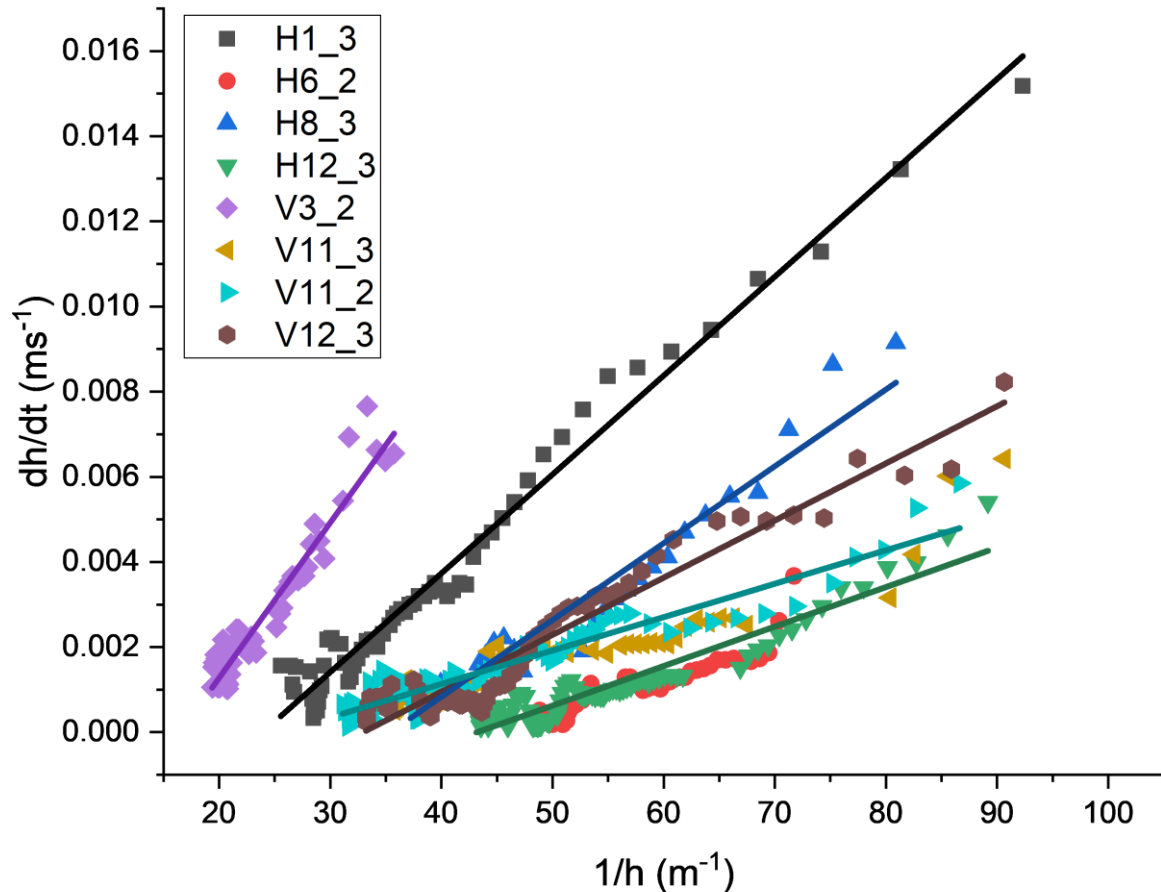


Figure 6-7. Example plot of $1/h$ against dh/dt for 8 different test points with several lines of best fits.

As seen in Figure 6-7, the data follows a relatively linear pattern. However, some discrepancies are present, resulting from image noise and minor height detection errors due to the limited processing capabilities within the Thermography Studio software package. Uncertainties are amplified for the calculation of velocity due to the resolution of the 0.10s capture rate. Nevertheless, these discrepancies have been captured well with line of best fit. Through repeating the test three times per sample, any variability in processing has been effectively accounted for. The average slope of each sample is shown in Figure 6-8.

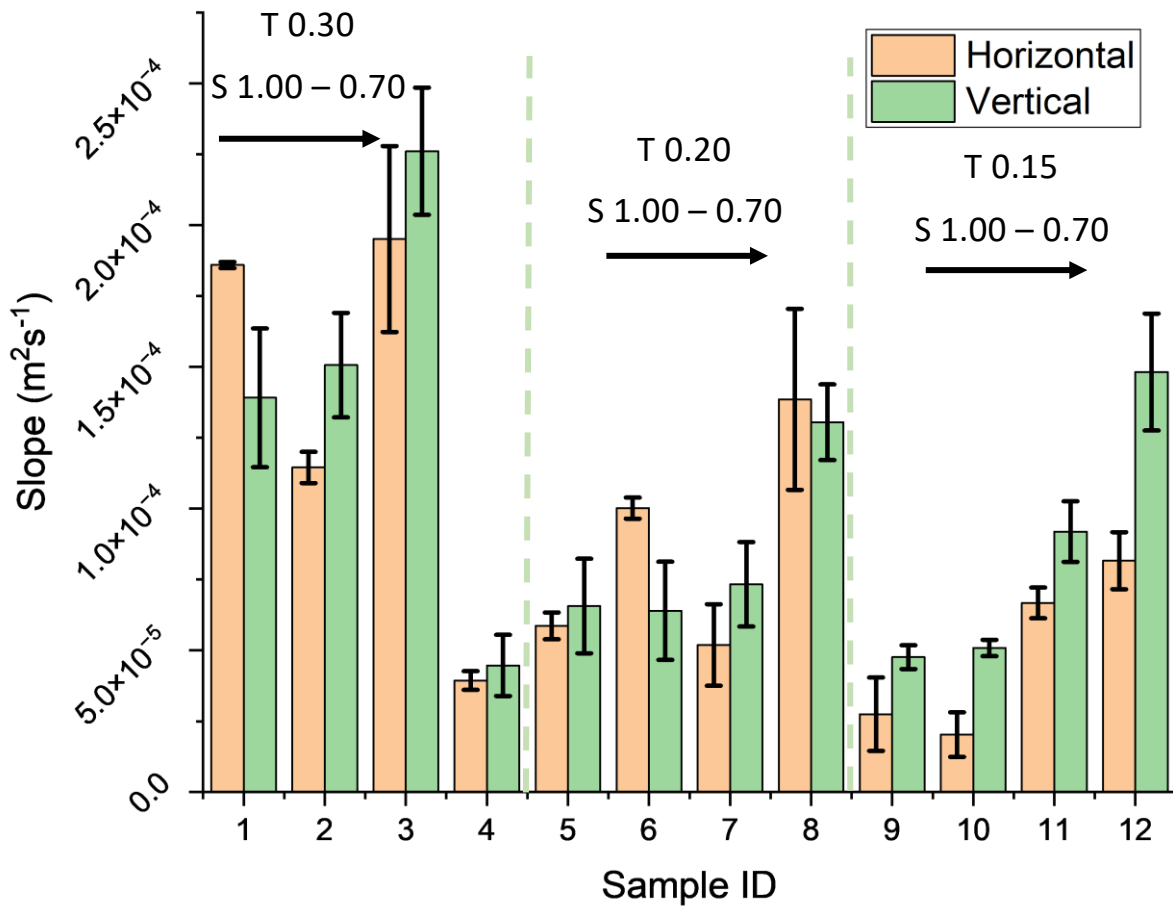


Figure 6-8. Averaged slope of each raw sample where $x = 1/h$ and $y = dh/dt$ with the standard deviation represented by the error bars.

The higher slopes correspond to an enhanced rate of rise for the samples, prompted by stronger driving forces (higher capillary forces). This is shown to align well with both a reduction in cell size and increased strut thickness resulting in a reduced pore size. This trend is shown to be more consistent for the vertical samples, adding to the defects and inferior characteristics of the horizontally printed samples identified throughout. Evidently, 75% of the vertical samples show a higher gradient compared to their horizontal counterparts. This indicates a higher capillary driving force for the vertical samples, despite their higher porosities and the little difference between the averaged measured pore sizes of both orientations. However, due to the detected warpage of the horizontal samples, the pores were measured to be larger at the ends of the samples, indicating weaker capillary forces. Furthermore, the vertical samples did show a significantly higher number of agglomerated particles on the strut surfaces which could act as additional micropillars providing supplementary capillary pathways and localised high capillary pressure for the fluid. Despite the smaller measured pore sizes of sample set 4, it shows a contradictory low gradient which

may be attributed to the blocked internal porosities significantly increasing the resistance of flow. Through considering fluid properties and sample porosities, the calculated capillary performance for both horizontal and vertical samples is shown in Figure 6-9, as per Equation (3-21).

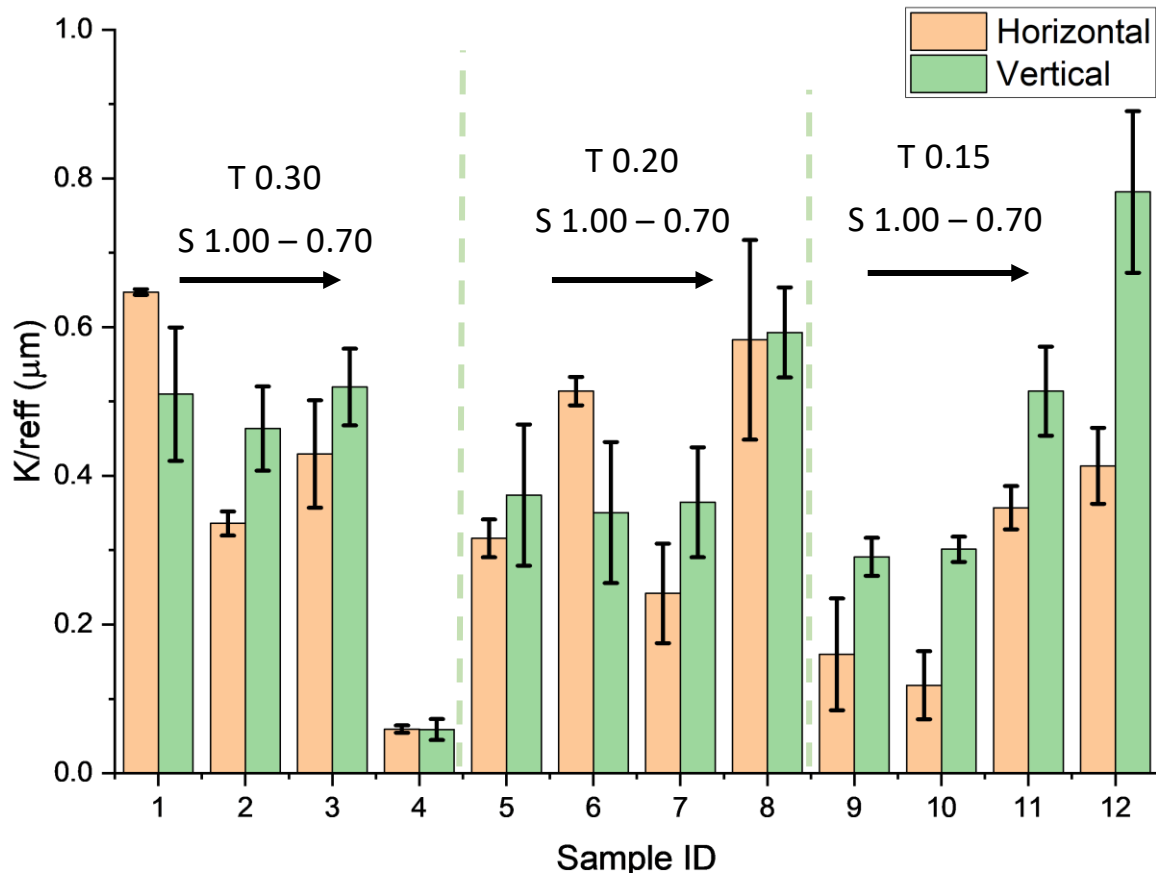


Figure 6-9. Averaged capillary performance (K/r_{eff}) of each raw sample with the standard deviation represented by the error bars.

A less perceptible trend is present between the capillary performance and sample design, compared to that previously highlighted for sample height and slope. However, for the 0.20 and 0.15mm strut thickness samples, it is found that capillary performance tends to increase with a reduction in cell size, aligning with a reduction in effective pore diameter, porosity and increased pore density. Although this highlights the significance of capillary pressure in determining the samples' operational limitations, consideration should also be made to the tortuosity and pore interconnectivity of the sample. As previously identified, sample set 4 resulted in significantly reduced pores compared to the intended CAD design. Although this would theoretically indicate higher capillary pressure and result in possible enhanced capillary rise, previously shown in Figure 6-2, the reduced line of sight and flow path through the samples has shown to be detrimental to the wicking structure's capillary performance

capabilities through significantly lowering their permeabilities and increasing flow restrictions. This study shows the importance of considering both capillary performance and permeability in the effective design of additively manufactured heat pipe wicking structures. Here, sample V12 is shown to be the most efficient design in terms of capillary performance whilst also showing appropriate rise height, previously highlighted in Figure 6-2. Figure 6-10 shows the effect both pore size and porosity had on the capillary performance distribution.

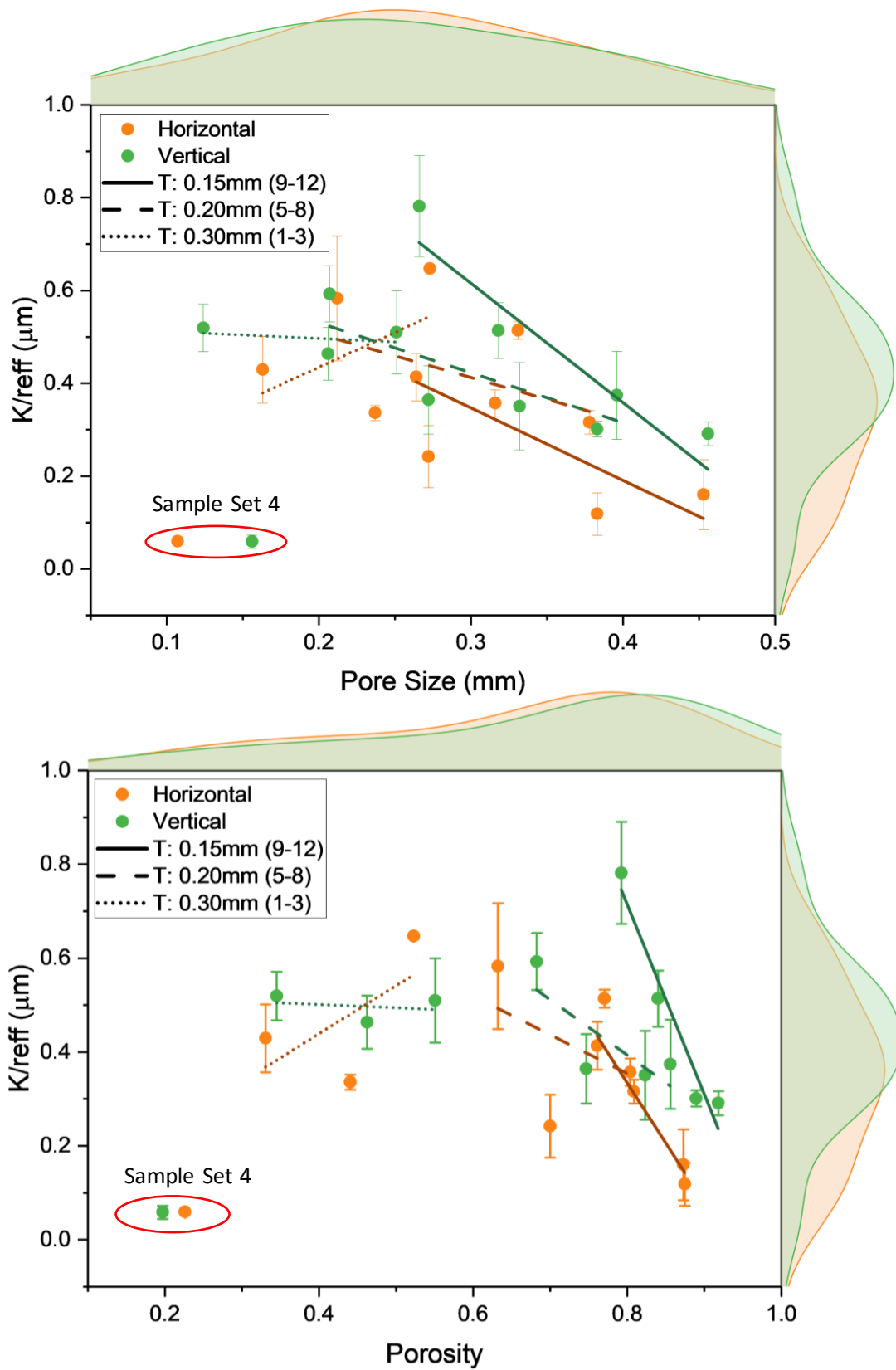


Figure 6-10. Effects of pore size (top) and porosity (bottom) on the capillary performance with histogram distribution, line of best fits for each strut thickness (T) grouping and the standard deviation represented by the error bars.

Through evaluation of Figure 6-10, it can be seen that the capillary performance tends to increase with a reduction in both porosity and pore size as the cell size is reduced within each strut thickness grouping. This is with the exception of the horizontal samples of 0.30mm strut thickness, which further adds to their inconsistencies.

This finding highlights the importance of the trade-off between capillary pressure and the porosity-governed flow capacity, as highlighted by the poor performance of sample set 4. As determined by the histogram distributions and lines of best fit, the vertical samples have resulted in a higher mean capillary performance while having higher mean porosities and marginally smaller pore diameters, further indicating the efficacy of the vertically orientated samples. As previously stated, the additional capillarity provided by the micro-capillary-like structures of the agglomerated particles have shown to enhance the capillary performance of the raw vertical samples.

Through analysis of this study, future research is directed to push the boundaries of AM to achieve higher capillary performances through attaining smaller unit cell sizes, which may well be possible with the current 0.15mm strut thickness designs. The steeper gradient of the 0.15mm strut thickness samples show that reducing the cell size had a larger impact for this grouping compared to the 0.30mm and 0.20mm strut thickness samples. As mentioned, further literature comparison of the capillary performance derived in this study is undertaken in Chapter 8.

6.2 Permeability

As a key performance parameter in the determination of heat pipe capabilities, in addition to other thermal heat transfer devices, permeability can be an effective method of comparison between design iterations. This section will determine the permeability of each manufactured sample, as set out in Section 3.5.2.

Ensuring accurate and reliable pressure readings is essential for effective calculation of permeability. As previously mentioned in Section 3.5.2, two separate static pressure transducers were used, one of which was a new purchase with a supplied calibration certificate, shown in Appendix 12.6. Nevertheless, in-house confirmation of calibration was undertaken in addition to calibrating the accompanying transducer. In order to do this, both pressure transducers were connected in a closed line with a calibrated Druck 705 IS Digital Indicator [169] and a Druck PV411A pneumatic hand pump [170] to supply the desired pressure, with results shown in Appendix 12.6.

6.2.1 Determination of Measurement Uncertainties

Due to the nature of both pressure transducers and the overall data acquisition system, fluctuations in current and subsequent pressure readings are inherent. For this work, the average measurement readings of each pressure transducer was taken over a 60s period. To exemplify this method, Figure 6-11 shows the raw data, captured at a rate of 100Hz, and a 2s moving average of the captured data for both pressure transducers for sample H3 at 4.00g/s flow.

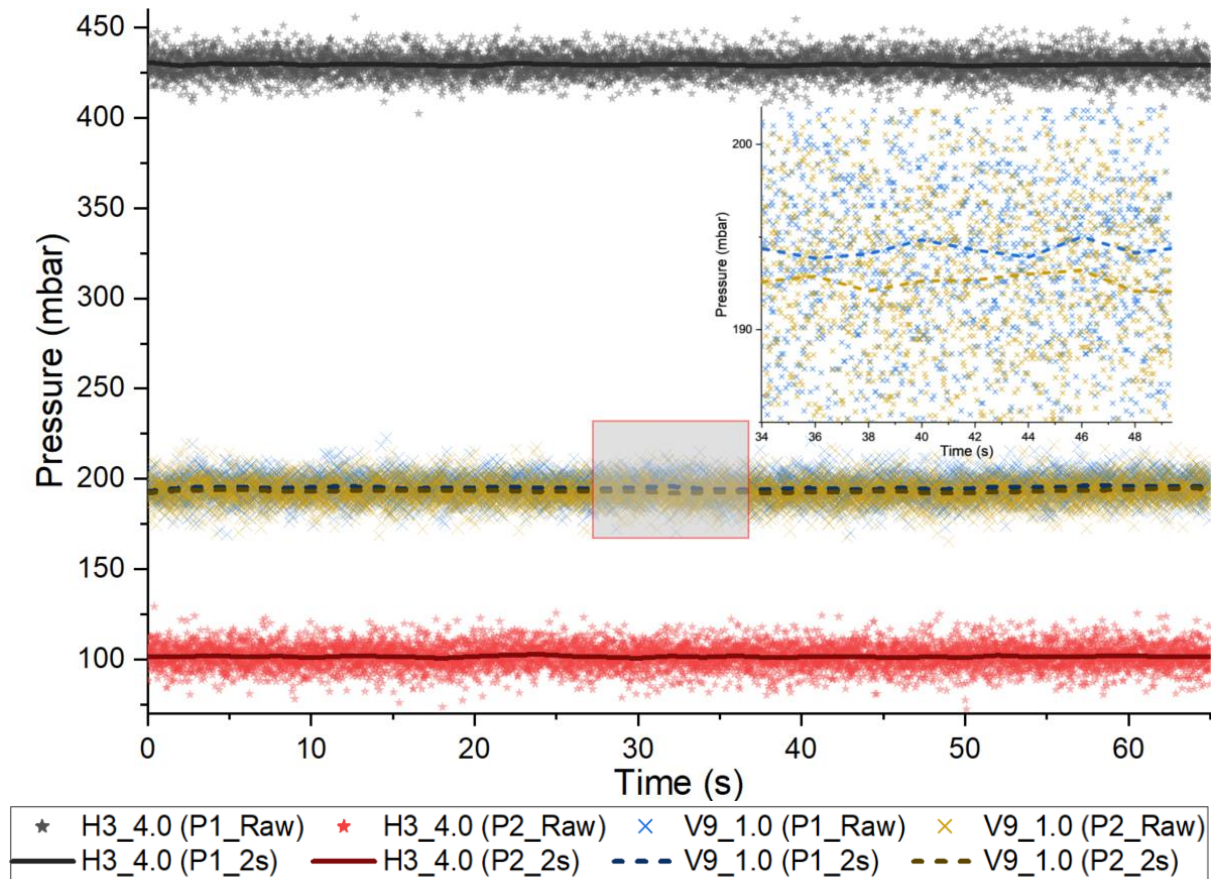


Figure 6-11. Inherent system noise for sample H3 at 4.00g/s and V9 at 1.00g/s with 2s moving average and enlarged section of sample V9.

Evidently, the averaged values over the moving 2s periods identify clear stability within both pressure transducer readings over a wide range of pressures. However, due to the larger pores and lower mass flow rate of test point V9_1.0, a significantly smaller pressure differential was seen. For this reason, further evaluation of the recorded uncertainty for the estimated means is required to fully quantify the results. This uncertainty was reported with the use of the Standard Error of the Mean, also referred to as Standard Error (SE) or standard deviation of the mean [171]. The SE evaluates the precision of the derived mean values, as per Equation (6-1).

$$SE_{(1,2)} = \frac{\sigma_{(1,2)}}{\sqrt{N_{(1,2)}}} \quad (6-1)$$

Where σ and N represent the standard deviation and sample size of each pressure transducer reading, respectively.

This is in contrast to the standard deviation alone which represents the average uncertainty of the individual measurements (scatter). Due to the intensified noise of the system, high number of sampling points and overall interest in the uncertainty of estimated mean, SE is the preferred method of representing the data [172]. The combined standard error of both transducers, relating to the differential pressure, was determined via the root sum of squares, shown in Equation (6-2).

$$SE_{(Combined)} = \sqrt{SE_{(1)}^2 + SE_{(2)}^2} \quad (6-2)$$

Through evaluating the combined SE values of approximately 300 test points, with the histogram shown in Figure 6-12, it can be seen that a narrow distribution of results is presented. Here, an average combined SE value of 0.1145mbar was achieved with an RSE of 1.90%.

Although the RSE is relatively small, it is vital to consider and investigate any trends between the combined SE and the measured differential pressure, as shown in Figure 6-13. Clearly, a cluster of test points can be seen at the lower range of the differential pressure, up to approximately 200mbar where the combined SE ranges from around 0.110 to 0.125mbar. An arbitrary trend is presented, demonstrating a decrease in combined SE as the differential pressure increases within this cluster, potentially indicating more consistent measurements at higher differential pressure readings. However, due to the distribution of the data points, identification of such a trend may be inaccurate. Furthermore, the combined SE across the whole range of all data points (~0.127 – 0.111 mbar) remains relatively low with respect to the measured values, and therefore, the impact on the uncertainty values is considered negligible. It can therefore be determined that the measured pressure differential has an insignificant effect on the overall uncertainty associated with the combined SE.

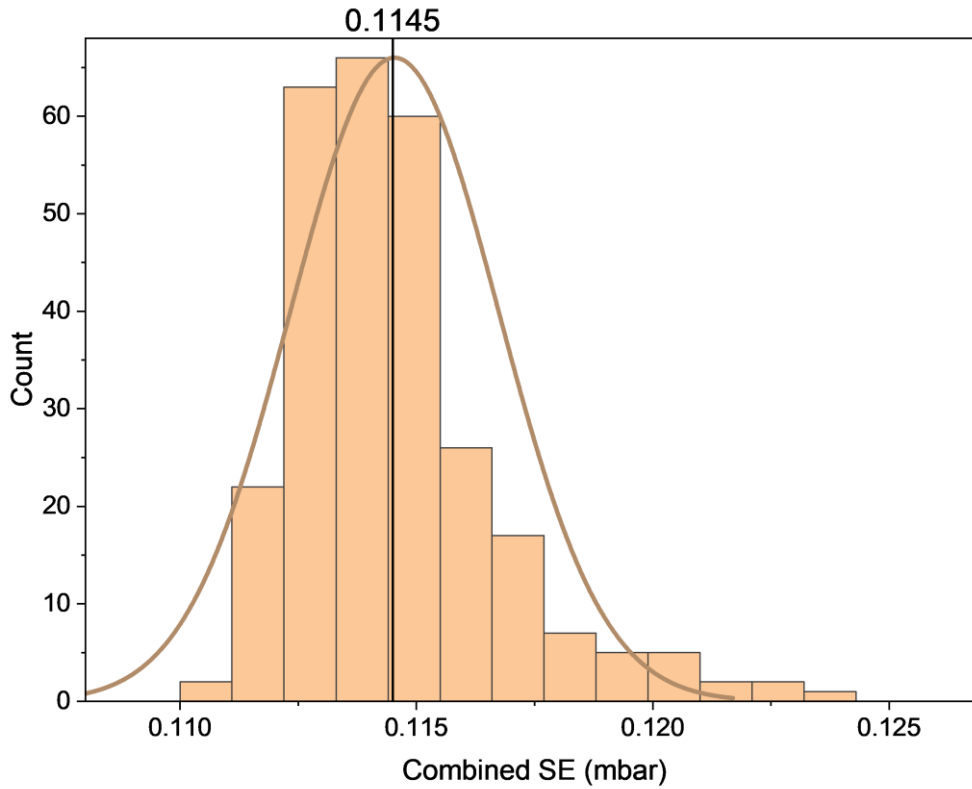


Figure 6-12. Histogram of calculated combined SE for 300 test points.

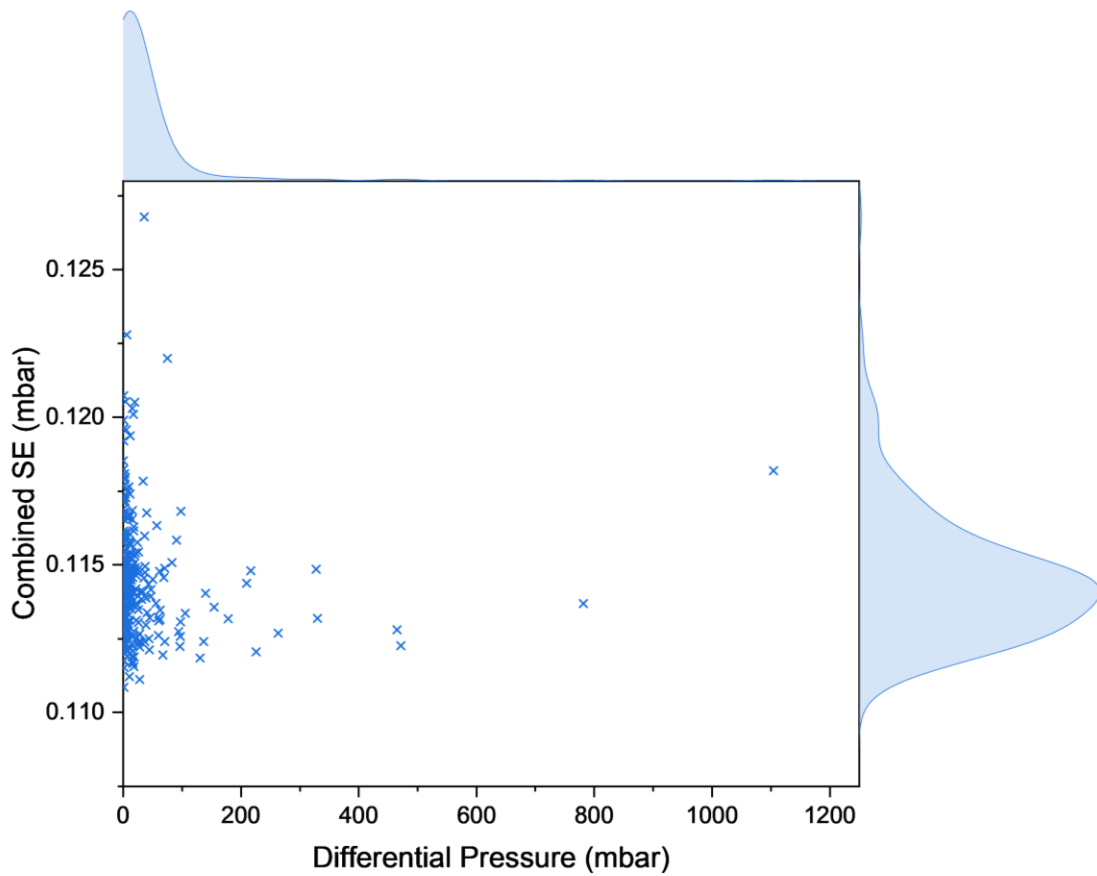


Figure 6-13. Variations of combined SE with differential pressure with distribution curves.

Due to time and lab access constraints, a full set of repeats for all samples was not possible. For this reason, the uncertainty relating to repeatability of the experiment was determined through repeating a selection of samples and data points three times. The Relative Standard Deviation (RSD) of each set of repeated test points was determined and shown in Figure 6-14.

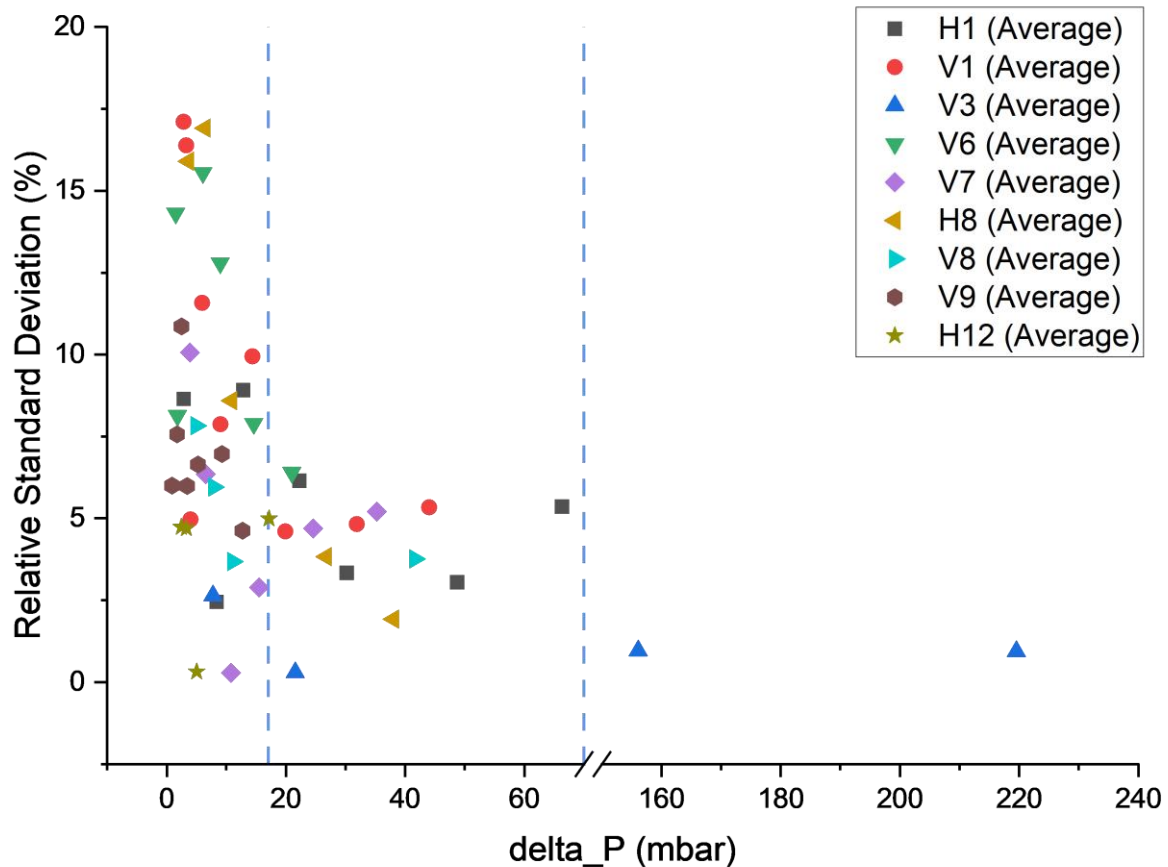


Figure 6-14. Relative Standard Deviation of repeated test.

Evidently, the RSD decreases as the measured differential pressure increases. Aligning with expectations, any small deviations within the experimental set up at the lower pressure range would have a larger relative impact on the results compared to that at the higher range of differential pressure. To accommodate the variable RSD values across the measured range of differential pressures and unrepeated test points, the results were categorised into three sections with the average values determined for each section, as per Table 6-1.

Table 6-1. Relative Standard Deviation breakdown.

Differential Pressure Range (mbar)	Averaged RSD (%)
< 17	8.82
17 – 70	5.33
> 70	0.95

Evidently, the averaged RSD decreases as the range of differential pressure increases. Due to the limited test points at the higher differential range, only two repeated test points were captured. As stated, the uncertainty of the Bronkhorst M14 mass flow controller is 0.20% [155] which is significantly less than the pressure differential uncertainties. This, therefore, has negligible effect on the combined uncertainties of permeability.

6.2.2 Differential Pressure

Measuring the pressure differential across a wide range of mass flow rates is the first step in determining both Darcy permeability and the respective Forchheimer corrections. Figure 6-15 shows the differential pressure for 12 samples over the analysed mass flow rates.

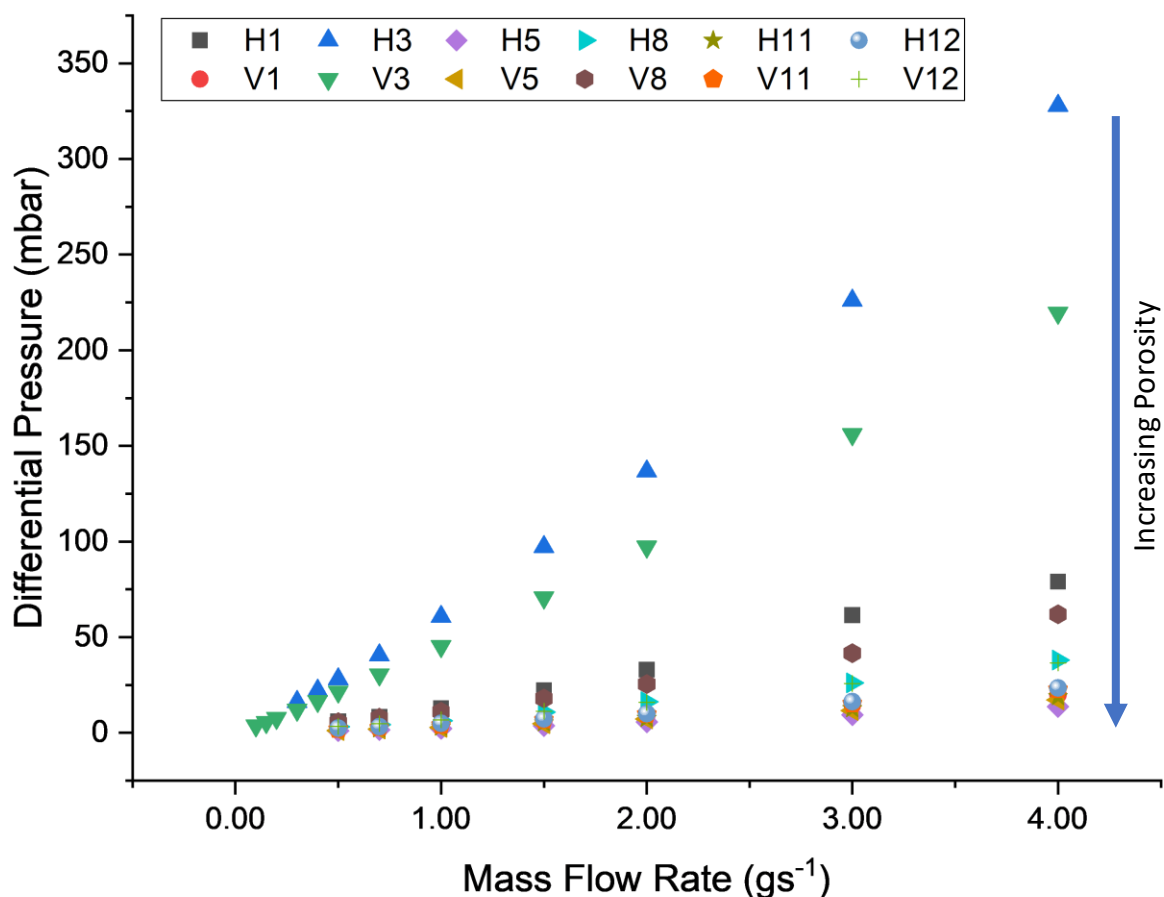


Figure 6-15. Differential pressure of selected samples over varying mass flow rates.

For clarity and enhanced readability, the measured pressure differential should be cross-referenced to the uncertainty values stated in Table 6-1. As expected, the differential pressure is shown to be directly proportional to the mass flow rate for all samples. Furthermore, the mass flow rate is shown to have significantly more effect on the pressure differential as porosity is decreased, evident from the steeper gradient of Samples H3 and V3 in Figure 6-15.

This aligns with expectations, as lower porosity increases flow resistance, resulting from amplified frictional and energy losses due to viscous dissipation. The permeability calculated via Darcy's Law, as per Equation (3-27), for a range of the analysed samples is shown in Figure 6-16.

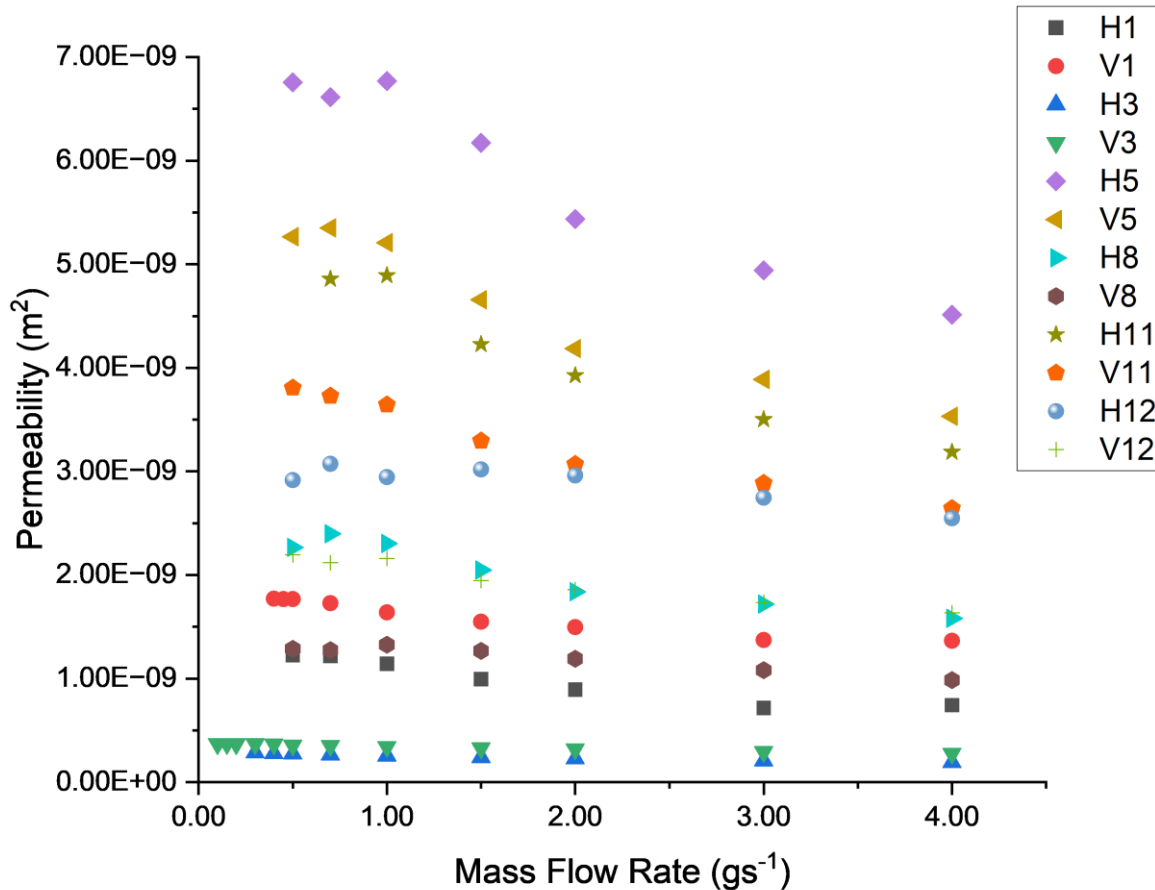


Figure 6-16. Calculated permeability of selected samples over varying mass flow rates.

As can be seen at lower flow rates, a region of relatively constant permeability exists where Darcy's law holds true. However, as the mass flow rate and hence velocity increases, inertial effects become more prominent resulting in deviations from Darcy's law. As discussed in Section 3.5.2, Forchheimer's Equation, (3-29), includes an additional term to account for this deviation offering a way of accurately predicting permeability at higher flow rates. This change in state from Darcyan flow to inertial flow may be characterised by the permeability-based Reynolds number, Re_k , as per Equation (3-33) and is discussed further throughout this section. A summary of the results including sample parameters, Darcyan permeability and Forchheimer's terms for all samples is shown in Table 6-2.

6. Assessment of Raw AM Components

Table 6-2. Summary of permeability results.

Sample ID	Sample Parameters	Darcyan Permeability – K (m ²)	Forchheimer Permeability – K ₁ (m ²)	Forchheimer Correction – K ₂ (m)
H1	S: 1.00mm T: 0.30mm Dp: 0.273mm Porosity: 0.5207	1.22E-09	1.31E-09	8.40E-04
H2	S: 0.90mm T: 0.30mm Dp: 0.238mm Porosity: 0.4368	6.00E-10	6.09E-10	1.13E-04
H3	S: 0.80mm T: 0.30mm Dp: 0.163mm Porosity: 0.3231	2.81E-10	2.94E-10	2.84E-05
H4	S: 0.70mm T: 0.30mm Dp: 0.107mm Porosity: 0.215	1.95E-10	2.00E-10	8.28E-06
H5	S: 1.00mm T: 0.20mm Dp: 0.378mm Porosity: 0.8082	6.71E-09	7.60E-09	5.83E-04
H6	S: 0.90mm T: 0.20mm Dp: 0.331mm Porosity: 0.7659	5.00E-09	5.15E-09	6.98E-04
H7	S: 0.80mm T: 0.20mm Dp: 0.272mm Porosity: 0.6967	1.97E-09	2.00E-09	1.79E-04
H8	S: 0.70mm T: 0.20mm Dp: 0.212mm Porosity: 0.6291	2.33E-09	2.60E-09	2.13E-04
H9	S: 1.00mm T: 0.15mm Dp: 0.453mm Porosity: 0.8707	1.31E-08	1.66E-08	5.03E-04
H10	S: 0.90mm T: 0.15mm Dp: 0.383mm Porosity: 0.8469	8.03E-09	9.64E-09	3.62E-04
H11	S: 0.80mm T: 0.15mm Dp: 0.316mm Porosity: 0.8007	4.87E-09	5.45E-09	4.25E-04
H12	S: 0.70mm T: 0.15mm Dp: 0.264mm Porosity: 0.7606	2.98E-09	3.47E-09	5.41E-04
V1	S: 1.00mm T: 0.3mm Dp: 0.251mm Porosity: 0.5485	1.77E-09	1.82E-09	2.71E-04
V2	S: 0.90mm T: 0.30mm Dp: 0.206mm Porosity: 0.4602	8.60E-10	8.94E-10	2.61E-04
V3	S: 0.80mm T: 0.30mm Dp: 0.124mm Porosity: 0.337	3.69E-10	3.73E-10	5.65E-05

6. Assessment of Raw AM Components

Sample ID	Sample Parameters	Darcyan Permeability – K (m ²)	Forchheimer Permeability – K ₁ (m ²)	Forchheimer Correction – K ₂ (m)
V4	S: 0.70mm T: 0.30mm Dp: 0.154mm Porosity: 0.143	8.32E-11	8.54E-11	8.07E-06
V5	S: 1.00mm T: 0.20mm Dp: 0.396mm Porosity: 0.8495	5.27E-09	5.95E-09	5.23E-04
V6	S: 0.90mm T: 0.20mm Dp: 0.332mm Porosity: 0.8189	4.10E-09	4.43E-09	4.76E-04
V7	S: 0.80mm T: 0.20mm Dp: 0.272mm Porosity: 0.7434	2.41E-09	2.47E-09	2.91E-04
V8	S: 0.70mm T: 0.20mm Dp: 0.207mm Porosity: 0.6812	1.28E-09	1.53E-09	1.47E-04
V9	S: 1.00mm T: 0.15mm Dp: 0.456mm Porosity: 0.9116	8.71E-09	1.03E-08	4.07E-04
V10	S: 0.90mm T: 0.15mm Dp: 0.383mm Porosity: 0.8831	6.63E-09	8.65E-09	3.16E-04
V11	S: 0.80mm T: 0.15mm Dp: 0.318mm Porosity: 0.8351	3.73E-09	3.86E-09	4.79E-04
V12	S: 0.70mm T: 0.15mm Dp: 0.266mm Porosity: 0.7898	2.16E-09	2.22E-09	3.41E-04

6.2.3 Darcy – Forchheimer Transition

As set out in Section 3.5.2.1, the point at which the flow regime transitions from Darcyan to non-Darcyan flow can be correlated to the permeability-based Reynolds Number (Re_K), as per Equation (3-33). As expected, as the flow becomes less laminar, Re_K increases with velocity for all samples, as shown in Figure 6-17.

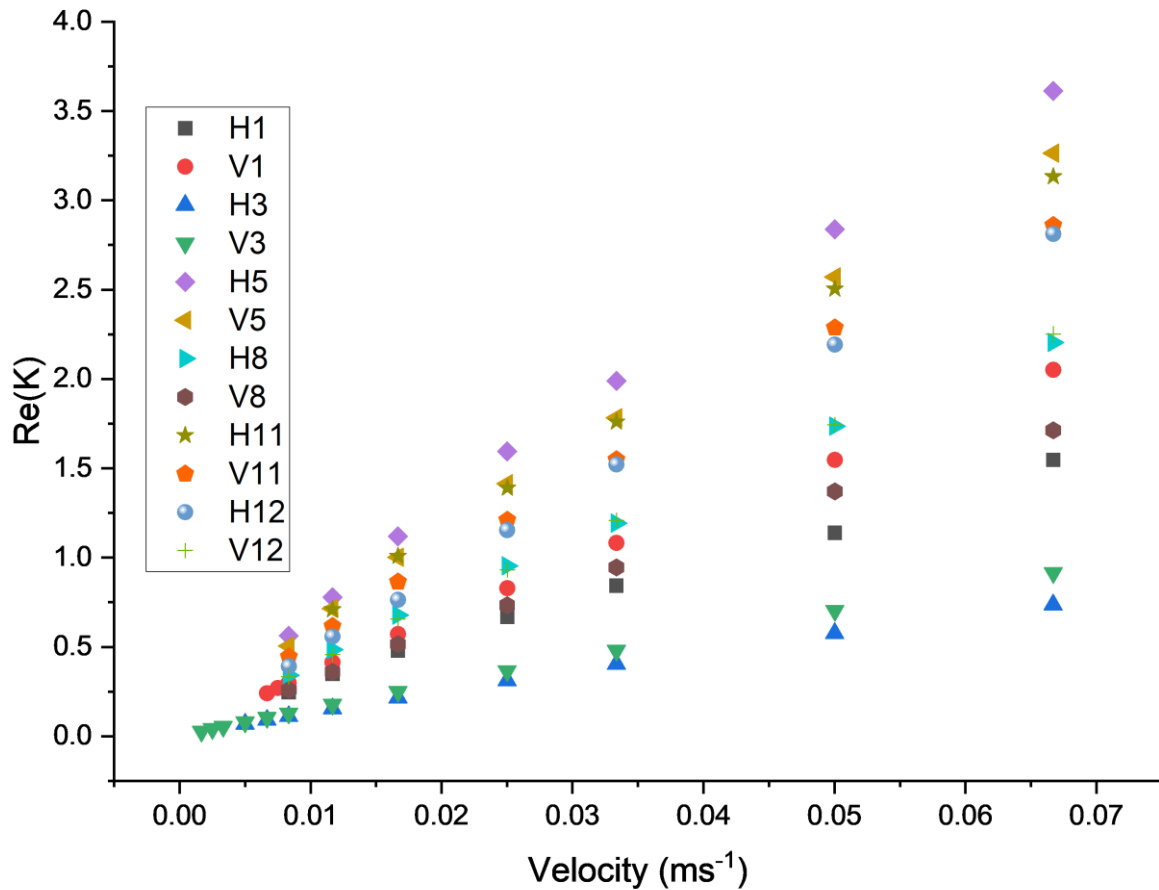


Figure 6-17. Effects of velocity on calculated Re_K values.

Notably, the Re_K values vary significantly across the range of samples with the higher Re_K values indicating a greater influence of inertial forces within the flow. Interestingly, none of the samples resulted in Re_K values greater than 10, indicating that with the resultant permeabilities at the set flow rates, none of the samples underwent a fully developed Forchheimer flow. The highest Re_K value was 4.24 for sample H9 at a mass flow rate of 4.00 gs^{-1} . As the typical internal flow regime within a heat pipe is considered to be laminar within Darcy's state [95], considerations beyond the transition zone are not of great importance for this study. Figure 6-18 shows the Re_K of each sample at the transition point where permeability deviates from Darcy's law.

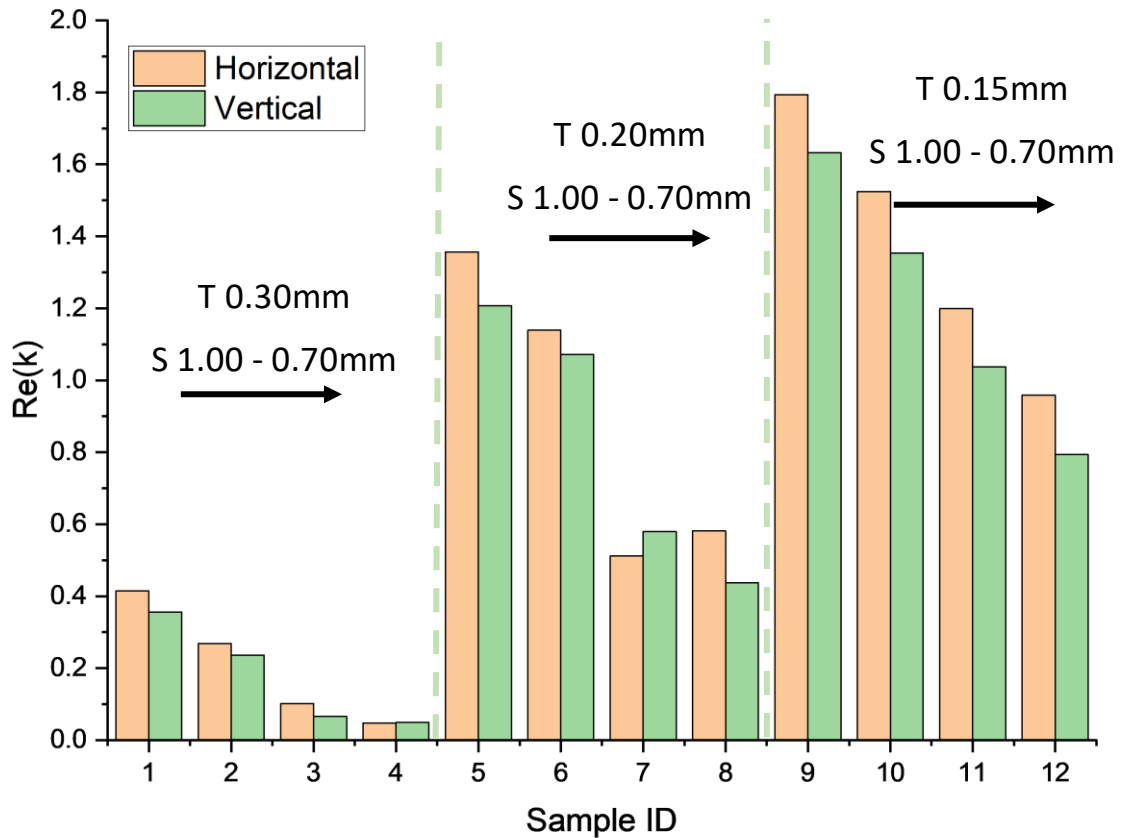


Figure 6-18. Permeability-based Reynolds Number (Re_k) at transition point for each sample.

Clearly, the horizontally orientated samples consistently result in a higher transition Re_k value compared to their vertical counterparts. As identified, their overall lower surface roughness and the reduced concentration of agglomerated particles could play a key part in this, resulting in less restrictions and disturbances within the flow and delaying the onset of inertial forces, which is well documented throughout literature [173]. Noticeably, the transition point is seen to increase with a reduction in strut thickness and an increase in cell size, aligning with increased pore size and porosity, as shown in Figure 6-19. The overall higher permeability of the more porous samples again enables less restriction for the flow, allowing it to maintain the higher velocities as less internal frictional losses are exerted on the flow. Through consideration of Figure 6-19, it can be determined that a linear relationship exists between Re_k and pore diameter for the analysed samples in this study. This is true for both horizontal and vertical sample sets with the superimposed trendlines indicating R^2 values of 0.86 and 0.94, respectively. Contrastingly, a more exponential relationship is present with

consideration of porosity. The sudden rise in the transitional value of Re_k at higher porosities indicates its greater influence in the transitional zone.

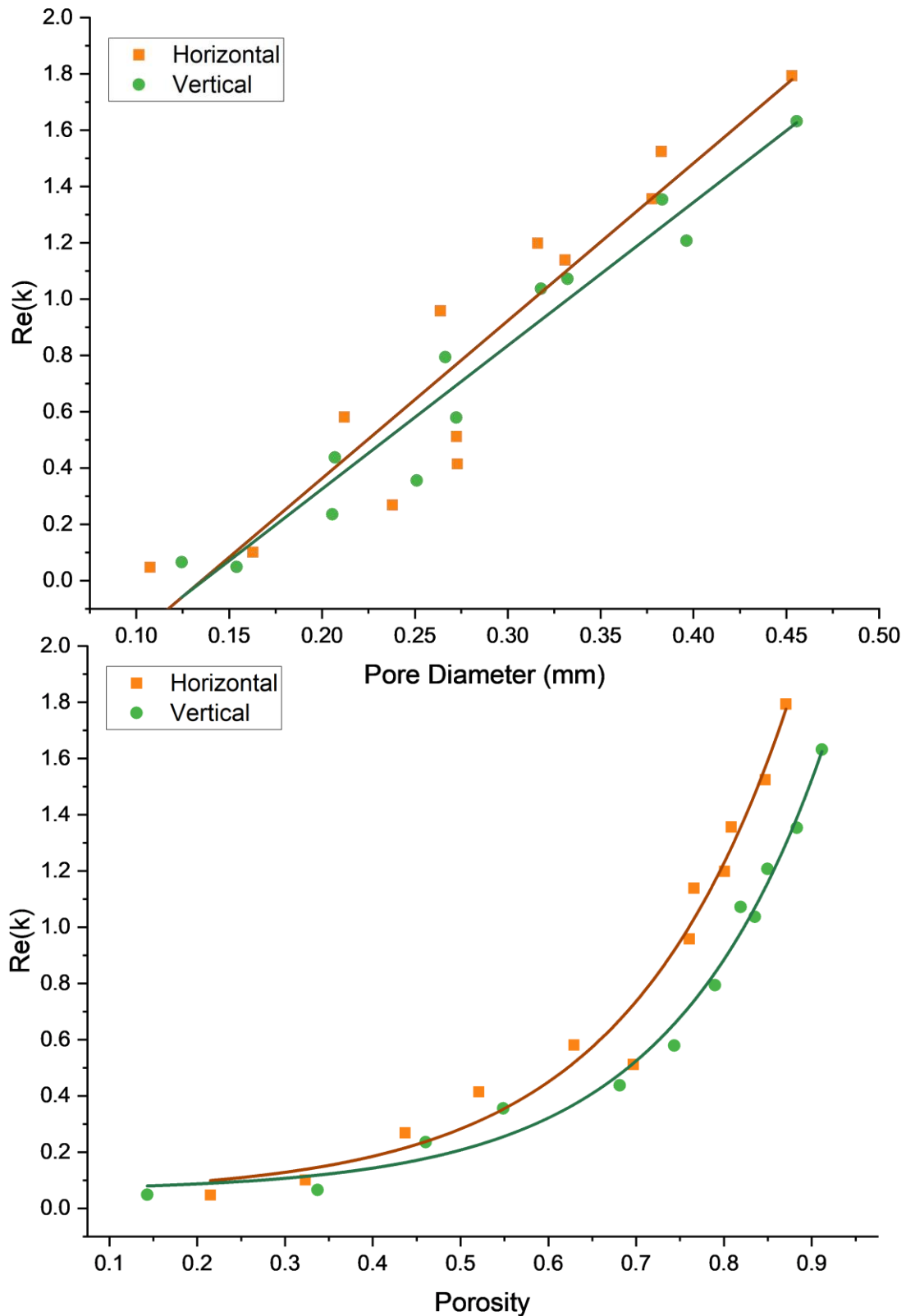


Figure 6-19. Influence of pore diameter (top) and porosity (bottom) and calculated permeability-based Reynolds number transition.

6.2.4 Darcy's Permeability

Firstly, the low flow Darcy permeability of all samples is evaluated. At low flow conditions, where Darcy's Law holds true, it became apparent that all low flow permeabilities, apart from samples V4 of 0.30mm strut thickness and 0.70mm cell size, occurred with differential pressure readings of less than 17mbar. Therefore, the associated repeatability uncertainty to be used for permeability under conditions relevant to Darcy's law is to be $\pm 8.82\%$. As stated, sample V4 had an average low flow pressure differential of 45.72mbar, resulting in a repeatability uncertainty of 5.33% at the Darcy state. Figure 6-20 shows the measured permeability of each sample with the respective uncertainties represented by the error bars.

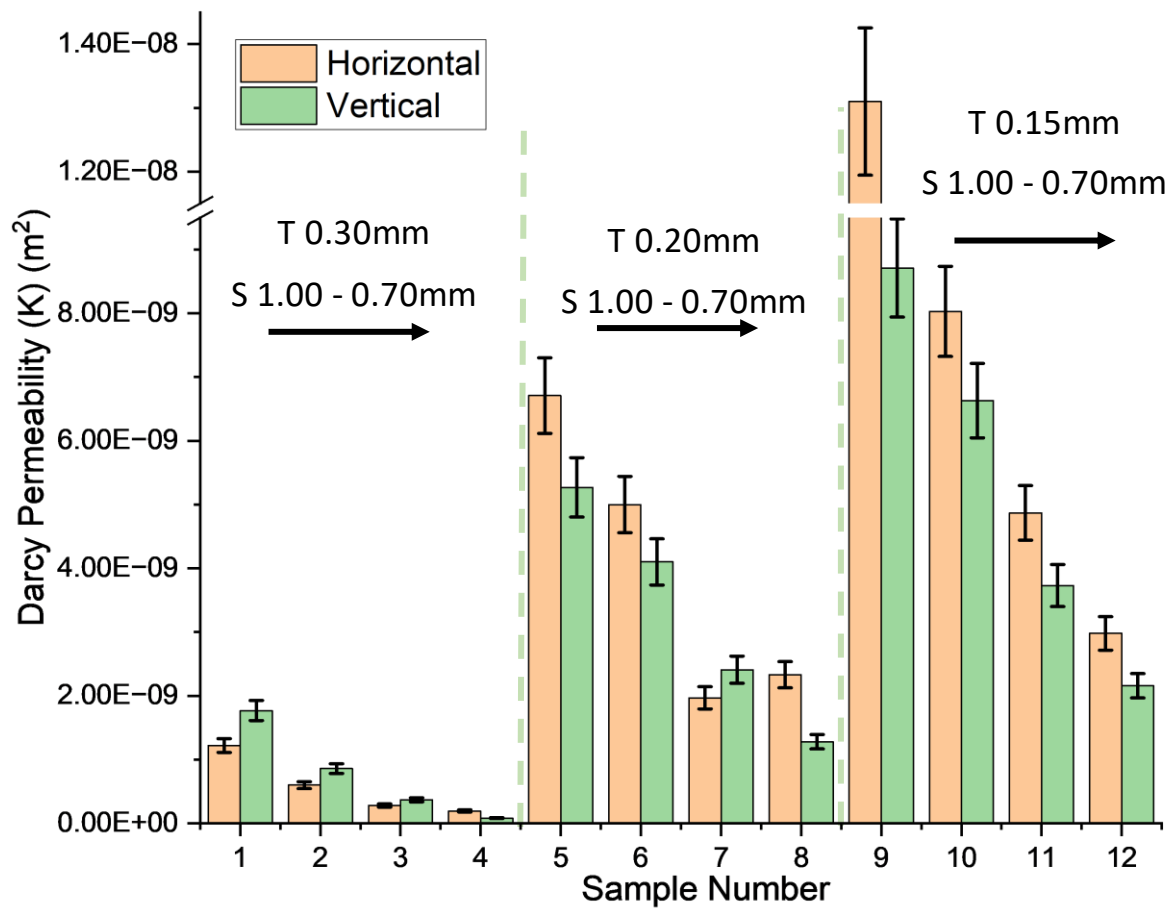


Figure 6-20. Darcy Permeability with respective uncertainty identified by the error bars.

Evidently, the measured permeability values are shown to increase with a reduction in strut thickness and an increase in unit cell size, falling in line with expectations indicating a proportional relationship between permeability and the lattice's porosity and pore size, as later shown in Figure 6-21. As alluded to throughout this study, samples 3 and 4 in both

orientations had porosities and pore sizes significantly lower than the designed parameters resulting in minimal visible line of sight through the samples. This was later confirmed for sample V4 with the use of μ -XCT analysis, highlighted in Section 5.5. The significant reduction in porosity of these samples has resulted in a significantly lower Darcy permeability compared to the other samples. This aligns with the lower slopes and capillary performance of sample set 4 for the rate of rise experiment, highlighted in Figure 6-8 and Figure 6-9 respectively, confirming that, despite the reduced pore diameters, lower permeabilities can have a detrimental effect on the capillarity of the wicking structures.

Interestingly, despite the marginally higher porosities of the vertical samples, the resultant permeability values are consistently smaller than for their horizontal counterparts. This is shown to be true for all 0.20 and 0.15mm strut thickness samples, with the consideration of the associated uncertainties, apart from sample set 7. Conversely, the higher permeability values of the vertical orientations of samples 1 – 3 reflect expectations due to their higher porosities. As previously established, the number of agglomerated particles was shown to increase with a reduction in designed strut thickness as well as being especially prevalent on the vertical samples. This has been shown to play a significant part in increasing both hydrodynamic drag and internal tortuosity, leading to greater energy dissipation and increased effective distance for the liquid to travel [174]. Both of these factors have contributed to the decreased permeability values of the vertical samples identified in Figure 6-20.

Through evaluation of the effects of porosity on permeability in Figure 6-21 (top), it can be seen that once a porosity of ~ 0.70 is achieved, permeability can be seen to rapidly increase. The sudden rise in permeability at higher porosities is also highlighted in the work of Xiao et al. [174]. As porosity increases, tortuosity is likely to decrease significantly, allowing for a more direct route for the flow, reducing internal pressure loss and increasing permeability. This sudden rise is likely less noticeable for the analysis of pore diameter due to porosity being approximately proportional to the cube of the pore diameter. Eleven of the total samples analysed have porosities of below 0.70 with an average permeability of $9.97 \times 10^{-10} \text{ m}^2$. This contrasts with the remaining 13 samples with porosities above 0.70 and an averaged permeability of $5.67 \times 10^{-09} \text{ m}^2$. However, it should be highlighted that as the associated error

is relative, the uncertainty of the larger porosity samples is significantly larger than that of the lower porosities.

The assessment of the effects of pore diameter in Figure 6-21 (bottom) shows a fairly linear relationship with coefficients of determination values of 0.82 and 0.93 for the horizontal and vertical samples, respectively. However, as various design combinations resulted in similar pore dimensions but vastly different porosities, the permeability can deviate significantly within a narrow band of pore diameters. This analysis shows the importance of both porosity and pore size when considering permeability.

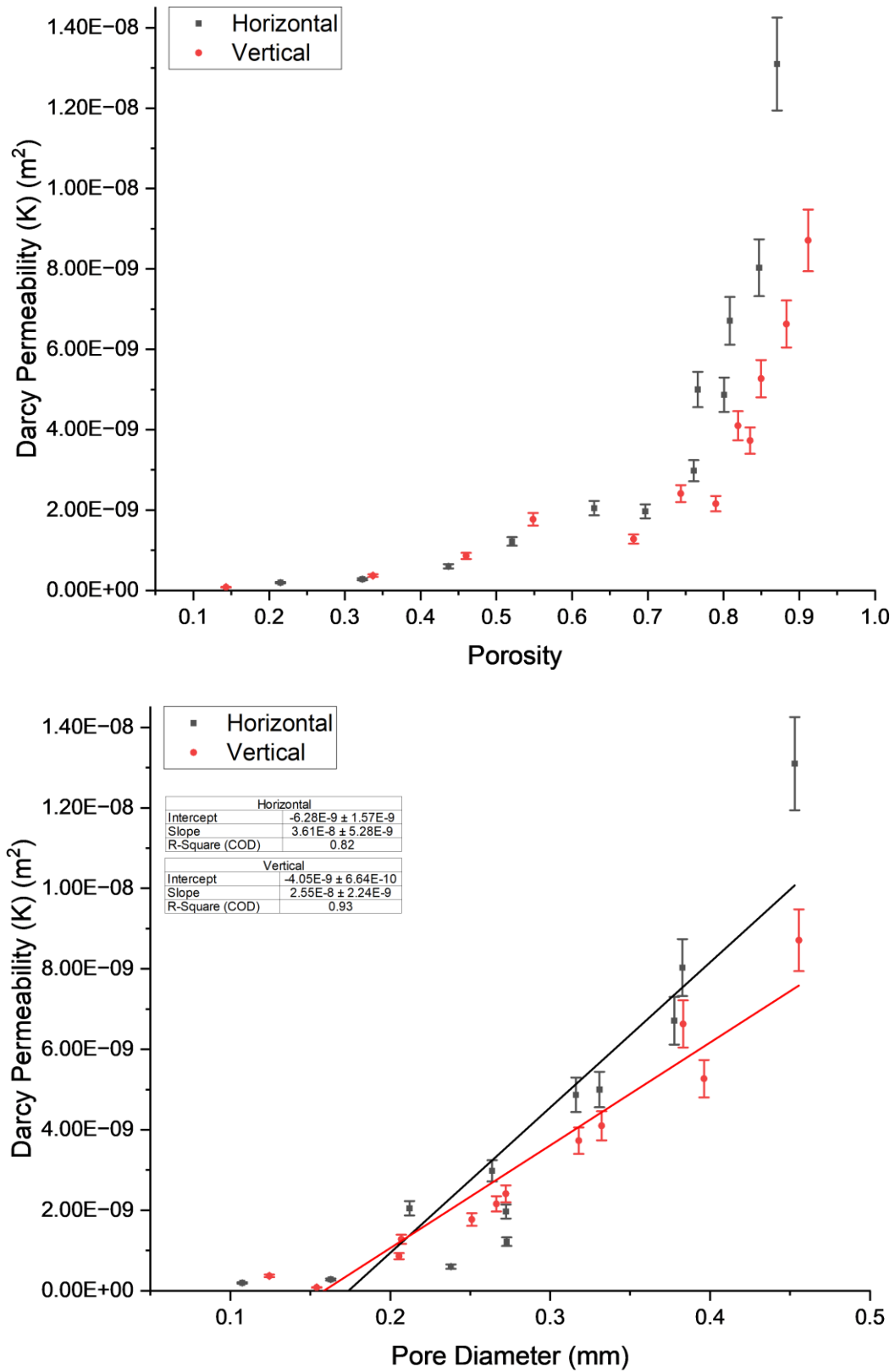


Figure 6-21. Effects of change in porosity (Top) and pore diameter (Bottom) on measured Darcy permeability

6.2.5 Forchheimer Correction

As set out in Section 3.5.2.1, determination of the Darcyan Forchheimer permeability (K_1) and associated non-Darcyan coefficient (K_2) may be determined through linear regression as per Equation (3-30). Figure 6-22 shows the fitted curves for a range of samples.

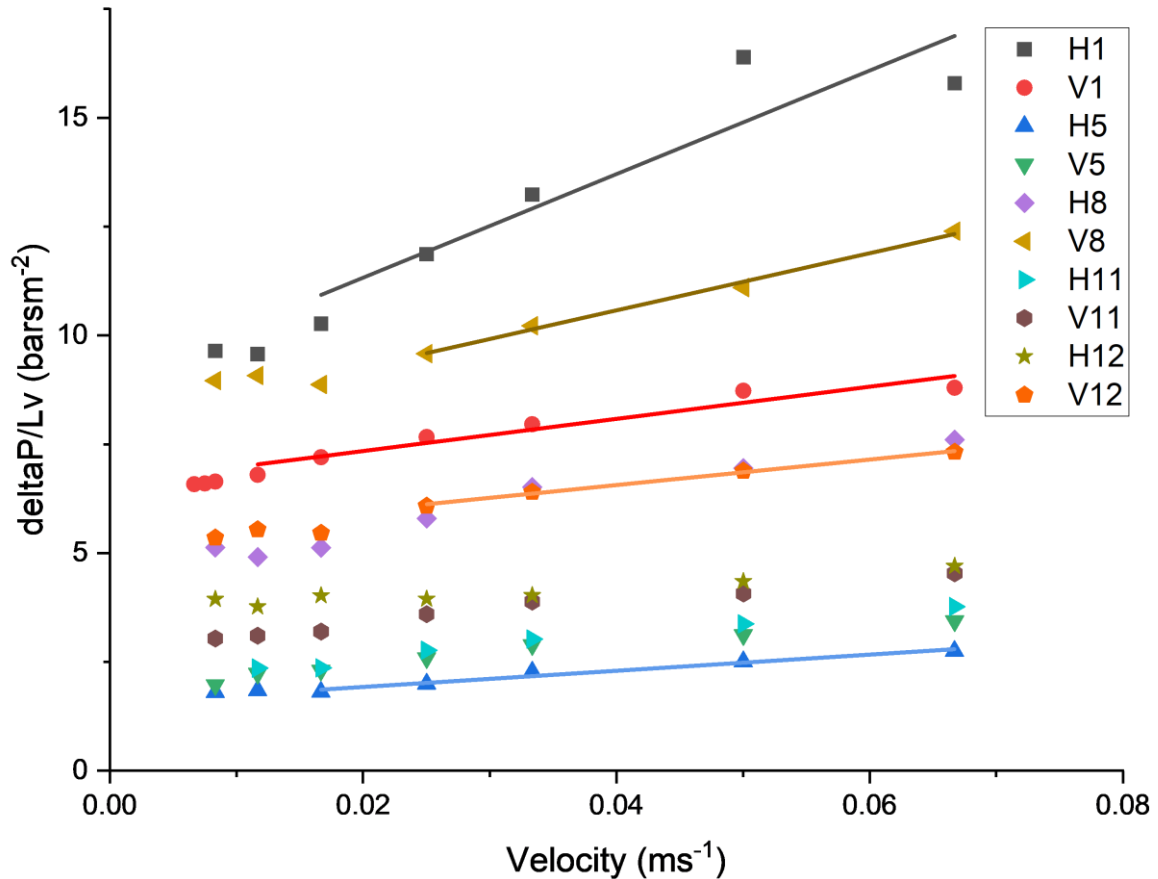


Figure 6-22. Example of fitted curves for a range of samples for determination of the Darcyan and non-Darcyan Forchheimer coefficients.

Evidently, both the gradient and intercept of the fitted curves change with each sample contributing towards K_1 and K_2 , respectively. The determined Darcyan Forchheimer permeability (K_1) of each sample is shown in Figure 6-23. A consistent trend between sample design parameters and determined permeability was seen, as previously identified in Figure 6-20. Clearly, the determined Forchheimer permeability (K_1) is higher than that previously calculated with Darcy's law by an average value of 9.54%. This is due to Forchheimer's equation accounting for both viscous and inertial losses, whereas Darcy's law only accounts for viscous losses. The consistency between the various relationships of K and K_1 , further add

to the validity of the experiment and increased uncertainty at the lower pressure differentials previously determined.

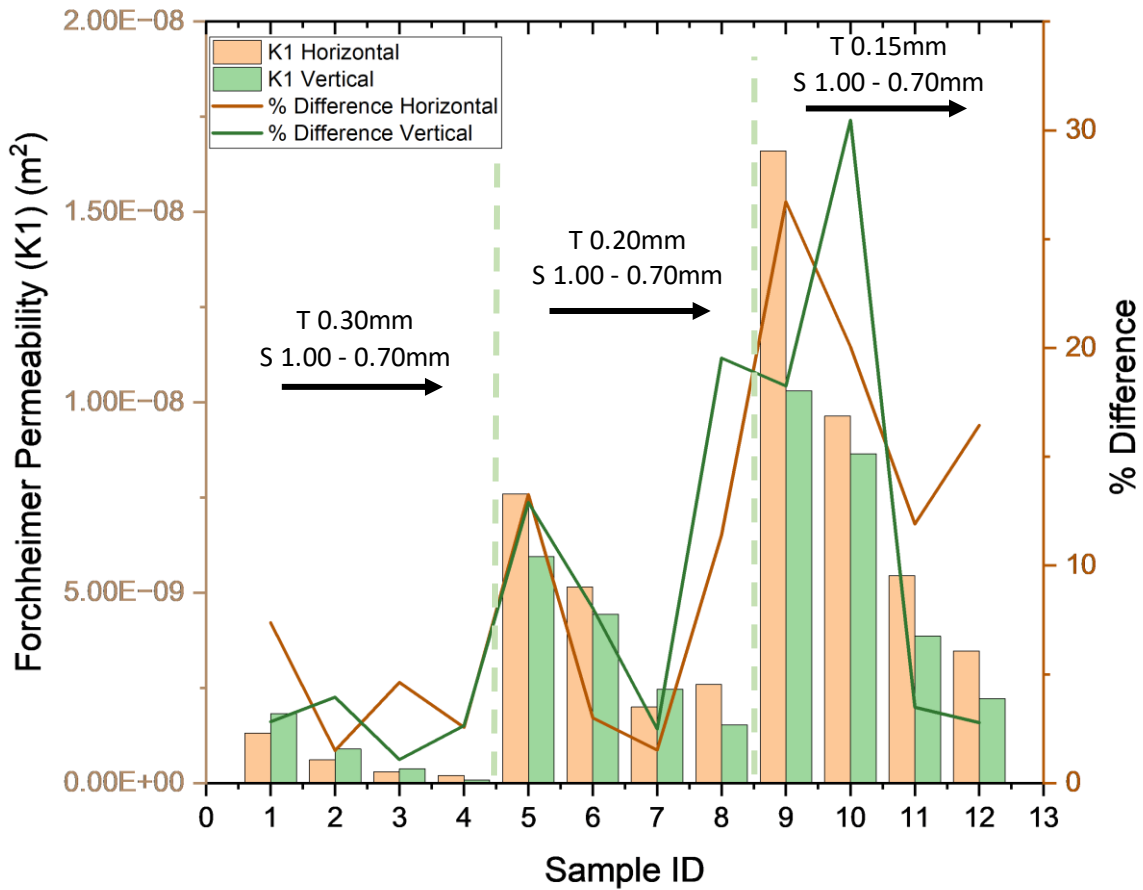


Figure 6-23. Forchheimer Permeability (K_1) for each sample along with % difference from Darcy permeability (K) values.

The determined Forchheimer coefficients, accounting for the inertial effects at higher flow rates, for each sample is shown in Figure 6-24. This highlights the ability of the sample to accommodate higher flow rates. A higher K_2 value results in a smaller Forchheimer term in Equation (3-29) and therefore, the quadratic relationship has less influence on the measured differential pressure. Further evaluation and discussion of the applicability of the Forchheimer Equation for AM lattice structures is shown in Section 7.5 in addition to a comprehensive literature-based comparison in Chapter 8.

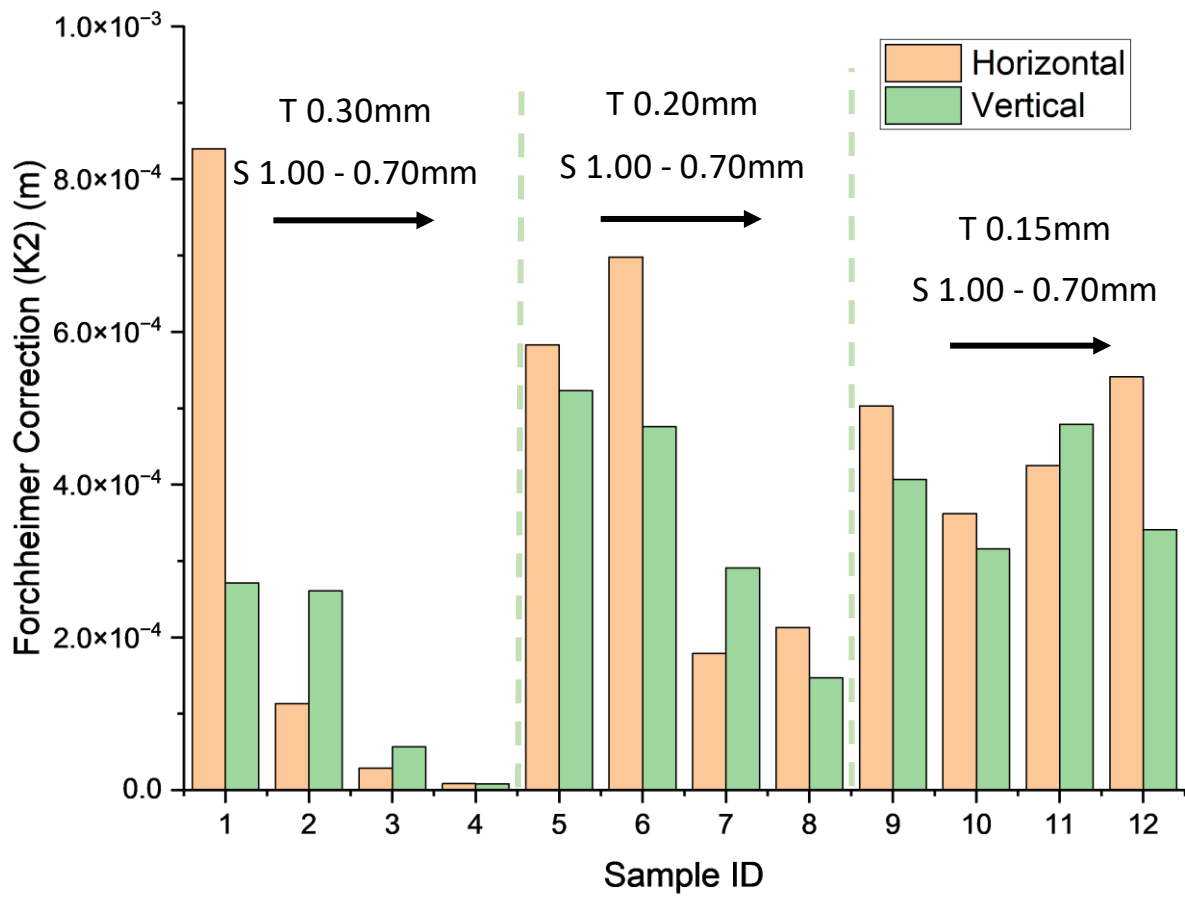


Figure 6-24. Forchheimer inertial term (K_2) for each sample.

6.3 Chapter Summary

This chapter characterised the efficacy and performance of the additively manufactured lattice structures in their raw state. This was achieved through performing two separate capillary rate of rise and permeability experiments while drawing on the findings of Chapter 5. The conclusions drawn from this chapter can be summarised as follows:

- The vertical samples consistently showed a higher equilibrium rise height compared to that of the horizontal set with a maximum rise of 57.9mm achieved for sample V3. Both orientations showed proportionality with the designed strut thickness and inverse proportionality to the cell size, aligning with a reduction in manufactured pore diameter. The pore size distribution of the horizontal samples was found to contribute to the overall deviation between orientations. For the 0.30mm strut thickness samples of smaller pore diameters, the rise height was able to approach the smaller pores located at the centre of the sample where an overall reduction in rise height deviation between orientations was seen.
- Jurin's law was shown to consistently over predict the rise height, with deviations increasing with a reduction in cell size. This aligned with an increase in pore density throughout the sample, adding to further deviations from Jurin's idealised capillary tube experiment. Cell size was shown to have little effect on the measured surface roughness, indicating that factors such as pore interconnectivity and tortuosity were influential in the determination of the structure's theoretical equilibrium rise height.
- The importance of the trade-off between capillary pressure and permeability was highlighted. The vertical samples generally resulted in higher K/r_{eff} values despite having higher mean porosities and similar pore diameters.
- Despite the increased amount of agglomerated particles on the vertical samples, they generally exhibited higher capillary performance. This could be a result of the additional structures providing additional flow paths and localised high capillary pressure. However, the inclusion of these features was shown to increase drag under forced flow conditions resulting in lower permeability.
- Through consideration of the permeability-based Reynolds number (Re_K), the transition between Darcyan and non-Darcyan flow was shown to be proportional to the designed cell size and inversely proportional to the strut thickness with transitional Re_K values

ranging from 0.047 for sample H4 to 1.794 for sample H9. The horizontal samples consistently showed higher Re_k values than their vertical counterparts. A linear trend was seen with respect to pore diameter, while porosity signified more of an exponential relationship with a sudden rise in Re_k at higher porosities.

- The Darcyan permeability of the samples varied from $8.32 \times 10^{-11} \text{ m}^2$ for sample V4 to $1.66 \times 10^{-8} \text{ m}^2$ for sample H9. Despite the higher porosity of the vertical samples of 0.20 and 0.15mm strut thickness, they consistently showed lower permeability under Darcy state, again highlighting the effects of the semi-sintered particles and increased surface roughness. The vertical orientations of samples 1 – 3 (0.30mm strut thickness) were shown to have significantly fewer agglomerated particles on the surface which resulted in a higher permeability value, aligning with their higher porosities.
- With the consideration of both capillary rate of rise and permeability experiments, sample V12 was identified as the most favourable design allowing for the trade-off between permeability, capillary performance and achievable rise height. Further developments to pursue reduced cell sizes may also be possible with the 0.15mm strut thickness samples.

7. Effects of Chemical Polishing

As identified throughout this study, the rate of agglomerated particles and surface roughness has been shown to have a significant effect on the capillary performance and permeability of the samples. This chapter will therefore present and discuss the results of the chemical polishing methodology set out in Section 3.5.3 while drawing on the previous findings of Chapters 5 and 6. A literature-based comparison to both other AM and conventional wicking structures is discussed in Chapter 8.

7.1 Initial Investigation

As mentioned in Section 3.5.3, although successful in reducing the surface roughness, removing semi-sintered particles and enhancing sample hydrophilicity, the initial trials with the sacrificial samples following the methodology set out by Sharma et al. [108, 109] proved unsuccessful at removing the insoluble reaction products of the phosphoric acid stage for this current investigation, as shown in Figure 7-1.

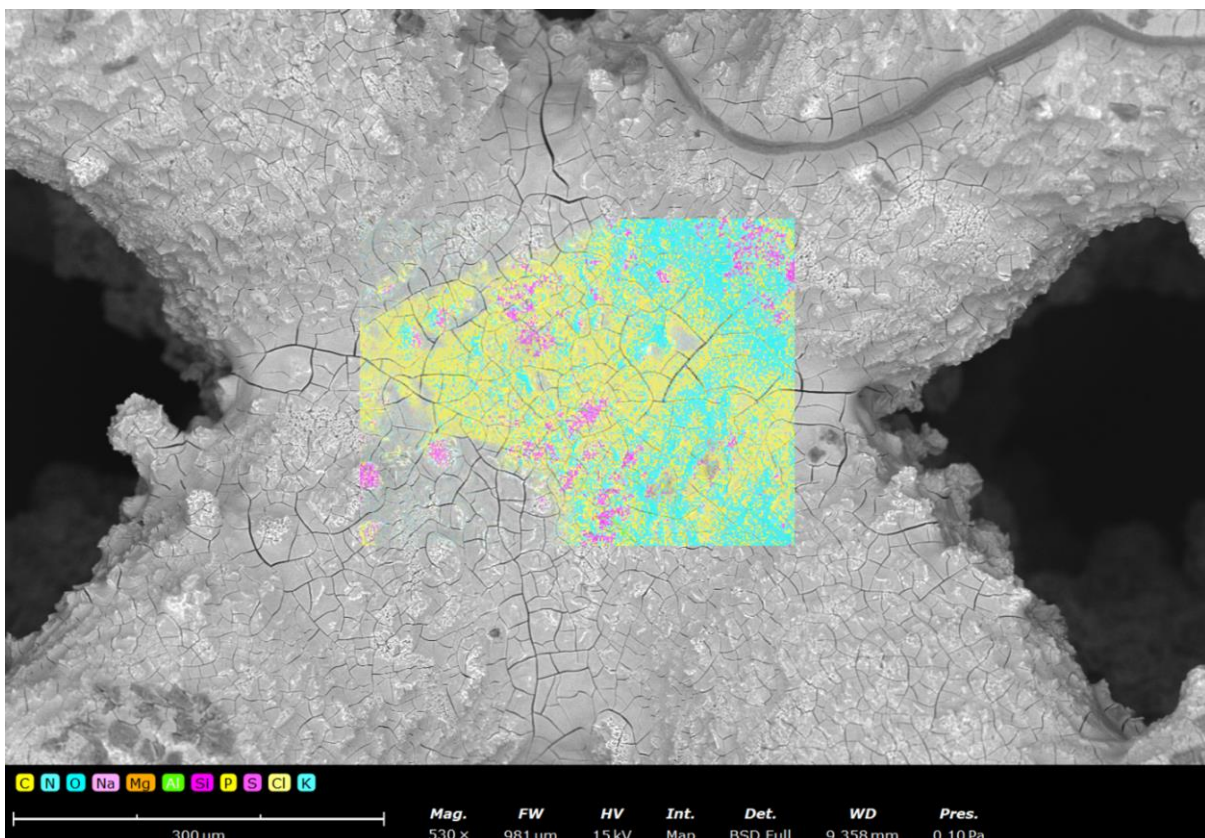


Figure 7-1. SEM Image and XCT analysis of Sample V1.2.

The cracked surface at the node trough shown in Figure 7-1, clearly identifies residual material on the sample's surface with high phosphorus and oxygen content – in line with the

insoluble products of the phosphoric acid reaction. Figure 7-2 identifies the intensity of the emitted x-rays for each detected element across the entire spectrum.

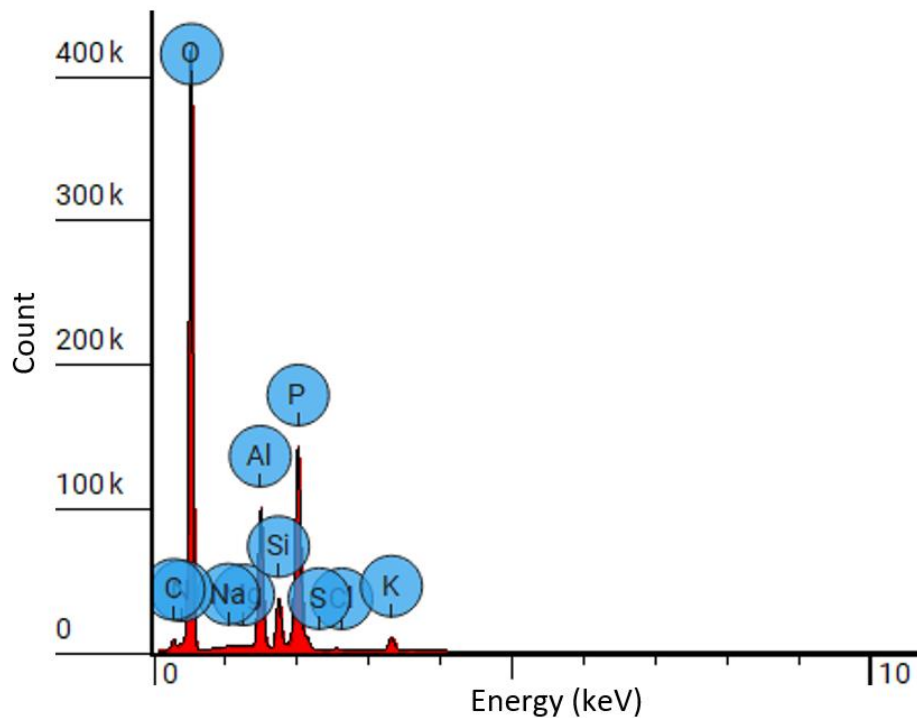


Figure 7-2. Element spectrum of EDX map scan on sacrificial sample V1.2

Through analysis of the defined area of the node trough, high oxygen and phosphorus content were detected. A similar result was also seen for sample H1.1 with the atomic and weight concentrations of each detected element shown in Table 7-1.

Table 7-1. EDX analysis summary of samples V1.2 and H1.1 after initial etching.

Element Number	Element Symbol	Element Name	V1.2		H1.1	
			Atomic Conc.	Weight Conc.	Atomic Conc.	Weight Conc.
6	C	Carbon	3.9	2.5	5.0	3.1
7	N	Nitrogen	1.6	1.2	2.3	1.4
8	O	Oxygen	71.9	60.9	63.5	52.2
11	Na	Sodium	0.0	0.0	0.0	0.0
12	Mg	Magnesium	0.0	0.0	0.0	0.0
13	Al	Aluminium	8.5	12.1	15.0	20.7
14	Si	Silicon	2.4	3.5	3.3	4.8
15	P	Phosphorus	10.4	17.1	10.0	15.9
16	S	Sulphur	0.0	0.0	0.0	0.0
17	Cl	Chlorine	0.0	0.0	0.0	0.0
19	K	Potassium	1.4	2.8	0.9	1.9

This analysis has confirmed the presence of a highly concentrated oxygen and phosphorus surface accounting for 60.839% and 17.083% by weight, respectively, for sample V1.2 and

52.200% and 15.900% for sample H1.1. As an elemental analysis technique, EDX concentrates analysis on the surface with limited sample penetration. With this in mind, for both analysed samples, no presence of magnesium and only low levels of silicon (3.497% / 4.800%) and aluminium (12.088% / 20.700%) were detected on the surface of the analysed area. This further points towards the presence of a residual surface covering the base material. This contrasts with the results of the same analysis of the raw samples prior to initial chemical etching shown in Table 7-2.

Table 7-2. Averaged EDX elemental analysis of additional raw samples.

Element Number	Element Symbol	Element Name	Atomic Conc.	Weight Conc.
6	C	Carbon	10.9	5.3
8	O	Oxygen	5.6	3.6
12	Mg	Magnesium	0.5	0.5
13	Al	Aluminium	75.2	81.8
14	Si	Silicon	7.8	8.8

Evidently, following the initial etching stage, aluminium content reduced by 85.23% and 74.71% for samples V1.2 and H1.1, respectively. The unknown long-term stability of aluminium phosphate and silicon dioxide under elevated temperatures and heat pipe thermal cycling operating conditions poses further problems. The excessively cracked residual surface, shown in Figure 7-1, could become dislocated from the main lattice body over time. This could result in significant blockages within the porous structures, resulting in decreased permeability and reduced heat pipe performance. This scenario would reflect the findings of Bhullar et al. [175], discussed further in Appendix 12.4.3. Furthermore, the improved wettability may be a result of the significant change in chemical composition of the surface, which again could change under possible surface deterioration. Therefore, removal of the fractured residual surface is essential for further development of this study.

Although hydrochloric acid was incorporated into the etching solution with the intention of promoting the dissolution of the solid aluminium phosphate and silicone dioxide products, it is clear that the concentration of hydrochloric acid within the etching solution is insufficient for this current study. For this work, the samples had undergone an additional etching stage with 10% hydrochloric acid. This was mainly due to laboratory access restrictions and time constraints. A further parameter study into the chemical concentrations and timings should be performed in future studies, which falls outside the scope of this work. Initial trials included

a 30s and 60s etch for sacrificial samples H1.1 and V1.2, respectively, having already undergone initial polishing in the original etching solution. Three separate EDX scans were taken for each sample with the average concentrations for each shown in Table 7-3.

Table 7-3. Averaged EDX analysis summary of samples V1.2 and H1.1 following additional HCl etching.

Element Number	Element Symbol	Element Name	V1.2 (60s)		H1.1 (30s)	
			Atomic Conc.	Weight Conc.	Atomic Conc.	Weight Conc.
6	C	Carbon	14.1	7.0	11.4	6.3
7	N	Nitrogen	0.4	0.2	0.0	0.0
8	O	Oxygen	6.8	4.5	5.8	3.5
11	Na	Sodium	0.1	0.1	0.0	0.0
12	Mg	Magnesium	0.3	0.3	0.3	0.3
13	Al	Aluminium	59.0	65.6	56.4	62.4
14	Si	Silicon	19.3	22.3	26.1	27.5
15	P	Phosphorus	0.0	0.0	0.0	0.0
16	S	Sulphur	0.0	0.0	0.0	0.0
17	Cl	Chlorine	0.0	0.0	0.0	0.0
19	K	Potassium	0.0	0.0	0.0	0.0

The efficacy of the additional hydrochloric etch step was undeniably shown to be an essential stage in the dissolution of the phosphorus and oxygen-rich residual surface, and may be visualised in the EDX combined map shown in Figure 7-3. Furthermore, as both the 30s

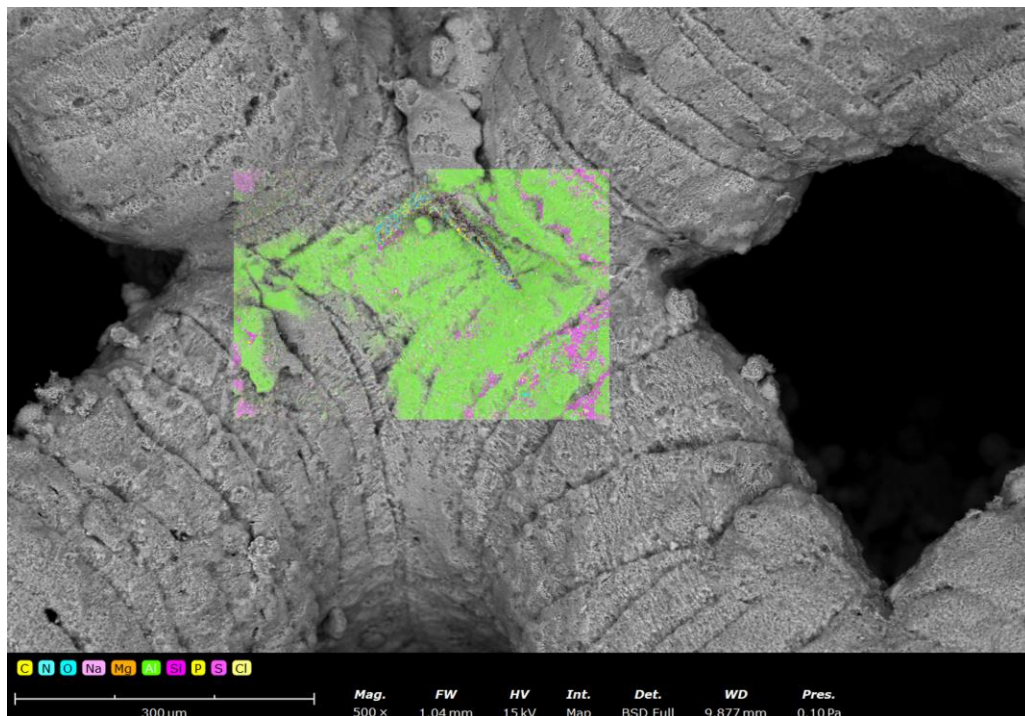


Figure 7-3. Combined EDX map of sample V1.2 after hydrochloric acid etch.

and 60s etched samples showed similar results, it was decided to proceed with the 30s hydrochloric etch stage, minimising the possibility of sample damage and structural losses.

Here, the residual surface has clearly been removed with minimal phosphorus and oxygen content identified across both analysed samples. Furthermore, the visibility of the build layers is clearly recognisable, exemplifying the staircase effect of the overhanging lattice beam structures. Prior to the hydrochloric acid etch, all trialled samples were showing limited lateral line of sight through the samples, indicating significant blocked pores due to internal residual material. However, following the additional measures carried out, all etched samples showed significant improvement resembling that of the as built components. However, as can be seen from Table 7-3, the samples showed increased Silicon content, indicating the solution's ineffectiveness for the removal of Silicon. Sharma et al. [108, 109] used the same solution to chemically polish $\text{AlSi}_{10}\text{Mg}$ bulk structures and found no change in the elemental concentrations of the material. Their previous study included the study of a flat surface and recommended further exploration of curved geometries. Nonetheless, as the purpose of this study is to determine whether chemical polishing could have an impact on the capillarity and permeability performance of these lattice structures, this increased Silicon content was deemed acceptable and paves the way for future research opportunities.

7.2 Analysis of polished samples

Upon performing the first stage chemical polishing of the original raw samples for the 3 minute period, sample H10 (S0.90mm, T0.15mm) appeared to show significant damage to the lattice matrix, especially on the outer edges. For this reason, it was decided to only perform the first stage for 1 minute for the remaining 0.15mm strut thickness samples. Following the completion of both etching stages, a distinct visual change was seen across all samples. Previously, the final layer of the raw horizontal samples was significantly darker in colour compared to the same face of their vertical counterparts. Subsequently, the colours across all faces of each sample had homogenised to a darker shade, with little difference between the horizontal and vertical samples. Furthermore, upon performing microscopy analysis, the excessive levels of agglomerated powder that were seen previously had been drastically reduced across all samples, as shown in Figure 7-4.



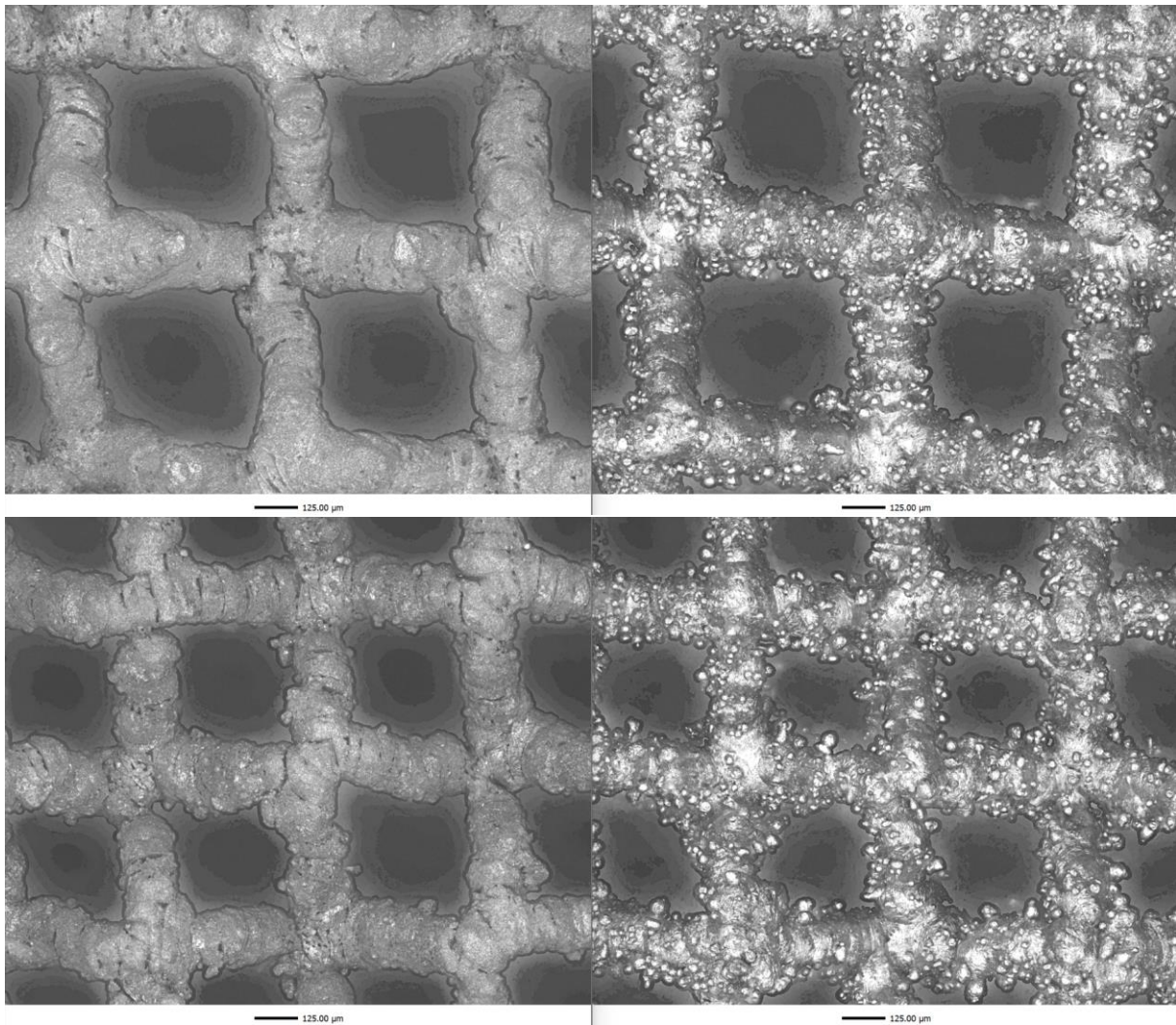


Figure 7-4. Chemically Polished (Left) and Raw (Right) stacked microscopy images of samples V6 (Top) and V12 (Bottom).

Some agglomerated particles were still present on sample V12 due to the reduced etching time. However, the severity of powder particles semi-sintered onto the surface were significantly reduced compared to its raw state. Adding to the defective characteristics of the horizontally printed samples, excessive strut dislocations were seen following chemical polishing. These defects were seen to progress throughout the thickness of the samples, with internal dislocations clearly visible in Figure 7-6.

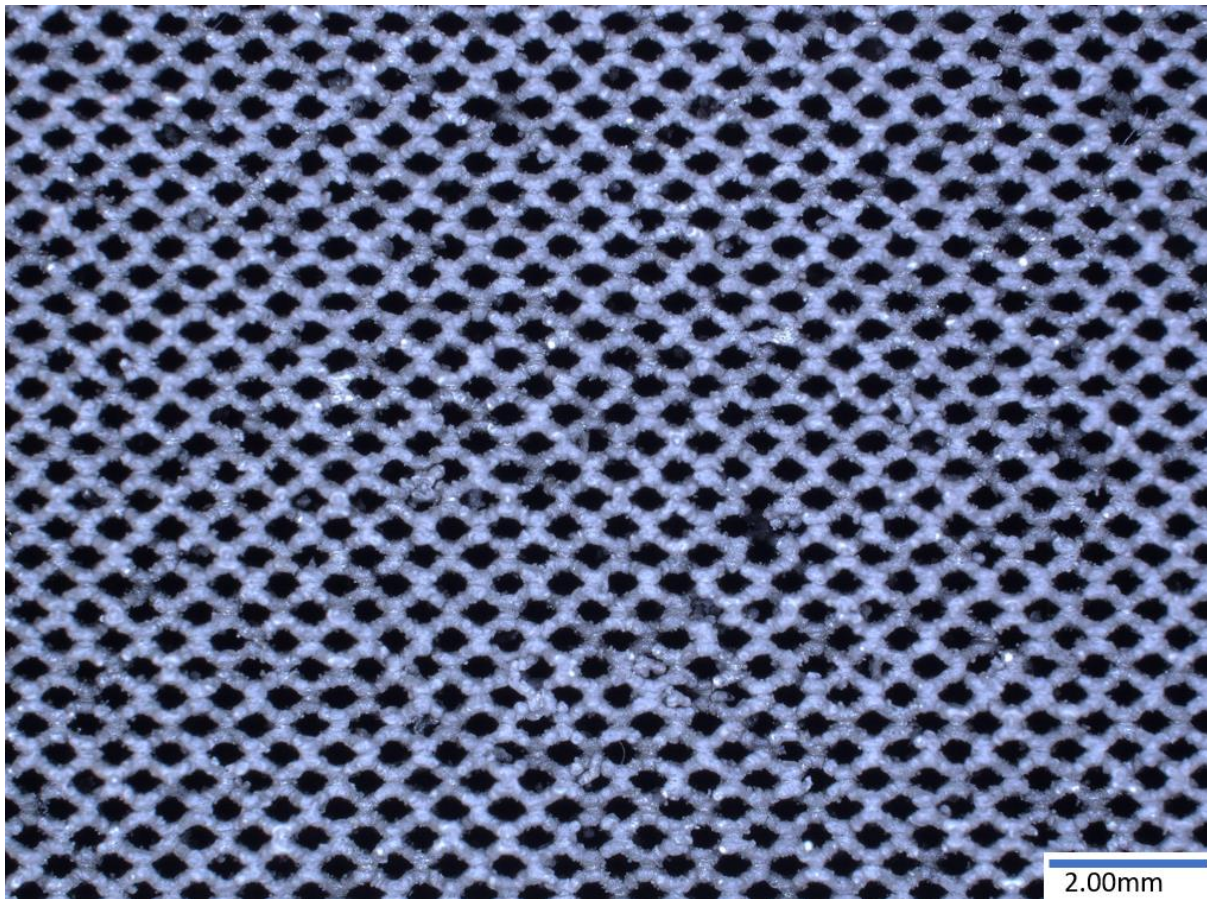


Figure 7-6. Microscope image of Chemically polished sample H12.

As previously discussed, the raw horizontal samples were warped due to excessive internal residual stresses resulting from the inherent high thermal gradient associated with the printing process. The additional damage to the structures was due to the removal of material during the chemical polishing process which resulted in imbalances of the stress distribution that were previously in equilibrium. This is further shown in Figure 7-5, where the internal damage previously identified through XCT and highlighted in Figure 5-50 has propagated towards the outer face.

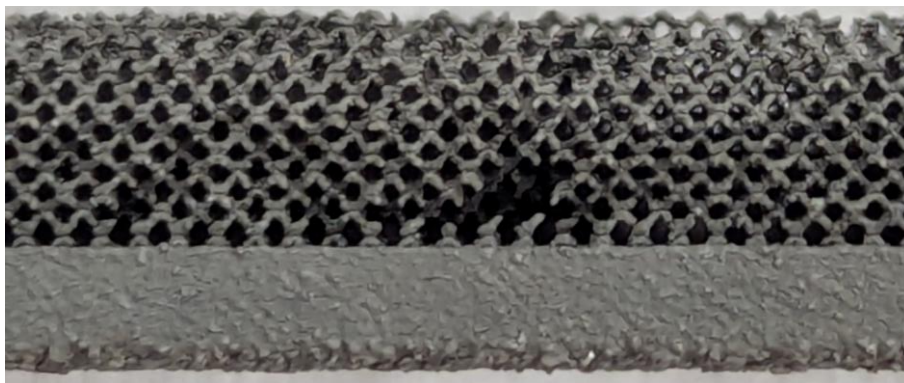


Figure 7-5. Damaged side face of sample H12 following chemical polishing.

Following EDX analysis at three different locations on each processed sample, shown in Table 7-4, it can be seen that no phosphorus, sulphur, chlorine, sodium or nitrogen was present. This indicated that no residual byproduct resulting from the use of potassium nitrate, or the surfactant, which could impact their fluidic performance, was present on the surface of the samples. Furthermore, as was the case for the trials, similarly high silicon content was also detected on the samples, as can be seen Table 7-4.

Table 7-4. Summary of averaged EDX analysis summary of final polishing of both horizontal and vertical samples following additional HCl etching.

Element Number	Element Symbol	Element Name	Averaged Horizontal Samples		Averaged Vertical Samples	
			Weight Conc.	Standard Deviation	Weight Conc.	Standard Deviation
6	C	Carbon	3.22	1.25	2.28	0.85
8	O	Oxygen	6.81	0.39	5.83	0.23
12	Mg	Magnesium	0.37	0.02	0.35	0.04
13	Al	Aluminium	63.96	1.03	66.20	1.56
14	Si	Silicon	25.27	1.58	25.06	1.72

The high presence of silicon, along with the identified oxygen content, could be a result of the insoluble SiO_2 byproduct of Equation (3-35). In its raw state, the presence of magnesium and silicon contributes to a harder and stronger structure, compared to pure aluminium, due to the formation of Mg_2Si precipitate. Furthermore, the formation of its naturally occurring oxide layer adds to the material's high corrosion resistance [176]. When considering the work undertaken in this study, the reduced aluminium surface concentration, balanced by the higher silicon concentration, could result in a harder and possibly more brittle structure. As a result, the durability and long-term resilience of the structures under dynamic and thermal cycling conditions should be examined, though this lies beyond the scope of the current research.

Through analysis of several studies, the surface energy of aluminium is typically shown to be between 0.71 and 1.27J/m^2 with an average value of 1.05J/m^2 [177, 178] which is lower than the surveyed literature results of silicon, identifying a range of $1.05 - 1.23\text{J/m}^2$ with a slightly higher averaged value of 1.15J/m^2 [179-182].

For clarity, a summary of polishing times and completed experiments for each sample is shown in Table 7-5.

7. Effects of Chemical Polishing

Table 7-5. Summary of etching time and completed experiments for polished samples.

Sample	Initial Etch Time (s)	Secondary Etch Time (s)	Rate of Rise	Permeability
H1	180	30	✓	✓
V1	180	30	✓	✓
H5	180	30	✓	✗
V5	180	30	✓	✓
H6	180	30	✓	✓
V6	180	30	✓	✗
H10	180	30	✓	✗
V10	60	30	✓	✗
H12	60	30	✓	✗
V12	60	30	✓	✓

7.3 Geometric Impact

As discussed throughout, reducing the surface roughness via chemical polishing is expected to lead to an increase in both pore size and porosity, as a result of a reduction in strut thickness.

7.3.1 Strut Thickness

With the aim of minimising the impact on the bulk geometry of the lattice structures, and hence their capillary characteristics, Figure 7-7 shows the averaged strut diameters across the whole sample along with the standard deviations represented by the error bars, in addition to the percentage reduction from their raw state and deviation from the intended CAD design.

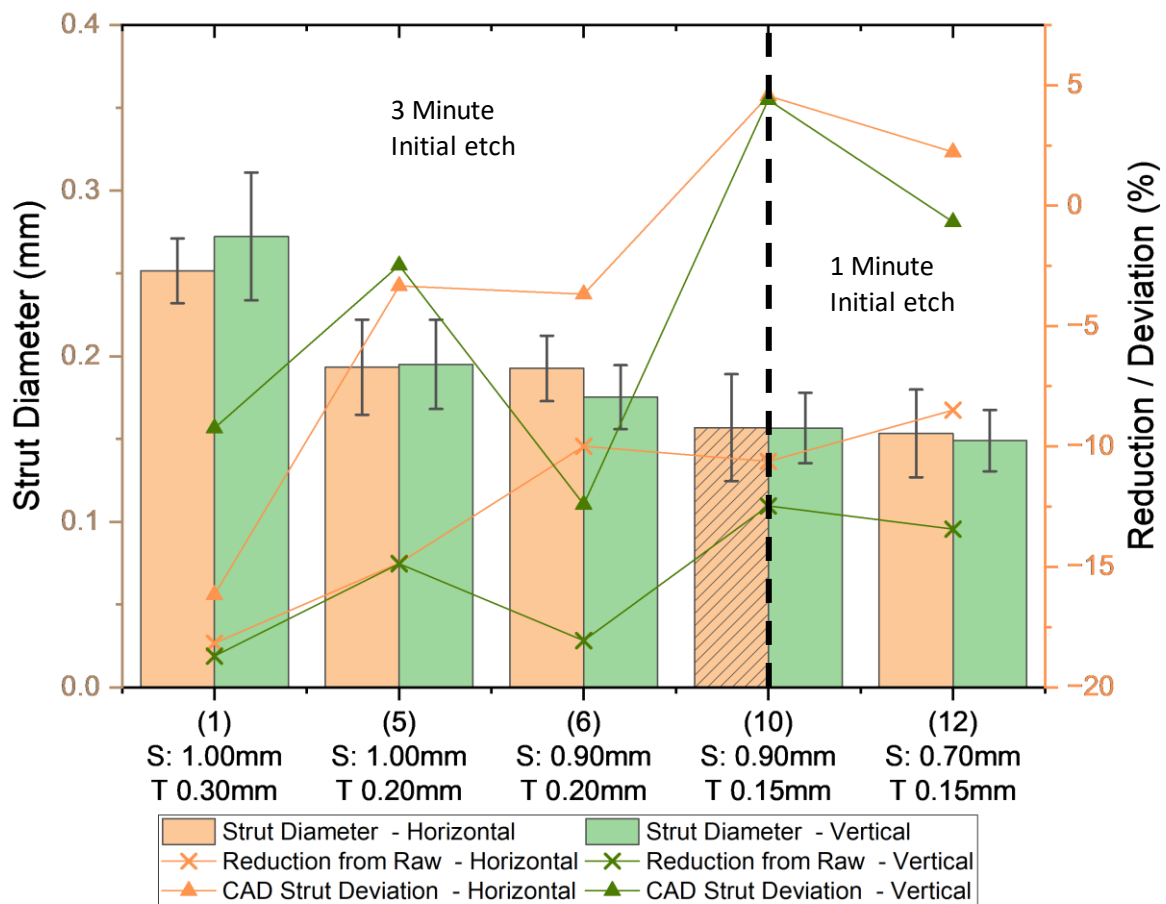


Figure 7-7. Measured strut diameters of polished samples with reduction from raw state and deviation from original CAD design. N.B. Sample H10 shows significant damage.

Similar to in their raw state, little deviation was measured between the horizontal and vertical orientations, with sample 1 showing the largest discrepancy. However, the vertical orientations did show a greater reduction in strut diameter, indicating increased etching rates

compared to that of the horizontal samples. This was due to the increased number of agglomerated particles and number of build layers seen within the vertically printed samples leading to weaker interfaces that were more vulnerable to etching from the solution. Additionally, potential difference in grain microstructure between the orientations could have contribute to increased etching of the vertical samples.

Interestingly, the 0.15mm strut thickness samples (9 and 10) now show the smallest deviation from the intended design. This is a sizable contrast to that of the raw samples, previously highlighted in Figure 5-8, where the 0.15mm strut thickness showed greatest deviation. The damage and dislocated struts previously identified on the horizontal samples, in particular that of sample 10, are characterised here with generally larger standard deviations, represented by the error bars, compared to that of the vertical samples.

7.3.2 Pore Characteristics

As previously highlighted through μ -XCT analysis shown in Section 5.5, the 0.30mm strut thickness samples showed significantly higher trapped porosities compared to the 0.20 and 0.15mm designs. Following on from the chemical polishing stage, the removal of material has resulted in the internal defects close to the surface being revealed, as shown in Figure 7-8.

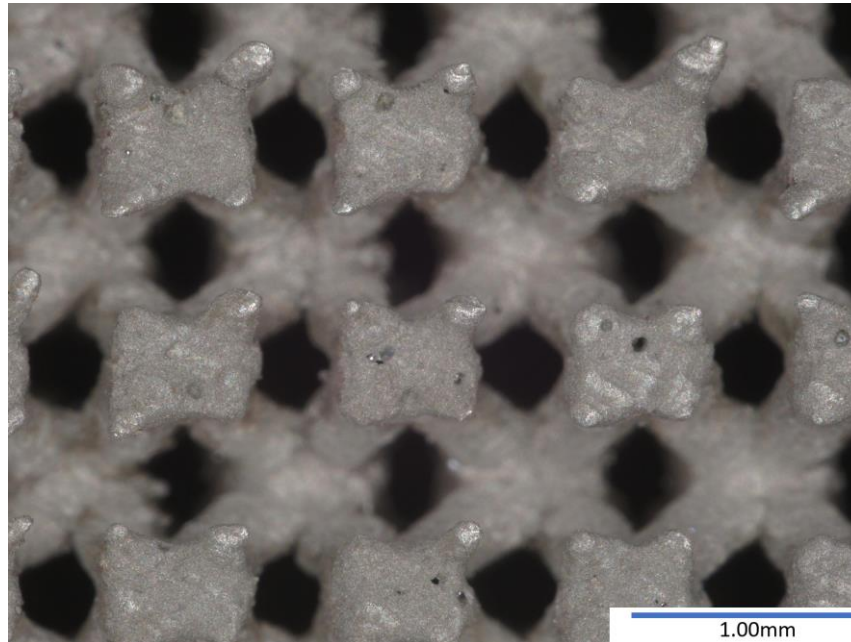


Figure 7-8. Microscope image of Sample V1 identifying surface keyhole pores.

With a full scan of the samples, LAT successfully identified numerous surface keyhole pores present, shown in Figure 7-9.

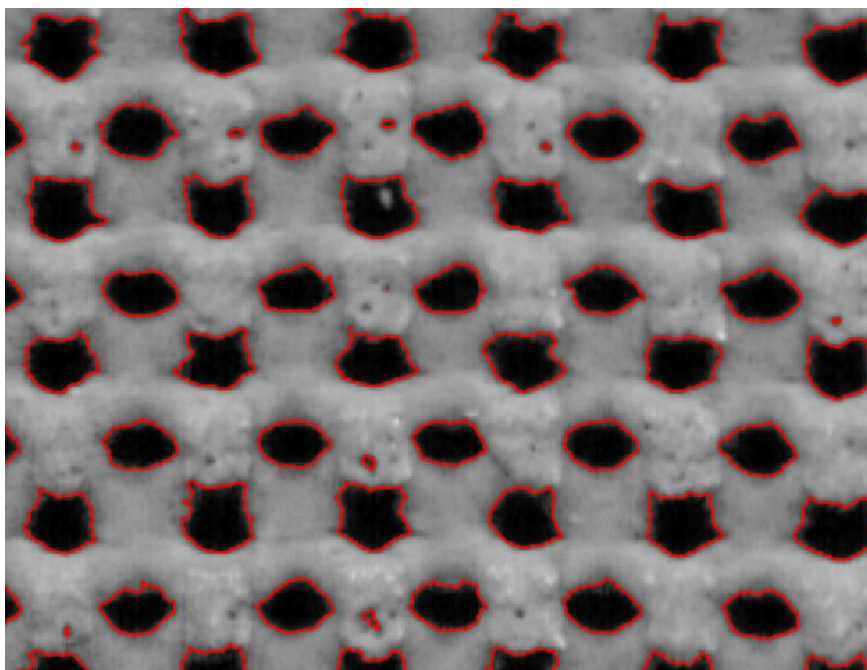


Figure 7-9. Sample V1 surface keyhole pores identification with LAT.

Although some of the smaller pores weren't detected due to the resolution of the scan, this methodology gives a good indication of their overall severity and the distribution of surface keyhole porosities, with pore diameter heatmaps for sample H1 shown in Figure 7-10.

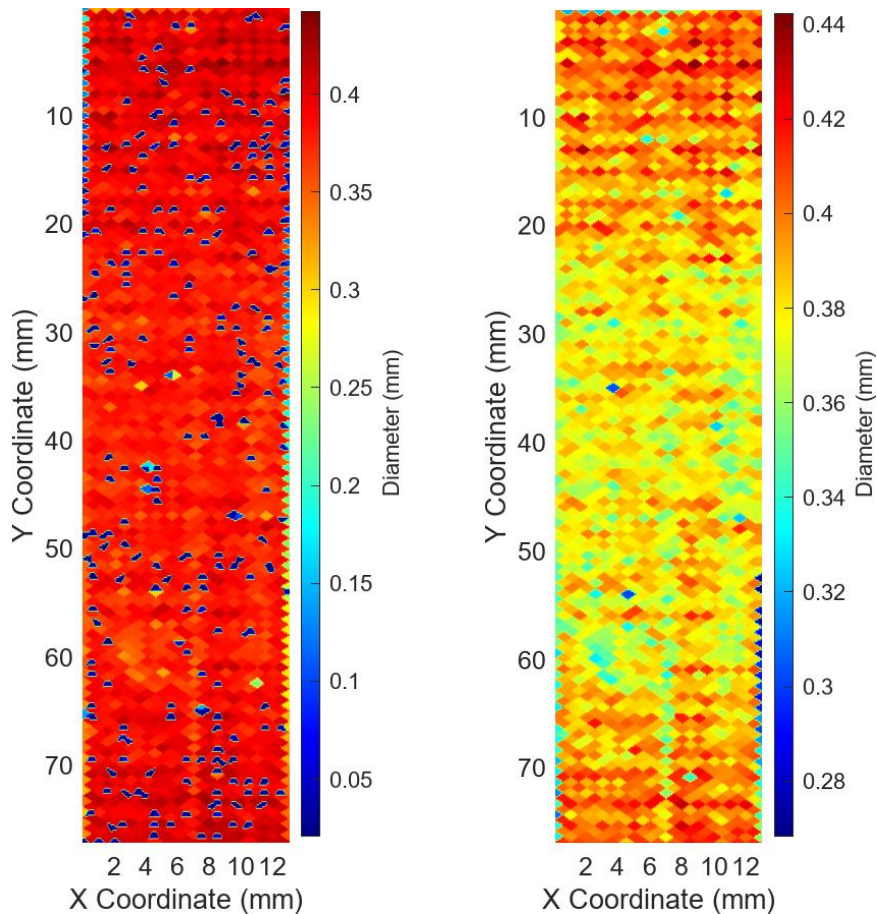


Figure 7-10. Pore diameter heatmap for sample H1 identifying surface keyhole pores (left) and warpage (right) with smaller keyhole pores disregarded.

As can be seen, through setting an appropriate threshold for the pore areas of interest, the heatmaps in Figure 7-10 emphasise both the keyhole pore distribution and the impact of warpage on the horizontal samples which resulted in smaller pores at the centre of their lengths. A similar trend was found for all other polished horizontal samples, in line with that previously seen for their raw states. Figure 7-11 shows the averaged pore diameters across the front face of each sample with the standard deviations represented by the error bars. Following the chemical polishing process, the vertical orientations of samples 5, 6, 10 and 12 showed larger pore diameters than their horizontal equivalents, in line with that previously identified for the raw samples in Figure 5-15. The measured pores of the horizontal

orientation of sample 1 were also shown to be larger than its vertical counterpart, again in line with that seen for the raw sample.

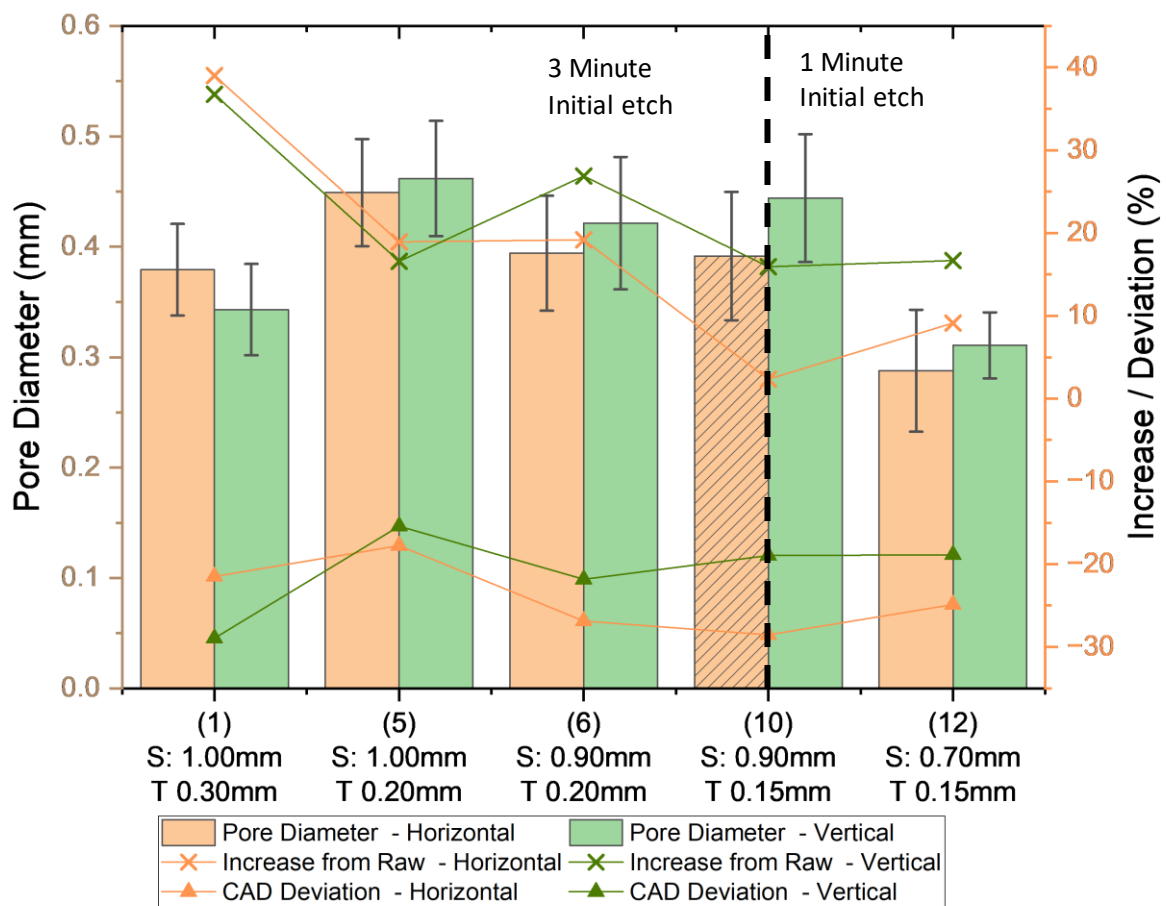


Figure 7-11. Measured pore diameters of polished samples with increase from raw state and deviation from original CAD design. N.B. Sample H10 shows significant damage.

With an increase of approximately 38% for both horizontal and vertical orientations of sample 1, significant reduction in delivered capillary pressure may be seen. However, this could be overcome by the reduced surface roughness and increased hydrophilicity of the polished samples, as discussed throughout this chapter.

7.3.3 Surface Roughness

In line with the methodology set out in Section 3.4.1, the L-filter nesting index cut-off value was kept to five times the scale of the coarsest structure of interest, as per ISO 25178 [131]. Due to the noticeable reduction in both count and diameter of the agglomerated particles on the surface following chemical polishing, the coarsest structure of interest, and hence the L-filter cut-off value, required re-evaluation. Again, twenty particle measurements were taken on three separate samples leading to an average diameter of 0.020mm, and a L-filter nesting index of 0.100mm. Interestingly, through comparing the measured particle diameters before and after the second hydrochloric etch stage, little difference in average particle size was seen with the former showing an average of 0.021. Interestingly, the standard deviation of the measured particles of interest had reduced from 5.896 μm to 4.912 μm following the second etch – further highlighting the benefits and necessity of this stage. The S-filter was kept to the same previous value of 8.000 μm . Similar to that previously set out in Section 3.4.1, the various roughness parameters were measured across three separate locations. Figure 7-12 shows the averaged arithmetic mean surface height of the polished samples along with the percentage difference from their raw state.

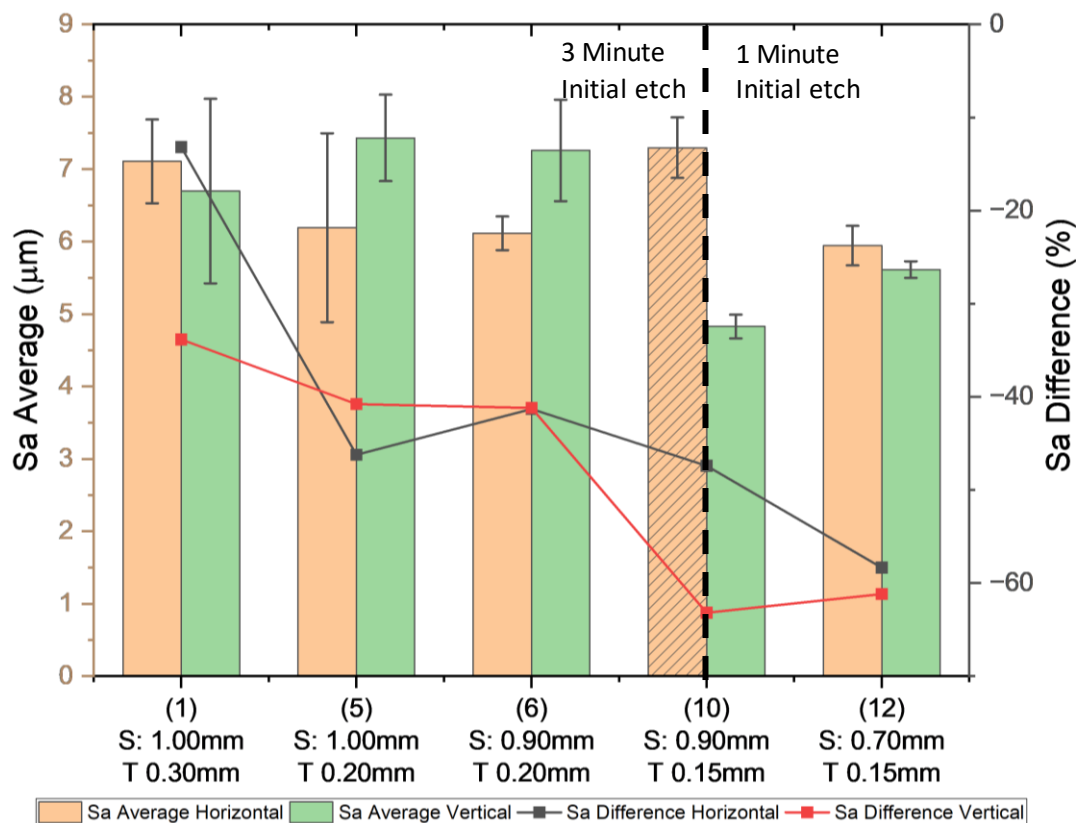


Figure 7-12. Arithmetic mean surface roughness of chemically polished samples with error bars representing the standard deviation of repeated measurements and percentage difference from raw state. N.B. Sample H10 shows significant damage.

The significantly higher Sa value of sample H10 compared to its vertical counterpart may be a result of over polishing. As previously stated in Section 7.2, excessive damage to the lattice matrix was seen for this sample, and the remaining 0.15mm strut thickness samples were only polished for 1 minute for the initial stage. It could therefore be concluded that over-polishing can result in excessive pitting of the structure and hinder the effectiveness of the technique's ability to reduce surface roughness. With evaluation of the arithmetic mean surface height of both polished samples, it can be determined that good agreement is now seen across both orientations with the average values of 6.532 and 6.367 μm for the horizontal and vertically printed samples, respectively.

Through assessment of the percentage reduction, the total reduction is increased with a reduction in strut thickness. This is primarily due to the combination of increased homogenisation of surface roughness across the polished samples and the contrary trend of the raw samples in Figure 5-20, where the surface roughness was shown to increase with a reduction in strut thickness. As previously highlighted, the extent of agglomerated particles on the raw samples was also seen to increase with a reduction in strut thickness. This indicates the effectiveness of the developed polishing technique in both removing these agglomerated particles and reducing the overall Sa values.

As discussed previously, Sa alone can't always quantify the topography characteristics of a surface. It is therefore important to consider the effects chemical polishing has had on the overall root mean square height of each processed sample, as shown in Figure 7-13.

Evidently, the averaged Sq values seem to reduce with both cell size and strut thickness, with the obvious exception of sample H10. Additionally, the horizontal orientations of samples 1, 5 and 6 seem to be noticeably lower than the vertical equivalents showing averaged values of 10.355 μm and 11.475 μm , respectively. This indicates a more consistent surface topography with less deviation from the mean for the horizontally printed samples.

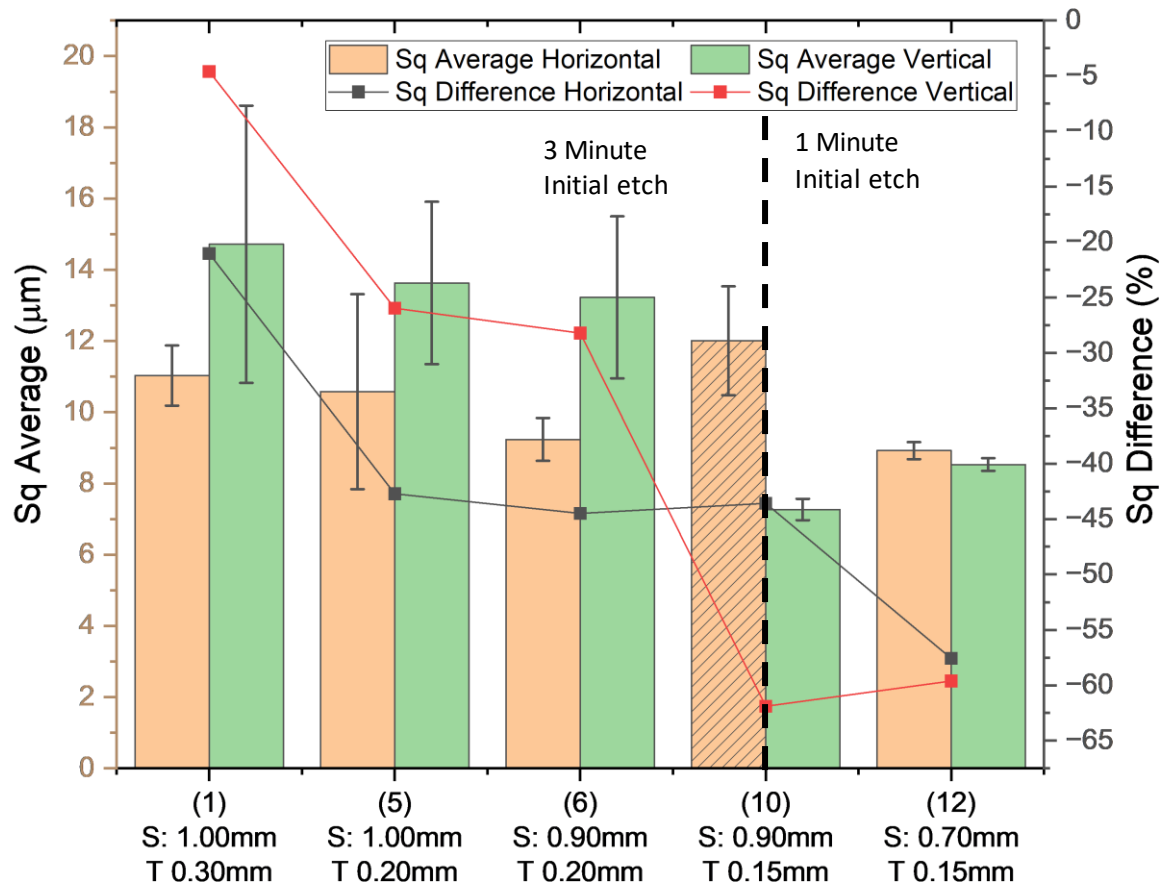


Figure 7-13. Root mean square height of chemically polished samples with error bars representing the standard deviation of repeated measurements and percentage change from raw state. N.B. Sample H10 shows significant damage.

Through consideration of the percentage reduction, again, the horizontal variations of samples 1, 5 and 6 showed a significantly larger reduction in Sq following the chemical polishing stage, compared to that of their vertical equivalents. This reduction in Sq was once more seen to increase with a reduction in both cell size and strut thickness. However, as a reduced initial etching time of 1 minute was used for samples V10, H12 and V12, further research to fully quantify the effects of both strut thickness and cell size is required.

7.3.4 Porosity

Both the true and apparent porosities of each chemically polished sample were determined via the methodology previously set out in Section 3.3. However, due to the removal of material and extent of damage seen on several of the lattice structures, determination of the overall bulk volume and lattice space had to be reevaluated. Three repeated measurements of both the bulk geometry and lattice space were taken across several samples with the averages and standard deviations calculated to determine the relative uncertainty. The polishing stage is shown to have little impact on the bulk geometry volume with only a 1% reduction. In contrast, the available pore space showed a significantly higher reduction of 10 %. This resulted in a combined uncertainty of the measured volume, and hence porosity, being $\pm 8\%$. Furthermore, as complete line of sight was seen through all polished samples, it was anticipated that trapped porosity results would align with that previously conducted via XCT in Section 5.5, apart from the pores nearest to the surface which are now reclassified as open porosities, as identified in Figure 7-8.

Figure 7-14 shows the apparent porosity of the processed samples, along with the percentage change from the raw state. Evidently, the horizontal samples are now indicating higher apparent porosities, contrary to that identified for the raw samples in Figure 5-35. However, the elevated damage, particularly seen on the horizontal samples, add additional uncertainties to the results.

The true porosity results, as well as the percentage change from the raw values, is shown in Figure 7-15. Due to their reduced processing time, samples V10, H12 and V12 showed the lowest reduction in apparent and true porosities, aligning with expectations. The results found here will be further examined throughout this chapter to explain and rationalise the performance change of each polished wicking structure.

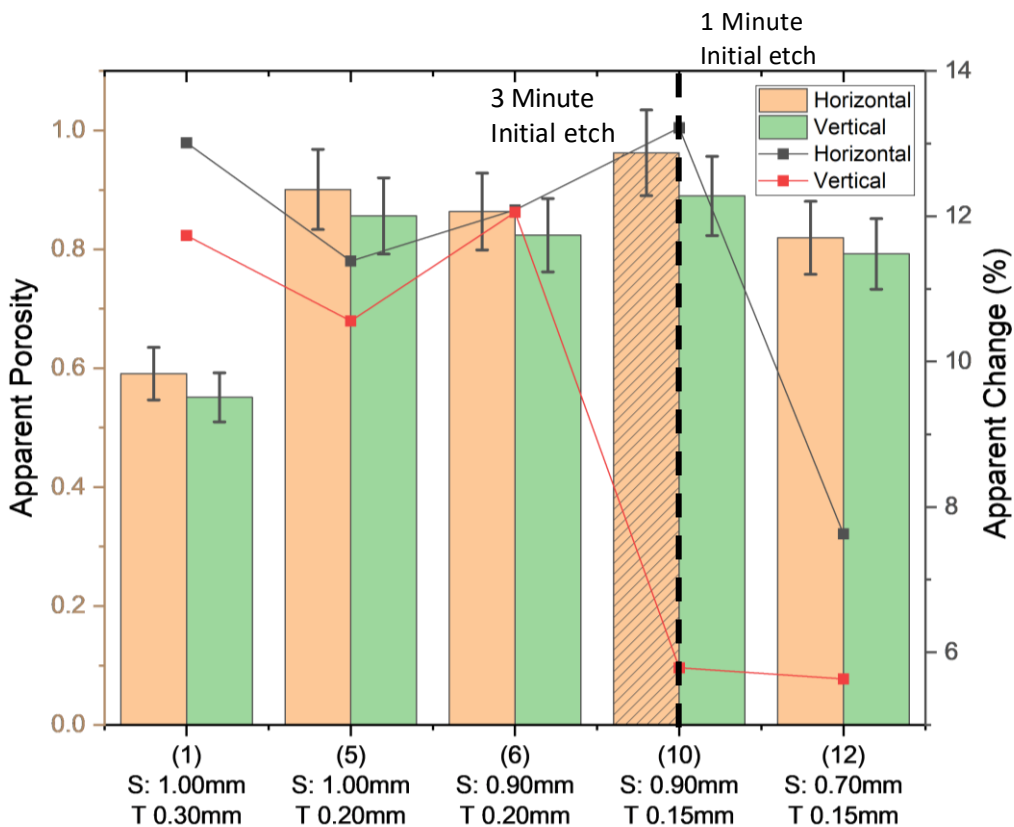


Figure 7-14. Apparent porosity with a 8% uncertainty error and apparent porosity change of chemically polished samples. N.B. Sample H10 shows significant damage.

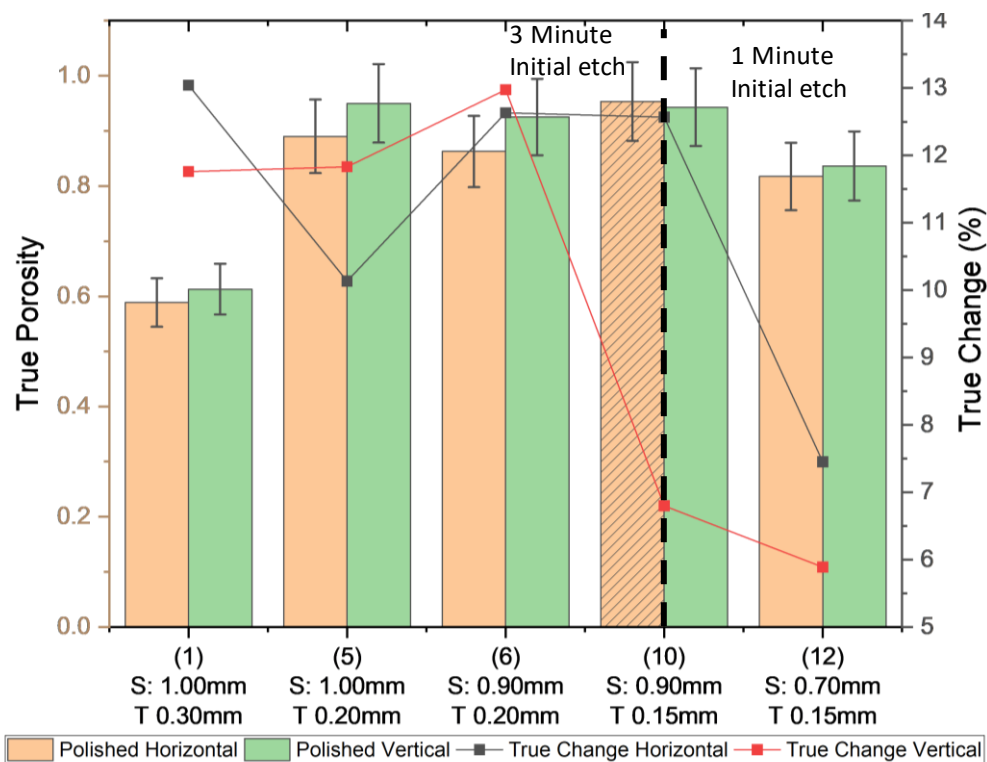


Figure 7-15. True porosity with a 8% uncertainty error and apparent porosity change of chemically polished samples. N.B. Sample H10 shows significant damage.

7.4 Capillarity of Polished Samples

With the removal of agglomerated particles, and hence significant reduction in surface roughness across all samples, the wettability of the samples was significantly improved, indicating a more hydrophilic nature between the working fluid and capillary structures. This was shown to be true for both acetone and water, as discussed throughout this section. As identified in Section 7.3, a noticeable decrease in strut thickness, and hence increased pore diameter, was measured following the chemical polishing procedure. Although this would indicate a lower rise height, coupled with the enhanced wettability of the structures further evaluation is essential to fully quantify the designs. As before, each test was completed three times with the averages and standard deviations determined and a literature-based comparison undertaken in Chapter 8.

7.4.1 Maximum Rise Height

Figure 7-16 shows the maximum equilibrium rise height of the polished samples with acetone as the working fluid.

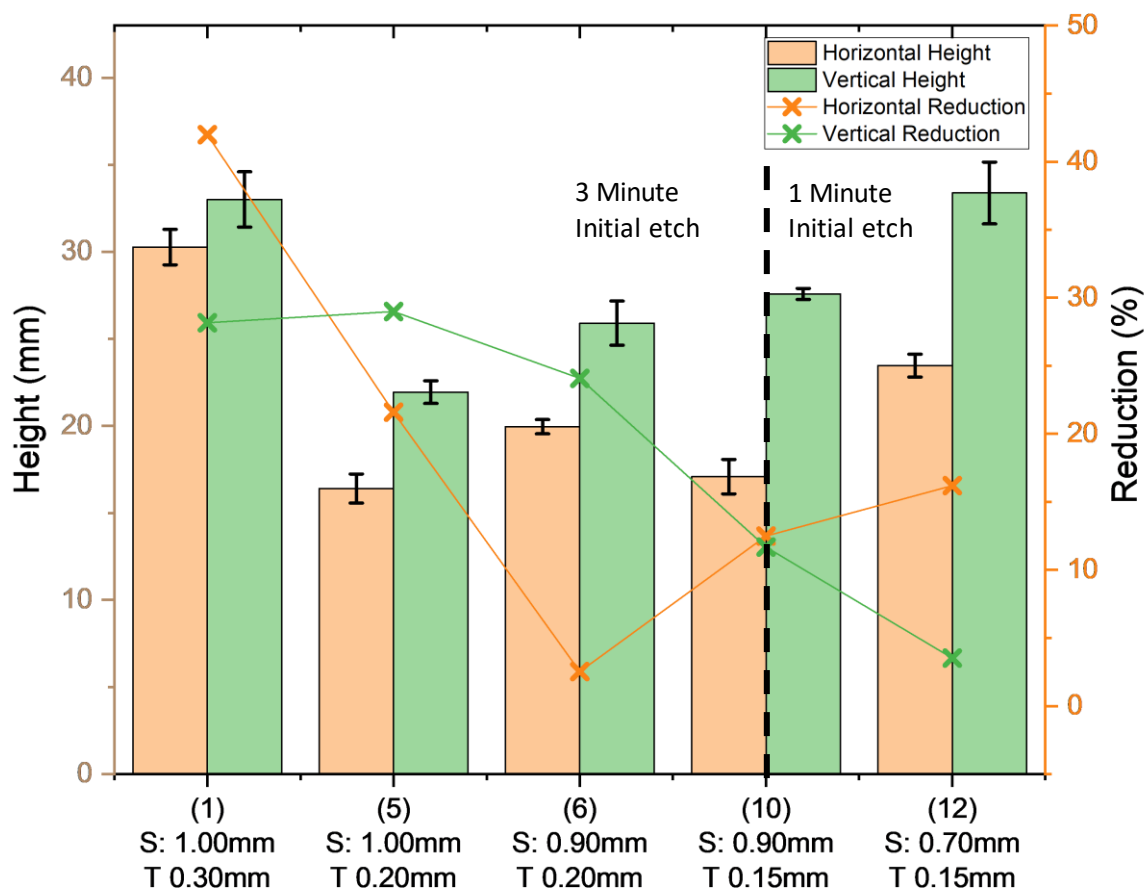


Figure 7-16. Equilibrium rise heights (Acetone) of the polished samples % reduction from their raw state and standard deviation represented by the error bars.

Evidently, all samples show a decrease in equilibrium rise height compared to their raw state. As previously discussed, this falls in line with expectations resulting from the increased pore sizes highlighted in Section 7.3.2. For the vertical samples, the percentage reduction was shown to generally reduce with both designed strut thickness and unit cell sizes. Despite sample H10 undergoing a 3 minute etch, compared to only 1 minute for that of V10, an equal percentage reduction in rise height of around 12% was seen for both. This may be a result of the pitted surface seen on sample H10 from the effects of over polishing, which allowed for additional micro capillaries. Without such features, sample H10 would likely have resulted in a significantly lower rise height. Sample V12 was found to have a 16.7% increase in pore size following chemical polishing and a minimal porosity increase of 5.9%. Contrary to expectations, sample V12 only showed a 3.5% reduction in rise height, which can be attributed to the removal agglomerated particles, and a 60% reduction in Sa surface roughness. This shows the benefits of chemical polishing indicating that further parameter studies could result in enhanced rise height through effective surface roughness reduction.

This trend reflects that of the detected increase in pore diameter previously shown in Figure 7-11. It indicates that the resultant reduction in equilibrium rise height is heavily influenced by the increase in pore diameters. According to Jurin's law, the maximum equilibrium rise height is inversely proportional to the effective pore radius. Following chemical treatment of the samples, and with the exception of sample H1, a clear linear relationship was seen between maximum rise height and the pore diameter as shown in Figure 7-17.

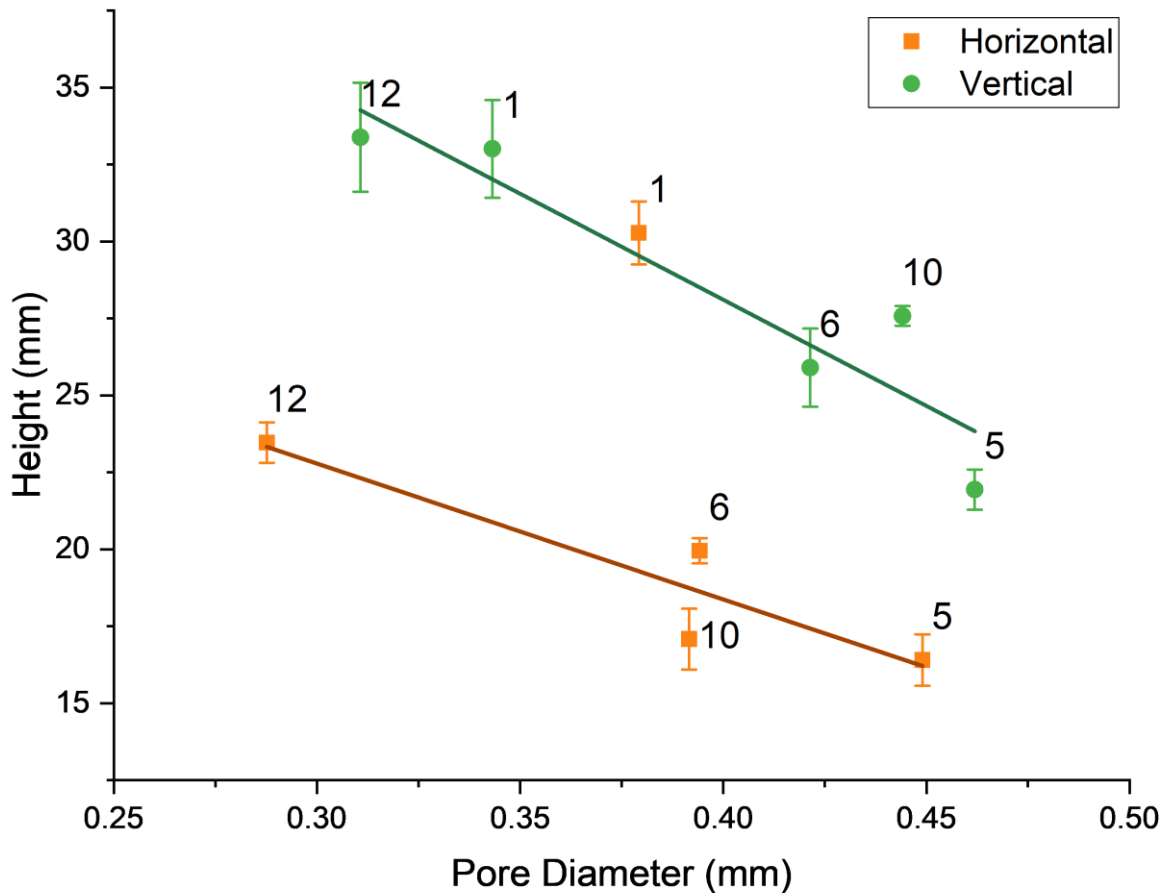


Figure 7-17. Effects of pore diameter on the equilibrium rise height with the standard deviations represented by the error bars.

This shows an increase in the coefficient of determination of the linear trend from 0.816 to 0.853 and 0.395 to 0.871 for the horizontal and vertical samples, respectively. Although linearity of results has significantly improved, non-conclusive patterns have been found for the consideration of the overall applicability of Jurin's law for the polished samples, as shown in Figure 7-18.

The combined uncertainties of both height (Figure 7-17) and pore measurements (Figure 7-11) account for the marginally positive deviations seen for samples V5(R) and V10(P). Although the overall averaged deviations of both orientations had not significantly changed, sample V12 showed a significantly reduced deviation compared to its raw state which may be attributed to the removal of agglomerated particles following the chemical polishing process.

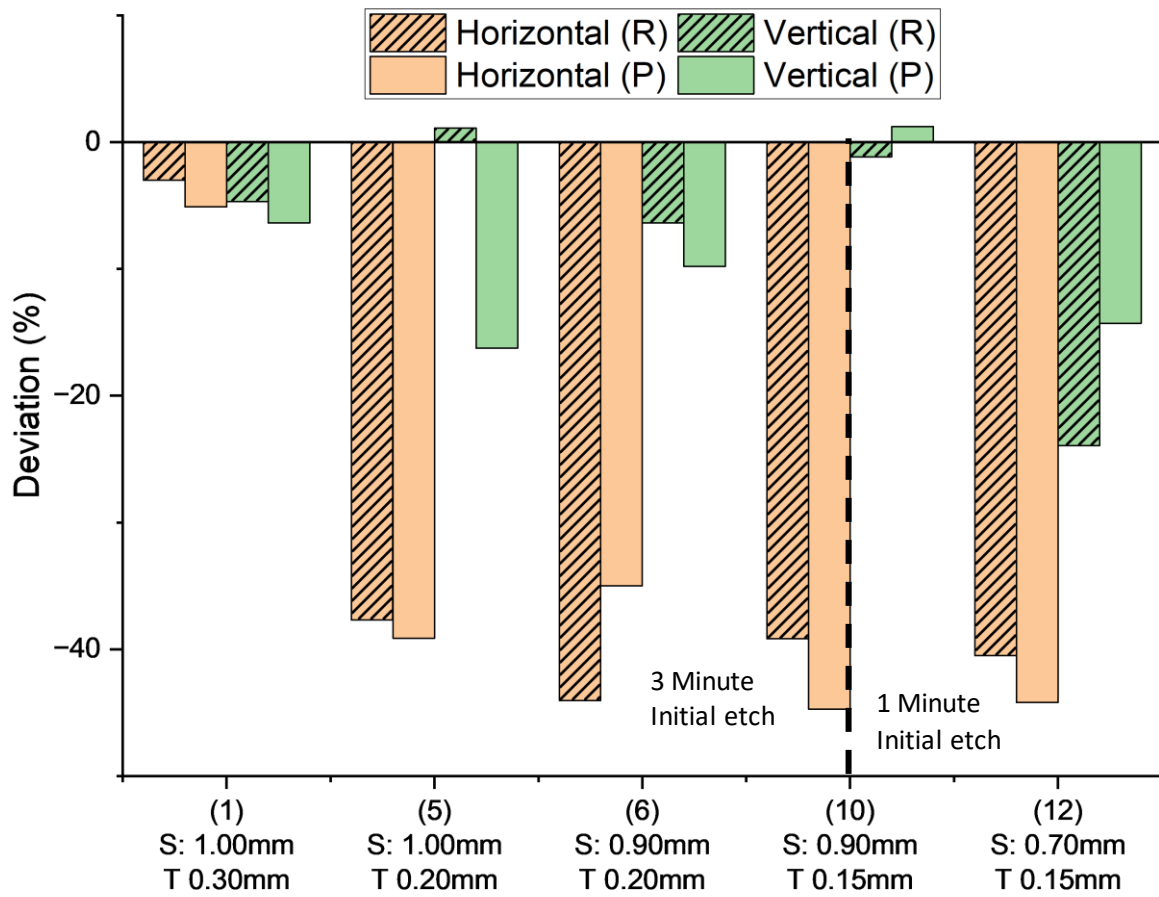


Figure 7-18. Percentage deviation of equilibrium rise heights from Jurin's law for both raw (R) and polished (P) samples.

7.4.2 Capillary Performance

Although all samples were identified to reach a lower equilibrium height, capillary performance considers the rate at which the rise occurs and is heavily influenced by several factors including both pore characteristic and distribution and fluid-solid interactions, as previously identified in Section 6.1.2. Figure 7-19 shows the averaged capillary performance of each polished sample along with percentage change from their raw states.

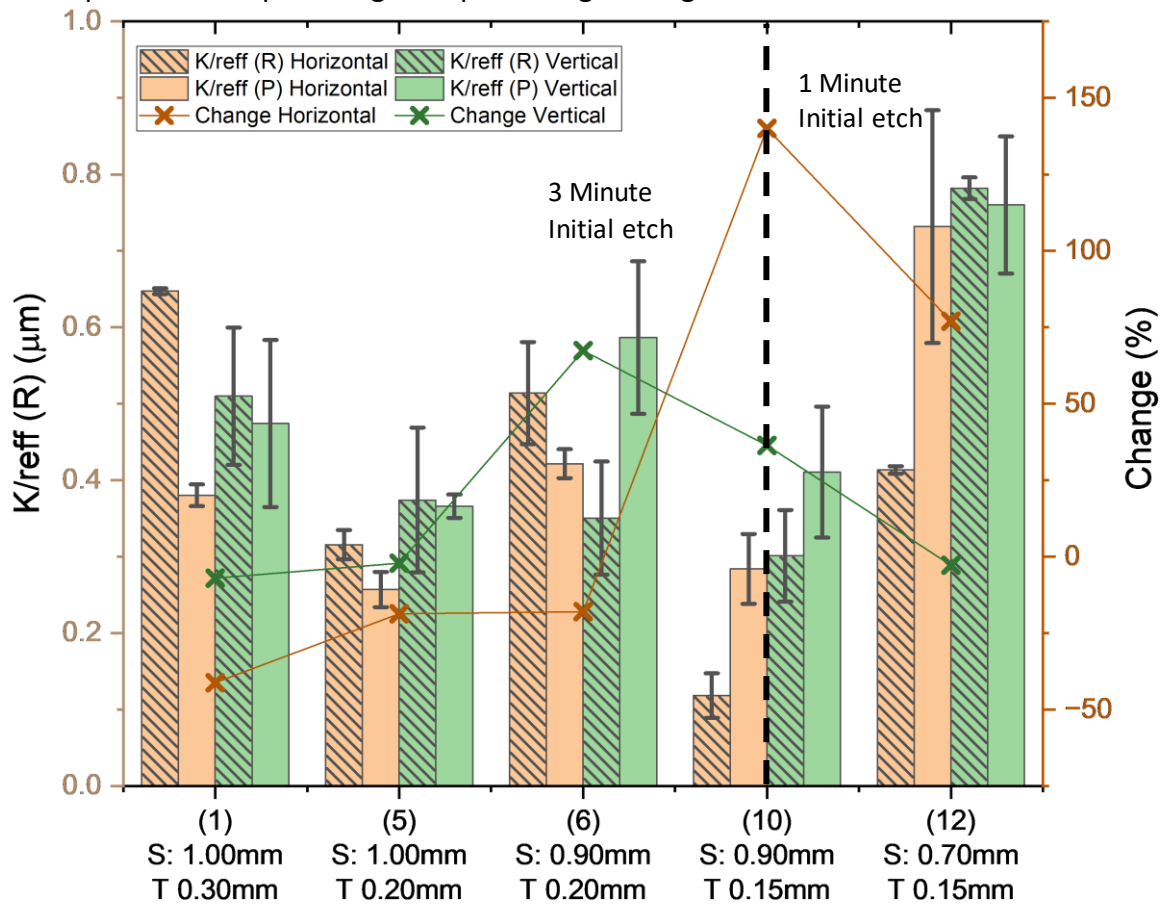


Figure 7-19. Averaged capillary performance of both raw (R) and polished (P) samples with standard deviation represented by the error bars and percentage change from their raw state.

As was the case for the samples in their raw state, the vertical samples tended to result in higher capillary performance compared to their horizontal counterparts. However, both horizontal orientations of samples 1 and 6 were shown to be superior in their raw state. Based on the evaluation of measured pore diameters, porosity, surface roughness, and elemental analysis, no definitive explanation could account for the conflicting results observed between samples 1 and 6. The contrasting results were likely due to a combination of factors, including anisotropic internal microstructure and localised chemical composition, leading to variations in surface energy and contact angle across different regions of the sample. On average, the

samples which had undergone the reduced 1 minute etch showed a 139.4% increase in slope and a 36.8% increase in capillary performance. It can be determined that due to the significant increase in the slope, the measured increase in capillary performance is mainly influenced by the enhanced capillarity and less influenced by the permeability factor. Disregarding the damaged sample H10, the 3 minute etching time resulted in a 3.3% reduction in capillary performance, on average. As previously undertaken, consideration of the relationship between both porosity and pore size and capillary performance is shown in Figure 7-20.

Through analysing the effects of both pore sizes and porosities on the resultant capillary performance in Figure 7-20, it can be determined that capillary performance tends to increase with a reduction in pore diameter and porosity, reflecting that previously highlighted for the raw samples in Section 6.1. However, the resultant capillary performance of sample set 1 with significantly reduced porosities, indicates the importance of optimising both porosity and pore sizes for effective capillarity.

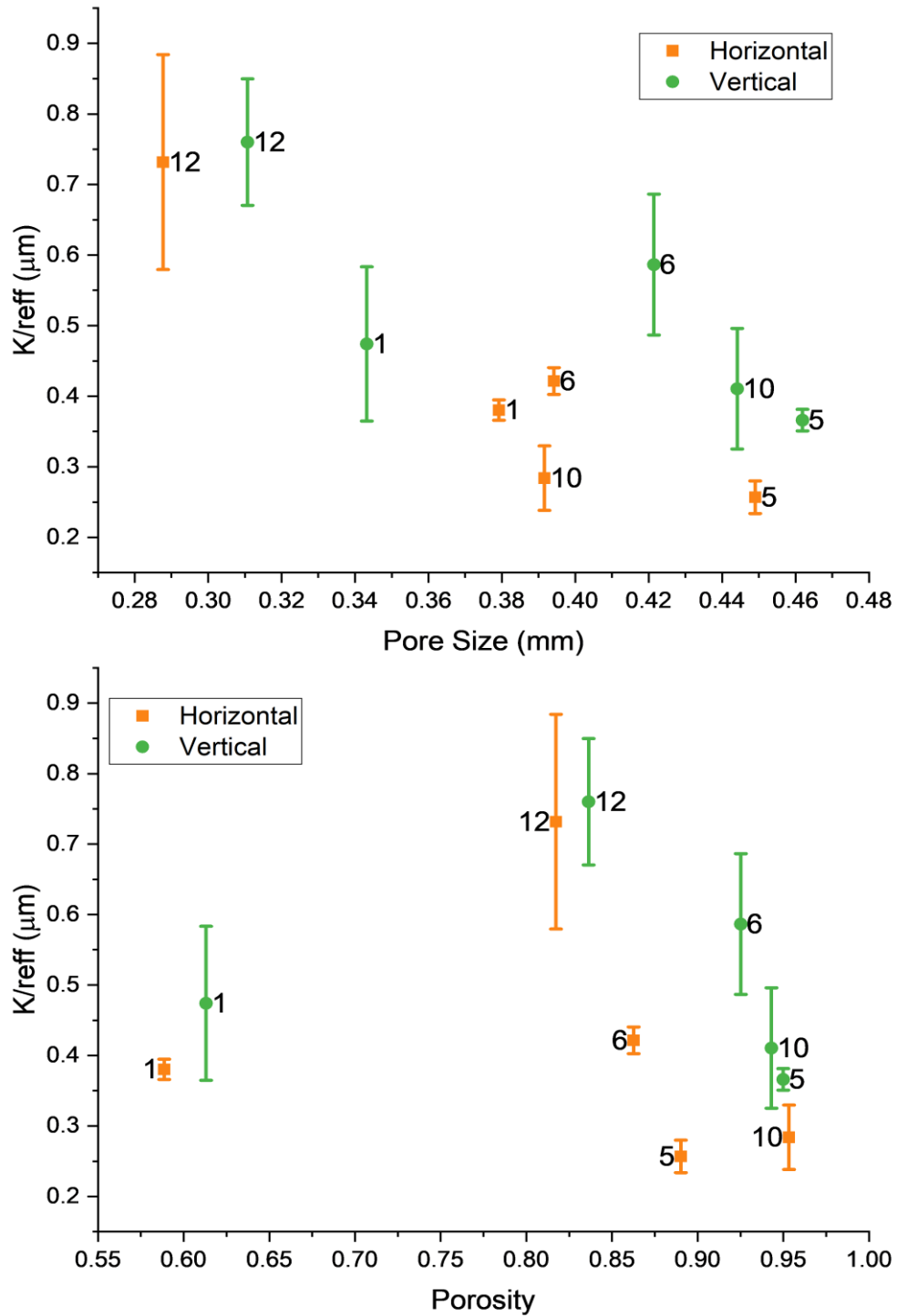


Figure 7-20. Effects of pore size (top) and porosity (bottom) on the capillary performance of acetone with the standard deviation represented by the error bars.

7.4.3 Water Trials

Interestingly, following the chemical polishing procedure, all samples showed successful capillary rise with the use of deionised water, in addition to that of acetone. Although water is typically considered to be a non-compatible working fluid with aluminium wick structures, as discussed in Section 2.3, this section will give a brief overview and comparison of using deionised water and acetone, in addition to the literature-based comparison conducted in Chapter 8.

7.4.3.1 Water Contact Angle

As indicated throughout Section 2, the contact angle between the fluid and contact surface plays a vital role in the structure's wettability and effectiveness of the supplied capillary pressure, as derived by Young-Laplace in Equation (3-12). As identified, the raw samples' inability to passively draw liquid through the lattice structure was the result of the structures' hydrophobic nature. Here, the static contact angle of deionised water on both the raw and chemically processed samples was measured. This was accomplished by placing a small sessile droplet onto the bulk surface and measuring the resultant equilibrium contact angle. The average and standard deviations of the measured droplet volume was $5.3 \pm 1.2 \mu\text{L}$. Using a droplet of this volume minimises the gravitational effect on the shape of the drop, retaining a more spherical shape. A total of 15 droplets were analysed per set with the as-built samples resulting in an averaged and standard deviation static contact angle of $99.1 \pm 7.5^\circ$ while the polished samples showed significantly lower results of $76.7 \pm 7.1^\circ$. The identified reduction in contact angle reflects that of the electropolished AM surfaces by Tyagi et al. [102] previously discussed in Section 2.8.

As the contact angle of the as-built samples was greater than 90° , the hydrophobic nature of the structures was confirmed rationalising their inability to provide capillarity with water. As outlined in Section 6.1, due to the enhanced wetting characteristics of acetone in the as-built state, measuring a static contact angle was not possible and assumed to be 5° . Like that of water, a clear improvement in wettability was achieved following the chemical polishing process, where again a measurable contact angle was unobtainable. When performing the sessile drop test, acetone was shown to near-instantaneously spread over a larger surface area of the polished samples compared to their raw state, indicating a fully wetted surface.

Nevertheless, as the contact angle approached zero, the cosine value used to determine the effective pore radius in Equation (3-13) approached unity. Therefore, for surface-liquid combinations where an extremely low contact angle was already seen, chemical polishing was shown to have little effect on maximising the deliverable capillary pressure. Contrary to this, the rate of change of the cosine factor was significantly higher for contact angles in the range of 30 - 150°, adding to the value and effectiveness chemical polishing had shown in reducing the contact angle of water.

Through consideration of the reduced surface roughness of the post-polished samples discussed in Section 7.3.3, the improved wetting behaviour indicates a shift in the contact angle regime from the Cassie-Baxter to the Wenzel model. In this scenario, all air pockets are minimised or eliminated, maximising the contact area between the liquid and solid surface resulting in improved wetting characteristics and reduced contact angle.

As the static contact angle was measured on a flat section of the samples, some disparity may be present in the actual internal contact angle within the lattice section. Due to the increased surface area and the effect of capillary action, the actual contact angle is likely to be less than that measured. This could also contribute to the implications of the minimum liquid entry pressure, previously investigated in Section 3.5.1.3, with the reduced internal contact angle improving the effectiveness of the delivered capillary pressure through the sample. Nonetheless, measuring the contact angle of a sessile droplet on the flat surface gives a good indication of the hydrophilicity of the liquid-surface interaction. Although outside the scope of this study, further evaluation to characterise and quantify the internal contact angles should be undertaken.

7.4.3.2 Water Equilibrium Height

As before, the maximum rise heights are evaluated at the wick's maximum head to operate against gravity with a comparison between acetone and water trials of the polished samples shown in Figure 7-21.

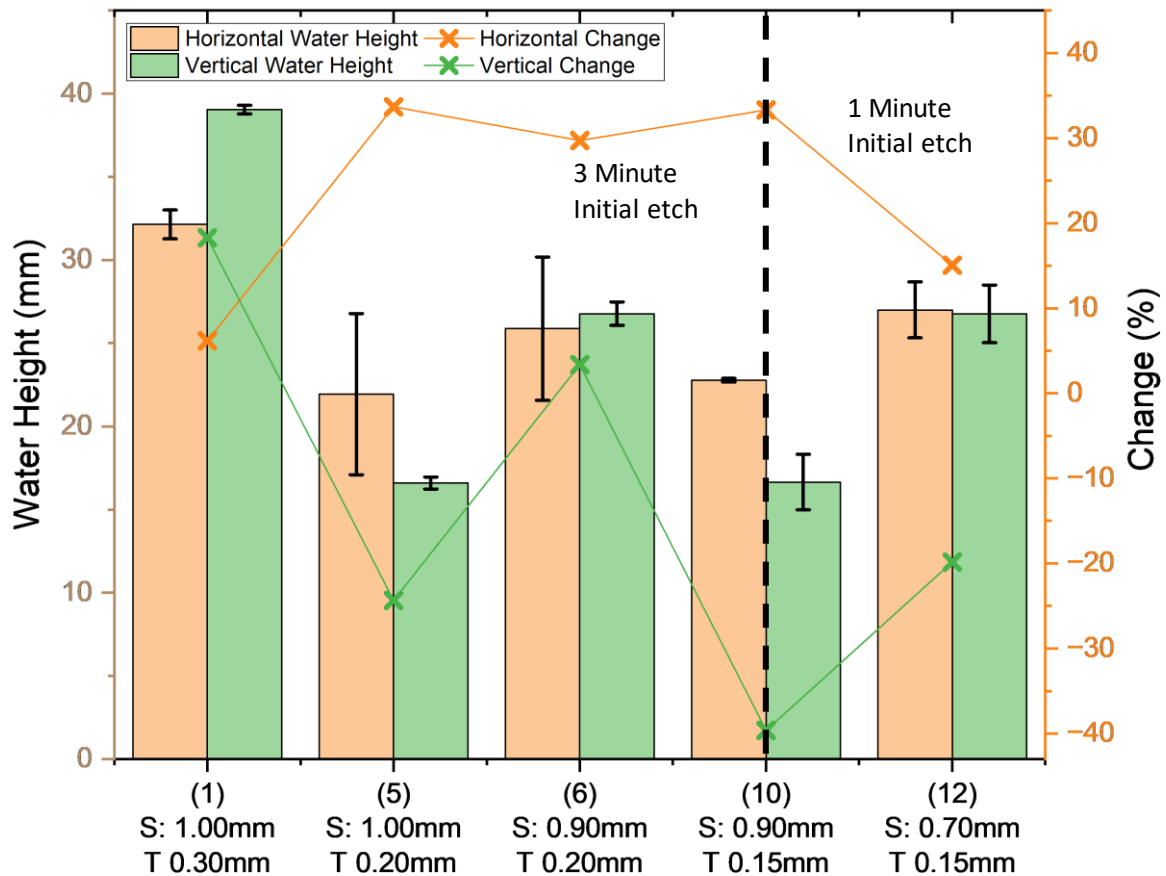


Figure 7-21. Maximum rise heights of water for the polished samples, with percentage change from acetone and the error bars representing the standard deviations of the repeated trials.

Previously, all vertically orientated polished samples were shown to be superior in terms of equilibrium rise height, as shown in Figure 7-16. This contrasts to the more arbitrary relationship seen with the use of water demonstrated in Figure 7-21. Furthermore, in accordance with Jurin's law, previously stated in Equation (3-22), the equilibrium rise height was expected to be greater for water due to its higher surface tension. This was found to be true for all horizontal samples. However, samples V5, V10 and V12 were shown to have a reduction in height of 24.3, 39.6 and 19.8%, respectively. The increased rise height of acetone for these samples may be a combined result of its lower density and significantly enhanced wetting properties favouring its complex interactions with the lattice structures, as discussed.

Through evaluation of both the capillary length and Bond number, highlighted in Section 3.5.1, it may be determined that surface tension was the dominating factor across all analysed samples for both acetone and water, demonstrated in Figure 7-22.

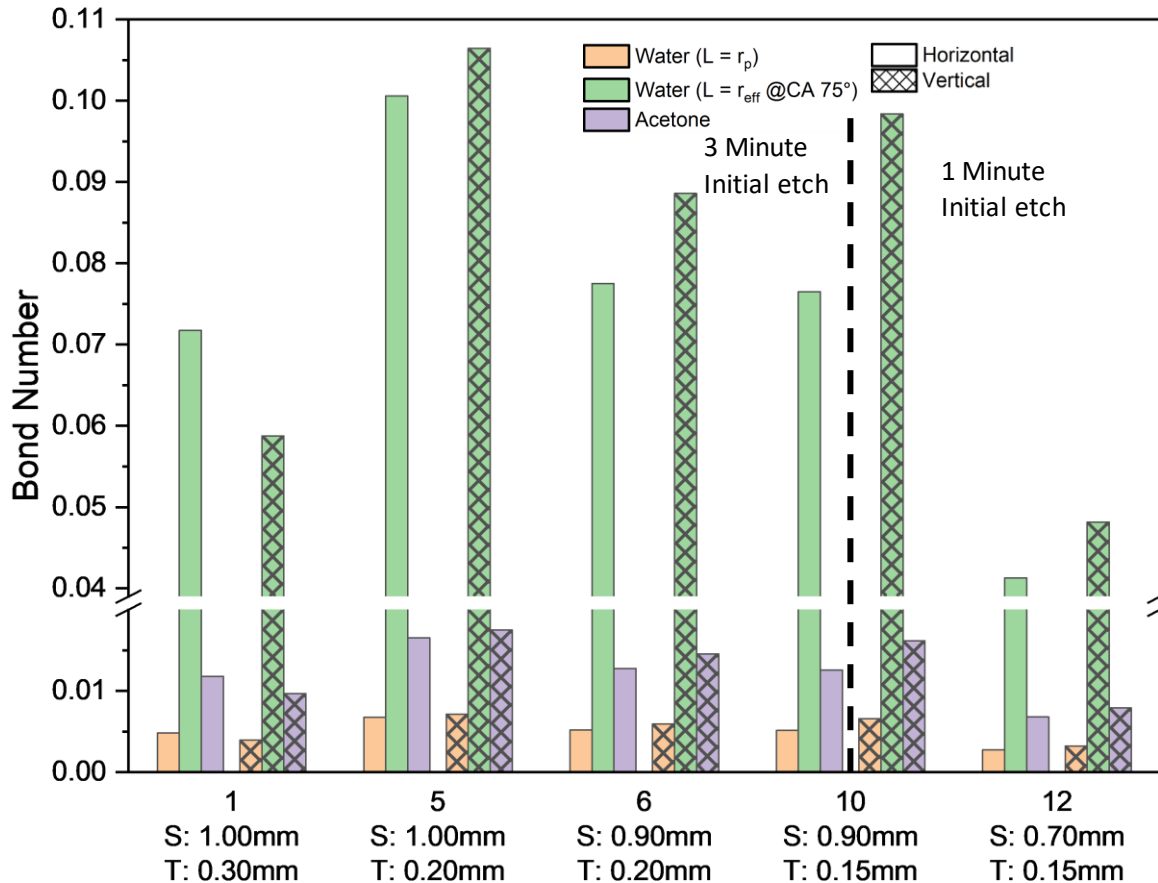


Figure 7-22. Calculated Bond numbers for all polished samples for acetone and water with a characteristic length of r_p and r_{eff} .

Clearly, the Bond number for all analysed cases is significantly less than unity, confirming that surface tension was the dominating factor. The characteristic length is typically categorised by the pore radius, as indicated by that of Acetone and water ($L = r_p$) in Figure 7-22. However, following such a method fails to include the effects of contact angle as is typically done for the analysis of capillarity through the Young-Laplace Equation (Equation (3-14)). As acetone resulted in excellent hydrophilicity characteristics and a low contact angle, little difference was found between the pore radius and the effective radius as the cosine factor of the contact angle approached unity. However, for that of water with a larger measurable contact angle, such difference can be significant, as exemplified with the Water ($L = r_{eff} @ CA 75^\circ$) case in Figure 7-22. Furthermore, the vertical samples showed slightly larger

Bond numbers, indicating that gravity had more of an effect. However, this was only marginal, and all values were well below unity.

Through further investigation of the collected SEM images for EDX analysis, chemical polishing resulted in nano/micro-scaled defects on the surface of sample V5, as shown in Figure 7-23.

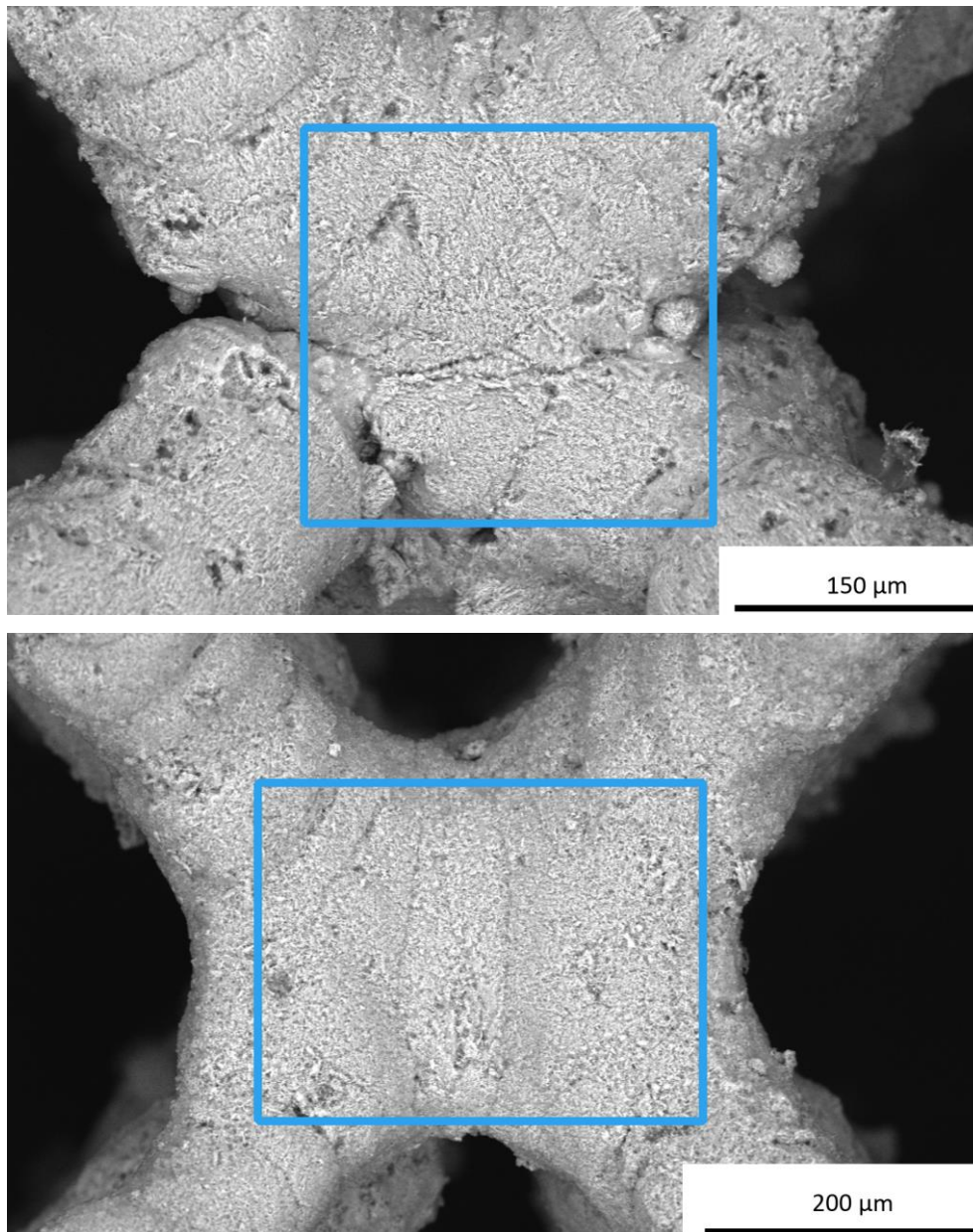


Figure 7-23. SEM images of samples V5 (top) and H5 (bottom) with blue squares representing EDX scan area.

These defects could act as micro capillaries, driving fluid through their groove-like structures. As acetone has a lower viscosity and surface tension compared to water, it may

be able to exploit these channels more effectively. Although these are not necessarily confluence channels, it may provide acetone the ability to pre-wet the surface and reduce the effective contact angle ahead of the main capillary-driven fluid front allowing the fluid to reach a higher equilibria. Furthermore, with consideration of water, these imperfections may result in a localised Cassie-Baxter regime contact angle, resulting in reduced hydrophilicity of the structure. Furthermore, as all SEM and EDX analysis was only taken on surface faces, quantification of internal elemental analysis was not undertaken.

7.4.3.3 Water Capillary Performance

Due to water's enhanced surface tension, the overall rate of rise significantly increased across all samples. This means that equilibrium height was achieved much sooner and as discussed, fewer data points were included in the analysis at the recorded frame rate of 10fps. Figure 7-24 shows the capillary performance of the polished samples with water, along with the % change from acetone.

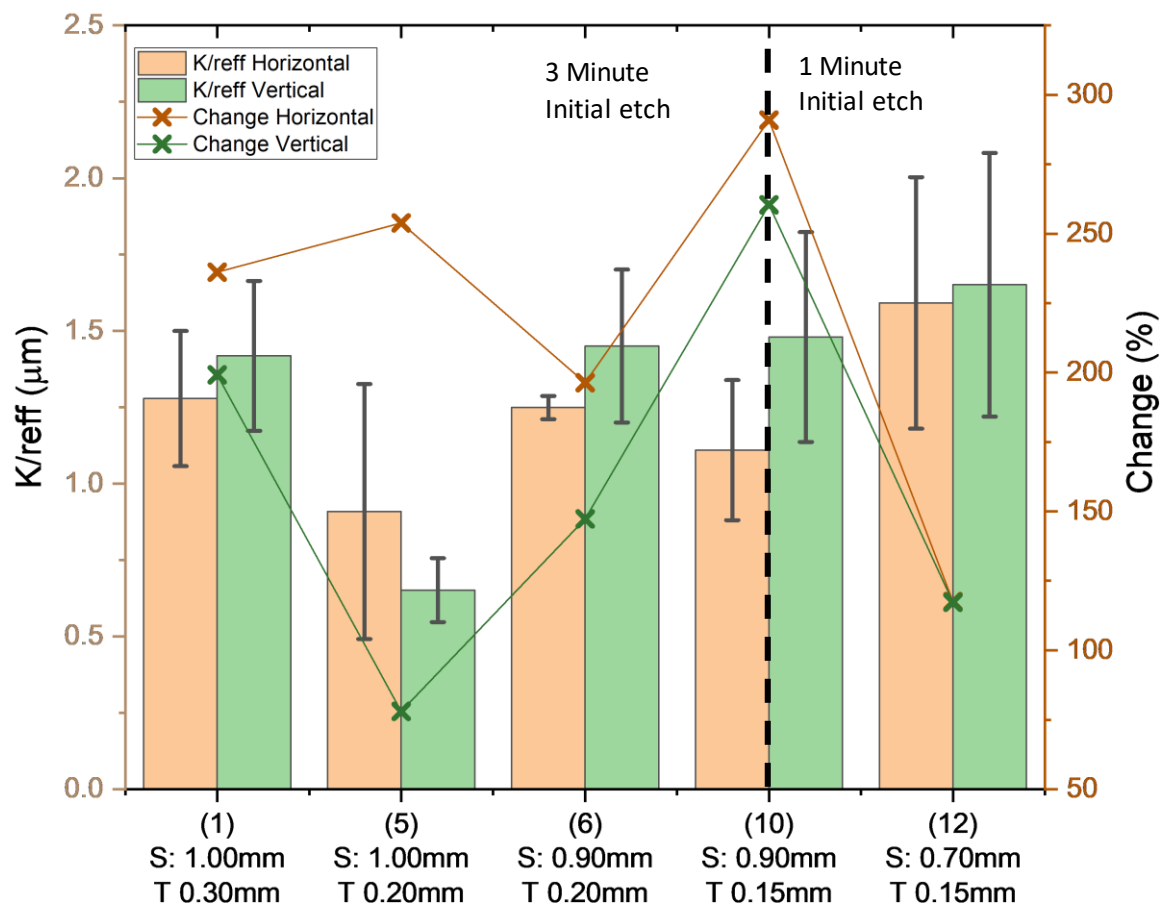


Figure 7-24. Capillary performance of polished samples with water as the working fluid and percentage change from acetone and the error bars representing the standard deviations of the repeated trials.

As a result, any integral system and processing noise had more of an effect on the overall result. This is demonstrated by the average RSD having increased from 13.1% for acetone to 21.3% for water. All processed samples showed significantly larger capillary performance with water, compared to that of acetone, with an average increase of 189.7%. This reiterates the importance of fluid and material selection to achieve optimal heat pipe performance and emphasises the benefits of the fluid's merit number, previously shown in Equation (2-2) and Figure 2-8. Interestingly, the horizontal samples consistently resulted in greater improvements with water.

The comparison between both pore size and porosity and capillary performance is shown in Figure 7-25. The overall trends identified in Figure 7-25 with relation to both pore size and porosity are similar to that shown for acetone in Figure 7-20, albeit on a significantly larger scale for water. Again, sample set 12 was shown to have the highest capillary performance, highlighting the need to achieve smaller pore sizes and greater pore densities while maintaining the high porosities. Through developments found in this study, this may be accomplished through further reduction in cell sizes for the 0.15mm strut thickness samples. Further considerations and comparison to literature-based results is shown in Chapter 8.

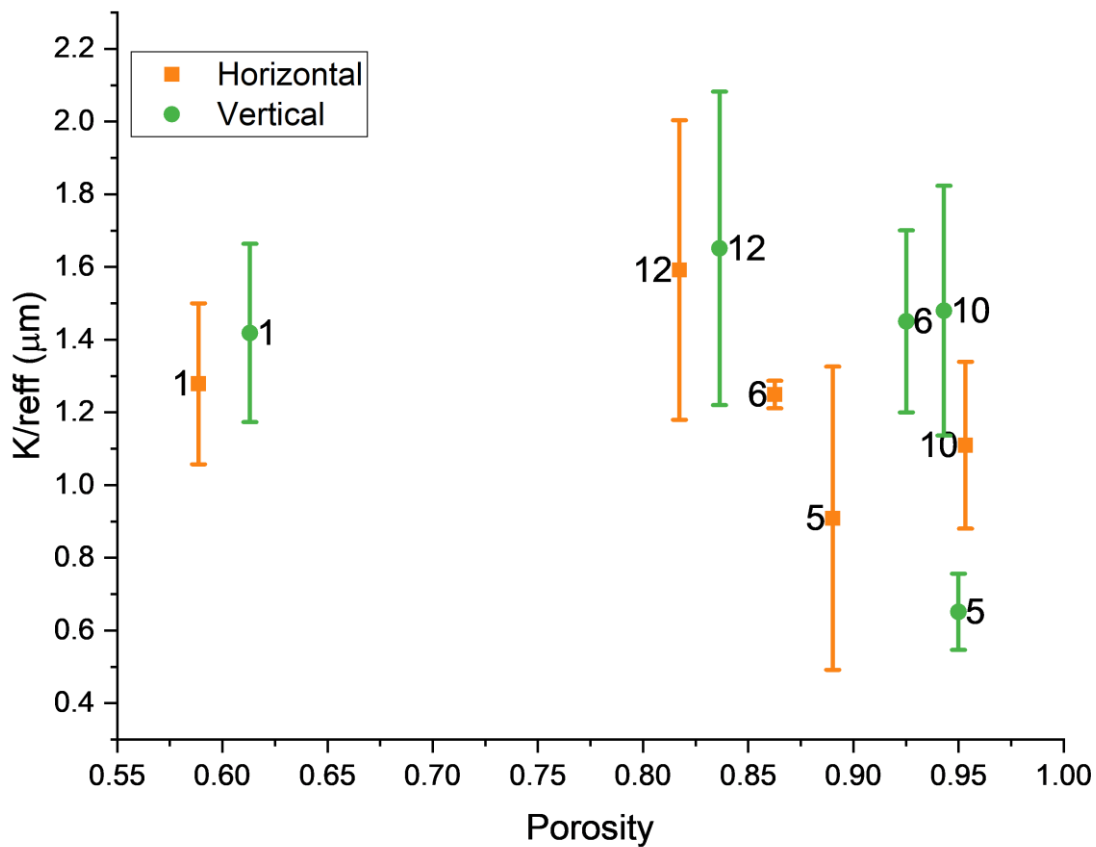
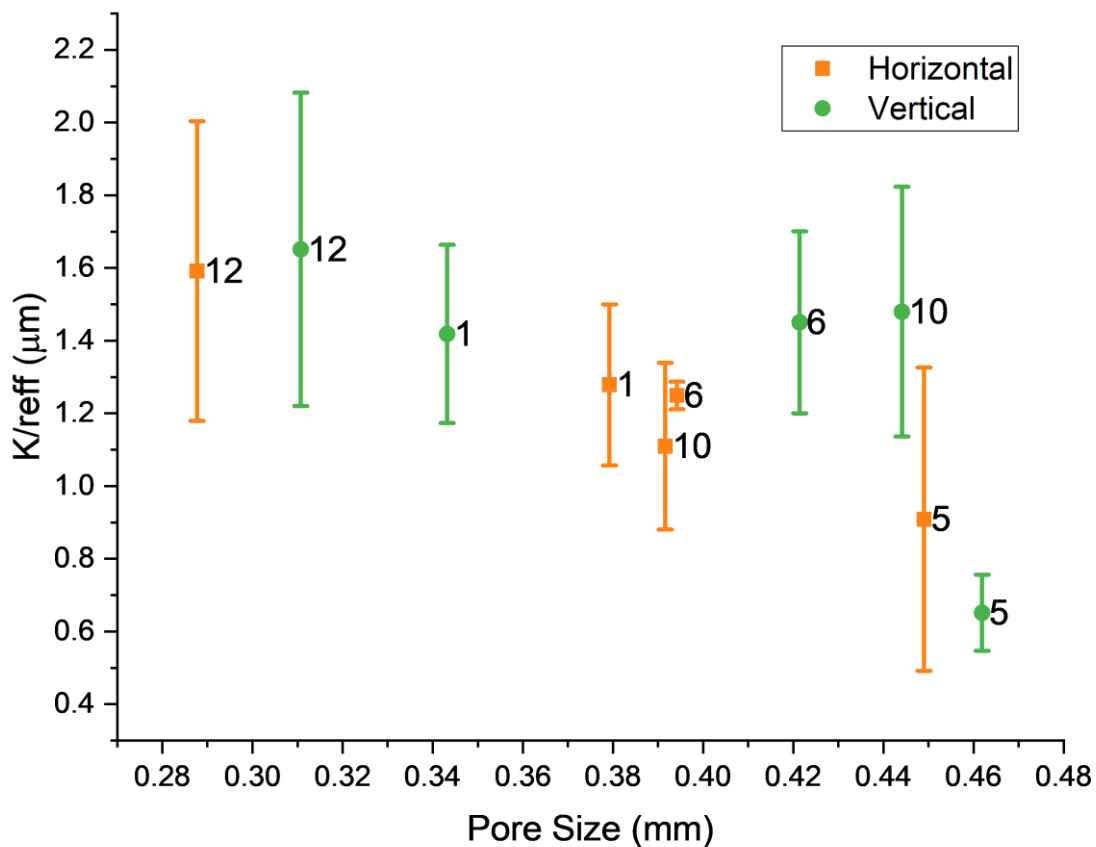


Figure 7-25. Effects of pore size (top) and porosity (bottom) on the capillary performance of water with the standard deviation represented by the error bars.

7.5 Permeability of Polished Samples

Although 10 samples had undergone chemical polishing, due to the extent of damage on some samples, especially around the top side edges, highlighted in Section 7.2, several samples proved to have insufficient sealing to direct the flow through the lattice structure, as illustrated in Figure 7-26.

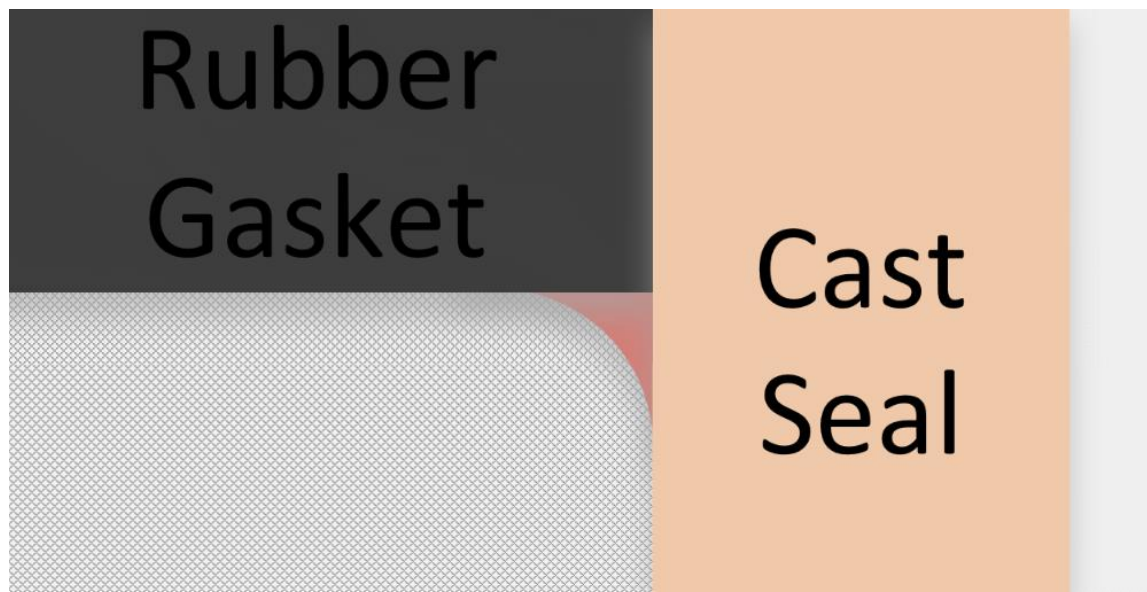


Figure 7-26. Exaggerated illustration of defective channel (Red) along the side edge of samples.

As the channels were found to be significantly larger than the designed pores, a significantly reduced pressure differential was measured due to the new path of least resistance for the flow. With this in mind, only samples H1, V1, V5, H6 and V12 were found to have no substantial defects that would significantly impact the flow through their analysed lengths. This was considered a sufficient number of samples to investigate the effects of chemical polishing on the sample structures. Due to the reduced number of testable samples, three repeated measurements were undertaken for each.

Again, determination of the differential pressure across each polished wick structure was completed for a range of mass flow rates as shown in Figure 7-27.

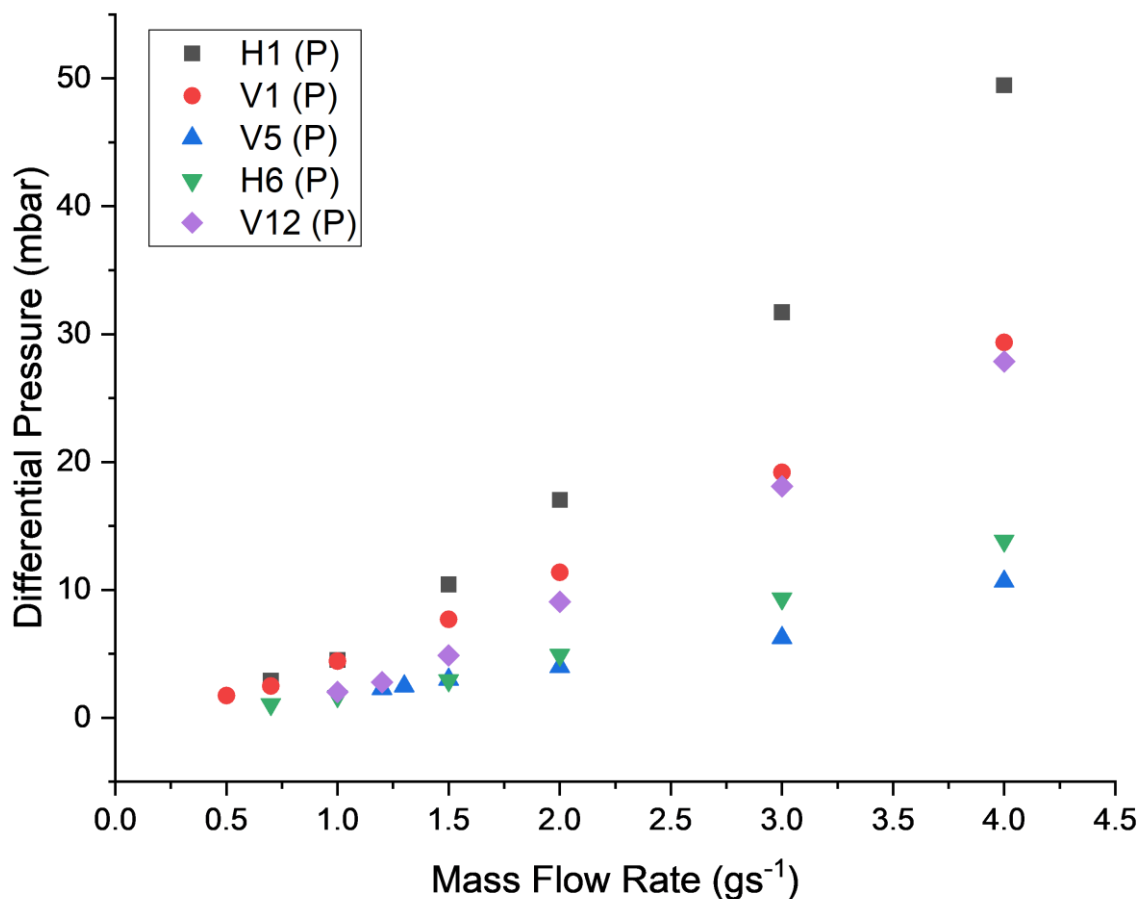


Figure 7-27. Averaged differential pressure measurements over a range of mass flow rates of the polished samples.

Similar to that seen for the samples in their raw state, the differential pressure was shown to increase with increase mass flow rates in a near linear relationship. Through comparison of the raw and polished samples, it can be determined that an averaged reduction of 51.82% was identified at a mass flow rate of 1.00gs^{-1} and a 30.45% reduction at 4.00gs^{-1} after chemical polishing. This decrease in differential pressure across the entire span of mass flow rates indicates a significant improvement in permeability in both Darcy and non-Darcy flow conditions, as is discussed.

Figure 7-28 shows the effect of mass flow rates on the measured permeability of each polished sample. As before, a distinct decrease in permeability is seen as the mass flow rate is increased. Due to the significantly reduced differential pressure of some of the more porous polished samples (V5 and V12), achieving accurate values at the lower flow rates with the given apparatus was shown to be ineffective. Therefore, approaching the 0.50gs^{-1} limit for these samples was not possible, as indicated in both Figure 7-27 and Figure 7-28. This shows

a less pronounced Darcy region of constant permeability at low flow conditions for some of the samples.

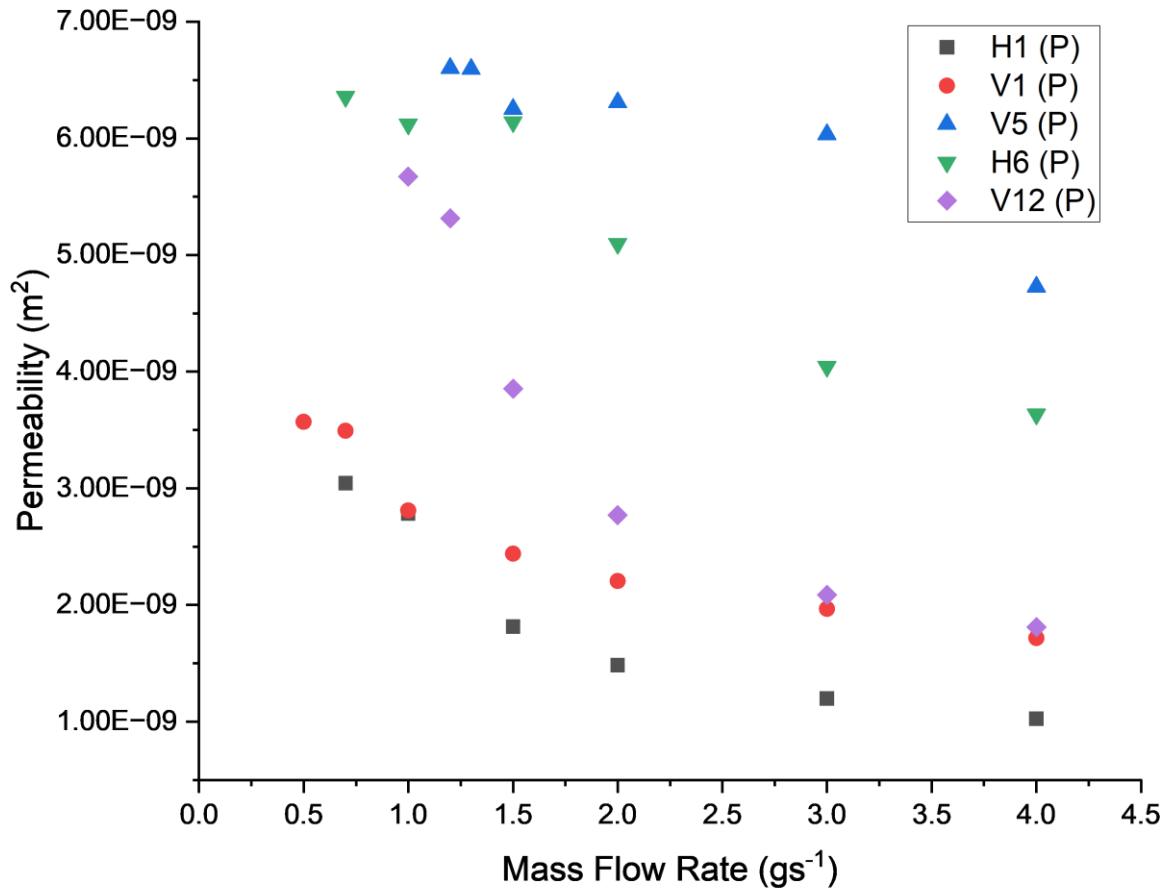


Figure 7-28. Measured permeability over a range of mass flow rates for all polished samples (P).

Through evaluation of the permeability-based Reynolds number (Re_K), shown in Figure 7-29, it can be determined that through comparison of the raw samples in Figure 6-17, Re_K has increased across the range of velocities for the polished samples. This is likely down to the noticeable decrease in surface agglomerated particles and surface roughness, coupled with the increased pore diameter, resulting in fewer internal frictional losses promoting higher internal pore velocities through the lattice structure. A distinct change in the transitional Re_K value between the Darcy and Forchheimer regime was also observed across all samples. This is shown in Figure 7-30, along with the percentage change from their raw state.

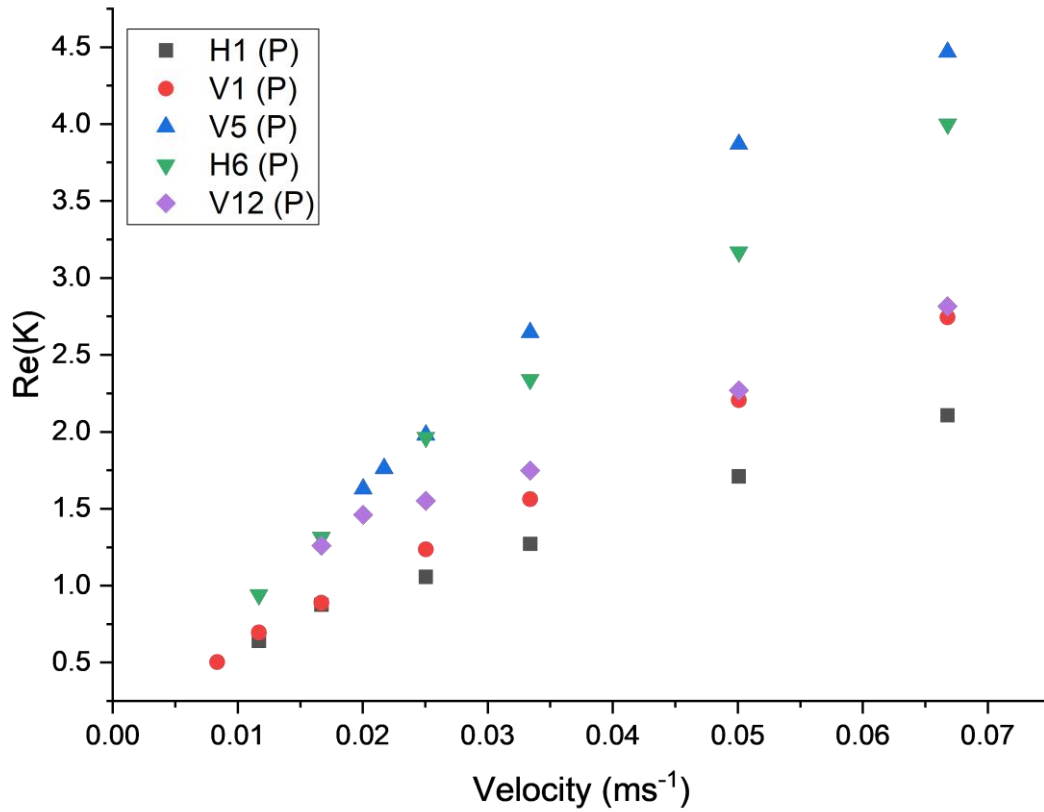


Figure 7-29. Influence of velocity on the permeability-based Reynolds number of the polished samples.

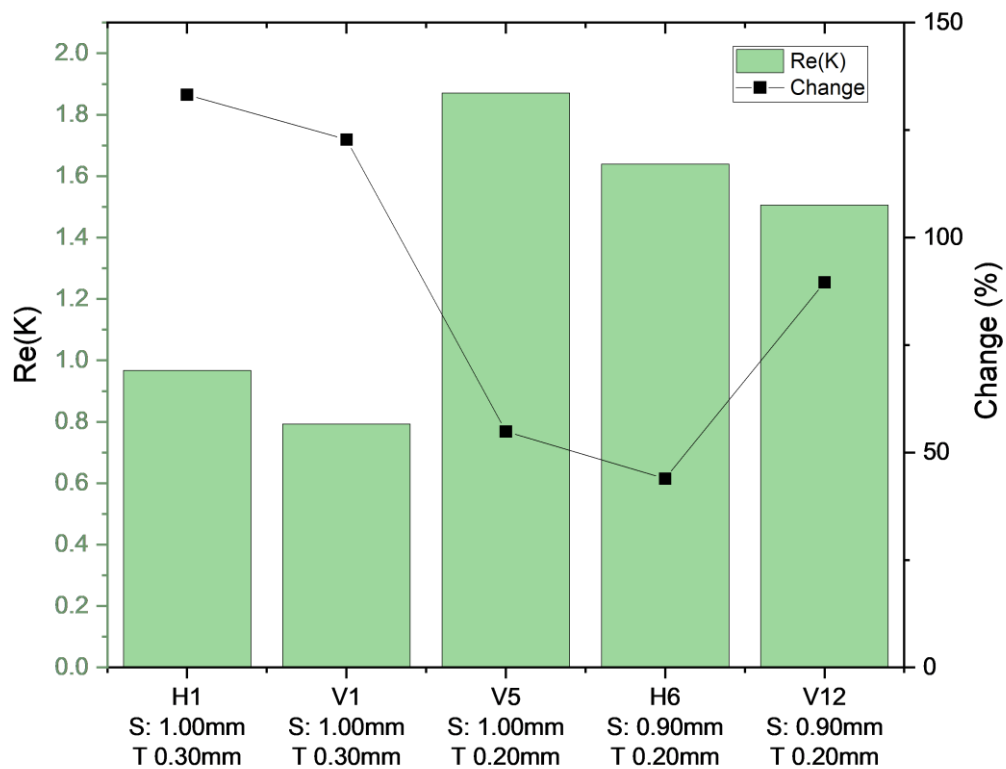


Figure 7-30. Transitional permeability-based Reynolds number for all polished samples with % change from raw state.

The linearity of the pressure drop with respect to flow rates in the Darcy regime, as opposed to the quadratic relationship of the Forchheimer regime, allowed for more efficient transport of fluid through the lattice structure. Therefore, enhancing the Darcy region is essential for heat pipe efficiency. Evidently, all samples resulted in significant improvements to the transitional Re_K with an average increase of 88.9%. This indicates that the pressure drop is governed by Darcy's law for a larger range of mass flow rates following chemical polishing. Such results can have several benefits for heat pipe applications, including:

- Extended operational flow velocities allowing for higher heat transport capacity.
- Reduced overall liquid pressure drop permitting longer length heat pipes.
- Enhanced liquid return preventing wick dry-out at higher heat loads.

Both Darcy (K) and Forchheimer (K_1) permeabilities for all polished samples are shown in Figure 7-31. As can be seen, all polished samples resulted in a noticeable increase in Darcyan permeability (K), with samples H1 and V12 showing significant increases of 138.5 and 129.2% respectively. Although the 13% increase in true porosity may contribute to the permeability improvement of sample H1, as shown in Figure 7-15, only an increase of 5.75% was recorded for the true porosity of the Sample V12. Therefore, further considerations must be made. Due to the reduced etching time of sample V12, no significant damage was identified which could hinder the reliability of the significant increase in measured permeability. As previously identified, the vertically orientated 0.15mm strut thickness samples suffered from elevated levels of agglomerated particles, the extent of which is shown in Figure 7-4. This was previously shown to be a contributing factor of the vertical samples' lower permeability readings in their raw state. The significantly reduced number and size of surface particles on sample V12, coupled with a 60% reduction in S_a value, in its polished state was found to significantly reduce internal pressure drop and hence result in the enhanced permeability measurements. Significant improvements were also found with regards to the transitional Reynolds number, shown in Figure 7-30, where an 89.6% increase in the Darcyan region was observed.

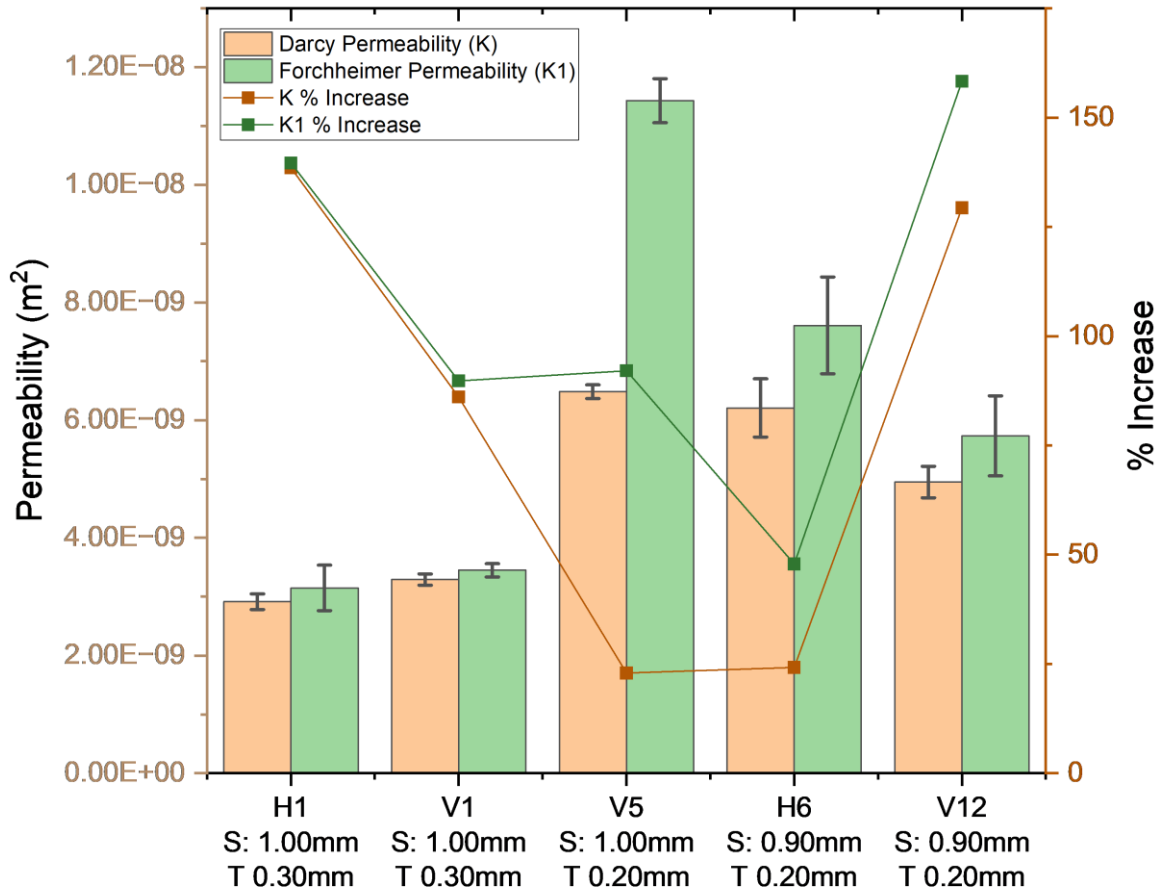


Figure 7-31. Darcy permeability (K) and Forchheimer permeability (K_1) of all polished samples with their respective % increase from the raw state and standard deviation represented by the error bars.

Evidently, the deviation between K and K_1 is shown to increase with the porosity of the samples with sample V5 having the largest porosity and deviation. This indicates the structures' ability to accommodate higher flow velocities before inertial effects become significant which leads to their ability to transition from the Darcy to Forchheimer regime at higher Reynolds numbers as previously discussed. Although not as applicable for standard heat pipe applications due to their general low Darcyan flow conditions, the determined relationship between the deviation of K and K_1 and porosity may be highly relevant to high temperature heat pipes and other lattice-based fluidic heat transfer applications. The higher heat flux naturally results in the requirement of higher fluid velocities to replenish the evaporator and change fluid properties at higher temperatures which can lead to a shift in significance of the quadratic inertial term in Forchheimer's Equation and drastically shift the regime's transition zone. The determined K_2 values are shown in Figure 7-32 along with the respective percentage change from their raw state.

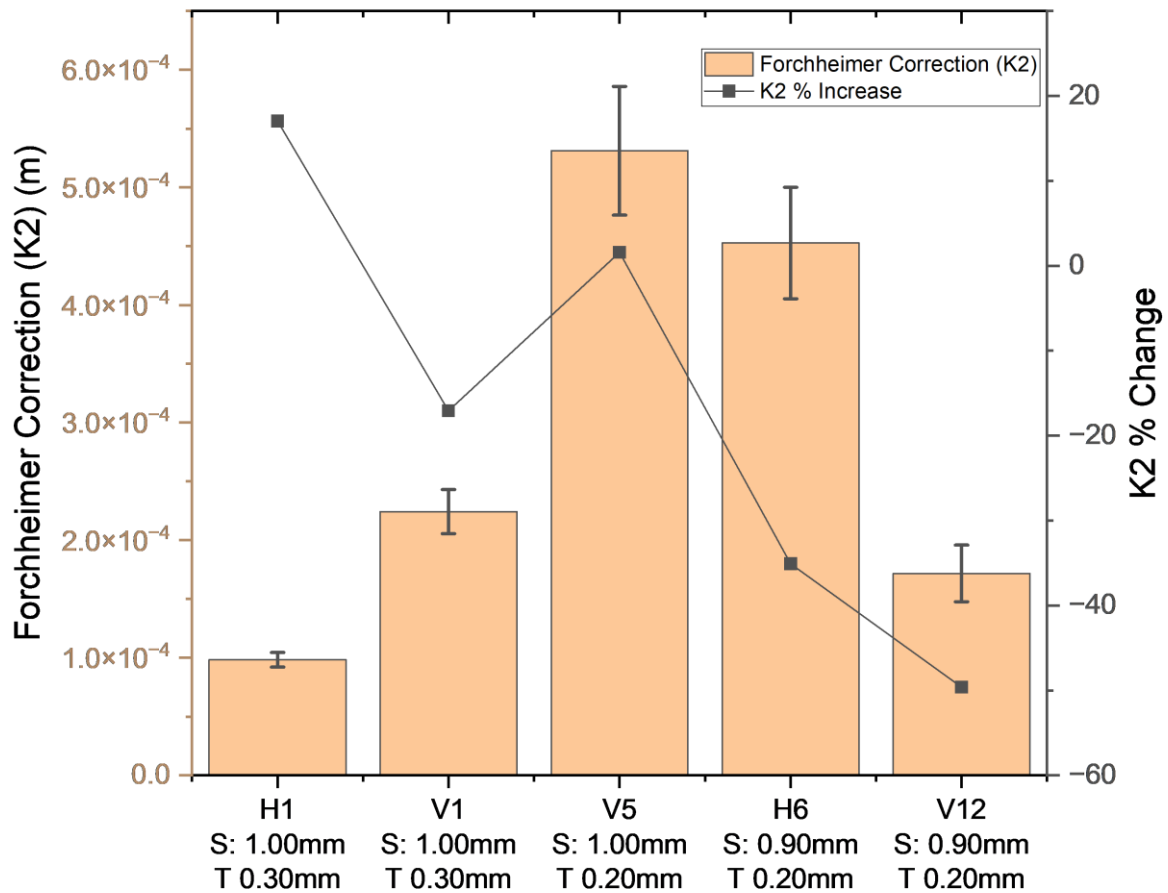


Figure 7-32. Determined Forchheimer correction (K_2) of polished samples with % increase from their raw state and standard deviation represented by the error bars.

Likewise, K_2 was found to generally increase with porosity with sample V5, which showed the largest coefficient value, closely reflecting the trends previously identified for the transitional Re_K values. The higher K_2 values indicate the samples' ability to accommodate higher flow rates. This therefore suggests that for high heat flux heat pipe applications where the Forchheimer regime may exist, utilising a more porous wicking structure may be of benefit. This is particularly true for micro/zero-gravity applications where less resistance against capillarity is exerted on the system.

The applicability and effectiveness of the Forchheimer Equation for the analysed samples is shown in Figure 7-33, further highlighting the reduction in the internal pressure drop following the chemical polishing process. Clearly, good agreement was found between the measured and predicted values for both raw and polished samples, indicating the effectiveness of the Forchheimer formulation. The onset of the quadratically governed inertial term can be visualised with the increasing gradient at higher flow velocities.

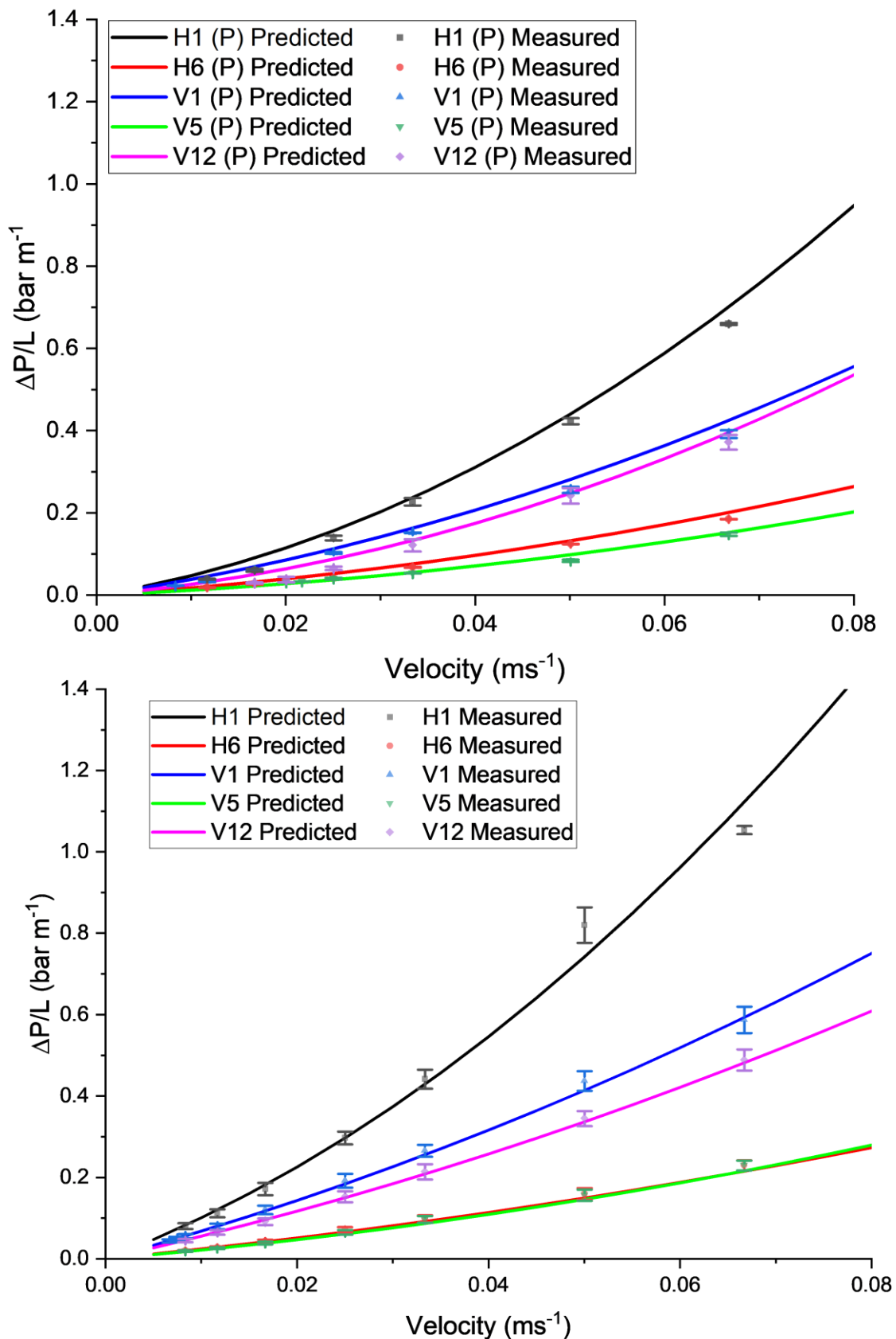


Figure 7-33. Comparison of the measured and predicted $\Delta P/L$ for both raw (bottom) and polished (top) samples where the error bars of the polished samples are represented by the standard deviation and that of the raw samples by the previously determined RSD (Table 6-1).

7.6 Chapter Summary

This chapter successfully analysed the effects of chemical polishing on the geometric characteristics of the lattice wicking structures in addition to their fluidic performance with respect to the capillary rate of rise and permeability experiments. An initial investigation was carried out, following the methodology set out by Sharma et al. [108, 109], which utilised a chemical solution of 80% phosphoric acid, 10% hydrochloric acid and 10% water in addition to 40 grams of Potassium Nitrate. However, processing of the samples in the described manner and subsequent EDX elemental analysis, indicated a highly concentrated oxygen (60.84 wt.%) and phosphorus (17.08 wt.%) residual surface.

For this study, the samples underwent an additional etching stage in 10% hydrochloric acid for 30 seconds. Results showed the complete dissolution of phosphorus and a significant reduction of oxygen down to 6.32 wt.%, similar to that identified on the raw samples. Following the second etching stage, increased concentration of silicon (25.27 wt.%) was detected on the analysed surfaces. The initial etching stage was completed for 3 minutes for all samples except for V10, H12 and V12 which were processed for 1 minute, following excessive damage being identified on sample H10. The key findings of the chemical polishing are identified below:

7.6.1 Geometric Summary of Chemical Polishing

- The thermally induced stresses of the horizontal samples, and subsequent sample warpage, was identified as a major contributor to the excessive damage seen on the polished horizontal samples. As the stresses were previously in an equilibrium state, the removal of material caused further strut dislocations. The severity of damage was found to be more significant for the thinner 0.20 and 0.15mm horizontal samples.
- The strut thickness of all polished samples reduced by varying degrees with a maximum reduction of 18.7% for sample V1 and minimum reduction of 8.5% for sample H12. Overall, the vertical samples experienced greater etching rates, compared to the horizontal orientations, as the increase in agglomerated particles and build layers induced weaker interfaces which are more readily etched within the solution.
- Pore diameter was seen to increase across all processed samples, with the vertical samples again experiencing a more significant change from their raw state. This increase varied from ~38.0% for sample set 1 to ~ 2.3% for sample H10.



- All samples measured a noticeable reduction in surface roughness following both chemical polishing stages. A ~60% reduction in both Sa and Sq values was recorded for sample set 12. The significantly higher Sa value of sample H10, compared to V10, was identified as being a result of over polishing causing excessive surface pitting.
- The percentage increase in both apparent and true porosities was seen to be fairly consistent ranging from around 13% for the samples polished for 3 minutes and down to only around a 5.5% for those which had undergone only a 1 minute initial etch.

7.6.2 Capillary Summary of Chemical Polishing

- The increased pore diameter of the polished samples resulted in a noticeable reduction in overall equilibrium rise height ranging from a ~40% reduction for sample H1 to only a ~4% decrease for sample V12. As was the case for the raw samples, the vertical orientations again showed superior rise height. With the exception of H1, a linear trend was identified between the equilibrium rise height of the polished samples and their pore diameters.
- Although a reduction in maximum rise height was seen across all polished samples, as capillary performance considers the rate at which the rise occurs, varying degrees of success were seen across the polished samples. The samples which had undergone a 3 minute etch had an average 3.3% decrease in K/r_{eff} values, contrasting with the 36.8% increase for those which had undergone a 1 minute etch, which was shown to be mainly influenced by increased capillary driving force.
- This study indicates that with optimised polishing parameters, a significant increase in capillary performance can be achieved to directly improve the heat pipe's capillary limit as stated in Equation (3-11).
- Chemical polishing of the lattice structures was found to significantly increase the hydrophilicity of the structures, enabling the successful capillarity of water. Although water and aluminium are generally considered non-compatible for heat pipe applications, this study enabled the comparison of water and acetone in addition to comparison to literature to highlight the importance of fluid selection. The enhanced wetting characteristics of the samples with water following the significant reduction in surface roughness and the removal of the hierarchical roughness structures, indicated a shift from the Cassie-Baxter to the Wenzel regime. All samples showed significantly enhanced

capillary performance with the use of water as the working fluid, with an averaged value of 189.7%.

7.6.3 Permeability Summary of Chemical Polishing

- An averaged differential pressure reduction of 51.82% was identified at 1.00gs^{-1} and 30.45% at 4.00gs^{-1} for the analysed samples following chemical polishing. The reduced differential pressure across the entire analysed flow rates resulted in significant improvements in both Darcy and Forchheimer derived permeabilities in delaying the onset of the quadratic relationship of the Forchheimer regime.
- Sample V12 showed an increase of 129.2% for permeability in Darcy's regime, despite having only exhibited a 5.8% increase in porosity. This was found to be a result of the significantly reduced number and size of surface agglomerate particles, coupled with the 60% reduction in S_a surface roughness identified following chemical polishing. The transitional Re_k of sample V12 also increased by 89.6%. In terms of heat pipe applications, this enables the wicking structure to extend its operational flow velocities allowing for higher heat transport capacity and reduced overall pressure drop, permitting longer heat pipe length and enhanced liquid return preventing wick dry-out.
- The transitional permeability-based Reynolds number was shown to increase by an average of 88.9% across the analysed samples indicating that the pressure drop was governed by Darcy's law for a greater range of mass flow rates following chemical polishing. The delay in the onset of the Forchheimer regime shows potential for extended heat pipe lengths, operating flow rates and thermal loads, enabling a broader range of applications.
- This study identified the benefits of utilising higher porosity wicking structures for high heat flux applications where the Forchheimer regime may exist which, coupled with the benefits of chemical polishing, delay the onset of the quadratically-governed pressure drops.
- The Forchheimer Equation was found to effectively predict the pressure drop of the analysed wicking structures in both their raw and polished states across a range of fluid velocities. The applicability of such correlations can improve the design efficiency of future AM lattice-based wicking structures.

8. Literature-Based Performance Benchmarking

Benchmarking of the current study may be accomplished through two separate comparisons to quantify performance and achieve the objectives set out in this thesis:

- Comparison to other AM-based wicking structure studies (Section 8.1.1), and
- Comparison to conventionally manufactured heat pipe wicking structures (Section 8.1.2).

8.1.1 AM Benchmarking

Through consideration of capillary performance, the findings of this study compare well with other AM-based wicking structures seen throughout literature, as shown in Figure 8-1 with additional data and studies highlighted in Table 8-1 at the end of this section.

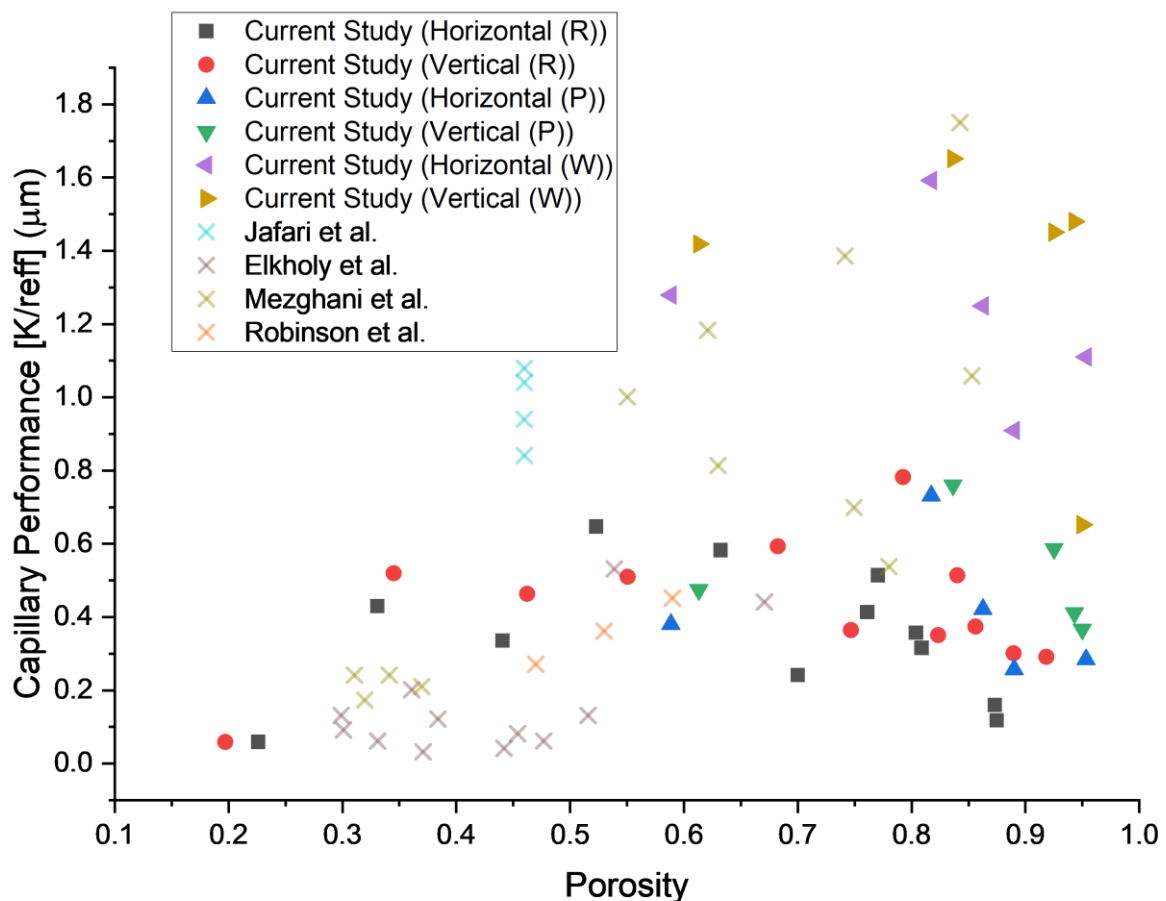


Figure 8-1. Literature comparison of capillary performance of raw samples with acetone (R), polished samples with acetone (P) and polished samples with water (W) to other AM-based wicking structures.

The range of capillary performance values vary significantly throughout the analysed AM-based literature from 0.060 – 1.182 μm with an average value of 0.516 μm . As expected, the wide range of porosities and pore sizes analysed in this study also resulted in significant

variations in capillary performance, showing strong agreement overall. The structures manufactured for this study were generally of higher porosities than the majority of compared test points found in literature. Nevertheless, sample V12 showed the best capillary performance for the raw samples with acetone as the working fluid, with a value of $0.782\mu\text{m}$. The general improvement in capillary performance following the chemical polishing process, as demonstrated by the removal of agglomerated particles for the lower strut thickness samples, shows potential for the use of higher porosity wicking structures for heat pipe applications.

The utilised working fluid and wicking material was found to have a significant effect on the capillary performance results, as demonstrated through the noticeable improvement in capillary performance of the polished samples with water. Comparing these results to literature, shows they surpass all other lattice-based geometries with only the AM micro-pin copper structures of Mezghani et al. [121, 183] and the sloped groove design of Kappe et al. [125] showing superior results. Although water and aluminium are not considered a compatible heat pipe combination, this shows the future potential of the benefits of chemical polishing as a post processing technique for heat pipe wicking structures.

Figure 8-2 shows the comparison of the measured Darcy permeability of both raw and polished sample sets to AM-based forced flow experimental studies found in literature. It can be concluded that the samples analysed in this study, are generally considered to be of higher permeability than that found in literature, mainly due to the higher concentration of high porosities within the sample sets. The variation between the studies can also be attributed to various degrees of tortuosity between the various wick designs.

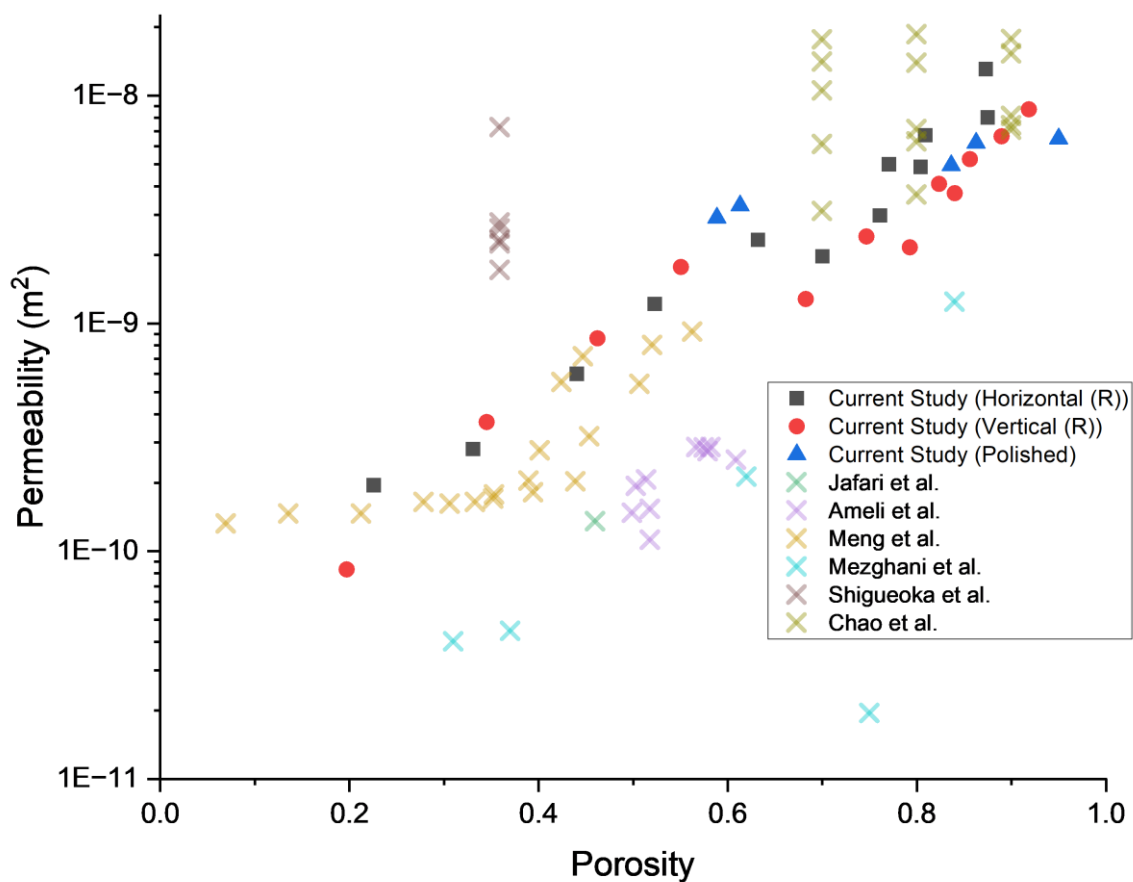


Figure 8-2. Literature comparison of permeability of raw samples (R) and polished samples to other AM-based wicking structures.

8. Literature-Based Performance Benchmarking

Table 8-1. Comparison of current study capillary performance and permeability parameters to other AM-based wicking structures found in literature

Wick & Fluid Characteristics	Capillary Performance (K/r_{eff})	Permeability	Reference
ϵ : 0.17 - 0.58 r_p : 0.06 – 0.140mm Material: AlSi ₁₀ Mg (Sinter-style) Fluid: Water		$1.65 \times 10^{-13} - 2.86 \times 10^{-10} \text{ m}^2$	Ameli et al. [88, 184]
ϵ : 0.20 – 0.60 D_p : 0.045mm Material: Scalmalloy® Fluid: Water	Grooved: 0.28 - 1.73 μm Slopped Grooves: 1.971 – 8.943 μm		Kappe et al. [125]
ϵ : 0.359 Material: PLA - mesh Fluid: Air		K_1 : 1.718 – 7.274 $\times 10^{-9} \text{ m}^2$ K_2 : 0.754 – 2.121 $\times 10^{-3} \text{ m}$	Shigueoka et al. [185]
ϵ : 0.46 D_p : 0.216mm Material: SS316 Fluid: Various	Water: 1.044 μm Methanol: 1.078 μm n-Hexane: 0.84 μm FC-72: 0.939 μm 0.03 – 0.53 μm	K : 1.35 $\times 10^{-10} \text{ m}^2$ K_1 : 1.67 $\times 10^{-10} \text{ m}^2$ K_2 : 5.03 $\times 10^{-5} \text{ m}$	Jafari et al. [95]
ϵ : 0.299 – 0.671 r_{eff} : 0.178 – 0.574mm Material: AlSi ₁₀ Mg Fluid: Ethanol		K : 9.488 – 147.41 $\times 10^{-6} \text{ m}^2$	Elkholy et al. [98, 186]
ϵ : 0.069 – 0.563 D_p : 0.146 – 0.506mm Material: Ti6Al4V Fluid: Water		K : $\sim 0.75 - 9.00 \times 10^{-10} \text{ m}^2$	Meng et al. [153]
ϵ : 0.31 – 0.37 (sintered), 0.55 – 0.85 (micro-pin) Material: micro-pin and sintered copper Fluid: Water	0.186 – 0.247 μm (sintered) 0.530 – 1.744 μm (micro-pin)	$\sim 5 \times 10^{-10} \text{ m}^2$ (Sintered) $\sim 2.2 - 125 \times 10^{-10} \text{ m}^2$ (micro-pin)	Mezghani et al. [121, 183]
ϵ : 0.46 – 0.59 r_{eff} : 0.088 – 0.122mm Material: AlSi ₁₀ Mg Fluid: Ethanol	0.27 – 0.45 μm		Robinson et al. [97]
ϵ : $\sim 0.10 - 0.58$ D_p : 0.112mm (Lattice) Material: SS 316L Fluid: Water	0.56 (Lattice) 0.31 (Porosity)	24.4 $\times 10^{-6} \text{ m}^2$ (Lattice) 11.34 $\times 10^{-6} \text{ m}^2$ (Porosity)	Reiche et al. [27]
ϵ : 0.70, 0.80, 0.90 D_p : 0.60, 0.70, 0.80, 0.90, 1.00mm Material: Voroni Ti6Al4V Fluid: Water		$\sim 0.312 - 1.864 \times 10^{-8} \text{ m}^2$	Chao et al. [187]

8.1.2 Conventional Benchmarking

As mentioned, comparing both the capillary performance and permeability results of this study to that of conventional wicking structures is an essential step to confirm the validity and future potential of additively manufactured heat pipes. Figure 8-3 shows the comparison of the capillary performance values derived from this study with those found in literature.

As with the literature found for AM-based wick structures, conventional wicking structures

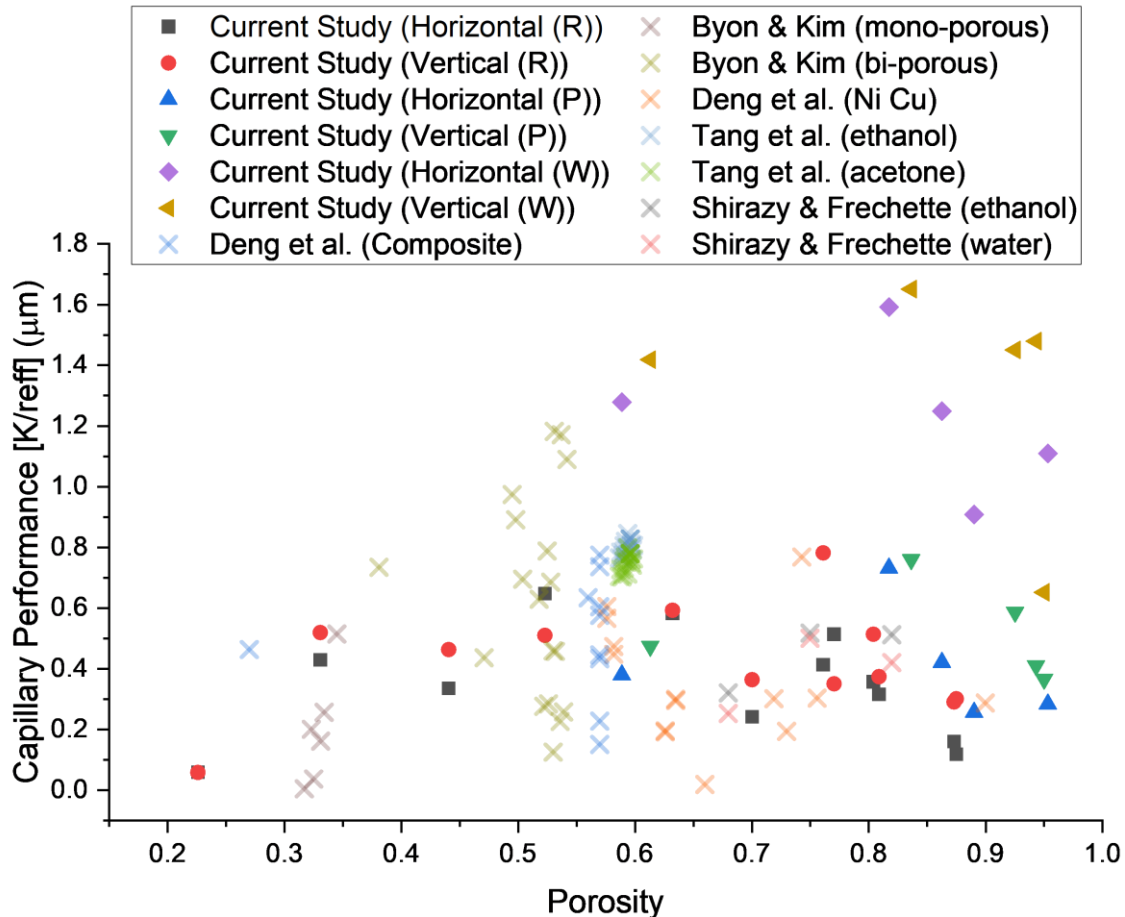


Figure 8-3. Literature comparison of capillary performance of raw samples with acetone (R), polished samples with acetone (P) and polished samples with water (W) to other conventional wicking structures.

also have a wide range of capillary performance values. The analysed samples within this study generally outperform that of conventional wicking structures, although it should also be noted that they show inferior results to the study of Byon & Kim [142] who investigated a novel bi-porous wicking structure. However, that study used sintered spherical glass beads to represent the metallic wicking structure. As identified in this current study, surface topography and roughness can have a significant effect on the results. Therefore, the glass beads used by Byon & Kim may not be representative of the metallic structure. Furthermore,

Deng et al. [43] compared their results to that of a grooved wicking structure of 0.5 porosity which showed a significantly enhanced capillary performance value of $12.9\mu\text{m}$ and showed significantly quicker capillary rise characteristics. Although the structures in this study have shown enhanced capillary performance over traditional wicking structures, their larger pore sizes do set operational limitations when operating against gravity, as is the case with grooved wicks. Therefore, the designed wick structures are better suited for applications operating with gravity (evaporator below condenser) or in microgravity climates such as spacecraft technologies.

Through evaluation of Figure 8-4, it can be determined that the permeability of the designed lattice structures within this study was significantly enhanced compared to traditional sintered wick configurations. The samples do however show similar values to the grooved wick of Deng et al. [43] and the copper fibre wicks analysed by Ling et al. [188]. The enhanced permeability of the manufactured lattice-based designs in this study, compared with traditional wicking structures, significantly improved fluid circulation through the wick. This in turn aids in increasing the heat pipe's heat transport capacity while reducing the temperature gradient and thermal resistance across the heat pipe's length.

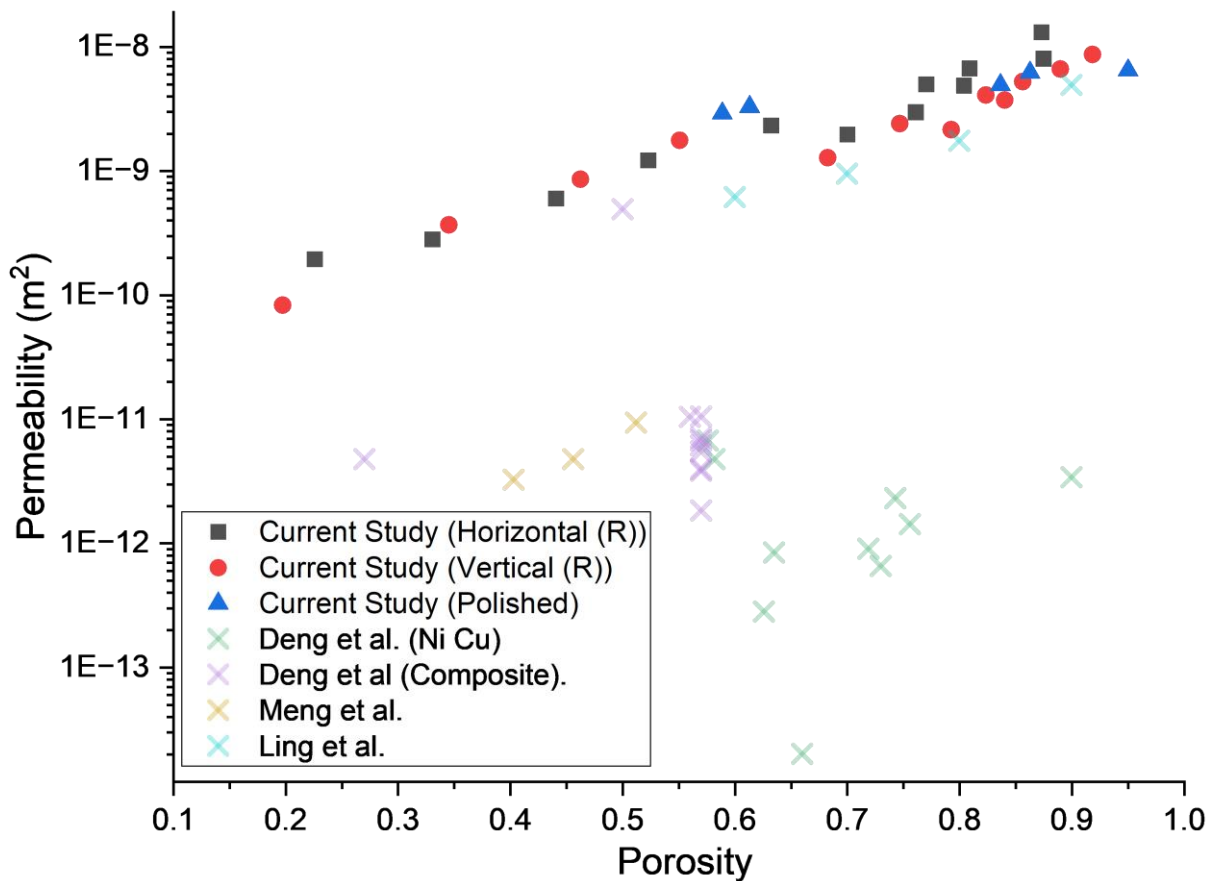


Figure 8-4. Literature comparison of permeability of raw samples (R) and polished samples to other conventional wicking structures.

8. Literature-Based Performance Benchmarking

Table 8-2. Comparison of current study capillary performance and permeability parameters to other conventionally manufactured heat pipe wicking structures found in literature

Wick & Fluid Characteristics	Capillary Performance (K/r_{eff})	Permeability	Reference
ϵ : 0.33 (Mono-), 0.52 (Bi-porous) D_p : N/A Material: Bi-porous sintered metal wicks / glass Fluid: Water	Mono-porous: 0.003 – 0.513 μm Bi-porous: 0.124 – 1.181 μm		Byon & Kim [142]
ϵ : 0.57 (Sintered), 0.50 (Grooved) D_p : N/A Material: Sintered Copper Fluid: Ethanol / Water	Sintered: 0.149 – 0.773 μm Grooved: 12.9 μm	Sintered: 1.83 – 10.05 $\times 10^{-12}\text{m}^2$ Grooved: 4.92 $\times 10^{-10}\text{m}^2$	Deng et al. [43]
ϵ : 0.68, 0.75, 0.82 D_p : N/A Material: Sintered Copper Fluid: Acetone and Water	Acetone: 0.319, 0.516, 0.511 μm Water: 0.251, 0.499, 0.419 μm		Shirazy & Frechette [143]
ϵ : 0.59 Material: Fluid: Ethanol / Acetone	Ethanol: 0.761 – 0.844 μm Acetone: 0.701 – 0.797 μm		Tang et al. [189]
ϵ : 0.57 – 0.64 r_{eff} : 1.5 – 11.9 μm Material: Sintered Copper & Sintered Nickel Fluid: Ethanol & Acetone	Ni: 0.190 – 0.298 μm Cu: 0.294 – 0.472 μm		Deng et al. [190]
ϵ : 0.403, 0.456, 0.512 r_p : 60, 95, 130 μm Material: Sintered Copper Fluid: Water		3.25, 4.76, 9.35 $\times 10^{-12}\text{m}^2$	Meng et al. [153]
ϵ : 0.6 – 0.90 Material: Copper fibre Fluid: Water		0.617 – 4.94 $\times 10^{-9}\text{m}^2$	Ling et al. [188]

9. Conclusions

This research aimed to further develop the understanding and potential of additively manufactured heat pipes, through designing, printing and evaluating a range of AlSi₁₀Mg Body-Centred-Cubic (BCC) lattice-based wicking structures with various designed strut thicknesses, cell sizes and printing orientations. This conclusion will summarise the key findings against the objectives previously set out in Section 2.10.

The study included a thorough evaluation of the printability, accuracy and topographical characteristics of the samples. Together, with the development of a 2D Lattice Analysis Tool (LAT), specifically designed for this study, numerous concluding remarks can be drawn. Excessive warpage on the horizontal samples resulted in numerous strut dislocations and compression of the pores at the centre of the samples, as highlighted with the heatmap distributions. The vertical samples were found to be superior in terms of printability but did suffer from an increased number of semi-sintered particles on the surface resulting in generally higher surface roughness. Surface roughness was shown to increase with a reduction in strut thickness, with a maximum Sa value of 14.46µm for sample V12, as the dimensional ratio between the roughness features and strut diameter became larger. The agglomerated particles were also shown to influence the deviation of the strut thickness from the intended CAD design with a maximum deviation of +26.4%, significantly less than the majority of results reported in literature.

Both capillary rate of rise and permeability experiments were conducted. Comparison of the operational limitations of the various samples showed that the wide range of design parameters utilised within this study were effective in determining the optimal design configuration with respect to both capillary performance and permeability. The vertical samples consistently showed superior equilibrium rise heights compared to the horizontal orientations, despite the vertical samples having higher porosities and similar pore dimensions. Capillary performance highlighted the importance of the trade-off between capillary pressure and permeability with the vertical samples found to be superior. Sample V12 was identified as having optimal parameters with a K/r_{eff} value of 0.782µm.

While the agglomeration of semi-sintered particles was shown to benefit the capillarity of the vertical samples, the additional internal pressure losses at forced flow conditions resulted

in noticeably reduced permeability. The measured Darcyan permeabilities varied from $8.32 \times 10^{-11} \text{ m}^2$ for sample V4 to $1.66 \times 10^{-8} \text{ m}^2$ for sample H9. The transitional permeability-based Reynolds number was shown to be lower for the vertical samples, indicating earlier onset of the quadratic Forchheimer regime.

The samples in this study generally outperformed traditional wicking structures in terms of both capillary performance and permeability. Further enhancements of capillary performance parameters may be achievable with the pursuit of smaller unit cell size geometries. Within the set parameters of this study, cell sizes of down to 0.50, and possibly 0.40mm, could be achieved with the 0.15mm strut thickness samples. Due to the effect of the agglomerations, further reductions in strut thickness may require smaller non-standard diameter feedstock. The larger pore sizes of the designed wicking structures in this study, do set operational limitations when operating against gravity meaning that, without further developments, they would be better suited to applications operating with gravity (evaporator above condenser) or in microgravity climates such as spacecraft technology applications.

Following chemical polishing, sample hydrophilicity was improved through the removal of semi-sintered particles and reduction in surface roughness, with up to a $\sim 60\%$ reduction in S_a and S_q values for sample set 12. An average improvement of 36.8% was seen for the capillary performance of the samples etched for 1 minute, mainly influenced by the improved capillarity, while a reduction of 3.3% was seen for those polished for 3 minutes. The most noticeable change following chemical polishing was the samples' ability to transfer water through capillary action. This study found an average 189.7% improvement in capillary performance with the use of water as the working fluid. The removal of agglomerated particles and substantial reduction in surface roughness also resulted in significant reduction in pressure drop across a range of flow rates while enhancing the permeability and delaying the onset of the Forchheimer regime. This aids in extending heat pipe operational heat transport capacity and permits the use of longer heat pipes through the enhancement of liquid return to the evaporator.

The potential of AM wicking structures for heat pipe applications, and their performance enhancement through post-processing, is undeniable, offering significant prospects for future developments.

10. Recommendations for Further Work

- Further development of the Lattice Analysis Tool (LAT) include enhancing the capabilities of the cell and strut analysis feature through incorporating further inbuilt analysis of the results such as heatmaps and histograms. Expanding LAT's capabilities for the wider AM sector should also be considered. This should include enhanced defect characterisation and improved CAD comparison techniques.
- Conduct a full parameter study into the various chemical polishing parameters, including optimising solution concentrations and etching time for each designed strut thickness. Refining these parameters would likely result in further wick capillary performance and permeability enhancements, solidifying the use of AM in the manufacture of heat pipe structures. Quantification of internal surface elemental analysis should also be undertaken.
- Perform further wick design iterations, specifically utilising the benefits of AM through the manufacture of variable wick geometry with properties tailored to the fluid characteristics and thermal requirements at specific locations of the heat pipe (evaporator, adiabatic and condenser sections).
- Strive to achieve finer lattice geometry with reductions in cell sizes for the 0.15mm strut thickness samples in addition to developing optimised build file parameters tailored for thinner structures to further enhance the deliverable capillary pressure and capabilities of AM wicking structures when operating against gravity.
- Investigate the use of Computational Fluid Dynamics (CFD) modelling coupled with further experimental campaigns to further the understanding of the fluid transport mechanisms and quantify the internal contact angles through the lattice structures. CFD could provide a detailed insight and visualisation into the internal flow dynamics, pressure distribution and velocity fields arising from the various design parameters, roughness features and structure defects.

11. References

1. United Nations, Paris Agreement. 2015. Available from: <https://unfccc.int/process-and-meetings/the-paris-agreement/the-paris-agreement>.
2. *Climate Change 2021: The Physical Basis*. 2021, IPCC.
3. *Climate Change 2014: Synthesis Report*. 2014, IPCC.
4. *Climate Change 2022: Mitigation of Climate Change*. 2022, IPCC.
5. Navigant Europe Ltd., *Pathways to Net-Zero: Decarbonising the Gas Networks in Great Britain*. 2019, Energy Networks Association.
6. International Renewable Energy Agency, *World Energy Transitions Outlook: 1.5°C Pathway*. 2021, Abu Dhabi.
7. Climate Change Committee, *Independent Assessment: The UK's Net Zero Strategy*. 2021.
8. Malinauskaite, J. and Jouhara, H., *A Theoretical Analysis of Waste Heat Recovery Technologies*, in *Sustainable Energy Technology, Business Models, and Policies*. 2024. p. 99-144.
9. Committee on Climate Change, *Net Zero Technical Report*. 2019.
10. International Energy Agency, *World Energy Outlook*. 2021.
11. Mochizuki, M., et al., *A Review of Heat Pipe Application Including New Opportunities*. *Frontiers in Heat Pipes*, 2011. **2**(1).
12. Advanced Cooling Technologies, *Smallsat Thermal Managements*. Lancaster, USA.
13. Sazali, N., et al., *New Perspectives on Fuel Cell Technology: A Brief Review*. *Membranes (Basel)*, 2020. **10**(5).
14. Faghri, A. and Guo, Z., *Integration of Heat Pipe into Fuel Cell Technology*. *Heat Transfer Engineering*, 2010. **29**(3): p. 232-238.
15. Savino, R., Paterna, D., and Abe, Y., *Current Developments in Heat Pipes - an Overview*. *Recent Patents on Engineering*, 2007. **1**(2): p. 153-161.
16. Faghri, A., *Heat Pipes: Review, Opportunities and Challenges*. *Frontiers in Heat Pipes*, 2014. **5**(1).
17. Dilberoglu, U.M., et al., *The Role of Additive Manufacturing in the Era of Industry 4.0*. *Procedia Manufacturing*, 2017. **11**: p. 545-554.
18. Queipo, P. and Gonzalez, D., *Fofam and Am - Motion Initiatives: A Strategic Framework for Additive Manufacturing Deployment in Europe*, in *Additive Manufacturing— Developments in Training and Education*, E. Pei, M. Monzon, and A. Bernard, Editors. 2019, Springer: Switzerland.
19. Bhavar, V., et al., *A Review on Powder Bed Fusion Technology of Metal Additive Manufacturing*. 2014.

20. Sauerwein, M., et al., *Exploring the Potential of Additive Manufacturing for Product Design in a Circular Economy*. Journal of Cleaner Production, 2019. **226**: p. 1138-1149.
21. Shi, Y., et al., *Materials for Additive Manufacturing*. 2021, London: Academic Press.
22. Körner, C., *Additive Manufacturing of Metallic Components by Selective Electron Beam Melting - a Review*. International Materials Reviews, 2016. **61**(5): p. 361-377.
23. Sing, S.L., et al., *Laser and Electron-Beam Powder-Bed Additive Manufacturing of Metallic Implants: A Review on Processes, Materials and Designs*. J Orthop Res, 2016. **34**(3): p. 369-85.
24. *An Overview on Extension and Limitations of Macroscopic Darcy's Law for a Single and Multi-Phase Fluid Flow through a Porous Medium*. International Journal of Mining Science, 2019. **5**(4).
25. Gokuldoss, P.K., Kolla, S., and Eckert, J., *Additive Manufacturing Processes: Selective Laser Melting, Electron Beam Melting and Binder Jetting-Selection Guidelines*. Materials, 2017. **10**(6).
26. Geerts, F. and Renda, V., *The Machine Tool Industry's Changing Skills Needs: What Is the Impact of Additive Manufacturing Technologies?*, in *Additive Manufacturing—Developments in Training and Education*, E. Pei, M. Monzon, and A. Bernard, Editors. 2019, Springer: Switzerland.
27. Reich, S., Bold, D., and Schleifenbaum, J.H., *Effect of Targeted Porosity in Additively Manufactured Heat Pipes*, in *Industrializing Additive Manufacturing*. 2024. p. 337-352.
28. van Zwol, P.J., Palasantzas, G., and De Hosson, J.T., *Influence of Roughness on Capillary Forces between Hydrophilic Surfaces*. Phys Rev E Stat Nonlin Soft Matter Phys, 2008. **78**(3 Pt 1): p. 031606.
29. Leary, M., et al., *Surface Roughness*, in *Fundamentals of Laser Powder Bed Fusion of Metals*. 2021. p. 179-213.
30. Vasiliev, L.L., *Heat Pipes in Modern Heat Exchangers*. Applied Thermal Engineering, 2005. **25**(1): p. 1-19.
31. Faghri, A., *Review and Advances in Heat Pipe Science and Technology*. Journal of Heat Transfer, 2012. **134**(12).
32. Vasiliev, L.L. and Vasiliev, L.L., *Heat Pipes to Increase the Efficiency of Fuel Cells*. International Journal of Low-Carbon Technologies, 2009. **4**(2): p. 96-103.
33. Esarte, J., et al., *Optimizing the Design of a Two-Phase Cooling System Loop Heat Pipe: Wick Manufacturing with the 3d Selective Laser Melting Printing Technique and Prototype Testing*. Applied Thermal Engineering, 2017. **111**: p. 407-419.
34. Szymanski, P., et al., *Recent Advances in Loop Heat Pipes with Flat Evaporator*. Entropy (Basel), 2021. **23**(11).
35. Reay, D.A., Kew, P.A., and McGlen, R.J., *Heat Pipes - Theory, Design and Applications*. Sixth Edition ed. Heat Pipes. 2014. 135-173.

36. Han, X., et al., *Review of the Development of Pulsating Heat Pipe for Heat Dissipation*. Renewable and Sustainable Energy Reviews, 2016. **59**: p. 692-709.
37. Sarraf, D., Bonner, R., and Colahan, D., *Passive Thermal Management for a Fuel Cell Reforming Process*, in *4th International Energy Conversion Engineering Conference and Exhibit (IECEC)*. 2006, American Institute of Aeronautics and Astronautics: San Diego, California.
38. Reay, D.A., *Thermal Energy Storage: The Role of the Heat Pipe in Performance Enhancement*. International Journal of Low-Carbon Technologies, 2015. **10**(2): p. 99-109.
39. Advanced Thermal Solutions, *Ats Engineering Ebook*, in *Collection of Technical Articles on Heat Pipes and Their Roles in the Thermal Management of Electronics*. 2020.
40. Ozguc, S., et al., *Experimental Demonstration of an Additively Manufactured Vapor Chamber Heat Spreader*, in *18th IEEE ITherm Conference*. 2019: Las Vegas.
41. Yang, X., Yan, Y.Y., and Mullen, D., *Recent Developments of Lightweight, High Performance Heat Pipes*. Applied Thermal Engineering, 2012. **33-34**: p. 1-14.
42. Vasiliev, L.L., *Micro and Miniature Heat Pipes – Electronic Component Coolers*. Applied Thermal Engineering, 2008. **28**(4): p. 266-273.
43. Deng, D., et al., *Characterization of Capillary Performance of Composite Wicks for Two-Phase Heat Transfer Devices*. International Journal of Heat and Mass Transfer, 2013. **56**(1-2): p. 283-293.
44. Tang, Y., et al., *Experimental Investigation on Capillary Force of Composite Wick Structure by Ir Thermal Imaging Camera*. Experimental Thermal and Fluid Science, 2010. **34**(2): p. 190-196.
45. Wang, Q., Hong, J., and Yan, Y., *Biomimetic Capillary Inspired Heat Pipe Wicks*. Journal of Bionic Engineering, 2014. **11**(3): p. 469-480.
46. Putra, N. and Septiadi, W.N., *Improvement of Heat Pipe Performance through Integration of a Coral Biomaterial Wick Structure into the Heat Pipe of a Cpu Cooling System*. Heat and Mass Transfer, 2016. **53**(4): p. 1163-1174.
47. Davison, H.W., *Compilation of Thermophysical Properties of Liquid Lithium*. 1968, NATIONAL AERONAUTICS AND SPACE ADMINISTRATION: Washington.
48. Roehlich, F., Tepper, F., and Rankin, R., *Surface Tension of Four Alkali Metals to 1000c*. JOURNAL OF CHEMICAL AND ENGINEERING DATA, 1968. **13**(4).
49. Jouhara, H., et al., *Heat Pipe Based Systems - Advances and Applications*. Energy, 2017. **128**: p. 729-754.
50. Reay, D.A., Kew, P.A., and McGlen, R.J., *Heat Transfer and Fluid Flow Theory*, in *Heat Pipes*. 2014. p. 15-64.
51. Bell, I., et al., *Pure and Pseudo-Pure Fluid Thermophysical Property Evaluation and the Open-Source Thermophysical Property Library Coolprop*. Industrial & Engineering Chemistry Research, 2014. **53**(6): p. 2498-2508.

52. Reay, D.A., Kew, P.A., and McGlen, R.J., *Heat Pipe Components and Materials*, in *Heat Pipes*. 2014. p. 65-94.
53. Shukla, K.N., *Heat Pipe for Aerospace Applications—an Overview*. Journal of Electronics Cooling and Thermal Control, 2015. **05**(01): p. 1-14.
54. Wenzel, R., *Resistance of Solid Surfaces to Wetting by Water*. Ind. Eng. Chem. , 1936. **28**(8): p. 988–994.
55. Cassie, A.B.D. and Baxter, S., *Wettability of Porous Surfaces*. Transactions of the Faraday Society, 1944. **40**(0): p. 546-551.
56. Kim, D.E., et al., *Review of Boiling Heat Transfer Enhancement on Micro/Nanostructured Surfaces*. Experimental Thermal and Fluid Science, 2015. **66**: p. 173-196.
57. Rezaei, M., et al., *Wetting Phenomena in Membrane Distillation: Mechanisms, Reversal, and Prevention*. Water Res, 2018. **139**: p. 329-352.
58. Azizian, S. and Khosravi, M., *Advanced Oil Spill Decontamination Techniques*, in *Advanced Low-Cost Separation Techniques in Interface Science*. 2019. p. 283-332.
59. Li, H., et al., *Advances in Organic Adsorption on Hydrophilic Hierarchical Structures for Bionic Superhydrophobicity: From Fundamentals to Applications*. Journal of Materials Chemistry A, 2024. **12**(25): p. 14885-14939.
60. Nguyen, D.H. and Ahn, H.S., *A Comprehensive Review on Micro/Nanoscale Surface Modification Techniques for Heat Transfer Enhancement in Heat Exchanger*. International Journal of Heat and Mass Transfer, 2021. **178**.
61. Smith, R. and Burns, M. *Analysis of Anti-Bacterial Properties and Cytological Location of Allelochemicals in Several Varieties of Hosta*. in *National Conference on Undergraduate Research (NCUR)*. 2011. New York.
62. Saubade, F., et al., *Principal Component Analysis to Determine the Surface Properties That Influence the Self-Cleaning Action of Hydrophobic Plant Leaves*. Langmuir, 2021. **37**(27): p. 8177-8189.
63. Darmanin, T. and Guittard, F., *Superhydrophobic and Superoleophobic Properties in Nature*. Materials Today, 2015. **18**(5): p. 273-285.
64. Ahmad, D., et al., *Hydrophilic and Hydrophobic Materials and Their Applications*. Energy Sources, Part A: Recovery, Utilization, and Environmental Effects, 2018. **40**(22): p. 2686-2725.
65. Bejan, A. and Kraus, A., *Heat Transfer Handbook*. 2003, New Jersey: John Wiley & Sons Inc.
66. Zohuri, B., *Functionality, Advancements and Industrial Applications of Heat Pipes*. 2020, London: Academic Press.
67. Putra, N. and Ariantara, B., *Electric Motor Thermal Management System Using L-Shaped Flat Heat Pipes*. Applied Thermal Engineering, 2017. **126**: p. 1156-1163.

68. Sun, Y., et al., *Experimental and Numerical Investigation on a Novel Heat Pipe Based Cooling Strategy for Permanent Magnet Synchronous Motors*. Applied Thermal Engineering, 2020. **170**.
69. Wrobel, R. and McGlen, R.J., *Opportunities and Challenges of Hp in Thermal Management of Electrical Machines*, in *International Conference on Electrical Machines (ICEM)*. 2020: Gothenberg, Sweden. p. 961-967.
70. National Aeronautics and Space Administration (NASA), *Small Spacecraft Technology State of the Art Report*. 2021: California.
71. Hallet, B., *Why Do Freezing Rocks Break*. Science, 2006. **314**: p. 1092-1093.
72. Alario, J.P. and Prager, R.C., *Space Shuttle Orbiter - Heat Pipe Applications*. 1972.
73. Harkness, R.E., *Performance of the Geos-1i*. 1969, APL.
74. Dussinger, P., Sarraf, D., and Anderson, W., *Loop Heat Pipe for Tacsat-4*, in *Space, Propulsion & Energy Sciences International Forum: SPESIF-2009*. 2009. p. 91-100.
75. Baturkin, V., et al., *Elaboration of Thermal Control Systems on Heat Pipes for Microsatellites Magion 4, 5 and Bird*. Applied Thermal Engineering, 2003. **23**(9): p. 1109-1117.
76. Cotter, T.P., *Theory of Heat Pipes*. 1965, LOS ALAMOS SCIENTIFIC LABORATORY: New Mexico.
77. Lee, K.-L., Tarau, C., and Anderson, W., *Titanium Water Heat Pipe Radiators for Space Fission System Thermal Management*, in *Joint 19th IHPC and 13th IHPS*. 2018: Pisa, Italy.
78. Li, Q., et al., *A Review on Temperature Control of Proton Exchange Membrane Fuel Cells*. Processes, 2021. **9**(2).
79. Burke, K., et al., *Demonstration of Passive Fuel Cell Thermal Management Technology*. 2012, National Aeronautics and Space Administration: Ohio.
80. Huang, B., et al., *Research on the in-Plane Temperature Distribution in a Pemfc Stack Integrated with Flat-Plate Heat Pipe under Different Startup Strategies and Inclination Angles*. Applied Thermal Engineering, 2020. **179**.
81. Veiga, C., Davim, J.P., and Loureiro, A.J.R., *Properties and Applications of Titanium Alloys: A Brief Review* Reviews on Advanced Materials Science, 2012. **32**: p. 14-34.
82. Burke, K. and Jakupca, I., *Unitized Regenerative Fuel Cell System Loop Heat Pipe*. Journal of Aerospace, 2004. **113**(1): p. 1807-1817.
83. Reay, D.A., Kew, P.A., and McGlen, R.J., *Applications of the Heat Pipe*, in *Heat Pipes*. 2014. p. 175-206.
84. Zohuri, B., *Heat Pipe Infrastructure*, in *Functionality, Advancements and Industrial Applications of Heat Pipes*. 2020. p. 1-45.
85. Jeerh, G., Zhang, M., and Tao, S., *Recent Progress in Ammonia Fuel Cells and Their Potential Applications*. Journal of Materials Chemistry A, 2021. **9**(2): p. 727-752.

86. Padmavathi, C., Agarwal, D., and Upadhyaya, A., *Microwave Sintering of Aluminum Alloy*. 2010.
87. Schaffer, G.B., Sercombe, T.B., and Lumley, R.N., *Liquid Phase Sintering of Aluminium Alloys*. Materials Chemistry and Physics, 2001. **67**(1-3): p. 85-91.
88. Ameli, M., et al., *A Novel Method for Manufacturing Sintered Aluminium Heat Pipes (Sahp)*. Applied Thermal Engineering, 2013. **52**(2): p. 498-504.
89. Gupta, R., Chen, C.-H., and Anderson, W., *Progress on 3d Printed Loop Heat Pipes*, in *50th International Conference on Environmental Systems*. 2021: Lisbon.
90. Hoenig, S., et al., *Development of a Passive Thermal Control Valve for 3dprinted Loop Heat Pipes*, in *50th International Conference on Environmental Systems*. 2021: Lisbon.
91. Richard, B., et al., *Development of a 3d Printed Loop Heat Pipe*, in *49th International Conference on Environmental Systems*. 2019: Boston.
92. Richard, B., Pellicone, D., and Anderson, B., *Loop Heat Pipe Wick Fabrication Via Additive Manufacturing*, in *47th International Conference on Environmental Systems*. 2017: Charleston.
93. ASTM, *Standard Test Method for Maximum Pore Diameter and Permeability of Rigid Porous Filters*. 2019.
94. du Plessis, A. and Macdonald, E., *Hot Isostatic Pressing in Metal Additive Manufacturing: X-Ray Tomography Reveals Details of Pore Closure*. Additive Manufacturing, 2020. **34**.
95. Jafari, D., Wits, W.W., and Geurts, B.J., *Metal 3d-Printed Wick Structures for Heat Pipe Application: Capillary Performance Analysis*. Applied Thermal Engineering, 2018. **143**: p. 403-414.
96. Jafari, D., Wits, W.W., and Geurts, B.J., *Phase Change Heat Transfer Characteristics of an Additively Manufactured Wick for Heat Pipe Applications*. Applied Thermal Engineering, 2020. **168**.
97. Robinson, A.J., et al., *A Wicked Heat Pipe Fabricated Using Metal Additive Manufacturing*. International Journal of Thermofluids, 2021. **12**.
98. Elkholy, A., Durfee, J., and Kempers, R., *Development of Additive Manufactured Metal Wick Structures for Two-Phase Heat Transfer Applications*, in *2022 21st IEEE Intersociety Conference on Thermal and Thermomechanical Phenomena in Electronic Systems (iTherm)*. 2022. p. 1-5.
99. Groth, J.-H., et al., *Stochastic Design for Additive Manufacture of True Biomimetic Populations*. Additive Manufacturing, 2022. **55**.
100. Kaur, I. and Singh, P., *State-of-the-Art in Heat Exchanger Additive Manufacturing*. International Journal of Heat and Mass Transfer, 2021. **178**.
101. Runyon, J., et al., *Characterization of Additive Layer Manufacturing Swirl Burner Surface Roughness and Its Effects on Flame Stability Using High-Speed Diagnostics*. Journal of Engineering for Gas Turbines and Power, 2020. **142**(4).

102. Tyagi, P., et al., *Reducing the Roughness of Internal Surface of an Additive Manufacturing Produced 316 Steel Component by Chempolishing and Electropolishing*. Additive Manufacturing, 2019. **25**: p. 32-38.
103. Acquesta, A. and Monetta, T., *The Electropolishing of Additively Manufactured Parts in Titanium: State of the Art*. Advanced Engineering Materials, 2021. **23**(12).
104. Ferchow, J., Hofmann, U., and Meboldt, M., *Enabling Electropolishing of Complex Selective Laser Melting Structures, in 30th CIRP Design*. 2020: Pretoria, South Africa. p. 472–47.
105. Gomez-Gallegos, A.A., Mill, F., and Mount, A.R., *Surface Finish Control by Electrochemical Polishing in Stainless Steel 316 Pipes*. Journal of Manufacturing Processes, 2016. **23**: p. 83-89.
106. Basha, M.M., et al., *State of the Art on Chemical and Electrochemical Based Finishing Processes for Additive Manufactured Features*. Additive Manufacturing, 2022. **58**.
107. Łyczkowska, E., et al., *Chemical Polishing of Scaffolds Made of Ti–6Al–7Nb Alloy by Additive Manufacturing*. Archives of Civil and Mechanical Engineering, 2014. **14**(4): p. 586-594.
108. Sharma, R., Kumar, S., and Saha, R., *Enhancing Surface Quality of Slm Produced Alsi10mg Components through Chemical Polishing*. International Journal of System Assurance Engineering and Management, 2023. **14**(5): p. 1955-1960.
109. Sharma, R., Kumar, S., and Saha, R.K., *Improving the Surface Quality of Laser Sintered Alsi10mg Using Chemical Method*. Gedrag & Organisatie Review, 2020. **33**(03).
110. Scherillo, F., *Chemical Surface Finishing of Alsi10mg Components Made by Additive Manufacturing*. Manufacturing Letters, 2019. **19**: p. 5-9.
111. Wang, X., et al., *Finishing of Additively Manufactured Metal Parts by Abrasive Flow Machining in Solid Freeform Fabrication 2016: Proceedings of the 27th Annual International*. 2016: Texas, USA.
112. Mason, B., et al., *Development of a Novel Laser Polishing Strategy for Additively Manufactured Alsi10mg Alloy Parts, in 9th International Conference on Sustainable Design and Manufacturing*. 2022, Springer.
113. Gisario, A., Barletta, M., and Veniali, F., *Laser Polishing: A Review of a Constantly Growing Technology in the Surface Finishing of Components Made by Additive Manufacturing*. The International Journal of Advanced Manufacturing Technology, 2022. **120**(3-4): p. 1433-1472.
114. Mirzaali, M.J., et al., *Lattice Structures Made by Laser Powder Bed Fusion, in Fundamentals of Laser Powder Bed Fusion of Metals*. 2021. p. 423-465.
115. Majeed, M., et al., *Influence of Post-Processing on Additively Manufactured Lattice Structures*. Journal of the Brazilian Society of Mechanical Sciences and Engineering, 2022. **44**(9).
116. Chmielewska, A., et al., *Chemical Polishing of Additively Manufactured, Porous, Nickel-Titanium Skeletal Fixation Plates*. 3D Print Addit Manuf, 2022. **9**(4): p. 269-277.

117. Echeta, I., et al., *Review of Defects in Lattice Structures Manufactured by Powder Bed Fusion*. The International Journal of Advanced Manufacturing Technology, 2019. **106**(5-6): p. 2649-2668.
118. Pyka, G., et al., *Surface Roughness and Morphology Customization of Additive Manufactured Open Porous Ti6Al4V Structures*. Materials (Basel), 2013. **6**(10): p. 4737-4757.
119. Calvet, M., et al., *Innovative Post-Processing for Complex Geometries and Inner Parts of 3d-Printed AlSi10Mg Devices*. Materials, 2023. **16**(21).
120. Renishaw-plc, *Renam 500 Series Additive Manufacturing Systems*. 2023.
121. Mezghani, A., et al., *Laser Powder Bed Fusion Additive Manufacturing of Copper Wicking Structures: Fabrication and Capillary Characterization*. Rapid Prototyping Journal, 2021. **27**(6): p. 1181-1188.
122. Renishaw-plc, *Aluminium AlSi10Mg Powder Safety Data Sheet*, in H-5800-0947-02-A_EN. 2023, Renishaw-plc.
123. Du Plessis, A., et al., *Non-Destructive Testing of Parts Produced by Laser Powder Bed Fusion*, in *Fundamentals of Laser Powder Bed Fusion of Metals*. 2021. p. 277-300.
124. Thompson, A., Maskery, I., and Leach, R.K., *X-Ray Computed Tomography for Additive Manufacturing: A Review*. Measurement Science and Technology, 2016. **27**(7).
125. Kappe, K., et al., *Design Concepts and Performance Characterization of Heat Pipe Wick Structures by Lpbf Additive Manufacturing*. Materials 2022. **15**(24).
126. Sensoscan, *Installation Manual S Mart Sensoscan 6.4 V2*, Sensoscan, Editor. 2017.
127. British Standard, *Geometrical Product Specifications (Gps) - Surface Texture: Profile Method*. 2009.
128. Townsend, A., *Characterisation of the Surface Topography of Additively Manufactured Parts*. 2018, University of Huddersfield: University of Huddersfield Repository.
129. Vorburger, T.V., et al., *Comparison of Optical and Stylus Methods for Measurement of Surface Texture*. The International Journal of Advanced Manufacturing Technology, 2007. **33**(1-2): p. 110-118.
130. Sensofar Tech S.L., *Sensoview 1.9.2*. 2022.
131. British Standard, *Geometrical Product Specifications (Gps) - Surface Texture: Areal Method*. 2023.
132. ThermoFisher Scientific, *Phenom Prox G6 Desktop Sem Datasheet*. 2021.
133. Sturm, R., *Stereoscopic Effects from Single Sem Images*. Microscopy Today, 2018. **26**(4): p. 34-39.
134. Nikon Xtek High Flux Bay. 2020 [cited 2024; Available from: <https://nxct.ac.uk/facilities/manchester/high-flux-bay/>].
135. RS_Pro, *Acrylic Tube Datasheet*.

136. Polyfluor, *Pla Filament Datasheet*. 2023.
137. *Dragonfly*. Comet Technologies Canada Inc. 2022; Available from: <https://www.theobjects.com/dragonfly>.
138. Boas, F.E. and Fleischmann, D., *Ct Artifacts: Causes and Reduction Techniques*. *Imaging Med.*, 2012. **4**(2): p. 229-240.
139. Townsend, A., et al., *Surface Texture Metrology for Metal Additive Manufacturing: A Review*. *Precision Engineering*, 2016. **46**: p. 34-47.
140. Otsu, N., *A Threshold Selection Method from Gray-Level Histograms*. *IEEE TRANSACTIONS ON SYSTEMS, MAN, AND CYBERNETICS*, 1979. **9**(1): p. 62-66.
141. Hazeli, K., et al., *Microstructure-Topology Relationship Effects on the Quasi-Static and Dynamic Behavior of Additively Manufactured Lattice Structures*. *Materials & Design*, 2019. **176**.
142. Byon, C. and Kim, S.J., *Capillary Performance of Bi-Porous Sintered Metal Wicks*. *International Journal of Heat and Mass Transfer*, 2012. **55**(15-16): p. 4096-4103.
143. Shirazy, M. and Frechette, L., *Investigation of Capillary Properties of Copper Metal Foams by the Rate of Rise Method in the Presence of Evaporation*, in *13th IEEE ITherm*. 2012.
144. Chamrathy, P., et al. *Novel Fluorescent Visualization Method to Characterize Transport Properties in Micro/Nano Heat Pipe Wick Structures*. in *ASME 2009 InterPACK Conference*. 2009. San Fransisco: ASME.
145. Jurin, J., *li. An Account of Some Experiments Shown before the Royal Society; with an Enquiry into the Cause of the Ascent and Suspension of Water in Capillary Tubes*. *Phil. Trans. R. Soc.*, 1718. **30**: p. 739-747.
146. Liu, S., Li, S., and Liu, J., *Jurin's Law Revisited: Exact Meniscus Shape and Column Height*. *Eur Phys J E Soft Matter*, 2018. **41**(3): p. 46.
147. NEC Avio Infrared Technologies. *Infrared Thermography H2640/H2630 Series*. 2013 [cited 2024 21/06/2024]; Available from: <https://www.infrared.avio.co.jp/en/products/ir-thermo/lineup/h2640/index.html>.
148. Sartorius, *Entri li Essential Line Operating Instructions*. 2021: Goettingen, Germany.
149. Whiteblue_Consulting. *Thermography Studio*. 2012.
150. Ravi, J., et al., *Polymeric Membranes for Desalination Using Membrane Distillation: A Review*. *Desalination*, 2020. **490**.
151. Claramunt, S., et al., *Membranes for the Gas/Liquid Phase Separation at Elevated Temperatures: Characterization of the Liquid Entry Pressure*. *Membranes (Basel)*, 2021. **11**(12).
152. Schindelin, J., et al., *Fiji: An Open-Source Platform for Biological-Image Analysis*. *Nat Methods*, 2012. **9**(7): p. 676-82.

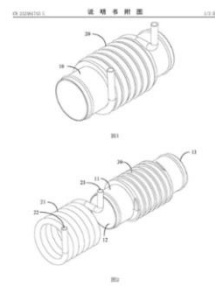
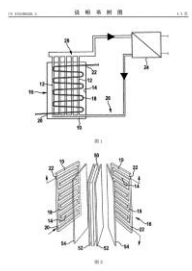
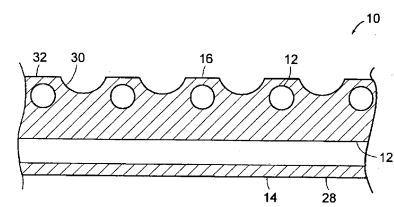
153. Meng, X., et al., *Performance Characterisation and Printing Parameter Modelling of Selective Laser Melting Printed Capillary Wicks*. Rapid Prototyping Journal, 2022. **28**(8): p. 1558-1572.
154. Kouidri, A. and Madani, B., *Experimental Hydrodynamic Study of Flow through Metallic Foams: Flow Regime Transitions and Surface Roughness Influence*. Mechanics of Materials, 2016. **99**: p. 79-87.
155. Bronkhorst, *Mini Cori-Flow M14 Datasheet*, in *Low Flow Coriolis Mass Flow Meter*.
156. Druck, *Unik5000 Pressure Sensing Platform Datasheet*. 2021.
157. Furumoto, T., et al., *Permeability and Strength of a Porous Metal Structure Fabricated by Additive Manufacturing*. Journal of Materials Processing Technology, 2015. **219**: p. 10-16.
158. Polytek, *Pt Flex Liquid Rubbers Datasheet*. 2015.
159. National_Instruments. *Flexlogger R1*. 2019; Available from: <https://www.ni.com/en/shop/data-acquisition-and-control/flexlogger.html>.
160. RS Pro, *Ptfe Datasheet*. 2020, RS Pro
161. Hughes, L., et al., *Development of a Matlab-Based Automatic Lattice 2d Analysis Tool for Heat Pipe Wick Structures*, in *Joint 21st IHPC and 15th IHPS*. 2023: Melbourne, Australia.
162. *Gnu General Public License, Version 3*, F.S. Foundation, Editor. 2007.
163. *Matlab*. 2022: Massachusetts.
164. The Mathworks Inc., *Matlab Function Reference*. 2024: massachusetts.
165. *Matlab*. 2022 [cited 2022; Available from: <https://uk.mathworks.com/help/images/ref/edge.html>].
166. Sensofar, *Compact 3d Optical Sensors for in-Line Applications*. 2018.
167. Sensofar, *Installation Manual S Mart Sensoscan*. 2017.
168. Zheng, M., et al., *Quantitative Surface Characterisation and Stress Concentration of Additively Manufactured Niti Lattice Struts*. The International Journal of Advanced Manufacturing Technology, 2024. **130**(9-10): p. 4861-4882.
169. Druck, *Dpi 705 Series Druck Handheld Pressure Indicators*. 2015.
170. Druck, *Pv411a Druck Four-in-One Hand Pump*. 2006.
171. Taylor, J.R., *An Introduction to Error Analysis: The Study of Uncertainties in Physical Measurements*. 2nd ed. 1997, New York: University Science Books.
172. Lee, D.K., In, J., and Lee, S., *Standard Deviation and Standard Error of the Mean*. Korean J Anesthesiol, 2015. **68**(3): p. 220-3.
173. Mishra, A., et al., *Prediction and Validation of Flow Properties in Porous Lattice Structures*. Journal of Fluids Engineering, 2023. **145**(4).

174. Xiao, T., et al., *An Analytical Fractal Model for Permeability in Isotropic Open-Cell Metal Foam with Surface Roughness*. International Communications in Heat and Mass Transfer, 2021. **126**.
175. Bhullar, B.S., Gangacharyulu, D., and Das, S.K., *Temporal Deterioration in Thermal Performance of Screen Mesh Wick Straight Heat Pipe Using Surfactant Free Aqueous Nanofluids*. Heat and Mass Transfer, 2016. **53**(1): p. 241-251.
176. Renishaw-plc, *Alsi10mg-0403 Powder for Additive Manufacturing, in H-5800-1084-01-B Data sheet*. 2015.
177. Zoesmar, N., Fuchs, D., and Taha, I., *Treatment of Additively Manufactured Alsi10mg Surfaces for Improved Bonding with Fiber Reinforced Composites for Sandwich Applications*. Journal of Sandwich Structures & Materials, 2021. **24**(2): p. 1152-1168.
178. Lee, J.Y., et al., *The Surface Energy and Stress of Metals*. Surface Science, 2018. **674**: p. 51-68.
179. Jaccodine, R.J., *Surface Energy of Germanium and Silicon*. Journal of the Electrochemical Society, 1963. **110**: p. 524-527.
180. Kamrani Moghaddam, L., et al., *The Inhibition of Epidermal Growth Factor Receptor Signaling by Hexagonal Selenium Nanoparticles Modified by Sirna*. Cancer Gene Ther, 2016. **23**(9): p. 321-5.
181. Hara, S., et al., *Surface Energy, Stress and Structure of Well-Relaxed Amorphous Silicon: A Combination Approach of Ab Initio and Classical Molecular Dynamics*. Surface Science, 2005. **585**(1-2): p. 17-24.
182. Lee, B.M., et al., *Surface Nucleation of the Annealed Si on Sio₂ (111) Plane of Excimer Laser Substrates: A Molecular Dynamics Study*. Journal of Applied Physics, 2007. **101**.
183. Mezghani, A., *Laser Powder Bed Fusion Additive Manufacturing of Copper Wicking Structures for Heat Pipes and Vapor Chambers*. 2020, Pennsylvania State University.
184. Ameli, M., *Additive Layer Manufactured Sinter-Style Aluminium/Ammonia Heat Pipes*, in *Faculty of Engineering and Environment*. 2013, University of Northumbria.
185. Shigueoka, M.O., et al. *Permeability Analysis of Polymeric Porous Media Obtained by Material Extrusion Additive Manufacturing in Solid Freeform Fabrication 2019: Proceedings of the 30th Annual International*. 2019. Texas, USA.
186. Elkholy, A., et al., *A Rate-of-Rise Facility for Measuring Properties of Wick Structures*. Measurement Science and Technology, 2023. **34**(4).
187. Chao, L., et al., *Analysis of Mechanical Properties and Permeability of Trabecular-Like Porous Scaffold by Additive Manufacturing*. Front Bioeng Biotechnol, 2021. **9**: p. 779854.
188. Ling, W., et al., *Capillary Pumping Performance of Porous Copper Fiber Sintered Wicks for Loop Heat Pipes*. Applied Thermal Engineering, 2018. **129**: p. 1582-1594.
189. Tang, Y., et al., *Effect of Fabrication Parameters on Capillary Performance of Composite Wicks for Two-Phase Heat Transfer Devices*. Energy Conversion and Management, 2013. **66**: p. 66-76.

190. Deng, D., et al., *Evaluation of Capillary Performance of Sintered Porous Wicks for Loop Heat Pipe*. Experimental Thermal and Fluid Science, 2013. **50**: p. 1-9.
191. STATE FUEL CELL CORP. *Heat Exchanger of Fuel Cell System and Fuel Cell Vehicle*. 2021. CN212461743U
192. Robert, B.G. *Bipolar Plate for Fuel Cell or Electrolysis*. 2015. CN105186026A
193. Faghri, A. *Integrated Bipolar Plate Heat Pipe for Fuel Cell Stacks*. 2015. US2005037253A1
194. KORRA FUEL CELL ENERGY CO LTE and Ho, L.C. *The Fuel Cell Cooling System*. 2018. KR101866955B1
195. TOYOTA ENG & MFG NORTH AMERICA, et al. *Heat Pipe Separator for Fuel Cell Assembly Thermal Management*. 2021. US2021313598A1
196. Boeing Co, et al. *Heat Pipe with Non-Uniform Cross-Section*. 2019. US10480866B2
197. McGlen, R.J. and Thayer, J.G. *Capillary Device for Use in Heat Pipe and Method of Manufacturing Such Capillary Device*. 2018. EP2715265B1
198. Xu, J. *Gas Turbine Fuel Injector with Heat Pipe Cooling*. 2019. US10458331
199. Hislop, D. *Pin Fin Heat Exchanger*. 2017. WO2017072493A1

12. Appendix

12.1 Patent information of various heat pipe and heat exchanger designs and system integration.

Title	Description	Date	Application Number	Applicants / Inventor	Status	Image	Reference
Heat exchanger of fuel cell system and fuel cell vehicle	Heat exchanger to utilise large amount of heat from the compressed air to preheat the intake hydrogen	02/02/2021	CN212461743U	STATE FUEL CELL CORP	Granted		[191]
Bipolar Plate for Fuel Cell or Electrolysis	The design uses heat pipe-integrated bipolar plates to cool down the fuel cell stack with heat being disposed through a connected heat exchanger The invention uses two sets of channels (axial and transverse) where micro-heat pipes may be inserted and bonded to improve thermal management within the stack while requiring significantly smaller thermal gradients and reduced volume/weight compared to other methods	23/12/2015 29/10/2015 24/11/2015	CN105186026A DE102014207594 A1 JP2015211036A	BOSCH GMBH ROBERT	INVENTION PATENT APPLICATION DEEMED WITHDRAWN AFTER PUBLICATION		[192]
Integrated bipolar plate heat pipe for fuel cell stacks		17/02/2015	US2005037253A1	FAGHRI AMIR	APPLICATION DISCONTINUATION		[193]

The fuel cell stack cooling system

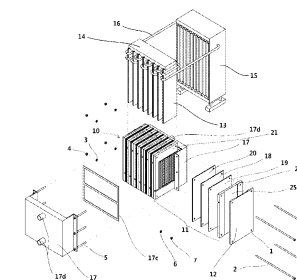
The present invention collects heat from inside the fuel cell stack with vertical flat plate heat pipes mounted in a recessed portion of the bipolar plate. The heat from the condenser is transferred via a cooling line to a separate radiator. The design resulted in unstable power generation under specific operating conditions by rapidly dissipating the heat within the stack.

12/06/2018

KR101866955B1

KORRA FUEL CELL ENERGY CO LTD

WRITTEN DECISION TO GRANT



[194]

HEAT PIPE SEPARATOR FOR FUEL CELL ASSEMBLY THERMAL MANAGEMENT

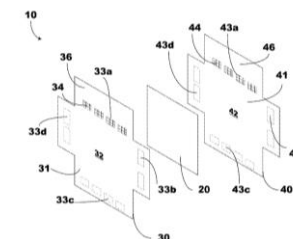
This design uses planar heat pipes to dissipate the heat within a fuel cell stack. Compared to a liquid cooled system, this design reduced the membrane temperature from 89°C to 70°C as well as the temperature gradient from 35°C to 10°C.

07/10/2021

US2021313598A1

TOYOTA ENG & MFG NORTH AMERICA

No data found yet



[195]

Heat pipe with non-uniform cross-section

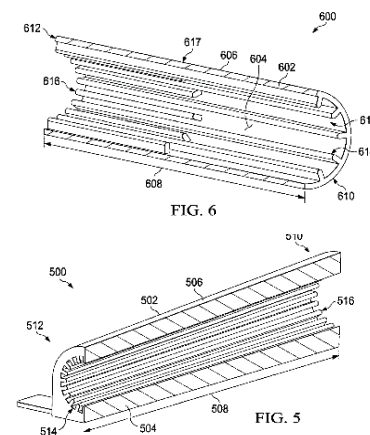
The groove-based wick structure with non-uniform cross-section manufactured through additive manufacturing aims to improve and enhance the heat pipes performance, specific to each section. A hot isotropic press and heat treatment process was conducted to reduce the porosity and increase strength of the monolithic component.

19/11/2019

CN108278915A
 CN108278915B
 EP3346220A1
 EP3346220B1
 JP2018162962A
 US10480866B2
 US2018187979A1

BOEING CO
 [US]

PATENTED
 CASE



[196]

Capillary device for use in heat pipe and method of manufacturing such capillary device

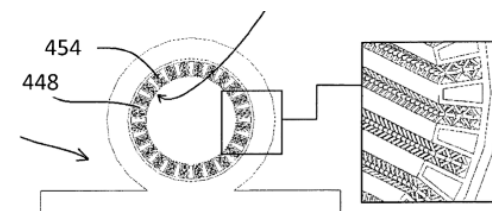
Believed to be the first patented heat pipe manufactured through laser powder bed fusion with integrated microscale lattice capillary wick structure

14/11/2018

EP2715265B1
 US11168944B2

R.J McGlen,
 J.G. Thayer
 Aavid
 Thermal
 Corp.

Granted



[197]

Gas Turbine Fuel Injector with Heat Pipe Cooling

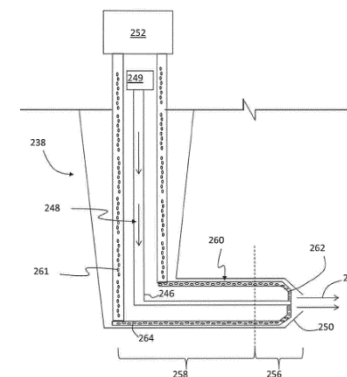
Utilising heat pipe technology to cool a GT fuel injector with the evaporator end in thermal contact with the nozzle and the condenser end is cooled by the fuel source. The injector and heat pipe may be integrated into a single component via additive manufacturing.

29/10/2019

US10458331 B2
EP3260780 B1

JinQuan Xu
United Technologies Corporation

Granted



[198]

Pin Fin Heat Exchanger

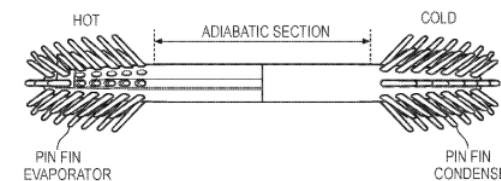
The pin fin heat exchanger includes a heat pipe with additional pin fins attached to the evaporator and condenser ends, each with fluid entrances and exits to the main tube. This design was manufactured via additive manufacturing for gas turbine recuperator application.

04.05.2017

WO2017072493A
1

Drummond Hislop

Granted



[199]

12.2 Merit Number Matlab Script

```

% Set Parameters
Fluid = ["water", "ammonia", "methanol", "ethanol", "Acetone"];
Fluid_num = length(Fluid); % Number of Fluids
% Temperature range
T_maxlim = 400; % Max Temp °C
T_minlim = -200; % Min Temp °C
T_step = 2; % Temp step °C
T = (T_minlim:T_step:T_maxlim); % Vector of temperature range
T_num = length(T); %Number of temperature points

%Set empty arrays
Rho = zeros(T_num, Fluid_num); %empty Matrix for Density
Rho_ac= zeros(51,1);
I = zeros(T_num, Fluid_num); %empty Matrix for Surface Tension
H_fg = zeros(T_num, Fluid_num); %empty Matrix for Latent Heat
V = zeros(T_num, Fluid_num); %empty Matrix for Liquid Viscosity
M = zeros(T_num, Fluid_num); %empty Matrix for Merit Number
T_triple = zeros(Fluid_num,1); %empty vector for triple temperature
T_crit = zeros(Fluid_num,1); %empty vector for critical temperature

for i = 1:T_num
    for j = 1:Fluid_num
        try
            Rho(i,j) = py.CoolProp.CoolProp.PropsSI('D','T',T(i)+273,'Q',0,Fluid(j)); %Density Kg/m3
            I(i,j) = py.CoolProp.CoolProp.PropsSI('I','T',T(i)+273,'Q',0,Fluid(j)); %Surface Tension
N/m
            H_fg(i,j) = py.CoolProp.CoolProp.PropsSI('H','T',T(i)+273,'Q',1,Fluid(j))-
py.CoolProp.CoolProp.PropsSI('H','T',T(i)+273,'Q',0,Fluid(j)); %Latent Heat J/kg
            V(i,j) = py.CoolProp.CoolProp.PropsSI('V','T',T(i)+273,'Q',0,Fluid(j)); %Liquid absolute
(dynamic) Viscosity Pa.s (Ns/m2)
        % end
    end
end

```



```

M(i,j) = (Rho(i,j)*l(i,j)*H_fg(i,j))/V(i,j); %Merit Number

continue %Skips to next iteration after error
end
T_triple(j) = py.CoolProp.CoolProp.PropsSI('Ttriple',Fluid(j))-273.15; %triple
temperature
T_crit(j) = py.CoolProp.CoolProp.PropsSI('Tcrit',Fluid(j))-273.15; %critical temperature
end
end

%Plot fluid triple and critical temperature
figure;
x = Fluid;
y= [T_triple, T_crit];
barh(y,'stacked')
yticklabels(Fluid)
title("Fluid Range")
xlabel('Temperature / °C')
ylabel('Fluid')
hold on
legend('Triple Temperature','Critical Temperature','Min. Temperature','Max.
Temperature')

%Plot Merit Number
figure;
xT1 = linspace(T_minlim,T_maxlim,T_num);
yM1 = M;
yM1(yM1==0)=NaN; %ignores zero values
plot (xT1, yN1,'--','LineWidth',2);
hold on
legend([Fluid,"Acetone"])
xlim([-150 400])
xlabel("Temperature (°C)")

```



```
ylabel("Merit Number (W/m^2)")

%plot Merit number with log scale
figure;
xT2 = linspace(T_minlim,T_maxlim,T_num);
yM2 = yM1;
plot (xT2, yM2,'--','LineWidth',2);
hold on
legend([Fluid,"Acetone"])
xlim([-150 400])
xlabel("Temperature (°C)")
ylabel("Merit Number (W/m^2) - Log")
set(gca, 'YScale', 'log')
```

12.3 Fixture Drawings

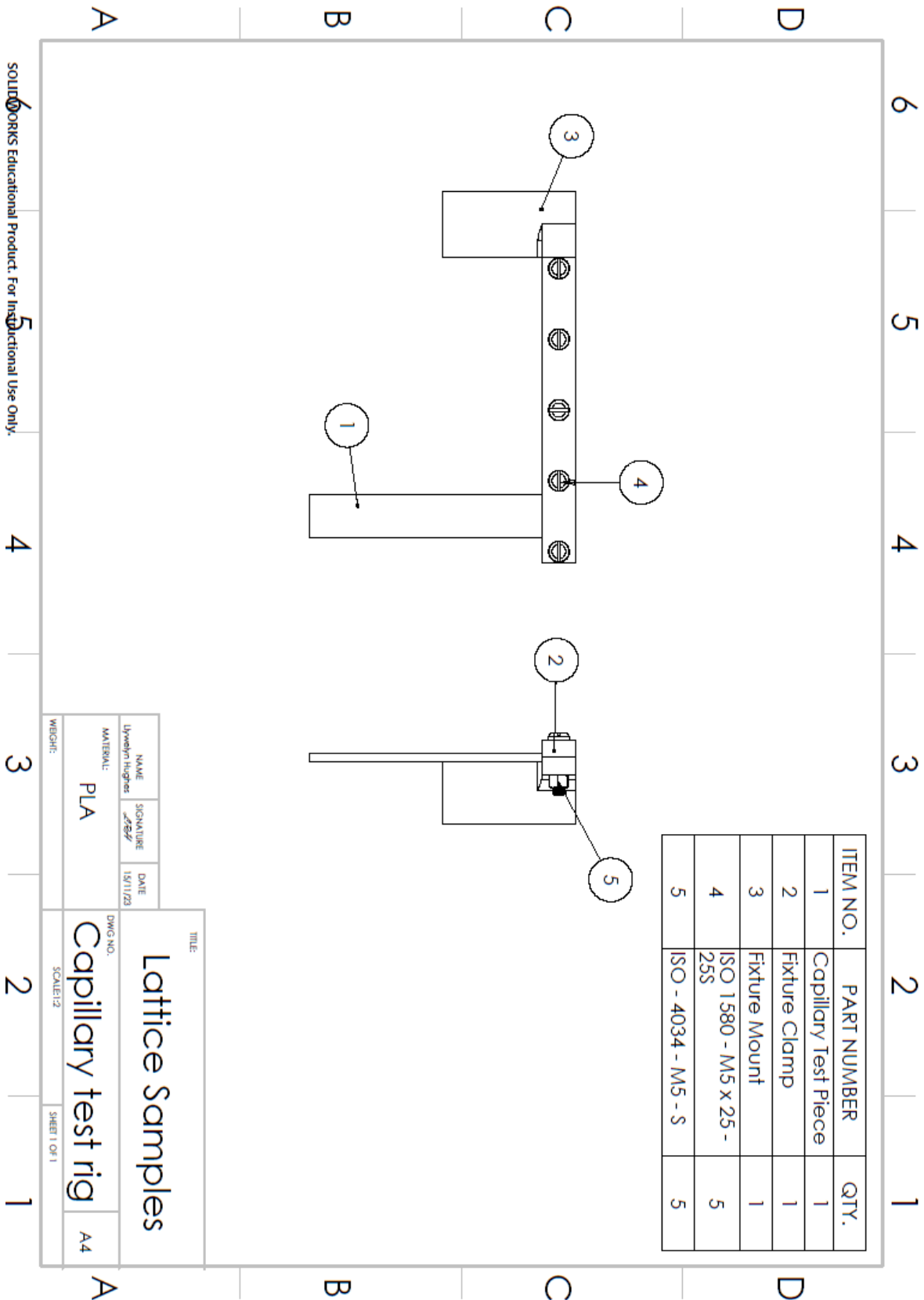


Figure 12-1. drawing of PLA capillary test rig.

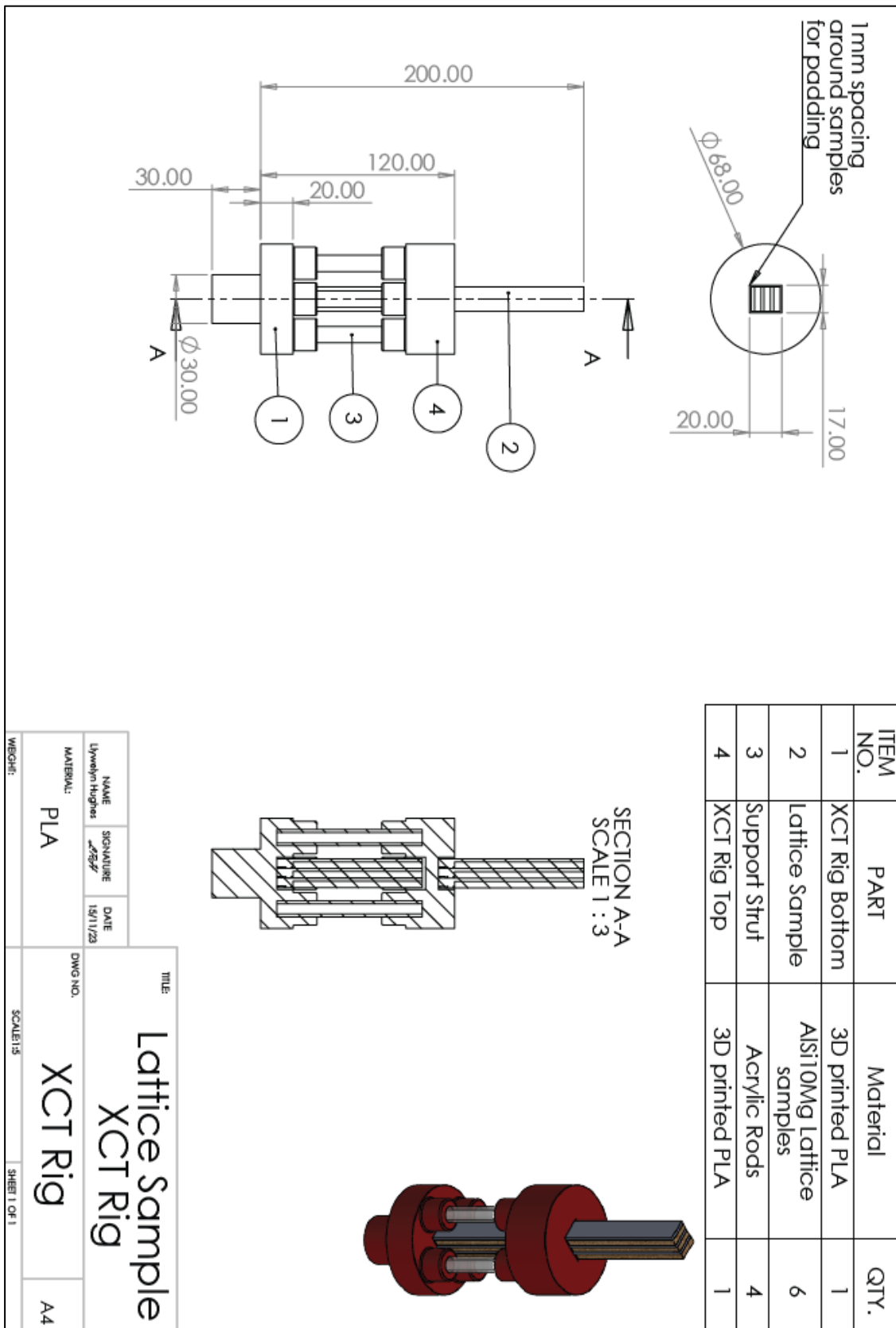


Figure 12-2. XCT sample mounting rig

12.4 LAT Practical Case Studies

The following section will exemplify the methodologies used for the development of LAT, demonstrating the tool's versatility for characterising additively manufactured lattice geometries and other heat transfer applications. Although not all applications are directly related to this research project, this section shows the benefits of such tool for the wider AM industry and community.

12.4.1 Additively Manufactured Lattice Structure

This section will undertake a deeper analysis of the additively manufactured lattice structure used for the development of the tool. Analysis was completed on all five visible external faces: x-y, both y-z and both x-z faces, relative to the build plate. The number of detected porous regions on each face ranged from 84 to 129, with all respective automatic pore analysis and aspect ratios shown in Table 12-1.

Table 12-1. Summary of lattice analysis.

Face	XY	XZ1	XZ2	YZ1	YZ2
Total Pores	98	120	129	84	112
Average Area (mm ²)	0.177	0.164	0.163	0.151	0.171
Average Diameter (mm)	0.470	0.453	0.447	0.413	0.461
Porosity (%)	39.73	37.12	37.49	38.14	37.65
Average Horizontal Cell Size (mm)	1.004	0.991	1.003	1.013	1.003
Average Vertical Cell Size (mm)	1.048	1.042	1.025	1.023	1.016
Aspect Ratio (x/y, x/z, y/z)	0.96	0.95	0.98	0.99	0.99
Manual - Strut Diameter (mm)	0.206	0.234	0.257	0.257	0.250
Automatic - Strut Diameter (mm)	0.214	0.248	0.260	0.245	0.267

The tool's manual measurement feature was used to measure both the horizontal and vertical cell sizes of each image as well as the strut thicknesses. For the manual measurements, a total of 10 data points were taken for each parameter while the automatic strut measurement feature detected between 80 and 141 struts. Figure 12-3 shows the comparative results for both automatic and manual measurement features.

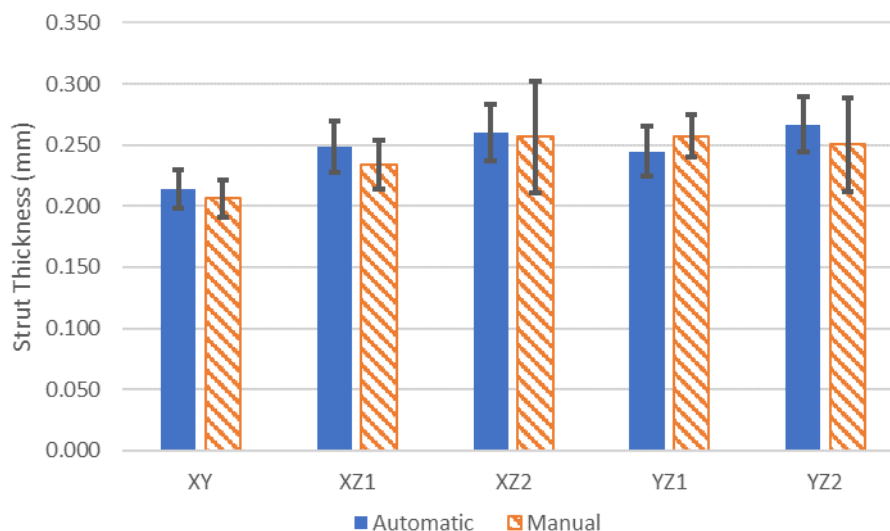


Figure 12-3 Comparative analysis of both automatic and manual strut measurement features.

Evidently, both techniques agree with no significant deviations. The standard deviation percentage of the mean exhibits a broader range in manual measurements, spanning from 6.78% to 17.80%, in contrast to the automatic measurements, which range from 7.41% to 8.74%. Overall, the average standard deviations of the means are 11.17% and 8.33% for the manual and automatic measurements, respectively. The larger value exhibited for the manual measurements reflects the smaller sample size, as standard deviation is inversely proportional to the root of the sample size [171]. This is in addition to the effect of other factors including the inherent human variability. Furthermore, it should be noted that the strut diameters of the x-y plane are measured up to ~ 0.05 smaller than the other x-z and y-z faces, which may be a result of different rates of heat dissipation through the sample resulting in irregular formation powder agglomeration on each face. Further investigation, outside the scope of this research is required to further quantify this occurrence.

LAT has effectively calculated a range of parameters, including pore areas, diameter, porosity, cell and strut sizes as well as aspect ratio. The values are consistent across all faces with an average pore diameter and porosity of 0.4485mm and 38.03% respectively. As can be seen, the aspect ratio of the unit cells lies very close to unity, as designed. Interestingly, the aspect ratio is below unity for all analysed images. For the x-z and y-z faces, this shows that the unit cells are slightly larger in the z direction, even though they show smaller sized pores. This may be a result of the anisotropic thermal expansion and contraction rates induced within the change of phase of the molten metal during the printing process, or difference in machine resolution of each axis. However, as this deviation is only a maximum of 5% and

considered relatively small, this may prove to have little effect on the wick performance. Further analysis should be undertaken for a larger dataset to increase confidence in the results. This example has demonstrated a possible method for heat pipe wick structure pore and strut analysis.

12.4.2 AM Heat Exchanger Channel

As the additive manufacturing industry strives towards achieving smaller features for improved heat transfer and flow characteristics, the repeatability of such designs is impacted. This example will analyse the repeatability of seven fine heat exchanger channels shown in Figure 12-4. Again, the tool will analyse the image in generic pixel count. The exported analysis data is shown in Table 12-2, with regions identified in Figure 12-4. Evidently, the area standard deviation accounts for the largest percentage of its average at 18.3%, compared to both perimeter and equivalent diameter indicating values of 4.0% and 8.9% respectively.

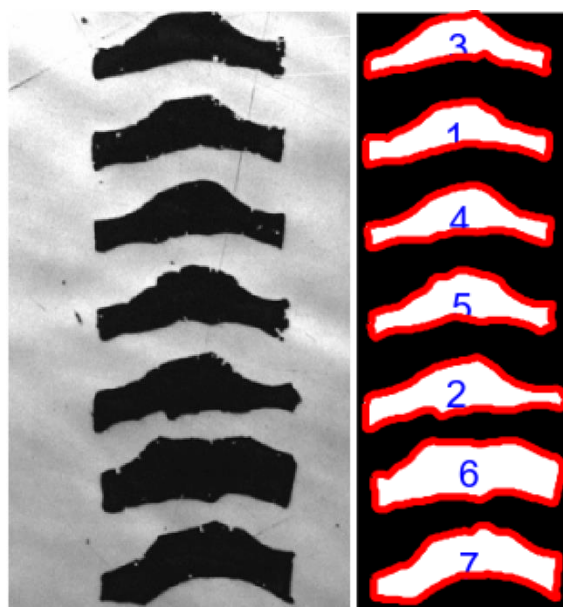


Figure 12-4. Heat exchanger channels cross-section. Original (Left), region identifier (Right).

Table 12-2. Tool analysis example data for heat exchange channels

Region	Area (Pix. ²)	Peri. (Pix.)	Dia. (Pix.)
1	2411	271.17	55.41
2	2780	289.28	59.49
3	2249	266.31	53.51
4	2377	267.07	55.01
5	2525	271.05	56.70
6	3666	288.44	68.32
7	3074	289.79	62.56
Average	2726	277.59	58.72
Std. Dev.	499.42	10.99	5.22

Upon inspection of the heatmaps, a trend is present where the areas, perimeters and equivalent diameters tend to increase from the top down, as illustrated in Figure 12-5. Utilising the manual measurements functions, the width, depth and minimum spacing averages/ standard deviations were measured as 119.92/ 2.78, 35.83/ 3.38 and 17.74/ 4.08 respectively. The largest percentage deviation (23%) was the minimum spacing, which may be attributed to the irregular and inconsistent geometry of the cross-sectional profiles. Further investigation may be required to identify any possible improvements in design, machine parameters or post processing of the structures.

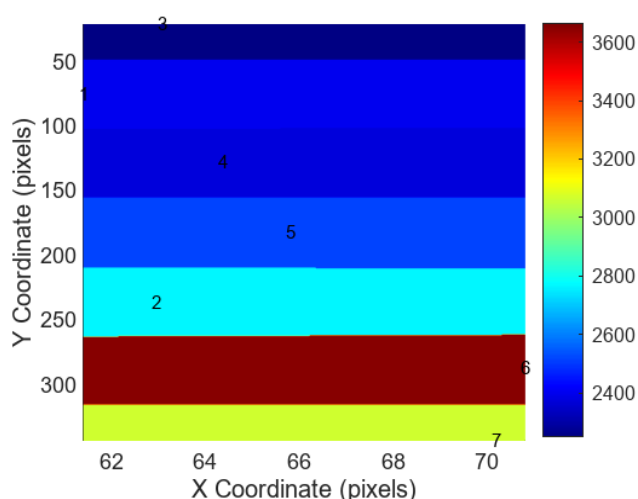


Figure 12-5. Example area heatmap of heat exchanger channels.

This tool has proven to be effective in analysing microscope images of heat exchanger channel profiles. To obtain results of greater accuracy and confidence, it is recommended to repeat the experiment with larger datasets.

12.4.3 Screen Mesh Wick Deterioration

A study conducted by Bhullar et al. [175] investigated the deterioration of screen mesh wick heat pipes due to the use of nanofluids, specifically Al_2O_3 / de-ionised water, as the working fluid. As stated in their findings, nanofluids are prone to agglomeration and sedimentation over time which can affect the heat pipe's thermal performance. Experiments were conducted at 12, 32 and 72W over a 9 month period. The use of these nanofluids resulted in improved thermal performance due to the nano-coating of Al_2O_3 on the mesh. This resulted in higher localised vapour pressure due to the sporadic flow acceleration, reduced contact angle and boiling limit enhancement. The work identified an increase in capillary action as a result of the deposition of nanoparticles and improved wick wettability, as shown in Figure 12-6. However, no further analysis into characterising the geometric difference was undertaken. Through utilising LATs features, porosity as well as areas and equivalent diameters were quickly calculated for evaluation, as shown in Table 12-3.

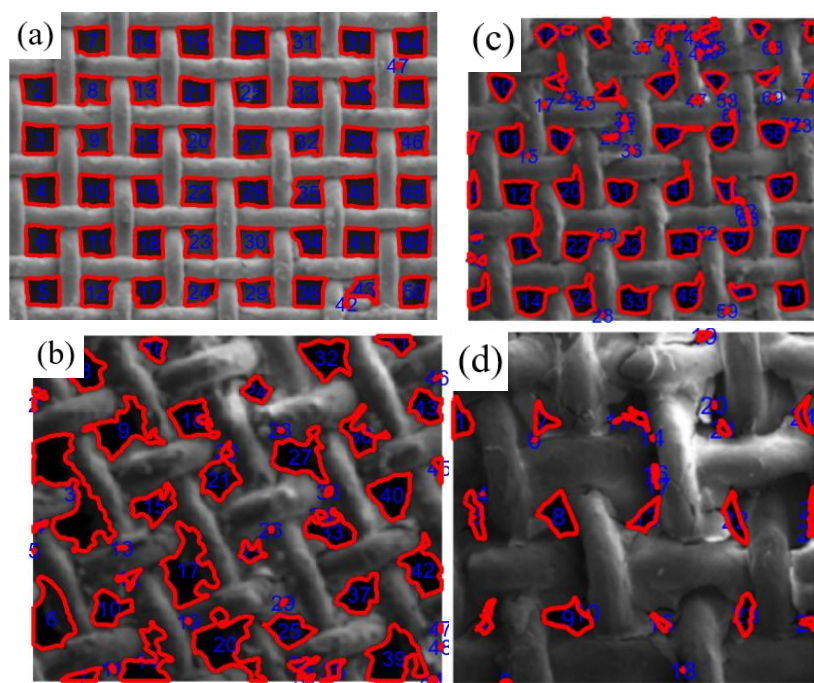


Figure 12-6. Analysed optical microscope images of mesh wick with Al_2O_3 /DI nanofluids as working fluid (a) at 0 months of manufacturing, (b) after 9 months of successive heat input of 72 W, and (c [x100], d [x200]) after 9 months of successive heat input of 12 W. Figure adapted from [175].

Table 12-3. Analysis of screen mesh wick.

	a	b	c	d
Area _{AV} (μm ²)	4624.27	1949.70	1643.78	515.60
Area _{Tot} (μm ²)	231213.47	93585.66	124927.05	13921.27
Area _{Std. Dev} (μm ²)	1048.64	2284.87	1735.56	629.77
Diameter _{AV} (μm)	75.50	40.47	37.44	20.59
Diameter Reduction (%)	-	46.39	50.41	72.73
Diameter _{Std. Dev.} (μm)	13.85	29.37	26.47	19.93
Porosity (%)	31.68	25.00	15.54	4.86
Porosity Reduction (%)	-	21.09	37.09	84.67

As can be seen, the tool has characterised the change in geometry while displaying the key characteristics necessary for heat pipe wick design and development. Further stated in the study was the choking of flow for the 12W (c and d) scenario after the 9 month period. This was a result of low internal vapour pressure allowing for increased agglomeration and sedimentation rates. LAT has successfully characterised this phenomenon, especially for case (d) where a reduction of 72.73% and 84.67% was exhibited for the equivalent diameter and porosity respectively. This significantly increased internal pressure drop while considerably reducing permeability. In addition to a detected porosity reduction, the agglomeration of particles had increased the measured wire diameter. LAT's strut analysis and manual measurement features were used to characterise this change, as shown in Figure 12-7.

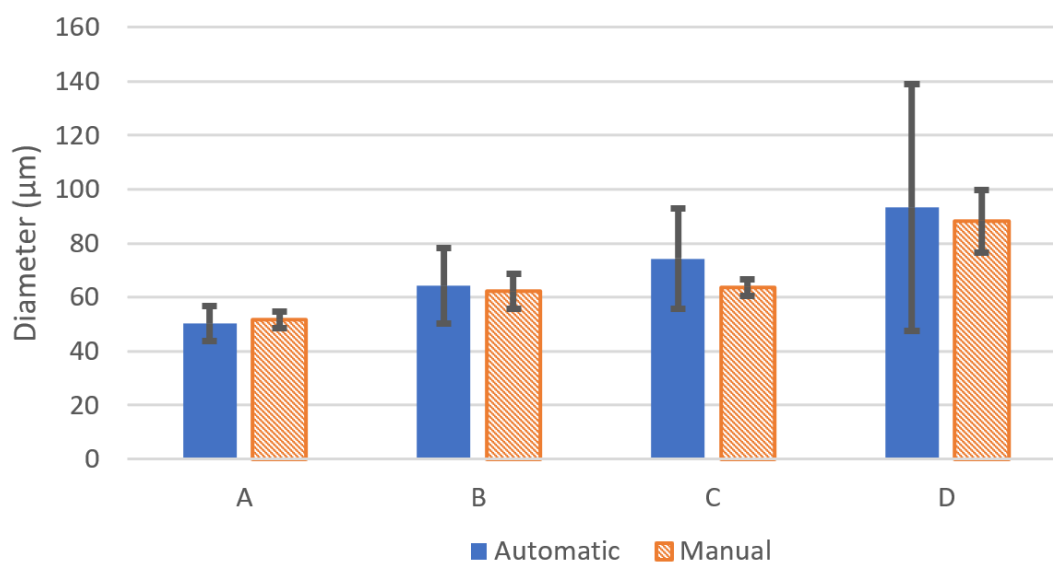


Figure 12-7. Wire comparative analysis with LAT's automatic strut analysis and manual features.

Evidently, a significant increase in wire diameter has been observed with up to 50 μm difference between cases (a) and (d). Furthermore, the deviation of wire diameters, as shown by the error bars, has significantly increased, especially for the measurements taken with the strut analysis feature. The smaller standard deviation seen for the manual measurements may be a result of excessive image noise and geometric defects resulting in inadequate identification of struts for the automatic method. For this reason, the manual method may be preferred to analyse structures with more stochastic features such as that seen in case d.

In addition to characterising the wick structure, the tool was also able to characterise the Al_2O_3 nanoparticles, as can be seen in Figure 12-8. However, due to the low quality of the original Transmission Electron Microscope (TEM) image extracted from the paper, additional noise and irregularities were present during the binarising and region identification process.

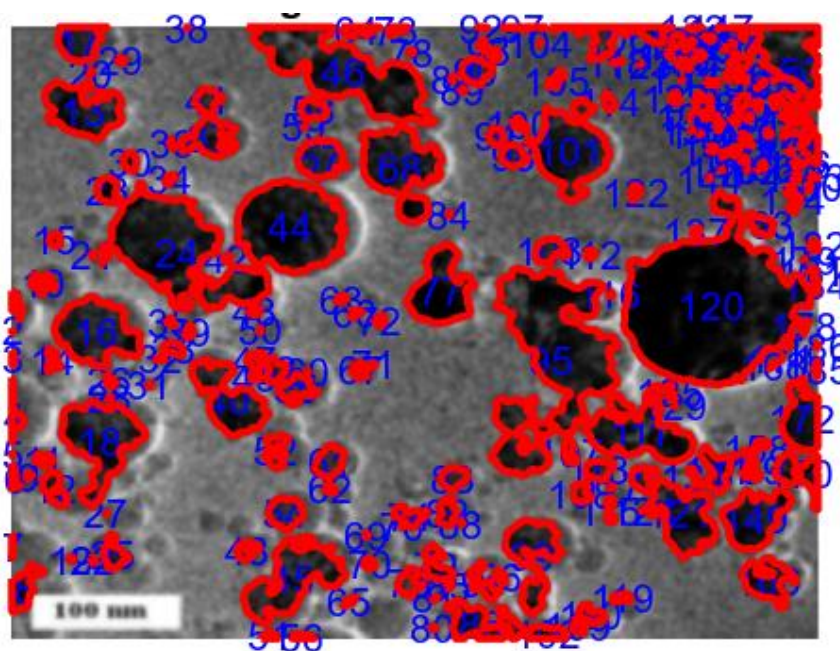


Figure 12-8. Al_2O_3 nanoparticle analysis regions from TEM [175].

This has resulted in poor particle separation. Nonetheless, the tool has successfully identified most particles as agglomerations, as opposed to individual particles. However, this may be acceptable for scenarios where total particle area is of interest, as opposed to individual particle count or properties.

This shows the value of an effective and efficient analysis tool, specifically designed for heat pipe wick structures. Further experimental work, in conjunction with this tool, could determine the limit at which choking occurs and estimate the life span of such heat pipes at

given operating conditions. As an additional application, LAT has shown the potential of particle analysis, although this falls outside of the scope of this current research.

12.4.4 AM Counterflow Burner Cooling Nozzle

A study into the development of an additively manufactured counterflow burner cooling nozzle encountered issues resulting in excessive leakage of water through the component. Upon initial investigation and slicing of the component, as shown in Figure 12-9, intolerable internal porosities were present within the component. High porosity levels resulted in sufficient pore interconnectivity allowing the flow of liquid through the walls.

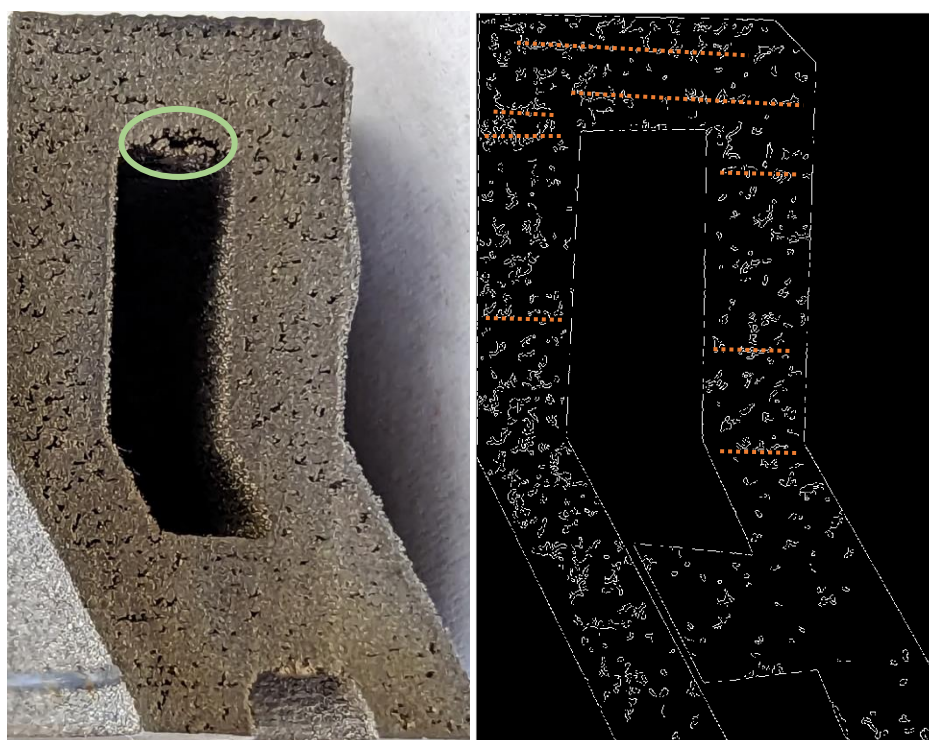


Figure 12-9: Defective AM Counterflow Burner Cooling Nozzle cross-section (Left) and Canny Edge detection (Right) with orange dashed lines representing the direction of porosity inline with the build plane

Multiple analysis of the cross-section with LAT calculated a porosity of $6.24\% \pm 1\%$ with an average pore area of 0.0241mm^2 . Through visual inspection of the edge detection image, its noticeable that the pores are often aligned in the horizontal plane. Evidently, this was also the x-y build plane during the print. Initial investigations indicate insufficient powder melting throughout the layers of the component resulting in excessive porosity due to powder sintering. This could be a result of incorrect machine parameters including laser power, scan

speed, hatch spacing or layer thickness. Another cause might include powder contamination within the machine due to regular material changes.

As can be seen from the left image of Figure 12-9, insufficient powder melting is present at the upper horizontal surface, represented by the green circle. As this is an enclosed section, the use of support material was not possible. As a result, the overhanging section has partially collapsed creating a large porous area and significant visible defects. Further design iterations to chamfer the edges to $\sim 45^\circ$ may alleviate this issue. With the use of the heatmap function, a visualisation of the pore size distribution throughout the cross-section is achieved, as shown in Figure 12-10.

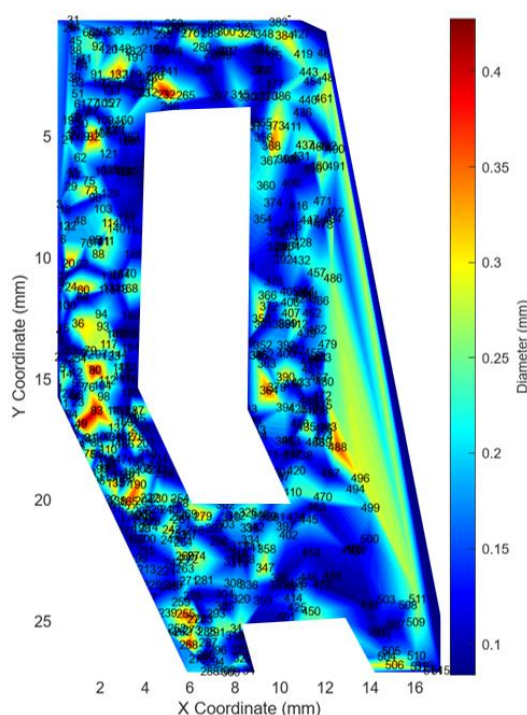


Figure 12-10 Visualisation of heatmap distribution of the pore diameter within the nozzle cross-section.

As can be seen from Figure 12-10, the larger pores are distributed around the thinner external surfaces, compared to the thicker horizontal sections. This may be a result of a combination of several factors including:

- Increased cooling rates at thinner sections, leading to incomplete fusion of the powder and the formation of keyhole porosities
- Inadequate scan strategy and laser parameters
- Inconsistent layer thickness or poor powder flow
- Increased thermal stress concentrations

Analysis of such component containing stochastic porosities has proven to be difficult in determining and setting the binarisation thresholding value. Furthermore, such analysis is only representative of the given image and could not be representative of the volumetric porosity. Further investigation including μ -XCT and improved surface preparation is required to increase the confidence of results. Here, the heatmap distribution function within LAT has shown to be beneficial in identifying pore distribution trends throughout the AM component.

12.5 Capillary Rise Matlab Script

```
% Replace with the path to your image folder
sample_name = 'H7_1_12.09';
image_folder = strcat('C:\Users\...',sample_name); %sample_name
file_pattern = fullfile(image_folder, '*.jpg');
jpeg_files = dir(file_pattern);
num_files = length(jpeg_files);
frame_time = zeros(num_files,1);
frame_rate = 10; % Change value to appropriate frame rate (fps)

% Extract the final digits from the file name using regular expressions
filename_col = jpeg_files.name';
digits = zeros(1,num_files);

[~,filename,~] = fileparts(filename_col);

for i = 1:numel(filename_col)
[~, filename, ~] = fileparts(filename_col(i)); % Process each filename individually

% Use regular expression to extract digits after the hyphen
match = regexp(filename, '-(\d+)', 'tokens', 'once');
digits_str = match(1); % Extract the matched digits as a string
digits(i) = str2double(digits_str); % Convert to a numeric value

% Calculate frame_time
```



```

    frame_time(i) = (digits(i) - digits(1)) * (1 / frame_rate);
end

% Load the first JPEG image and display it
%directory = 'C:\Users\....';
fileList = dir([image_folder '*.jpg']);
fileName = fullfile(image_folder, strcat(sample_name, '-200.jpg')); % Enter name of
initialising image
image = imread(fileName);
figure;
imshow(image);

```

Scaling

```

% % % Draw scaling Line
scale_line = drawline;
end_position = scale_line.Position; % Find x, y position of each end point
x1 = end_position(1,1);
y1 = end_position(1,2);
x2 = end_position(2,1);
y2 = end_position(2,2);

%Calculate length of line in pixels
pix_dist = sqrt( (x2-x1).^2 + (y2-y1).^2);

%Create popup to ask for physical distance
prompt = 'Enter Physical distance:','Enter units (m, cm, mm, um)';
phys_dist = inputdlg(prompt,'Physical Distance');
LengthEditField.Value = str2double(phys_dist(1));
UnitsEditField.Value = phys_dist(2);

resolution = LengthEditField.Value / pix_dist;

```

Crop



```
roi = drawrectangle; %Prompt User to draw rectangle  
position = roi.Position;
```

Analyse Image

```
filenames = cell(num_files, 1);
```

```
% Loop through remaining images, crop and detect maximum height of horizontal marker
```

```
%max_heights = zeros(num_files,1);
```

```
readImage = false;
```

```
last_frame = 450; %num_files
```

```
max_height = zeros(last_frame, 1);
```

```
scaled_heights = zeros(last_frame, 1);
```

```
for i = 1:last_frame
```

```
    % Load image and convert to grayscale
```

```
    img = imread(fullfile(jpeg_files(i).folder, jpeg_files(i).name));
```

```
    img_cropped = imcrop(img, position);
```

```
    img_cropped = imnlmfilt(img_cropped);
```

```
    img_cropped = imgaussfilt(img_cropped, gaus_filt);
```

```
    img_gray = rgb2gray(img_cropped);
```

```
    thresh = graythresh(img_cropped)-0.15;
```

```
    img_bin = imbinarize(img_gray, thresh);
```

```
    img_fill = imfill(img_bin, "holes");
```

```
    img_props = regionprops(img_fill, 'BoundingBox');
```

```
    num_regions = length(img_props);
```

```
    height = zeros(num_regions, 1);
```



```

for k = 1:num_regions
    height(k) = img_props(k).BoundingBox(4);
end
max_height(i) = max(height);
scaled_heights(i) = max_height(i)*resolution;

% Store the results
filenames(i) = jpeg_files(i).name;
%hold on

if ((i == 2) || (i == 20) || (i == 80) || (i == 100) || (i == 150) || (i == 200) || (i == 321))
    figure
    montage(img_bin,img_gray, img_cropped, "size", [1 3])
    title("Frame "+i+ ", Time: " +(i-1)/frame_rate+ "s")
end

end

```

Analyse Data

```

% Moving average to smooth data
av_Size = 40;

[filtered_heights, TFrm] = rmoutliers(scaled_heights,"movmedian",5);
%filtered_heights = filtered_heights';
%filtered_heights(1) = 0;

num_outliers = nnz(TFrm) %Nuber of Outliers
num_filtered = length(filtered_heights);
frame_time = frame_time(1:last_frame);

try
    %Remove outliers from analysis
    filename_col = filename_col(~TFrm,:);

```



```

    frame_time = frame_time(~TFrm,:);
end
smoothed_heights = smoothdata(filtered_heights,"movmean",10);
filtered_vel = zeros(num_filtered, 1);
filtered_acc = zeros(num_filtered, 1);
num_filtered = length(smoothed_heights);

%Calculate Velocity
for i=1:num_filtered-1
    filtered_vel(i) = (smoothed_heights(i+1)-smoothed_heights(i))./(frame_time(i+1)-
frame_time(i));
end
smoothed_vel = filtered_vel;

%Calculate Acceleration
for i=1:num_filtered-1
    filtered_acc(i) = (smoothed_vel(i+1)-smoothed_vel(i))./(frame_time(i+1)-
frame_time(i));
end
smoothed_acc = filtered_acc;

Display Data
max_height = max(smoothed_heights)

table_data = table(filename_col, frame_time, filtered_heights, smoothed_heights,
smoothed_vel, smoothed_acc);
table_data.Properties.VariableNames = 'Filename', 'time (s)', 'Filtered Height
(mm)', 'Smoothed Heights (mm)', ...
'VeLOCITY (mm/s)', 'Acceleration (mm/s^2)';
disp(table_data);

%Plot Height Chart
figure;
plot(frame_time, filtered_heights,"b--", "LineWidth", 2);

```



```
hold on
plot(frame_time, smoothed_heights, "r-", "LineWidth", 3);
legend("Filtered Height", "Smoothed Height")
ylabel('Rise Height (mm)');
xlabel('Time (s)');
title('Rise Height vs Time');

%Plot Velocity Chart
hold off
figure;
plot(frame_time, smoothed_vel, "r-", "LineWidth", 2);
ylabel('dh/dt (mm/s)');
xlabel('Time (s)');
title('Rate of Rise (dh/dt) vs Time');

%Plot Acceleration Chart
figure
plot(frame_time(2:end), smoothed_acc(2:end), "r-", "LineWidth", 2);
ylabel('d^2x/dt^2 (mm/s^2)');
xlabel('Time (s)');
ylim([-3,3]);
title('Acceleration (d2h/dt2) vs Time');

%Plot dx/dt vs h
figure
plot(smoothed_heights, smoothed_vel, "r-", "LineWidth", 3);
xlabel('Rise Height (mm)');
ylabel('dh/dt (mm/s)');
title('Rate of Rise (dh/dt) vs Rise Height');

% Plot 1/h vs dh/dt
figure
h_inv = 1./smoothed_heights;
```



```
plot(h_inv,smoothed_vel,"r-","LineWidth",3);  
xlabel('1/h (mm^-1)');  
ylabel('dh/dt (mm/s)');
```

12.6 Pressure Transducer Calibration

<h1 style="margin: 0;">CERTIFICATE OF CALIBRATION</h1>	Certificate No. 1851606
 RS Calibration Calibration and Repair Service	Page 2 of 2 Pages

Environment

The ambient temperature and relative humidity throughout the calibration were $(20 \pm 2) ^\circ\text{C}$ and $(40 \pm 20) \%RH$ respectively.

Method

The instrument was held in a temperature controlled environment for a period of not less than 4 hours prior to calibration.

The instrument was powered up by a PSU set to approximately 15 V DC and allowed to stabilise for approximately 5 minutes.

The instrument was positioned in the vertical position with its pressure entry port facing downwards. The instrument was calibrated using a Fluke 6270A Pressure Calibrator, applying values of gauge pressure and recording the instrument's output using a digital multimeter.

Prior to calibration the instrument was exercised to full scale pressure and then returned to zero.

The pressure medium used was BOC nitrogen (oxygen free) SDS No. TG-8347

Range Gauge	Applied Pressure	Nominal Output	Measured Output	Percentage of Tolerance
10 bar	0 bar	4.000 mA	3.999 mA	2 %
	2 bar	7.200 mA	7.190 mA	25 %
	4 bar	10.400 mA	10.385 mA	38 %
	6 bar	13.600 mA	13.583 mA	43 %
	8 bar	16.800 mA	16.787 mA	33 %
	10 bar	20.000 mA	19.995 mA	12 %

Measurement uncertainties:

Measurement uncertainty of the measured dc current: ± 450 ppm

Measurement uncertainty of the applied pressure: ± 0.0010 bar

CALIBRATED BY:- DOH

Reported values

The uncertainties quoted refer to the applied values, which include any identified contribution of the instrument under test and not to the ability of the instrument to maintain its calibration.

END OF CALIBRATION



The current-pressure calibration curves have been shown in Figure 12-11.

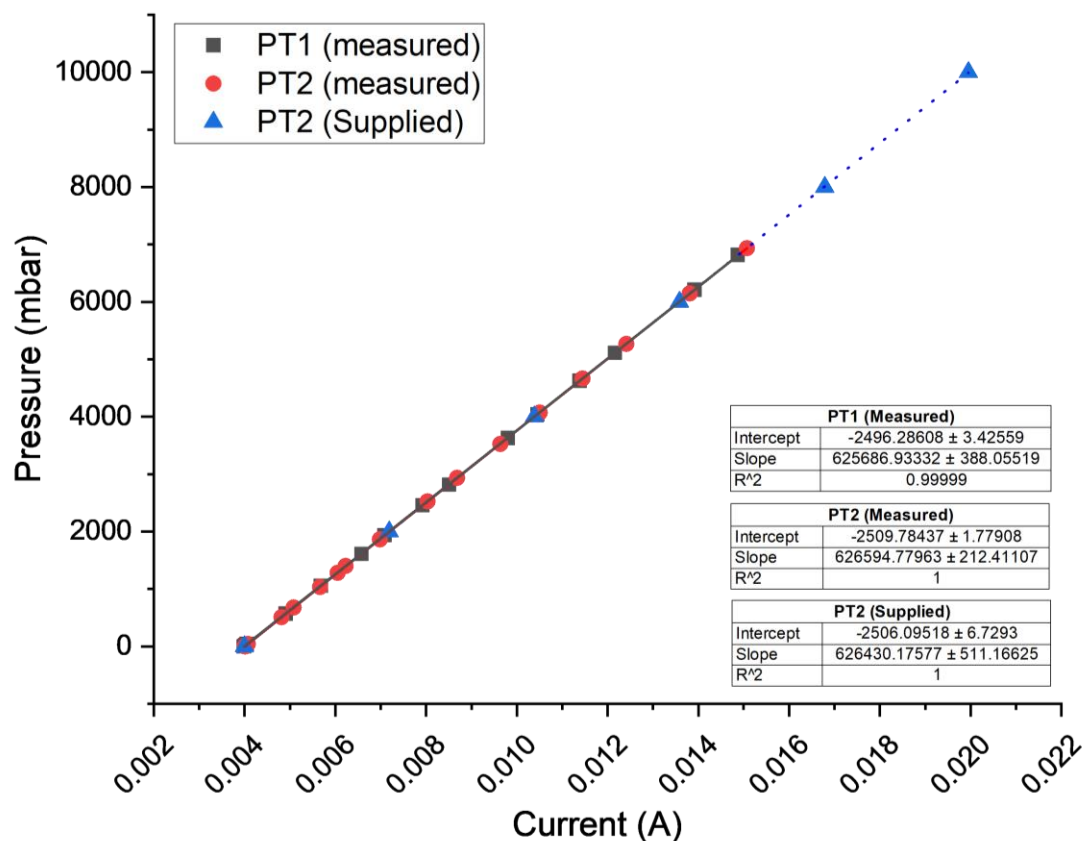


Figure 12-11. Calibration curves for PT1 and PT2.

Clearly, the measured and supplied calibration curves for PT2 are in very good agreement with only a 0.1471% and 0.0263% difference between their intercepts and slopes, respectively. The agreement between the supplied and measured calibration curves confirms the methodology used and validates the results achieved for PT1 where again, clear agreement is present. The determined slopes and intercept values of both transducers were later imported directly into the National Instruments FlexLogger software.